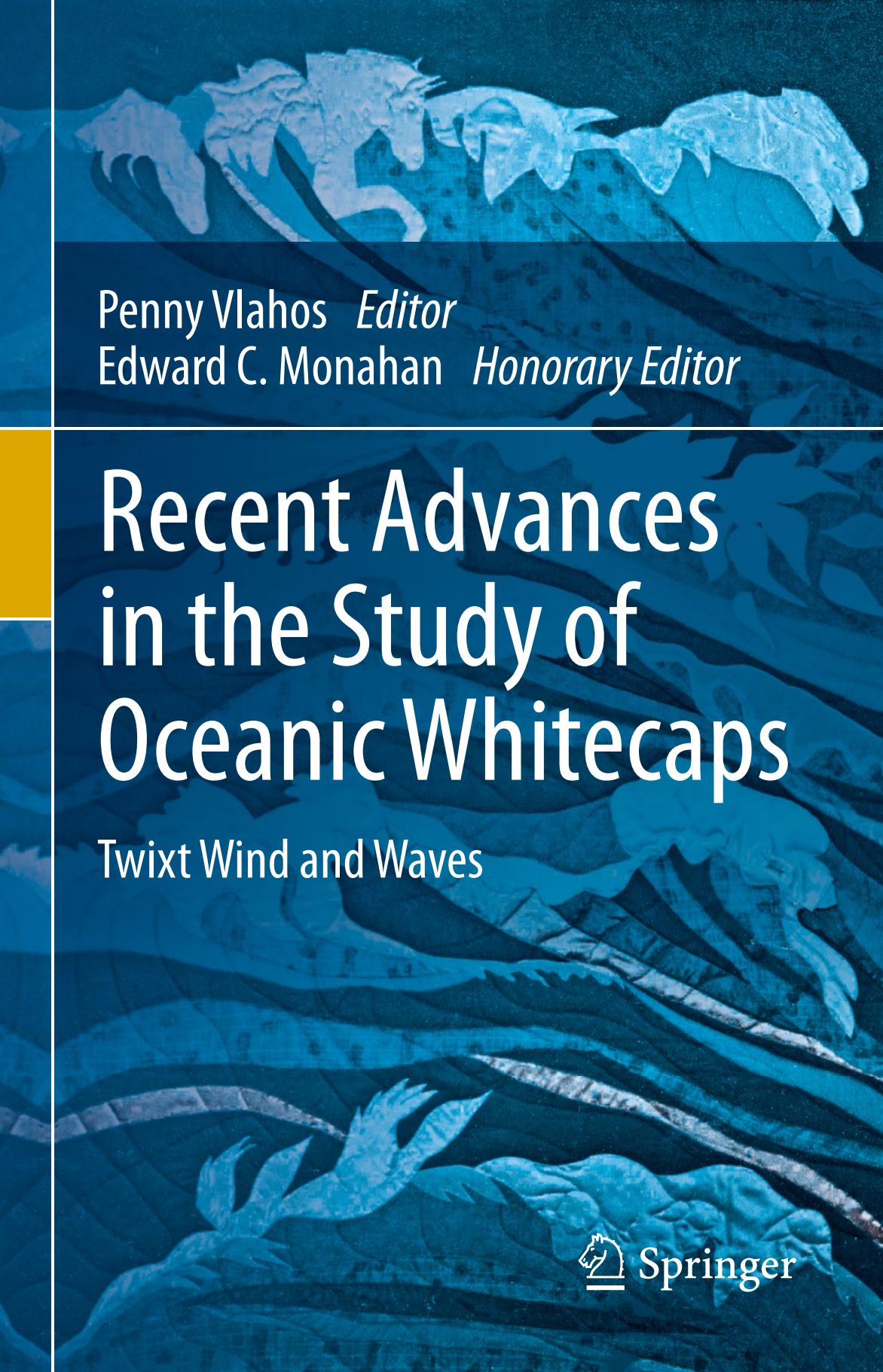
Penny Vlahos Editor
Edward C. Monahan Honorary Editor
Recent Advances in the Study of Oceanic Whitecaps
Twixt Wind and Waves
Springer

Recent Advances in the Study of Oceanic Whitecaps

Penny Vlahos
Editor

Edward C. Monahan
Honorary Editor

Recent Advances in the Study of Oceanic Whitecaps

Twixt Wind and Waves

Springer

Editor
Penny Vlahos
Department of Marine Sciences
University of Connecticut
Groton, CT, USA

Honorary Editor
Edward C. Monahan
Department of Marine Sciences
University of Connecticut
Groton, CT, USA

ISBN 978-3-030-36370-3 ISBN 978-3-030-36371-0 (eBook)
https://doi.org/10.1007/978-3-030-36371-0

This Springer imprint is published by the registered company Springer Nature Switzerland AG.
The registered company address is: Gewerbestrasse 11, 6330 Cham, Switzerland

Acknowledgements

The authors would like to thank Margaret Van Patten for her talented editorial assistance.

Contents

Contributors

Magdalena D. Anguelova Remote Sensing Division, Naval Research Laboratory, Washington, DC, USA

Sophia E. Brumer Laboratoire d'Océanographie Physique et Spatiale (LOPS), University of Brest, CNRS, IRD, Ifremer, IUEM, Brest, France

Marc P. Buckley Institute of Coastal Research, Helmholtz-Zentrum Geesthacht, Geesthacht, Germany

Adrian H. Callaghan Department of Civil and Environmental Engineering, Imperial College London, London, UK

Luigi Cavaleri CNR-ISMAR, Institute of marine Sciences, Venice, Italy

Alejandro Cifuentes-Lorenzen California State University Maritime Academy, Vallejo, CA, USA

Heidi M. Dierssen Department of Marine Sciences, University of Connecticut, Groton, CT, USA

Shungudzemwoyo P. Garaba Marine Sensor Systems Group, Institute for Chemistry and Biology of the Marine Environment, Carl von Ossietzky University of Oldenburg, Wilhelmshaven, Germany

Giles Hooker Department of Statistics and Data Science, Cornell University, Ithaca, NY, USA

Bernd Jähne HCI and IWR at Institute of Environmental Physics, Heidelberg University, Heidelberg, Germany

S. G. Jennings School of Physics and Ryan Institute, National University of Ireland, Galway, Ireland

Jun-Hong Liang Department of Oceanography and Coastal Sciences & Center for Computation and Technology, Louisiana State University, Baton Rouge, LA, USA

Edward C. Monahan Department of Marine Sciences, University of Connecticut, Groton, CT, USA

C. O'Dowd School of Physics and Ryan Institute, National University of Ireland, Galway, Ireland

Kaylan Randolph California State University Maritime Academy, Vallejo, CA, USA

B. Scanlon School of Physics and Ryan Institute, National University of Ireland, Galway, Ireland

A. Staniec Department of Marine Sciences, University of Connecticut Groton, Groton, CT, USA

Fabrice Veron School of Marine Science and Policy, University of Delaware, Newark, DE, USA

Penny Vlahos Department of Marine Sciences, University of Connecticut, Groton, CT, USA

B. Ward School of Physics and Ryan Institute, National University of Ireland, Galway, Ireland

Kianoosh Yousefi Department of Mechanical Engineering, University of Delaware, Newark, DE, USA
School of Marine Science and Policy, University of Delaware, Newark, DE, USA

Christopher J. Zappa Lamont-Doherty Earth Observatory, Columbia University, Palisades, NY, USA

Chapter 1
Introduction

Penny Vlahos

> The fair breeze blew, The white foam flew, And the forrow followed free. We were the first to ever burst into the silent sea.
> — Samuel Taylor Coleridge, The Rime of the Ancient Mariner

The interaction between the surface ocean and the atmosphere is arguably the most important interface of climate control on our planet. Amidst a dynamic and changing climate, it is our challenge to understand and constrain this interface in order to accurately predict future climate conditions. Edward C. Monahan set out to tackle one of the most esoteric aspects of this interaction, namely the physics that can describe the nature of breaking waves and their resulting bubble plumes. He has dedicated his career to enhancing our understanding of the frequency, nature and characteristics of these turbulent phenomena that serve to introduce discontinuity in the seas surface boundary layer and to in effect, increase the surface area of air-water exchange.

To date the largely empirical algorithms that have been developed continue to be based on the parameterizations developed by Monahan and colleagues. The contributions to this collection are testimony to this.

Part I "Whitecap Parameterizations" addresses the current state of parameterizations and the potential for improvements in light of new technology. Breaking waves represent an instability in the continuous sea surface that leads to a transfer of energy through the discontinuity represented by whitecaps. As the energy fields that lead to these surface ocean features are complex, several approaches have been applied to characterize them. Scanlon et al. (Chap. 2) present a thorough review of whitecap parameterizations and techniques resulting from sea surface imagery. The authors emphasize that "future advancement of whitecap functions will likely consider multiple-environmental-parameter functions". A.H. Callaghan (Chap. 3) addresses

P. Vlahos (✉)
Department of Marine Sciences, University of Connecticut, Groton, CT, USA
e-mail: Penny.vlahos@uconn.edu

P. Vlahos (ed.), *Recent Advances in the Study of Oceanic Whitecaps*,
https://doi.org/10.1007/978-3-030-36371-0_1

the energy delivered to the ocean surface at different wind speeds and energy dissipation due to whitecaps within the context of energy conservation and compellingly argues that whitecaps are the dominant balance to wind energy at high wind speeds. Globally, the relationship between whitecaps and windspeed differs and this is addressed in Chap. 4 by Hooker et al. They investigate the relationship of wind speed and whitecap coverage, confirming a significant increase in the dependence of whitecapping on wind speeds as one moves to higher sea surface temperature waters. They propose a model to account for this. Chapter 5 by L. Cavaleri reflects on the interactions of whitecapping and windspeed during precipitation events. Finally, among these improvements in parameterizations are the direct measurements of the airside viscous tangential stress presented in Chap. 6 by Yousefi et al. These observations are based on combined particle image velocimetry (PIV) and laser-induced fluorescence (LIF) techniques and identify the wind thresholds in which viscous effects have significant impact on wave generation, wave crests and the peak of separation.

Part II "Whitecaps and Gas Transfer" introduces the implications of these parameterizations for air-sea gas exchange. It has long been recognized that differences among gases that include molecule size and non-ideal effects such as polarity should alter gas exchange rates. In Chap. 7 Vlahos and Monahan address the emerging research that addresses the physical-chemical differences among diffusing gases and how investigators have incorporated this "chemical enhancement" to date. Current algorithms remain largely empirical. As many of the measurements required at high wind speeds remain a challenge, modelling approaches are necessary to test hypotheses. In Chap. 8 Liang compares Eularian and Lagrangian approaches to bubble modeling. Liang emphasizes that "gas dissolution is the dominant factor shaping the distribution of bubbles" in an oceanic surface boundary layer and notes that often laboratory experiments cannot not simulate this effect. Staniec et al. examine in Chap. 9 the flipside of breaking waves by investigating the potential role of sea spray in gas exchange. The role of sea spray in terms of heat and momentum transfer has been well characterized but its role in the transfer of gases has only recently been examined. This section concludes with Chap. 10, which provides both an historical perspective of gas transfer and a description of more recent transfer velocities of gases measured in a laboratory setting. Jahne's synopsis in Chap. 10 illustrates the many remaining mechanistic questions in air-sea gas transfer.

Part III "Whitecaps and Remote Sensing" addresses the current state of whitecap quantification through remote sensing. The synoptic power of remote sensing offers a breakthrough in our understanding of ocean whitecaps and their contribution to heat, momentum and biogeochemical exchanges including aerosol formation. One would anticipate that the next 30 years will bring significant improvements in our understanding of air-sea coupling. Chapter 11 by Anguelova reviews the current state of use of visible, infrared, and radio electro-magnetic frequencies to observe and measure whitecaps. Surface brightness and temperature may also estimate whitecap coverage after atmospheric corrections. Chapter 12 by Cifuentes and Lorenzen experiment with ocean color intensity in relation to total kinetic energy dissipation rates using a preliminary data set from the Southern Ocean. Their results imply promise for this application of ocean color, though separating ocean swell and wind driven waves remains a challenge. This section concludes with Chap. 13 by Dierssen and Garaba who explain the current shortcomings in remote sensing

correction techniques with regards to estimating whitecap coverage and how additional reflectance from plastics, coccolithophores, etc., may be identified by the application of recent higher resolution satellite capabilities.

The collection was inspired by and concludes with, “Twixt Wind and Waves”, an historic perspective by E.C. Monahan himself. This account begins from his entry as an undergraduate into Engineering Physics at Cornell and his research involvement with the then evolving discipline of Oceanography as a graduate student at the Massachusetts Institute of Technology where he decided to focus on the correlation between sea spray, whitecap coverage, and wind speed. It would be nearly 20 years after this that these efforts would converge into the most widely used whitecap source function still in use today, 60 years after that unknowing undergrad entered his first lecture halls. E.C. Monahan walks us through 6 decades of whitecap research and the efforts to shift between empirical to theoretically based algorithms. He takes us across the air water interface of lakes and oceans in an effort to show us how energy transferred across this boundary is influenced by the stability of the boundary layer, the sea state, and how these translate into the degree of whitecapping observed across global regions.

Part I
Whitecap Parameterizations

Chapter 2
Parameterising Whitecap Coverage Using Sea Surface Imagery

B. Scanlon, B. Ward, C. O'Dowd, and S. G. Jennings

Abstract Although Edward C. Monahan (ECM) spend the majority of his working career at The Department of Marine Sciences of the University of Connecticut (33 years), he also spent 10 years at University College Galway (UCG), Ireland (now known as the National University of Ireland Galway-NUI Galway) where he developed four key strands of research: simulated laboratory tank experiment into bubble-mediated aerosol production from artificial breaking waves; field and studies of spray-generated aerosol production; modelling and statistical analysis of sea-spray production aerosol measurements; analysis of whitecaps coverage. The evolution of the technologies, theories, and approaches used to elucidate and quantify oceanic whitecapping, pioneered by ECM, are reviewed here.

2.1 Preamble

This chapter is a contribution to Edward C. Monahan's (ECM) Festschrift to celebrate his 33rd year at the Department of Marine Sciences of the University of Connecticut (UConn). Prior to taking up his position at UConn, ECM spent 10 years at University College Galway (UCG), Ireland, now known as the National University of Ireland, Galway (NUI Galway). ECM joined the Department of Oceanography at UCG as Statutory Lecturer in 1976. He established the Physical Oceanography Research Unit, and adopted a logo, shown in Fig. 2.1 (left) – 'Capaill Mhananáinn agus Caitheadh na dtonn' with the wording at the lower end of the logo: 'Aigeaneolaíocht Fhisiciúil' or 'Physical Oceanography'. Mananánn (mac Lir) is the old Irish mythological name for God of the sea who is often depicted as a masterful or capable sailor who is riding on the ocean like a horse – hence the 'Capaill Mananáinn' or 'the horses of Mananánn'. 'Caitheamh na dtonn' translates as 'spray from the waves'.

ECM's initial research work at UCG concentrated on oceanic currents; study of oceanic circulation in Irish waters; and on sea surface properties including

B. Scanlon (✉) · B. Ward · C. O'Dowd · S. G. Jennings
School of Physics and Ryan Institute, National University of Ireland, Galway, Ireland
e-mail: brian.scanlon@nuigalway.ie; bward@nuigalway.ie

P. Vlahos (ed.), *Recent Advances in the Study of Oceanic Whitecaps*,
https://doi.org/10.1007/978-3-030-36371-0_2

Fig. 2.1 The Logo of the Physical Oceanography Research Unit at UCG (left), with explanations given in the text. A quilted patchwork wall-hanging, depicting oceanic whitecaps, produced by Helen Hardesty and Elizabeth Monahan on the occasion of the Whitecap Workshop at UCG in September 1983 (right)

absorbance and sea-water colour (Monahan et al. 1981). Thereafter, and following on from some of his earlier work (Monahan 1968, 1971), ECM's research concentrated more on whitecap formation and associated marine aerosol production. In 1978, ECM, along with initial co-investigators Tom O'Connor and Aodhagán Ó Rodaighe from the Department of Physics, was awarded a fairly substantial grant from the U.S. Office of Naval Research, to study the influence of whitecaps on the physical character of the lower atmosphere. The funding continued for a further 7 years and enabled ECM to build up an active Research Group at UCG, members of which included: Peter A. Bowyer, Postgraduate student (Ph.D., 1986); David M. Doyle, Postgraduate student (M.Sc., 1984); Michael P. Fitzgerald (Research Assistant); M.R. Higgins (Research Assistant); Michael C. Spillane (Post-Doctoral Fellow); P.J. Stabeno (Post-Doctoral Fellow); Jan J. Taper (Research Assistant); and David K. Woolf, Postgraduate student (Ph.D., 1988). Within UCG, ECM collaborated closely with Iognáid Ó Muircheartaigh (Department of Mathematics/Statistics) on statistical relationships between oceanic whitecaps and meteorological parameters. During his time at UCG, ECM also developed several collaborations abroad including: K.L. Davidson and D.E. Spiel (Departments of Meteorology & Physics, Naval Postgraduate School, Monterey, CA); R. Doerffer. GKSS Forschungszentrum, Geesthacht. Federal Republic of Germany, S. Hellerman of the NOAA Geophysical Fluid Dynamics Laboratory, Princeton; G. de Leeuw, Physics Laboratory, TNO, The Netherlands; K.A. Rahn, Graduate School of Oceanography, University of Rhode Island; and D.C. Blanchard, R.J. Cipriano, and L.D. Syzdek, of the State University of New York, Albany. During his tenure at UCG, ECM developed a strong marine-focussed research cluster, which exists to

this day. There were 4 main strands of research work carried out by ECM while at UCG, which are briefly outlined below together with some related publications: Simulated laboratory tank experiments of aerosol production from artificially breaking waves (Bowyer et al. 1990; Cipriano et al. 1987; Monahan and O'Muircheartaigh 1980; Woolf et al. 1987); Field aerosol measurements at Gort na gCapall, Inishmore, Aran Islands, Co. Galway; Modelling and statistical studies of marine aerosol formation and related environmental parameters (Monahan and Woolf 1989; Monahan and Zietlow 1969; Monahan et al. 1982; Muircheartaigh and Monahan 1986); and analyses of whitecap observations and whitecap coverage from ship cruises – JASIN (1978), STREX (1980), MIZEX (1983, 1984), and HEXOS (1984) (Monahan and O'Muircheartaigh 1986; Spillane et al. 1986).ECM convened a Whitecap Workshop in September 1983 which resulted in the publication (Monahan and Wilson 1993) – the first such volume – on ocean white-capping and of the role these whitecaps play in satellite marine remote sensing, in marine aerosol generation, and in air-sea gas exchange. A quilted patchwork wall-hanging ($6' \times 4'$) depicting sea foam (oceanic whitecaps) as perceived in various cultures was executed by Helen Hardesty and Elizabeth Monahan on the occasion of the Whitecap Workshop and is shown in Fig. 2.1b. ECM was awarded the D.Sc. degree from the National University of Ireland in 1984, based on published research work – mainly on whitecaps and marine aerosol. ECM resigned from UCG in 1986 and took up a position in the Department of Marine Sciences at the University of Connecticut.

ECM has made significant contributions to the science of wave breaking, and it is clear that the research that is being conducted today on this topic is a direct legacy of ECM's time at UCG.

2.2 Introduction

Breaking waves serve as an important mechanism for air–sea fluxes of gas (Asher and Wanninkhof 1998; Goddijn-Murphy et al. 2016; Monahan et al. 1983) and aerosols (de Leeuw et al. 2011; Monahan 1986; Monahan et al. 1984; O'Dowd and de Leeuw 2007), wave–ocean fluxes of momentum and energy (Melville 1996; Phillips 1985; Schwendeman and Thomson 2015; Thomson et al. 2009), and sea surface albedo (Monahan and Zietlow 1969; Moore et al. 2000). Breaking gravity waves disrupt the water surface layer by trapping and entraining air, resulting in the formation of clouds of subsurface bubbles. The visible signatures of these bubble plumes are known as whitecaps.

Over the past six decades or so, numerous studies have been undertaken to better understand and quantify the stochastic nature (and influences) of breaking waves. Several environmental and wave-field dependencies have been identified (Anguelova and Webster 2006; Bortkovski and Novak 1993; Brumer et al. 2017; Callaghan and White 2009; Callaghan et al. 2008a; Goddijn-Murphy et al. 2016; Monahan 1971; Monahan and Zietlow 1969; Scanlon et al. 2015; Schwendeman and Thomson 2015), with wind speed being the primary driver. Independent of wind, the

influences of salinity (Anguelova and Huq 2017; Monahan et al. 2015), water temperature (Bortkovski and Novak 1993; Callaghan et al. 2012), atmospheric stability (sea – air temperature) (Monahan and Lu 1990; Monahan and Zietlow 1969; Thorpe 1982), presence (or absence) of surfactants (Callaghan et al. 2008b; Hanson 1997; Scott 1986), fetch (Monahan and Mac Niocaill 1986; Nordberg et al. 1971), wind duration (Callaghan and White 2009), wave height (Brumer et al. 2017; Toba and Koga 1986) wave age (Bortkovski and Novak 1993; Lafon et al. 2004; Schwendeman and Thomson 2015; Toba and Koga 1986) and current velocity (Kraan et al. 1996) have been identified. The use of multi-variable dimensionless parameters have also been considered (Brumer et al. 2017; Goddjin-Murphy et al. 2011; Monahan and Spillane 1984; Scanlon et al. 2015; Schwendeman and Thomson 2015; Toba and Koga 1986; Woolf 2005; Zhao and Toba 2001).

In this article we review a selection of technologies, theories and approaches that have helped further our understanding of whitecap variability. We begin with an overview of technological advancements in photography and image processing, followed by an overview of statistical fitting approaches. Next, we consider the theory that the evolution of a whitecap can be split into more than one stage, each with distinguishable characteristics and thus requiring different parameterisations (Bondur and Sharkov 1982; Monahan and Spillane 1984; Monahan et al. 1986). Finally, we review the use of additional function-dependent parameters to help better parameterise whitecap coverage such as sea surface temperature (SST), sea-air temperature (_T), wave height, friction velocity, wave age, wave slope, fetch, wind duration and relative wind-wave direction.

2.3 Technological Advancement

Digital image records and processing techniques are perhaps the greatest technological benefits for the study of whitecap coverage today. Before the mid 1980s, whitecap cover was quantified from photographic film records by means of cutting out and weighing whitecap silhouettes (Monahan 1969). The cost associated with such an arduous and intricate image processing workload (Fig. 2.2, left) greatly limited the number of images that could be analysed, and as a consequence, it was common to use (of the order of) tens of images per whitecap cover estimate (Table 2.1).

The use of digital image processing (Monahan and Lu 1990; Monahan and Mac Niocaill 1986; Monahan et al. 1985) in the mid 1980's allowed for the quantification of smaller whitecap fractions and led to a considerable reduction in the image processing effort (Fig. 2.2, right). Whitecap percentage coverage estimates of seven significant figures were now achievable (Fig. 2.3). The processing involved converting video film imagery of the sea surface into their digital greyscale equivalent, followed by manual setting of an appropriate pixel intensity threshold to distinguish whitecaps from the background sea. The pixels representing whitecap regions would then be summed and presented as a fractional total. This greyscale

Fig. 2.2 Illustrations of the efforts involved in processing filmographic images using "cutting and weighing" method (Monahan 1969) (left), and for processing digital images using greyscale thresholding techniques (Monahan and Lu 1990)

pixel intensity threshold processing technique has proved immensely useful for processing images containing whitecaps and is still used to this day.

With the advent of digital cameras in the late 1990's and the ever-reducing costs of memory, whitecap studies can now effectively manage the capture of tens of thousands of images of the sea surface (Bakhoday-Paskyabi et al. 2016; Callaghan et al. 2008a; Sugihara et al. 2007; Villarino et al. 2016). In response, autonomous processing algorithms were developed to estimate whitecap fractions from images in an efficient and objective manner. The Autonomous Whitecap Extraction (AWE) algorithm (Callaghan et al. 2014) is perhaps the most widely used.

The aforementioned technological advancements provide today's whitecap researchers with the means to acquire and process large image sets with little manual effort. However qualitative whitecap estimates still require careful attention, usually by means of manual intervention (Scanlon and Ward 2014), batch statistics (Sugihara et al. 2007) and/or convergence metrics (Brumer et al. 2017; Callaghan et al. 2014), as the greyscale thresholding technique is susceptible to images containing contaminants of sky, sunglint, ice sea-going birds, fish broaching and raindrops on the camera lens and ship wake (Scanlon and Ward 2014).

2.4 Fitting Practices

2.4.1 Whitecap Functions

The evolution of statistical techniques and tools have also benefited the parameterisation of whitecap coverage. Toward the end of the 1970s, it was

Table 2.1 Table of historical whitecap observations extracted from mentioned sources

Dataset	Type	Number of observations	Images per observation	Wind range (m s^{-1})
Blanchard-63 (Blanchard 1963)	Film	3	–	4–9
BOMEX (Monahan 1971)	Film	61	6.2	0.6–13.4
Nordberg-71 (Nordberg et al. 1971)	Film	6	–	5–25
TC-73 (Toba and Chaen 1973)	Film	38	–	2–16
JASIN-78 (Monahan and Lu 1990)	Film	55	20	2.5–15.3
RC-74 (Ross and Cardone 1974)	Film	13	32.8	10–25
STREX-80 (Doyle 1984)	Film	85	26	2.7–17.2
Bortkovskii-83 (Monahan et al. 1984)	Film	96	–	5–24
MIZEX-83 (Monahan et al. 1984)	Film	43	22	1.1–14.0
MIZEX-83 (Monahan et al. 1984)	Video	47	74	1.3–14.3
MIZEX-84 (Monahan et al. 1984)	Film	56	37	0.1–13.1
MIZEX-84 (Monahan et al. 1984)	Video	88	73	1.5–16.4
HEXOS-84 (Monahan et al. 1984)	Video	28	77	5.2–14.1
CapeHatteras-90 (Asher and Wanninkhof 1998)	Video	32	–	1–16.9
Fetch-98 (Lafon et al. 2007)	Digital	45	10–25	6.0–17.2
GasEx-98 (Asher et al. 2002)	Video	59	–	5.7–16.3
Oceana-98 (Stramska and Petelski 2003)	Digital	66	32.8	4.8–13.5
EMMA-02 (Lafon et al. 2004)	Digital	29	24	10.0–17.9
SPACE-02 (Callaghan et al. 2008a)	Digital	101	<1200	2.6–12.2
MAP-06 (Callaghan and White 2009)	Digital	107	403	3.7–23.1
Sugihara-07 (Sugihara et al. 2007)	Digital	91	<600	4.7–16.6
SEASAW-07 (Norris et al. 2013a)	Digital	63	<900	5–18
Knorr-11 (Scanlon et al. 2015)	Digital	584 (125)	193 (900[a])	0.9–18.1
HighWinGs-13 (Brumer et al. 2017)	Digital	273 (176[b])	<72,000	3.6–25.3
SOGasEx-15 (Monahan and Pybus 1978)	Digital	91	–	4–18.5
ST-15 (Schwendeman and Thomson 2015)	Digital	77	9000–13,000	5–16

[a]1-Hourly estimates are instead presented, and later used for fitting analysis
[b]To avoid possible repetition, the SO GasEx dataset is omitted

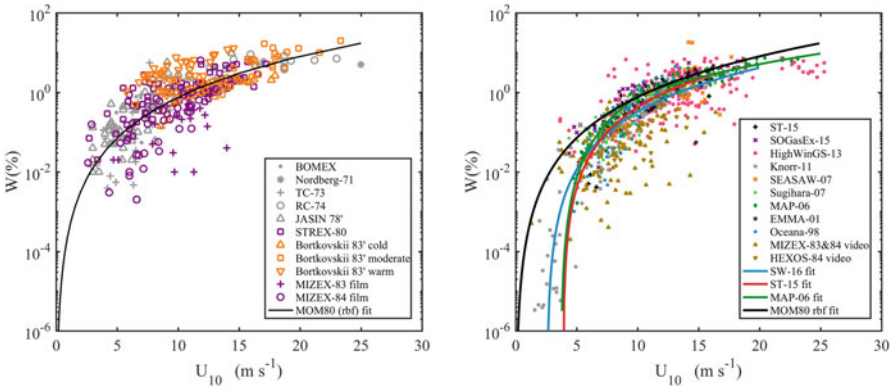

Fig. 2.3 Percentage whitecap coverage observations from film (left) and digital (right) datasets presented in Table 2.1 are plotted against wind speed at 10-meter elevation U_{10}

recognised that statistical tools were crucial for deducing representative functions from whitecap observation datasets (Monahan 1971; Wu 1979). Consequently, classical (Legendre 1805), analysis of variance (Fisher 1954) and robust (Huber 1996; Huber et al. 1964; Mosteller and Tukey 1977) statistical fitting methodologies, and performance indicators (mean square error, correlation coefficients, etc.) were applied to deduce and evaluate various whitecap functions (Callaghan and White 2009; Monahan and Woolf 1989; Monahan and Zietlow 1969; Toba and Koga 1986).

The quadratic whitecap coverage function (Blanchard 1963) was soon refined and a wind-dependent power-law exponent was proposed (Monahan 1971) consisting of two coefficients a, b:

$$W = aU_{10}^{b} \tag{2.1}$$

where U_{10} is wind speed at 10-meter reference height. Many studies (Bortkovski 1987; Monahan 1993) agreed that a power exponent value of b=3 was sufficient, and so the following wind threshold function variant became popular

$$W = a(U_{10} - b)^{3} \tag{2.2}$$

where b is interpreted as a wind-speed threshold for the onset of whitecapping (Monahan and Zietlow 1969). Whitecap functions with wind speed threshold (Eq. 2.2) provided the ability to identify the wind speed (b) at which wave breaking begins to occur. The presence of such a wind speed threshold has basis, both from observations (Monahan 1971) and theoretical frameworks (Cardone 1969). Bar some exceptions, whitecap studies have deemed Eq. 2.2 to be suitable fit to whitecap observations. Holthuijsen et al. (2012) demonstrated using archived aerial images of the sea surface that current power-law functions (Eqs. 2.1 and 2.2) are not apable of estimating whitecap coverage in hurricane conditions. Similarly Brumer et al. (2017)

observed whitecap coverage reaching a maxima at approximately 22.5 m s^{-1} wind speed. Also, Callaghan et al. (2008a) observed optimum fitting performance when two separate equations were derived for high and low winds. Indeed future advancement of whitecap functions will likely consider multiple-environmental-parameter functions.

2.4.2 *Statistical Considerations*

Whitecap values span multiple orders of magnitude over a typical range of wind speeds (Fig. 2.3). Consequently whitecap observations require some rescaling so that the various whitecap magnitudes each have an equivalent influence during the fitting process (Scanlon and Ward 2016). Monahan and O'Muircheartaigh (1980) considered the use of two scales, natural logarithm and inverse power exponent. While both are effective, the logarithmic scaling fails to accommodate zero-value whitecap observations, whereas the inverse power exponent scaling could achieve this.

The presence of zero-value whitecap observations can serve as an advantage or a disadvantage during linear regression fitting. If normally distributed, zero-whitecap values can serve to better estimate the U_{10} threshold b in Eq. 2.2. Oversampling zero-valued whitecap conditions (i.e. conditions where $U_{10} < b$, if $b > 0$) can result in left-hand skewed distribution of U_{10} ($W_{1/3} = 0$) values, serving to bias b. It is thus recommended to investigate the distribution of zero-value whitecap observations using normality testing (e.g. Jarque and Bera (1987)).

Uneven data distribution across the U_{10} range can also influence the best fit (Scanlon and Ward 2016). It is thus important to consider using bin averaging to achieve an even distribution of observations across the U_{10} range prior to fitting.

2.5 Active and Maturing Whitecaps

Whitecaps have been distinguished as being actively breaking or maturing and subsequently quantified by many researchers (Bondur and Sharkov 1982; Bortkovski and Novak 1993; Monahan and Spillane 1984; Monahan et al. 1986; Scanlon and Ward 2016; Scanlon et al. 2015). The primary driver is that actively breaking whitecap coverage (W_A) represents different processes than maturing whitecap coverage (W_B). W_A is a measure of area of the water surface which is breaking, and so it should be a suitable parameter for quantifying processes concerning wave breaking (Callaghan 2018; Kraan et al. 1996; Scanlon and Ward 2014). W_B is a measure of the water surface undergoing bubble bursting, and so should be a suitable parameter for aerosol production (Monahan 1986). Actively breaking whitecaps are short-lived (of order 1 sec) while maturing whitecaps can persist for much longer (Monahan and Spillane 1984). Consequently it is hypothesised that W_A is less susceptible to effects of bubble persistence and is

thus more reliable as an oceanographic parameter than W and W_B. Bondur and Sharkov (1982) identified whitecap regions and distinguished them as either crests (actively breaking) or foam (maturing) by eye. Through use of digital image processing, Monahan and Woolf (1989) applied an additional greyscale pixel threshold to distinguish whitecap pixels as contributions of either W_A or W_B. Scanlon and Ward (2014) reported that the double greyscale threshold method introduced errors on the order of 30%, and instead presented a processing alternative – the spatial separation of whitecap pixels (SSWP) method. This technique recommended appealing to four visual characteristics of a whitecap (texture, shape, brightness, and location with respect to the wave crest). The image processing method developed by Kleiss and Melville (2010) was considered for quantifying W_A autonomously by appealing to a whitecaps brightness, velocity and location (with respect to the nearest wave crest). Finally the use of infrared imaging has been demonstrated (Marmorino and Smith 2005; Sutherland and Melville 2015) to distinguish between W_A and W_B due to disrupting the diurnal thermocline (Scanlon et al. 2013).

Most recently, Scanlon and Ward (2016) published U_{10} functions for W_A and W_B, and reported that separating W into W_A and W_B served to reduce fitting performance. They concluded that the W_B contribution in W may serve to conceal the true variability of breaking waves.

2.6 Effects of Environmental Parameters on Whitecaps

Wind-wave interaction, responsible for driving growth and eventual breaking of waves, is a highly complex phenomenon. Various interactions between turbulent wind, underlying currents and wave scales can each lead to different wave breaking scenarios (Banner et al. 2010; Melville and Rapp 1985) and instabilities (such as spume production (Soloviev and Lukas 2010)). Observational methods of quantifying wave breaking and measuring turbulent environmental parameters prove challenging, especially in extreme conditions. In addition, the evolution and characteristics of whitecap bubbles serve to compound complexity, whereby variations in temperature, scale of breaking and surfactant concentrations can alter the lifetime and spatial extent of a typical whitecap. Consequently wind-speed-only parameterisations of whitecap cover will not account for all the observed variabilities, and so the inclusion of additional environmental parameter dependencies will be required.

2.6.1 Water Temperature

Sea temperature (T_S) has been noted in previous studies, to have an influencing impact on the magnitude of whitecap coverage (Bortkovski and Novak 1993;

Callaghan et al. 2008a, 2012; Hanson 1997; Monahan and Zietlow 1969; Salisbury et al. 2013). Viscosity and surface tension are highest in cold waters, which are both noted to govern the requirements for the onset of wave breaking, bubble lifetimes, and velocities of plunging and rising bubbles. Viscous effects can reduce by half if T_S increases from 5 to 25 °C (Monahan and Zietlow 1969) highlighting the importance of T_S for controlling the critical requirements of wave breaking (Bortkovski and Novak 1993; Bortkovskii 2012). Gas solubility is also governed by water temperature, with less air being dissolved in warmer waters. This effect leads to increased bubble lifetimes, resulting in denser bubble populations with increases of T_S (Hanson 1997). Sea surface temperature has been observed to effect the lifetimes of whitecap foam (Abe 1955; Callaghan et al. 2012).

Despite T_S being noted to influence a large number of processes that can affect W, it has proved difficult to extract a clear relationship in previous studies (Callaghan et al. 2008a; Monahan 1986; Stramska and Petelski 2003). Using large photographic data sets, Bortkovskii and Novak (1993) witnessed an increasing magnitude of W with temperature; coinciding with results obtained by (Callaghan et al. 2012) following a tank experiment, and contrary to a decreasing trend attained from global satellite sensed W retrievals (Salisbury et al. 2013).

2.6.2 Atmospheric Stability

Thermal atmospheric stability ΔT ($TS - T_A$, where T_A denotes air temperature), has been noted to directly affect whitecap coverage (Monahan et al. 1986) by influencing the wind profile over the sea surface and by affecting the dispersion of bubbles as they rise to the surface during the maturing phase due to the near surface vertical heat flux (Thorpe 1982). Kara et al. (2007) showed that thermal atmospheric stability ΔT influences the drag coefficient of the wind on the sea surface. ΔT has been shown to have a spatially increasing effect for whitecap coverage (Monahan 1986; Monahan et al. 1986). Thorpe (1982) observed that when ΔT is unstable ($\Delta T > 0$), the bubble plumes beneath whitecap events display undisrupted vertical rises to the surface, reflecting a dependence of vertical convection and low shear in the formation of the observed columnar-like rising bubble structures. For stable conditions ($\Delta T < 0$), the downward heat flux was shown to promote billow-like bubble plume structures, reported to be a response to eddies developing in the stably stratified shear flow resulting from the downward net heat flux. This serves as an ample explanation to interpret the decreasing trend of ΔT; by which the spatial expansion of a decaying whitecap plume (and thus it's surface whitecap), and the bubble rise velocity (affecting bubble lifetimes) are strongly influenced by ΔT.

2.6.3 Wave-Field Dependence

Reynolds numbers have been used in previous studies to estimate whitecap coverage (Goddjin-Murphy et al. 2011; Scanlon and Ward 2016; Sugihara et al. 2007; Zhao and Toba 2001), estimate air–sea gas transfer (Woolf 2005; Zhao et al. 2003) and estimate aerosol production resulting from spume droplets (Zhao et al. 2006). Examples of Reynolds numbers are the breaking wave parameter R_B, and R_H (Zhao and Toba 2001), and its variants, are considered as suitable proxies for quantifying whitecap coverage. These proxies attempt to quantify the growth of the wave-field and input of wind momentum:

$$R_B = u_*/v_a\omega_{p,}R_H = u_*H_S/v_a \tag{2.3}$$

where v_a is the kinematic viscosity of air, u_* is the air-side friction velocity, ω_p is the peak angular frequency of the wind-wave spectrum, and HS is the significant wave height. The terms ω_p; a transient measurement, and H_S; a spatial amplitude measurement, can estimate the growth of the wave-field, with lower values of ω_p and higher values of H_S typically being associated with developed seas. Recent studies (Norris et al. 2013b; Ovadnevaite et al. 2014; Scanlon and Ward 2016) observed a 2-phase Reynolds relation approximately as it had been observed in previous studies (Callaghan et al. 2008a; Goddjin-Murphy et al. 2011; Sugihara et al. 2007) that pure wind seas, where the wind and waves blow in the same direction, induce a significantly high rate of wave breaking occurrence, when compared to other wind-wave directional coupling regimes. In open-ocean conditions, wind direction can change significantly on short timescales, resulting in different wind-wave directional coupling scenarios. It has been remarked by the same authors that wind blowing across, and against the propagation of swell dominated seas induces reduced rates of wave breaking.

2.6.4 Surfactant Dependence

The presence of surface active substances of biogenic origin (such as lipidic and proteinaceous material and humic substances) could be a responsible factor when elucidating whitecap coverage variability (Callaghan et al. 2008a, 2013; Monahan and Spillane 1984) by affecting the persistence of whitecap foam at the air–sea interface. It is indeed plausible that surfactants influence only the persistent maturing whitecaps, where the majority of film and jet droplets are produced (Andreas et al. 1995). Surfactants by their name, reside on the surface of the ocean and play an influential role in wind–wave interaction, wave breaking and bubble evolution.

Surfactants increase the lifetimes of bubbles by providing a stabilizing coating to seawater bubbles (Callaghan et al. 2008b; Scott 1986; Woolf 1997, 2005) and due to the reduced rate of bubble dissolution, the latter being a result of supersaturation of atmospheric gases in upwelling and biologically active regions of the ocean (Hanson 1997). Both of these mechanisms, should lead to larger population bubble plumes in the presence of higher surfactant levels. Scott (1986) explains the potential role of surfactants stabilizing wave growth, dampening their motion and reducing the wind energy transfer to waves. The author notes the reduction of 'ripples' forming on developed waves due to the presence of surfactants, altering the surface roughness, and thus reducing the effect of wind shear on the wave. The theory is related to the old maritime story of the use of oil on troubled waters, to reduce the chance of breaking. This effect, if substantial, should play a role in regulating the onset of wave breaking in low energy pure wind sea conditions while having little-to-no effect on wave–wave induced breaking.

2.7 Discussion and Conclusions

In this study, 26 historical datasets of whitecap observations have been presented (Table 2.1). All observations are accompanied by wind speed U_{10} information, and few are accompanied by additional parameters describing temperature, atmospheric stability and wave-field conditions. The majority (98.4%) of observations represent wind speed conditions within 0 and 20 m s^{-1}.

Prior to fitting analysis, the following considerations are noted. The distribution of observations across the wind speed range is uneven (Fig. 2.4, left), and so bin averaging will be applied. The presence of outliers is assumed, and so median function will be adopted for determining locations and scales of each observation group.

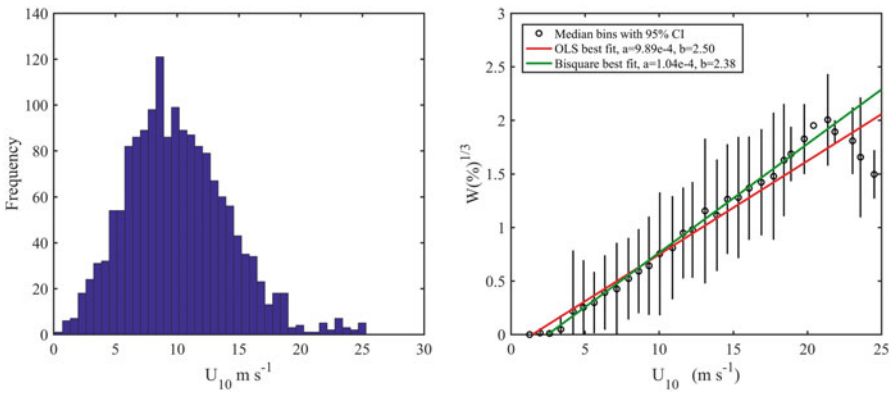

Fig. 2.4 Histogram of all gathered whitecap coverage observations mentioned in Table 2.1 (left). The median averages for each whitecap bin are plotted against wind speed at 10-meter elevation U_{10} (right). The correlation coefficients R2 are 0.94 and 0.99 for the OLS and RBF fits respectively

All the gathered whitecap observations are grouped into 40 linearly spaced U_{10} bins in 1/3-power whitecap space. The median location and 95% confidence intervals are calculated (using median absolute deviation scale estimator) for each group (Fig. 2.4, right). Median averaging is applied here to minimise the influence of outliers present in each group. A selection of fitting techniques (Ordinary Least Squares (OLS) and bisquares (RBF) (Huber 1996)) are then applied to deduce best-fit coefficients for Eq. 2.2.

Figure 2.4 illustrates nicely the progress made over the previous decades in parameterising whitecap coverage. By considering the validity of all data presented, fitting analysis reveals that there exists a non-zero wind-speed threshold (i.e. $b > 0$), while also supporting that Eq. 2.2 suitably represents whitecap coverage for the majority of conditions (0–20 m s^{-1}). There are few observations for U_{10}>20 m s^{-1}, and so their outlying presence suggests (albeit with small confidence) that Eq. 2.2 is not suitable. The gathering of more observations will thus be required.

Significant progress has been achieved over the past six decades on parameterising whitecap coverage from sea surface imagery. While technological and data-handling advancements have played a positive role, the extraordinary efforts invested by the growing number of participating researchers must be credited. The mentoring, data open-access policies and cooperation exercised by experienced researchers has served to ensure progression toward better understanding wave breaking processes. With the collection of further datasets which encompass additional environmental parameters, the roles of additional environmental parameters will be better understood.

References

Abe, T. (1955). A study on the foaming of sea water. *Papers in Meteorology and Geophysics, 6*(2), 164–171. https://doi.org/10.2467/mripapers1950.6.2_164.

Andreas, E. L., Edson, E., Monahan, E. C., Rouault, M., & Smith, S. (1995). The spray contribution to the net evaporation from the sea: A review of recent progress. *Boundary-Layer Meteorology, 72*, 3–52. https://doi.org/10.1007/BF00712389.

Anguelova, M. D., & Huq, P. (2017). Effects of salinity on surface lifetime of large individual bubbles. *Journal of Marine Science and Engineering, 5*(3). https://doi.org/10.3390/jmse5030041.

Anguelova, M. D., & Webster, F. (2006). Whitecap coverage from satellite measurements: A first step toward modeling the variability of oceanic whitecaps. *Journal of Geophysical Research: Oceans, 111*(C3), C03017. https://doi.org/10.1029/2005JC003158.

Asher, W. E., & Wanninkhof, R. (1998). The effect of bubble-mediated gas transfer on purposeful dual-gaseous tracer experiments. *Journal of Geophysical Research: Oceans, 103*(C5), 10555–10560. https://doi.org/10.1029/98JC00245.

Asher, W., Edson, J., Mcgillis, W., Wanninkhof, R., Ho, D. T., & Litchendor, T. (2002). *Fractional area whitecap coverage and air-sea gas transfer velocities measured during GasEx-98* (pp. 199–203). Washington, DC: American Geophysical Union (AGU). https://doi.org/10.1029/GM127p0199.

Bakhoday-Paskyabi, M., Reuder, J., & Flügge, M. (2016). Automated measurements of whitecaps on the ocean surface from a buoy-mounted camera. *Methods in Oceanography, 17*, 14–31. https://doi.org/10.1016/j.mio.2016.05.002.

Banner, M. L., Babanin, A. V., & Young, I. R. (2010). Breaking probability for dominant waves on the sea surface. *Journal of Physical Oceanography, 30*(12), 3145–3160. https://doi.org/10.1175/1520-0485(2000)030<3145:BPFDWO>2.0.CO;2.

Blanchard, D. C. (1963). The electrification of the atmosphere by particles from bubbles in the sea. *Progress in Oceanography, 1*, 73–202. https://doi.org/10.1016/0079-6611(63)90004-1.

Bondur, V. G., & Sharkov, E. A. (1982). Statistical properties of whitecaps on a rough sea. *Oceanology, 22*, 274–279.

Bortkovski, R. S. (1987). *Air-sea exchange of heat and moisture during storms*. Dordrecht: Reidel Publishing Company. (Revised English edition).

Bortkovski, R. S., & Novak, V. A. (1993). Statistical dependencies of sea state characteristics on water temperature and wind-wave age. *Journal of Marine Systems, 4*, 161–169.

Bortkovskii, R. S. (2012). Water-temperature effect on the spectral density of wind gravity waves and on sea-surface roughness. *Izvestiya, Atmospheric and Oceanic Physics, 48*(2), 193–199.

Bowyer, P. A., Woolf, D. K., & Monahan, E. C. (1990). Temperature dependence of the charge and aerosol production associated with a breaking wave in a whitecap simulation tank. *Journal of Geophysical Research: Oceans, 95*(C4), 5313–5319. https://doi.org/10.1029/JC095iC04p05313.

Brumer, S. E., Zappa, C. J., Brooks, I. M., Tamura, H., Brown, S. M., Blomquist, B. W., Fairall, C. W., & Cifuentes-Lorenzen, A. (2017). Whitecap coverage dependence on wind and wave statistics as observed during SO GasEx and HiWinGS. *Journal of Physical Oceanography, 47*(9), 2211–2235. https://doi.org/10.1175/JPO-D-17-0005.1.

Callaghan, A. H. (2018). On the relationship between the energy dissipation rate of surface-breaking waves and oceanic whitecap coverage. *Journal of Physical Oceanography, 48*(11), 2609–2626. https://doi.org/10.1175/JPO-D-17-0124.1.

Callaghan, A. H., & White, M. (2009). Automated processing of sea surface images for the determination of whitecap coverage. *Journal of Atmospheric and Oceanic Technology, 26*(2), 383–394. https://doi.org/10.1175/2008JTECHO634.1.

Callaghan, A. H., de Leeuw, G., & O'Dowd, C. D. (2008a). Relationship of oceanic whitecap coverage to wind speed and wind history. *Geophysical Research Letters, 35*, L23609. https://doi.org/10.1029/2008JC036165.

Callaghan, A. H., Deane, G. B., & Stokes, M. D. (2008b). Observed physical and environmental causes of scatter in whitecap coverage values in a fetch-limited costal zone. *Journal of Geophysical Research, 113*, C05022. https://doi.org/10.1029/2007JC004453.

Callaghan, A. H., Deane, G. B., Stokes, M. D., & Ward, B. (2012). Observed variation in the decay time of oceanic whitecap foam. *Journal of Geophysical Research, 117*, C09015. https://doi.org/10.1029/2012JC008147.

Callaghan, A. H., Deane, G. B., & Stokes, M. D. (2013). Two regimes of laboratory whitecap foam decay: bubble-plume controlled and surfactant stabilized. *Journal of Physical Oceanography, 43*, 1114–1126. https://doi.org/10.1175/JPO-D-12-0148.1.

Callaghan, A. H., Deane, G. B., & Stokes, M. D. (2014). The effect of water temperature on air entrainment, bubble plumes, and surface foam in a laboratory breaking-wave analog. *Journal of Geophysical Research, 119*, 1114–1126. https://doi.org/10.1002/2014JC010351.

Cardone, V. J. (1969). *Specification of the wind distribution in the marine boundary layer for wave forecasting. Technical report*. New York: New York University.

Cipriano, R. J., Monahan, E. C., Bowyer, P. A., & Woolf, D. K. (1987). Marine condensation nucleus generation inferred from whitecap simulation tank results. *Journal of Geophysical Research Oceans, 92*(C6), 6569–6576. https://doi.org/10.1029/JC092iC06p06569.

de Leeuw, G., Andreas, E. L., Anguelova, M. D., Fairall, C. W., Lewis, E. R., O'Dowd, C., Schulz, M., & Schwartz, S. E. (2011). Production flux of sea spray aerosol. *Reviews of Geophysics, 49*(2), RG2001. https://doi.org/10.1029/2010RG000349.

Doyle, D. M. (1984). *Whitecaps and the marine atmosphere report no. 6. Technical report*. Galway: UCG. URL http://hdl.handle.net/10379/4435.

Fisher, R. A. (1954). *Statistical methods for research workers* (12th edn.). Edinburgh: Oliver and Boyd.

Goddijn-Murphy, L., Woolf, D. K., Callaghan, A. H., Nightingale, P. D., & Shutler, J. D. (2016). A reconciliation of empirical and mechanistic models of the air-sea gas transfer velocity. *Journal of Geophysical Research Oceans, 121*(1), 818–835. https://doi.org/10.1002/2015JC011096.

Goddijn-Murphy, L., Woolf, D. K., & Callaghan, A. H. (2011). Parameterizations and algorithms for oceanic whitecap coverage. *Journal of Physical Oceanography, 41*, 742–756. https://doi.org/10.1175/2010JPO4533.1.

Hanson, J. L. (1997). *Physical and biological descriptors for ocean bubbles and acoustic surface backscatter. Technical report*. Laurel: John Hopkins University.

Holthuijsen, L. H., Powell, M. D., & Pietrzak, J. D. (2012). Wind and waves in extreme hurricanes. *Journal of Geophysical Research Oceans, 117*(C9), 1–15. https://doi.org/10.1029/2012JC007983.

Huber, P. J. (1996). *Robust statistical procedures*. Philadelphia: Society for Industrial and Applied Mathematics.

Huber, P. J., et al. (1964). Robust estimation of a location parameter. *The Annals of Mathematical Statistics, 35*(1), 73–101.

Jarque, C. M., & Bera, A. K. (1987). A test for normality of observations and regression residuals. *International Statistical Review /Revue Internationale de Statistique, 55*(2), 163–172.

Kara, A. B., Metzger, E. J., & Bourassa, M. A. (2007). Ocean current and wave effects on wind stress drag coefficient over the global ocean. *Geophysical Research Letters, 34*, L01604. https://doi.org/10.1029/2006GL027849.

Kleiss, J. M., & Melville, W. K. (2010). Observations of wave breaking kinematics in fetch-limited seas. *Journal of Atmospheric and Oceanic Technology, 40*(12), 2575–2604. https://doi.org/10.1175/2010JPO4383.1.

Kraan, G., Oost, W. A., & Janssen, P. A. E. M. (1996). Wave energy dissipation by whitecaps. *Journal of Atmospheric and Oceanic Technology, 13*(1), 262–267. https://doi.org/10.1175/1520-0426(1996)013<0262:WEDBW>2.0.CO;2.

Lafon, C., Piazzola, J., Forget, P., le Calve, O., & Despiau, S. (2004). Analysis of the variations of the whitecap fraction as measured in a coastal zone. *Boundary-Layer Meteorology, 111*, 339–360. https://doi.org/10.1023/B:BOUN.0000016490.83880.63.

Lafon, C., Piazzola, J., Forget, P., & Despiau, S. (2007). Whitecap coverage in coastal environment for steady and unsteady wave field conditions. *Journal of Marine Systems, 66*, 38–46. https://doi.org/10.1016/j.jmarsys.2006.02.013.

Legendre, A. M. (1805). *Nouvelles méthodes pour la détermination des orbites des comètes*. Paris: F. Didot.

Marmorino, G. O., & Smith, G. B. (2005). Bright and dark ocean whitecaps observed in the infrared. *Geophysical Research Letters, 32*, L11604. https://doi.org/10.1029/2005GL023176.

Melville, W. K. (1996). The role of surface-wave breaking in airsea interaction. *Annual Review of Fluid Mechanics, 28*, 279–321. https://doi.org/10.1146/annurev.fl.28.010196.001431.

Melville, W. K., & Rapp, R. J. (1985). Momentum flux in breaking waves. *Nature, 317*(6037), 514–516. https://doi.org/10.1038/317514a0.

Monahan, E. C. (1968). Sea spray as a function of low elevation wind speed. *Journal of Geophysical Research, 73*(4), 1127–1137. https://doi.org/10.1029/JB073i004p01127.

Monahan, E. C. (1969). Fresh water whitecaps. *Journal of Atmospheric and Oceanic Technology, 26*, 1026–1029. https://doi.org/10.1175/1520-0469(1969)026<1026:FWW>2.0.CO;2.

Monahan, E. C. (1971). Oceanic whitecaps. *Journal of Physical Oceanography, 1*, 139–144. https://doi.org/10.1175/1520-0485(1971)001<0139:OW>2.0.CO;2.

Monahan, E. C. (1986). The ocean as a source for atmospheric particles. In *The role of air-sea exchange in geochemical cycling* (pp. 129–163). Dordrecht: Springer.

Monahan, E. C. (1993). Occurence and evolution of acoustically relevant sub-surface bubble plumes and their associated, remotely, monitorable surface whitecaps. In B. Kerman (Ed.), *Natural physical sources of underwater sound* (pp. 503–517). New York: Springer.

Monahan, E. C., & Lu, M. (1990). Acoustically relevant bubble assemblages and their dependence on meteorological parameters. *IEEE Journal of Oceanic Engineering, 15*(4), 340–349. https://doi.org/10.1109/48.103530.

Monahan, E. C., & Mac Niocaill, G. (Eds.). (1986). *Oceanic whitecaps and their role in air-sea exchange processes*. Dordrecht: D. Reidel Publishing Company.

Monahan, E. C., & O'Muircheartaigh, I. G. (1980). Optimal power-law of oceanic whitecap coverage dependence on wind speed. *Journal of Physical Oceanography, 10*, 2094–2099.

Monahan, E. C., & O'Muircheartaigh, I. G. (1986). Whitecaps and the passive remote sensing of the ocean surface. *International Journal of Remote Sensing, 7*, 627–642. https://doi.org/10.1175/1520-0485(1980)010<2094:OPLDOO>2.0.CO;2.

Monahan, E. C., & Pybus, M. J. (1978). Colour, ultraviolet absorbance and salinity of the surface waters off the west coast of ireland. *Nature, 274*(5673), 782. https://doi.org/10.1038/274782a0.

Monahan, E. C., & Spillane, M. C. (1984). The role of oceanic whitecaps in air-sea gas exchange. In W. Brutsaert & G. H. Jirka (Eds.), *Gas transfer at water surfaces* (pp. 495–503). Dordrecht: Springer.

Monahan, E. C., & Wilson, M. B. (1993). *Chapter 16. Whitecap measurements. Technical report*. Groton: University of Connecticut.

Monahan, E. C., & Woolf, D. K. (1989). Comments on 'variations of whitecap coverage with wind stress and water temperature'. *Journal of Physical Oceanography, 19*, 706–709. https://doi.org/10.1175/1520-0485(1989)019<0706:COOWCW>2.0.CO;2.

Monahan, E. C., & Zietlow, C. R. (1969). Laboratory comparisons of freshwater and salt-water whitecaps. *Journal of Geophysical Research, 74*, 6961–6966. https://doi.org/10.1029/JC074i028p06961.

Monahan, E. C., Bowyer, P. A., Doyle, D. M., Fitzgearld, M. P., O'Muircheartaigh, I. G., Spillane, M. C., & Taper, J. J. (1981). *Whitecaps and the marine atmosphere report no. 3. Technical report*. Galway: UCG.

Monahan, E. C., Davidson, K. L., & Spiel, D. E. (1982). Whitecap aerosol productivity deduced from simulation tank measurements. *Journal of Geophysical Research Oceans, 87*(C11), 8898–8904. https://doi.org/10.1029/JC087iC11p08898.

Monahan, E. C., Fairall, C. W., Davidson, K. L., & Boyle, P. J. (1983). Observed interrelations between 10m winds, ocean whitecaps and marine aerosols. *Quarterly Journal of the Royal Meteorological Society, 109*(460), 379–392. https://doi.org/10.1002/qj.49710946010.

Monahan, E. C., Bowyer, P. A., Doyle, D. M., Higgins, M. R., & Woolf, D. K. (1984). *Whitecaps and the marine atmosphere report no. 7. Technical report*. Galway: UCG. http://hdl.handle.net/10379/4263.

Monahan, E. C., Spillane, M. C., Bowyer, P. A., Higgins, M. R., & Stabeno, P. J. (1985). *Whitecaps and the marine atmosphere report no. 8. Technical report*. Galway: UCG. http://hdl.handle.net/10379/4265.

Monahan, E. C., Spiel, D. E., & Davidson, K. L. (1986). Amodel ofmarine aerosol generation via whitecaps and wave disruption. In E. C. Monahan & G. M. Niocaill (Eds.), *Oceanic whitecaps: And their role in air-sea exchange processes* (pp. 167–174). Dordrecht: Springer Netherlands. https://doi.org/10.1007/978-94-009-4668-2_16.

Monahan, E. C., Hooker, G., & Zappa, C. J. (2015). The latitudinal variation in the wind-speed parameterization of oceanic whitecap coverage; Implications for global modelling of air-sea gas flux and sea surface aerosol generation. In 19th Air-Sea Interaction Conference, 4–8th January, Phoenix, AZ.

Moore, K. D., Voss, K. J., & Gordon, H. R. (2000). Spectral reflectance of whitecaps: Their contribution to water-leaving radiance. *Journal of Geophysical Research, 105*, 6493–6499. https://doi.org/10.1029/1999JC900334.

Mosteller, F., & Tukey, J. W. (1977). *Data analysis and regression: A second course in statistics* (Addison-Wesley series in behavioral science: Quantitative methods). Reading: Addison-Wesley.

Muircheartaigh, I. G. Ó., & Monahan, E. C. (1986). *Statistical aspects of the relationship between oceanic whitecap coverage wind speed and other environmental factors* (pp. 125–128). Dordrecht: Springer Netherlands. https://doi.org/10.1007/978-94-009-4668-2_12.

Nordberg, W., Conway, J., Ross, D. B., & Wilheit, T. (1971). Measurements of microwave emission from a foam-covered, wind-driven sea. *Journal of Atmospheric and Oceanic Technology, 28*, 429–435. https://doi.org/10.1175/1520-0469(1971)028<0429:MOMEFA>2.0.CO;2.

Norris, S. J., Brooks, I. M., Moat, B. I., Yelland, M. J., de Leeuw, G., Pascal, R. W., & Brooks, B. (2013a). Near-surface measurements of sea spray aerosol production over whitecaps in the open ocean. *Ocean Science, 9*(1), 133–145. https://doi.org/10.5194/os-9-133-2013.

Norris, S. J., Brooks, I. M., & Salisbury, D. J. (2013b). A wave roughness Reynolds number of the sea spray source flux. *Geophysical Research Letters, 40*, 1–5. https://doi.org/10.1002/grl.50795.

O'Dowd, C. D., & de Leeuw, G. (2007). Marine aerosol production: A review of the current knowledge. *Philosophical Transactions of the Royal Society, 365*(1856), 1753–1774. https://doi.org/10.1098/rsta.2007.2043.

Ovadnevaite, J., Manders, A., De Leeuw, G., Monahan, C., Cerbinis, D., & O'Dowd, C. D. (2014). A sea spray aerosol flux parametrization encapsulating wave state. *Atmospheric Chemistry and Physics, 14*, 1837–1852. https://doi.org/10.5194/acp-14-1837-2014.

Phillips, O. M. (1985). Spectral and statistical properties of the equilibrium range in wind-generated gravity waves. *Journal of Fluid Mechanics, 156*, 505–531. https://doi.org/10.1017/S0022112085002221.

Ross, D., & Cardone, V. (1974). Observations of oceanic whitecaps and their relation to remote measurements of surface wind speed. *Journal of Geophysical Research, 79*, 444–452. https://doi.org/10.1029/JC079i003p00444.

Salisbury, D. J., Anguelova, M. D., & Brooks, I. M. (2013). On the variability of whitecap fraction using satellite-based observations. *Journal of Geophysical Research, 118*(11), 6201–6222. https://doi.org/10.1002/2013JC008797.

Scanlon, B., & Ward, B. (2014). Oceanic wave breaking coverage separation techniques for active and maturing whitecaps. *Methods in Oceanography, 8*, 1–12. https://doi.org/10.1016/j.mio.2014.03.001.

Scanlon, B., & Ward, B. (2016). The influence of environmental parameters on active and maturing oceanic whitecaps. *Journal of Geophysical Research Oceans, 121*, 3325–3326. https://doi.org/10.1002/2015JC011230.

Scanlon, B., Wick, G. A., & Ward, B. (2013). Near-surface diurnal warming simulations: Validation with high resolution profile measurements. *Ocean Science, 9*(6), 977–986. https://doi.org/10.5194/os-9-977-2013.

Scanlon, B., Breivik, Ø., Bidlot, J.-R., Janssen, P. A. E. M., Callaghan, A. H., & Ward, B. (2015). Modelling whitecap coverage with a wave model. *Journal of Physical Oceanography, 46*(3), 887–894. https://doi.org/10.1175/JPO-D-15-0158.1.

Schwendeman, M., & Thomson, J. (2015). Observations of whitecap coverage and the relation to wind stress, wave slope, and turbulent dissipation. *Journal of Geophysical Research Oceans, 120*(12), 8346–8363. https://doi.org/10.1002/2015JC011196.

Scott, J. C. (1986). The effect of organic films on water surface motions. In E. C. Monahan & G. M. Niocaill (Eds.), *Oceanic whitecaps* (2nd ed., p. 159). Dordrecht: Reidel Publishing Company.

Soloviev, A., & Lukas, R. (2010). Effects of bubbles and sea spray on air–sea exchange in hurricane conditions. *Boundary-Layer Meteorology, 136*(3), 365–376.

Spillane, M. C., Monahan, E. C., Bowyer, P. A., Doyle, D. M., & Stabeno, P. J. (1986). Whitecaps and global fluxes. In E. C. Monahan & G. M. Niocaill (Eds.), *Oceanic whitecaps: And their role in air-sea exchange processes* (pp. 209–218). Dordrecht: Springer Netherlands.

Stramska, M., & Petelski, T. (2003). Observations of oceanic whitecaps in the north polar waters of the Atlantic. *Journal of Geophysical Research, 108*, C03086. https://doi.org/10.1029/2002JC001321.

Sugihara, Y., Tsumori, H., Ohga, T., Yoshioka, H., & Serizawa, S. (2007). Variation of whitecap coverage with wave-field conditions. *Journal of Marine Systems, 66*, 47–60. https://doi.org/10.1016/j.jmarsys.2006.01.014.

Sutherland, P., & Melville, W. K. (2015). Field measurements of surface and near-surface turbulence in the presence of breaking waves. *Journal of Physical Oceanography, 45*(4), 943–965. https://doi.org/10.1175/JPO-D-14-0133.1.

Thomson, J., Gemmrich, J. R., & Jessup, A. T. (2009). Energy dissipation and the spectral distribution of whitecaps. *Geophysical Research Letters, 36*, L11601. https://doi.org/10.1029/2009GL038201.

Thorpe, S. A. (1982). On the clouds of bubbles formed by breaking wind-waves in deep water, and their role in air – sea gas transfer. *Philosophical Transactions of the Royal Society of London. Series A, Mathematical and Physical Sciences, 304*(1483), 155–210.

Toba, Y., & Chaen, M. (1973). Quantitative expression of the breaking of wind waves on the sea surface. *Records of oceanographic works in Japan, 12*, 1–11.

Toba, Y., & Koga, M. (1986). A parameter describing overall conditions of wave breaking, whitecapping, sea-spray production and wind stress. In E. C. Monahan & G. Mac Niocaill (Eds.), *Oceanic whitecaps* (pp. 37–47). Dordrecht: Reidel Publishing Company.

Villarino, R., Camps, A., Vall-Ilossera, M., Miranda, J., & Arenas, J. (2016). Sea foam effects on the brightness temperature at l-band. In *Proceedings of Geoscience and Remote Sensing Symposium (IGARSS âĂŹ03)* (Vol. 5, pp. 3076–3078). Piscataway: IGARSS.

Woolf, D. K. (1997). Bubbles and their role in gas exchange. In P. S. Liss & R. A. Duce (Eds.), *The sea surface and global change* (pp. 173–205). Cambridge: Cambridge University Press.

Woolf, D. K. (2005). Parametrization of gas transfer velocities and sea-state-dependent wave breaking. *Tellus, 57B*, 87–94. https://doi.org/10.3402/tellusb.v57i2.16783.

Woolf, D. K., Bowyer, P. A., & Monahan, E. C. (1987). Discriminating between the film drops and jet drops produced by a simulated whitecap. *Journal of Geophysical Research Oceans, 92*(C5), 5142–5150. https://doi.org/10.1029/JC092iC05p05142.

Wu, J. (1979). Oceanic whitecaps and sea state. *Journal of Physical Oceanography, 9*, 1064–1068. https://doi.org/10.1175/1520-0485(1979)0092.0.CO;2.

Zhao, D., & Toba, Y. (2001). Dependence of whitecap coverage on wind and wind-wave properties. *Journal of Physical Oceanography, 57*, 603–616. https://doi.org/10.1023/A:1021215904955.

Zhao, D., Toba, Y., Suzuki, Y., & Komori, S. (2003). Effect of wind waves on air-sea gas exchange: proposal of an overall co2 transfer velocity formula as a function of breaking-wave parameter. *Tellus, 55*(B), 478–487. https://doi.org/10.1034/j.1600-0889.2003.00055.x.

Zhao, D., Toba, Y., Suzuki, Y., & Komori, S. (2006). New sea spray generation function for spume droplets. *Journal of Geophysical Research, 111*, CO2007. https://doi.org/10.1029/2005JC002960.

Chapter 3
Estimates of Wave Breaking Energy Dissipation Rate from Measurements of Whitecap Coverage

Adrian H. Callaghan

Abstract The easiest way to identify the occurrence, or recent occurrence of oceanic air-entraining breaking waves (whitecaps) from above the water surface is through photographic remote sensing of the sea surface. In this paper I estimate the energy dissipation rate due to breaking wave whitecaps using measurements of whitecap coverage of the sea surface. Several datasets are used that employed different methodologies for determining the whitecap coverage spanning almost 4 decades of research. The results show that, on average, the ratio of the energy dissipation rate due to whitecaps to the wind energy input rate to the upper ocean and wave field is close to unity above wind speeds of about 10 m s^{-1}. Below 10 m s^{-1}, this energy flux ratio decreases steadily from unity as wind speed decreases, in agreement with several recent studies. The implication is that other dissipative processes play an important role in dissipating the wind energy input to the upper ocean and wave field at low wind speeds. These results suggest that variability in this energy flux ratio may be responsible for differences in measurements and parameterisations of whitecap coverage at low wind speeds.

3.1 Introduction

"Anyone who has stood on a clifftop and looked seaward on a windy day is aware that whitecaps are brighter than those regions of the sea surface which are devoid of bubble rafts" (Monahan and O'Muircheartaigh 1986). The essence of this statement has influenced much of the remote sensing of sea surface whitecaps for almost half a century (Monahan 1971), and continues to be the basis on which new datasets of breaking wave whitecaps are collected and analysed with routine digital image acquisition and automated analysis procedures (Brumer et al. 2017). The associated broadband scattering of light by the turbulent aerated two-phase flow allows whitecaps to be recorded, measured and analysed in terms of areal coverage of the sea surface, whitecap kinematics and energy dissipation (Melville and Matusov 2002;

A. H. Callaghan (✉)
Department of Civil and Environmental Engineering, Imperial College London, London, UK
e-mail: a.callaghan@imperial.ac.uk

P. Vlahos (ed.), *Recent Advances in the Study of Oceanic Whitecaps*,
https://doi.org/10.1007/978-3-030-36371-0_3

Monahan and O'Muircheartaigh 1980; Schwendeman et al. 2014). Therefore, it is precisely because of their nature that whitecaps are an important driver of air-sea exchange processes and that whitecap occurrence can be measured with conventional photographic remote sensing techniques.

Whitecap foam at the ocean surface indicates the occurrence or recent occurrence of air-entraining wave breaking. The turbulent two-phase flow associated with whitecaps plays a critical role in many bubble-mediated air sea fluxes. Consequently, many studies have sought to characterise the relationships between air-sea fluxes of heat, gas and mass with the instantaneous coverage of the sea surface in whitecap foam, termed whitecap coverage (W). For example, E.C. Monahan and colleagues have used measurements and parameterisations of whitecap coverage to estimate variability in air-sea exchange of gas, sea spray aerosols, heat and carbon, as well as looking at effects of whitecaps on ocean acoustics (Andreas and Monahan 2000; Monahan and Spillane 1984; Monahan et al. 1982, 1986; Monahan and Lu 1990; Monahan and Dam 2001; Monahan and Callaghan 2015).

It is clear that much work has been carried out to relate the whitecap coverage of the oceans to various air-sea exchange processes. Moreover, an improved physical understanding and interpretation of whitecap coverage has the potential to benefit parameterisations of a wide number of air-sea exchange and upper ocean properties. Whitecap coverage is critically related to the rate of energy dissipation by whitecaps (S_{wcap}), such that if S_{wcap} is known, it should be possible to estimate W. Conversely, if W is measured, then estimates of S_{wcap} could be made. A quantitative relationship between S_{wcap} and W can introduce new possibilities to estimate W on a global scale using spectral wave models, thus moving away from single parameter wind speed parameterisations of W. This is desirable because sea state, wave breaking and whitecap-driven energy dissipation are not uniquely controlled by wind speed. In recognition of the importance of sea state in driving variability in whitecap coverage, several recent studies have parameterised and modelled whitecap coverage in terms of wind and sea state variables (Anguelova and Hwang 2016; Brumer et al. 2017; Scanlon et al. 2016).

In this paper, I follow the model outlined in Callaghan (2018) and derive estimates of S_{wcap} using measurements of whitecap coverage from several field datasets that also contain estimates of the wave energy dissipation rate, S_{ds}. The model emphasises the 3-dimensional nature of whitecaps with an explicit representation of the bubble plume penetration depth beneath actively breaking whitecaps. The model also accounts for the fraction of the wind energy input that is not dissipated by whitecaps, but by other processes. In a stationary sea state that is in dynamical equilibrium with the overlying wind forcing, the rate wind energy input to the wave field and upper ocean (S_{in}) is balanced by the wave field energy dissipation rate, and it is expected that $S_{in} \approx S_{ds}$. Several distinct physical processes contribute to S_{ds} such as Langmuir turbulence, micro-breaking waves, swell wave dissipation and whitecapping. Therefore, inverse estimates of S_{wcap} from observations of whitecap coverage can be a useful tool to evaluate the dissipative role of whitecapping in comparison to the other dissipative processes listed above. Recent work by Sutherland and Melville (2015), and subsequently by Banner and Morison (2018), suggest

that in old, swell dominated seas at low wind speeds, the energy flux ratio S_{wcap}/S_{in} can be as low as 0.1–0.2. Constraining variability in S_{wcap}/S_{in}, therefore has important implications for how whitecap coverage, and bubble-mediated air sea exchange processes, might be parameterised in terms of wind speed or S_{in}.

The paper proceeds as follows. Section 3.2 presents an overview of the Callaghan (2018) model. Estimates of S_{wcap} are made in Sect. 3.3 and compared to values of S_{in} and the variability in S_{wcap}/S_{in} is explored as a function of wind speed. This is followed by some conclusions in Sect. 3.4.

3.2 The Whitecap Energy Dissipation Model

The model relating the energy dissipation rate of whitecaps to whitecap coverage is described in Callaghan (2018) (hereafter referred to as C18), and a brief overview is given here. The model is derived from the laboratory results of Callaghan et al. (2016) which relates the total energy dissipated by a single breaking wave to the volume of the two-phase flow integrated in time until the maximum whitecap foam area is reached. This quantity is called the volume-time-integral (VTI). The breaking waves used in Callaghan et al. (2016) (hereafter referred to as CDS16) were unforced 2-dimensional breaking waves generated in a wave channel at the Scripps Institution of Oceanography. The experiments showed a linear relationship between the VTI and the measured total energy dissipation (ΔE_T – kg m^2 s^{-2}) for a series of 20 breaking wave packets that varied from weakly spilling to strongly plunging. Specifically, the following relationship was found:

$$\Delta E_T = \Omega \rho A_o \widehat{z}_p \tau_{growth} \tag{3.1}$$

Here, ρ is water density, A_o is the maximum foam area of a whitecap during wave breaking, $\widehat{z}_p$ is the whitecap area-weighted average bubble plume penetration depth during active wave breaking (see CDS16 for further details), and τ_{growth} is an integral timescale that characterises the breaking wave duration. Together, the terms $A_o \widehat{z}_p \tau_{growth}$ quantify the VTI of an individual breaking wave. The term Ω is the turbulence strength parameter with units W kg^{-1}. Its value was found to be 0.88 ($\pm$0.04) W kg^{-1}, determined as the slope of a least mean-squares linear fit between the measured ΔE_T and the VTI. This model was also found to be an excellent fit to the combined laboratory datasets of Duncan (1981), Lamarre and Melville (1991), and Blenkinsopp and Chaplin (2007).

Taking Eq. (3.1) as a representative model of the energy dissipated by a single whitecap, C18 derived a relationship between the energy dissipation rate of a population of whitecaps (S_{wcap}, with units W m^{-2}), whitecap coverage and the ensemble average bubble plume penetration depth of the total whitecap population ($\widehat{z}_p^*$). The model can be written in terms of total whitecap coverage (W) or growth phase whitecap coverage (W_{growth}). The latter determines the contribution of

whitecap foam area from actively breaking waves only, thereby neglecting the foam coverage contribution from decaying whitecap foam patches W_{decay} which is driven by degassing bubble plumes and surfactant effects (Callaghan et al. 2017). The whitecap energy dissipation rate models using W_{growth} and W are written, respectively, as:

$$S_{wcap} = \Omega \rho \widehat{z}_p^* W_{growth} = S_{in} - S_{other} \tag{3.2}$$

and

$$S_{wcap} = \frac{\Omega \rho \widehat{z}_p^* W}{(1+\delta)} = S_{in} - S_{other} \tag{3.3}$$

The right hand side of Eqs. 3.2 and 3.3 recognises the fact that energy dissipation by whitecaps is not the only process responsible for energy dissipation. The term S_{in} quantifies the rate of energy input to the wave field and upper ocean from the overlying wind field, and S_{other} quantifies the energy dissipation by processes such as the mechanical wind stirring of the upper-ocean, Langmuir turbulence and swell wave dissipation. The δ term in Eq. 3.3 is defined as the ratio of decay phase whitecap coverage to growth phase whitecap coverage, W_{decay}/W_{growth}, and the analysis of oceanic whitecaps in CDS18 suggest that its value is an increasing function of $\widehat{z}_p^*$.

There are some important points to mention about Eqs. 3.2 and 3.3. Firstly, Eq. 3.2 suggests that both W_{growth} and $\widehat{z}_p^*$ are needed to estimate S_{wcap} because a value of W_{growth} may not necessarily have a unique value of $\widehat{z}_p^*$. This relationship stems directly from the results of CDS16 which shows that VTI during the whitecap growth phase is linearly proportional to the total energy dissipated by the breaking wave. Therefore, the whitecap energy dissipation rate for a population of whitecaps is inextricably linked to both the surface whitecap coverage and the average vertical bubble plume penetration depth.

Secondly, it is only when S_{other} is negligible that S_{wcap} can be assumed to be approximately equal to S_{in}. This has shown to be true in ocean measurements of Sutherland and Melville (2015). The implications of this will be explored in more detail in Sect. 3.3.

Finally, whitecap coverage can be written as the sum of the whitecap coverage growth and decay contributions such that $W = W_{growth} + W_{decay}$. The decay term can be further decomposed into a degassing term, W_{degas} and a surfactant stabilised term, W_{stab}. The degassing term (W_{degas}) recognises the fact that after active breaking has ceased, the optically resolvable surface whitecap is only sustained for as long as there is a sufficient flux of bubbles to the water surface (Callaghan et al. 2013; Monahan and O'Muircheartaigh 1986). Therefore, the value of W_{degas} is directly dependent on $\widehat{z}_p^*$ because deeper bubble plumes take longer to rise to the surface.

Once at the surface, whitecap foam can be stabilised by naturally occurring surfactants that act to reduce the rate at which fluid drains from the whitecap foam

cell walls thereby extending the lifetime of patches of whitecap foam. The consequence is that W can also be affected by variations in water chemistry or surfactant concentration and type. Little is known about the magnitude of this surfactant effect, but previous studies suggest that the contribution of foam streaks to W, caused by surfactant-driven foam stabilisation, becomes larger with increasing wind speed, especially at wind speeds above 15 m s^{-1} (e.g. Holthuijsen et al. 2012; Ross and Cardone 1974). Callaghan et al. (2017) defined a foam stabilisation metric, Θ, to quantify surfactant-driven foam stabilisation of individual whitecaps and found that Θ tended to increase with increasing wind speed, in general agreement with Ross and Cardone (1974) and Holthuijsen et al. (2012).

The previous analysis indicates that using W in place of W_{growth}, but without accounting for how W is influenced by surfactant stabilisation effects would lead to an overestimation of S_{wcap}. When W_{stab} is negligible, however, the δ term in Eq. 3.3 can be parameterised in terms of $\widehat{z}_p^*$ alone, and either W or W_{growth} can be used to estimate S_{Wcap} as described in C18. In the analysis that follows, it is assumed that $W_{stab} \approx 0$ such that $W_{degas} = W_{decay}$.

In order to use either Eqs. 3.2 or 3.3 to estimate S_{wcap}, an estimate of $\widehat{z}_p^*$ is required. A wind speed dependent parameterisation of $\widehat{z}_p^*$, was proposed by C18, and is given by:

$$\widehat{z}_p^* = 0.0098 \frac{u_{10}^2}{g} + 0.02 \tag{3.4}$$

The parameterisation was derived from field observations of the ratio of stage A whitecap coverage (W_A) to whitecap coverage reported in Scanlon and Ward (2016). In C18, the assumption that $W_{growth} \approx W_A$ was made which allowed the measured ratio W_A/W to be used to estimate the value of $\widehat{z}_p^*$ as a function of u_{10} following the model in C18. Stage A whitecap coverage has been defined by Monahan and Woolf (1989) as the "surface manifestation of plunging aerated plumes" and it is directly linked to actively breaking whitecaps. W_{growth} is a measure of the foam area integrated in time from incipient breaking to maximum foam area and is therefore also related to the active phase of wave breaking. Therefore, the assumption that $W_{growth} \approx W_A$ is reasonable.

3.3 Results and Discussion

In this section the whitecap model described in Sect. 3.2 is applied to two datasets of whitecap coverage measurements and used to estimate S_{wcap}. These datasets also have accompanying estimates of the wave field energy dissipation rate, S_{ds}. In what follows the assumption of dynamical equilibrium is applied such that $S_{in} \approx S_{ds}$, thereby characterising a stationary wave field in dynamical equilibrium with the overlying wind forcing. This assumption neglects energy attributed to wave growth,

and is expected to be accurate within 5–10% (Hwang and Sletten 2008). The assumption of $S_{in} \approx S_{ds}$ was also made in C18, however in that study, independent estimates of S_{ds} were not used, and were determined from the overlying wind speed. Therefore, the present datasets to be used have more direct estimates of S_{ds} than C18.

The two datasets of measurements used in this study are taken from Hwang and Sletten (2008) (hereafter referred to as HS08) and Hanson and Phillips (1999) (hereafter referred to as HP99), and details of these are given below. These datasets are used to estimate the energy dissipation rate due to whitecaps, S_{wcap}, and the ratio S_{wcap}/S_{in} as a function of wind speed. The use of a wide range of datasets of whitecap coverage from various authors is useful because of the disparity of measurement and image analysis techniques used.

3.3.1 The TLS and HP99 Datasets

HS08 collected a dataset of whitecap coverage, wind speed and wave field measurements from the studies of E C Monahan (1971), Toba and Chaen (1973), Ross and Cardone (1974), Xu et al. (2000), (Lafon et al. 2004, 2007), and Sugihara et al. (2007), which was collectively termed "MTRXLS" in HS08. Of these datasets, Toba and Chaen (1973), Lafon et al. (2004, 2007) and Sugihara et al. (2007) were accompanied by wave measurements. Data from these studies will be used in this study, and the collective dataset is termed "TLS" hereafter. The wave measurements consisted of values of wave peak frequency (ω_p) and significant wave height (H_S), and the whitecap measurements were of total whitecap coverage, W. The wave energy dissipation rate (S_{ds}) estimates were calculated in HS08 as $S_{ds} = \alpha \rho_{air} U_{10}^3$, where $\alpha = 0.20\omega_*^{3.3}\eta_*$. The terms ω_* and η_* are non-dimensional wave frequency and non-dimensional wave variance, respectively, as defined in HS08 to which the reader is referred. These data were kindly provided by P. Hwang.

HP99 made measurements of the wave spectrum in the North Pacific and used accompanying measurements of Stage A whitecap coverage, W_A, which were provided by E.C. Monahan from the Monahan and Wilson (1993) study. The in-situ measured wave spectrum data were used to calculate S_{ds} following the equilibrium range theory of Phillips (1985). The HP99 dataset is characterised by variable wind forcing and mixed wave conditions which were often swell-dominated (see their figures 1 and 2). Furthermore, their S_{ds} calculations showed strong correlation with wind acceleration: for a given wind speed, S_{ds} was larger in decreasing winds than in rising winds. The HP99 data used here were digitised from their Figure 10 and Figure 11.

Figure 3.1a shows the wind speed dependence of the TLS W dataset and the HP99 W_A dataset. As expected, the HP99 W_A datapoints fall below the TLS W data. Both datasets exhibit scatter of 1–2 orders of magnitude at low wind speeds and this scatter tends to decrease with increasing wind speed. For example, the HP99 data show a distinct decrease in scatter at wind speeds above 10 m s^{-1}. For reference,

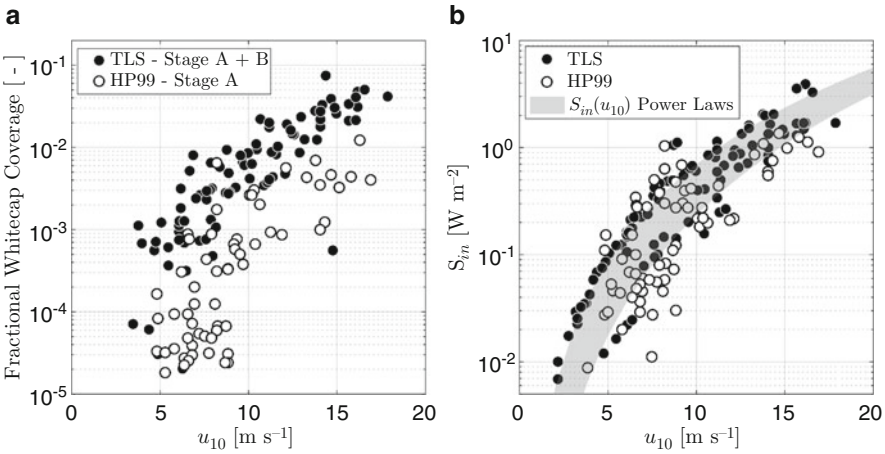

Fig. 3.1 (a, b). Panel (**a**) shows the variation of the measured whitecap coverage as a function of wind speed for the two datasets used here. The TLS dataset reports W measurements, whereas W_A was measured in HP99. Panel (**b**) shows the corresponding estimates of S_{in} derived from S_{ds} under the assumption that $S_{in} \approx S_{ds}$. The shaded region shows the range of $S_{in}(u_{10})$ estimates from the wind speed power laws reported in HP99, HS08 and C18

Figure 2 in HP99 shows that at wind speeds above about 10 m s^{-1}, the contribution of wind-wave significant wave height to the overall significant wave height increases signifying the decreasing contribution of swell waves to the overall wave spectral energy.

Figure 3.1b shows the estimates of the rate of energy input to the wave field and upper ocean (S_{in}) from each of the two datasets derived from wave field measurements under the assumption adopted here that $S_{in} \approx S_{ds}$. The shaded region shows the upper and lower range of S_{in} as a function of u_{10} from parameterisations reported in HS08 and HP99. The figure clearly demonstrates that while S_{in} is a strong function of wind speed, variations in sea state at a given wind speed introduce up to an order of magnitude variability in S_{in}.

3.3.2 *Variation in* $\mathbf{S_{wcap}}$ *as a Function of* $\mathbf{u_{10}}$

Estimates of S_{wcap} can be made for the TLS and HP99 datasets from their whitecap and wind speed measurements, along with the estimate of $\widehat{z}_p^*$ from Eq. 3.4. Note that for the HP99 dataset, the assumption that $W_{growth} \approx W_A$ has been made. Furthermore, for the TLS dataset, the assumption of negligible foam stabilisation by surfactants has been made, and equation (21) in C18 has been used to estimate δ in Eq. 3.3.

Figure 3.2 shows the relationship between wind speed and S_{wcap} for both datasets together. Above wind speed of about 10 m s^{-1}, there is good agreement between the S_{wcap} estimates for both datasets. This is encouraging for several reasons. Firstly, the whitecap measurements were made with different photographic techniques ranging

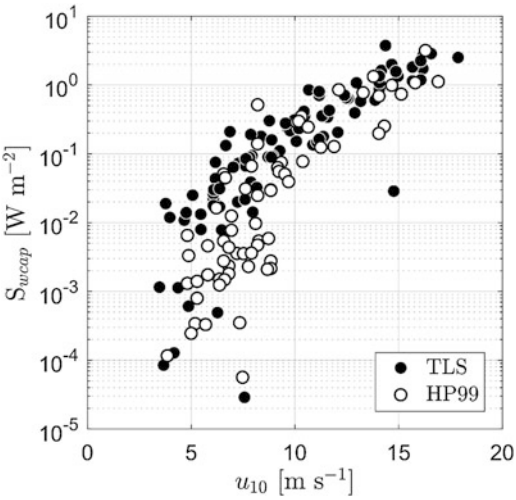

Fig. 3.2 The variation of the wave energy dissipation rate associated with whitecaps computed following the model in Callaghan (2018)

from the original manual analysis technique in Toba and Chaen (1973) to the digital image processing techniques in, for example, Sugihara et al. (2007). Secondly, the values of S_{wcap} were derived from both total whitecap fraction and growth phase whitecap fraction, measurements which often differ by a factor of 10 in magnitude as seen in Fig. 3.1a above. Thirdly, the S_{wcap} model was derived based upon unforced laboratory braking waves in a narrow wave channel, yet when applied to different whitecap datasets from different investigators provides good agreement in S_{wcap} at relatively high wind speeds.

At lower wind speeds below about 9–10 m s^{-1}, there is much more scatter in both datasets of S_{wcap}, and the HP99 values tend to lie below those of the TLS dataset. This may be explained by the very large swell presence in the wave field for the HP99 dataset, as evidenced by their figure 2. It has been shown in previous studies that in older-swell dominated seas, wave breaking is reduced and more variable compared to locally wind-driven seas (Callaghan et al. 2008b; Sugihara et al. 2007). Furthermore, the fraction of the wind energy input to the upper ocean that is dissipated by air-entraining whitecaps has been found to be reduced in low wind swell-dominated seas when compared to younger locally-forced wind-driven seas (Banner and Morison 2018; Sutherland and Melville 2013, 2015). This may be due to a misalignment of the wind stress and wind velocity vectors at low wind speeds caused by swell waves in a swell-dominated or mixed sea (Chen et al. 2018).

3.3.3 *Comparisons of* $\mathbf{S_{in}}$ *and* $\mathbf{S_{wcap}}$

In this section, the estimates of S_{wcap} generated for the TLS and HP99 datasets in Sect. 3.2 are compared against the corresponding estimates of S_{in}. This is done in

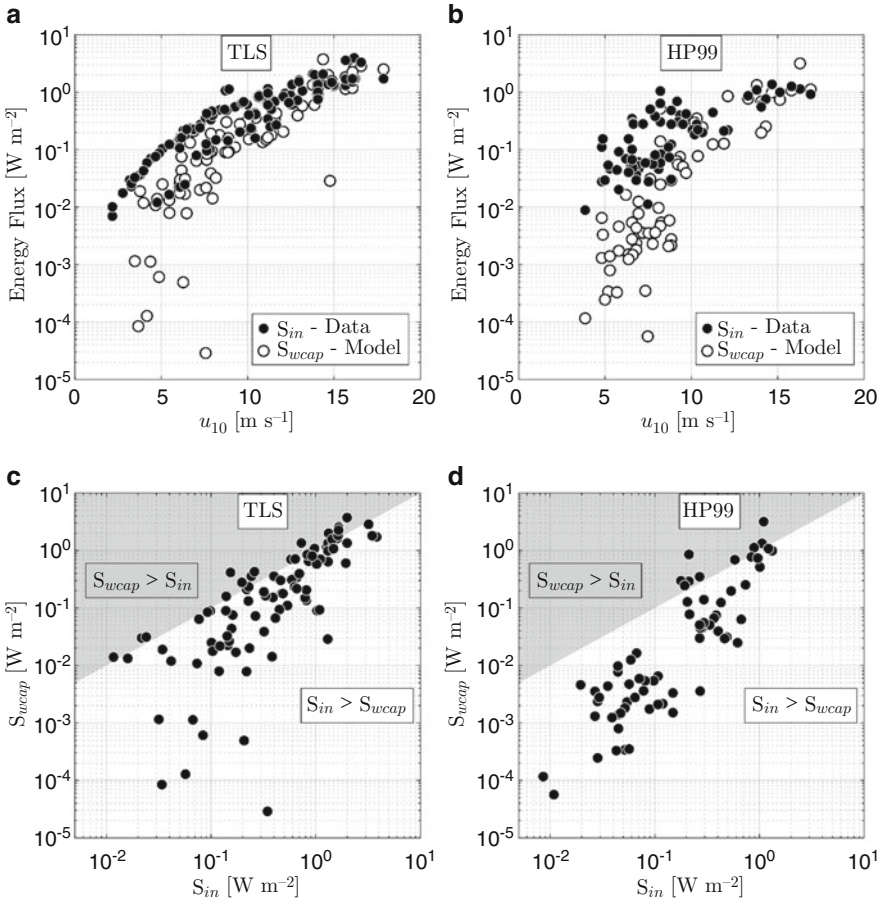

Fig. 3.3 **(a–d)** Panel a and panel b shows a comparison of the variation of S_{in} and S_{ds} as a function of wind speed for the TLS and HP99 datasets, respectively. Panel c and d are scatter plots of S_{in} and S_{ds} for the TLS and HP99 datasets, respectively. The grey shaded region is where the energy dissipation rate of whitecaps exceeds the energy input to the wave field from the overlying wind. Below the shaded region the energy input to the wave field from the overlying wind is greater than the energy dissipation rate of whitecaps

order to estimate how much of the wind energy input to the wave field is balanced by whitecap-driven energy dissipation.

Figure 3.3a, b show how S_{in} and S_{wcap} for the TLS and HP99 datasets vary with wind speed, respectively. In both datasets, there is a strong degree of overlap between the S_{in} and S_{wcap} values at wind speeds greater than about 9–10 m s^{-1}. The implication is that air-entraining whitecaps are the dominant mechanism of dissipating wave energy at these wind speeds, and they dissipate this energy in sufficient quantities to balance the energy input from the wind. This finding is in

general agreement with the field measurements of Sutherland and Melville (2015) and the conclusions of Banner and Morison (2018).

At lower wind speeds, the S_{wcap} model estimates tend to lie below the S_{in} measurements. The implication is that the relative importance of whitecapping as a dissipative mechanism reduces at low wind speeds and the relative dissipative role of other processes increases. Again, this agrees with the findings of Sutherland and Melville (2015) and Banner and Morison (2018). At these low wind speeds, the HP99 S_{wcap} estimates are consistently lower than S_{in}, which likely reflects the preponderance for reduced wave breaking in swell-dominated seas. For example, when Sugihara et al. (2007) classified their sea states as either pure wind-driven seas and seas with swell waves they found consistently lower whitecap coverage values in swell-dominated conditions than in pure wind seas (see their figure 12).

Figure 3.3c, d directly compare values of S_{wcap} and S_{in} for the TLS and HP99 datasets, respectively. In both datasets, it is clear that the estimated S_{wcap} rarely exceeds S_{in}. This result provides confidence that the C18 model provides realistic estimates of S_{wcap} from measurements of either W or W_{growth}. Importantly, it confirms the importance of incorporating a variable estimate of bubble plume penetration depth when interpreting whitecap measurements in terms of energy dissipation rate.

3.3.4 *Comparing of* S_{wcap}/S_{in} *to Field Data*

The results in Sect. 3.3.3 suggest that, at sufficiently large wind speeds, whitecaps are the dominant dissipative mechanism balancing the wind energy input to the wave field and upper ocean. To examine this more closely, the ratio S_{wcap}/S_{in} is plotted as a function of wind speed in Fig. 3.4a, b for the TLS and HP99 datasets, respectively. A value of unity suggests that wind energy input is balanced through dissipation by whitecaps.

At low wind speeds of less than about 10 m s^{-1}, there is a considerable degree of scatter in the S_{wcap}/S_{in} energy flux ratios, with many data points falling considerably below unity. This is a common feature in both datasets, but is more pronounced in the HP99 dataset, which may be a reflection of the strong swell influence at low wind speeds, as mentioned above. Indeed, the HP99 energy flux ratios do not approach unity until the wind speed exceeds 10 m s^{-1}. In contrast, the energy flux ratios in the TLS dataset do reach unity at wind speeds as low as 5 m s^{-1}, but also with considerable scatter.

At higher wind speeds of 10 m s^{-1} and above, most of the data points in figure 4a and figure 4b lie within a factor of 2 of unity. When the data points are averaged and binned by wind speed, the average data points lie very close to unity in the TLS dataset. There is somewhat more variability in S_{wcap}/S_{in} for the HP99 dataset, but still the variability is scattered around unity. Importantly in both datasets, there does not appear to any bias in S_{wcap}/S_{in} above or below unity at these larger wind speeds. The data suggest that on average, whitecapping is the dominant dissipative process at wind speeds above about 10 m s^{-1}, and is sufficient to balance the wind energy input.

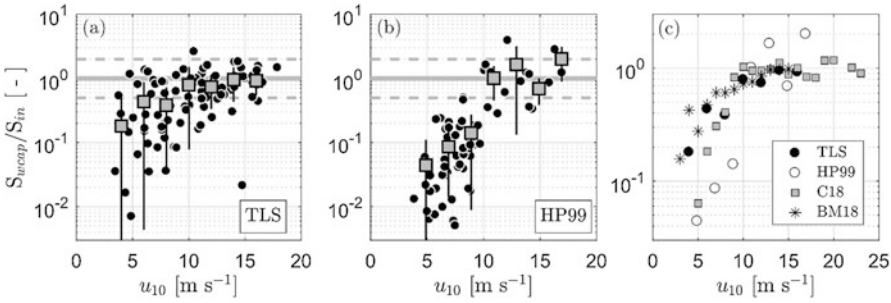

Fig. 3.4 **(a–c)** Panel a shows the ratio of the estimated energy dissipation rate due to whitecaps and wind energy input rate to the wave field for the TLS dataset. The squares are average values in 2 m s^{-1} wind speed bins, and vertical lines represent ±1 standard deviation around the mean. The solid grey line shows a value of unity, and the dashed lines show a variation of a factor of 2 around unity. Panel b has the same format as panel a but using the HP99 dataset. Panel c shows average values binned by wind speed for several datasets (note the change in vertical scale from panels a and b). The filled and open circles are the binned TLS and HP99 data from panel a and panel b, respectively. The grey squares are whitecap coverage based estimates from Callaghan (2018) (C18). The asterisks are derived from the *in-situ* ocean measurements of Sutherland and Melville (2015) as reported in Banner and Morison (2018) (BM18). Standard deviations of the mean data points have been omitted for clarity

In order to compare the energy flux ratio estimates from the TLS and HP99 datasets, Fig. 3.4c compares the bin average S_{wcap}/S_{in} values to average values from two other studies. Firstly, C18 use a dataset of whitecap coverage measurements to estimate S_{wcap} that span wind speeds of between 4 m s^{-1} and 23 m s^{-1} reported in Callaghan et al. (2008a). These data were taken as part of the Marine Aerosol Production (MAP) campaign which took place in the North Atlantic in the summer of 2006. Estimates of S_{in} for that study came from a least mean squares fit to the S_{wcap} data at wind speed above 10 m s^{-1}, which was then extrapolated to lower wind speeds. While this approach was a necessary approximation, these resulting estimates of $S_{in}(u_{10})$ were in excellent agreement with the $S_{in}(u_{10})$ parameterisations given in HS08 and HP99 for wind speeds larger than 10 m s^{-1}.

Secondly, but more importantly, data from figure 13 in BM18 were digitised and used to estimate S_{wcap} and S_{in}, and the ratio of these quantities is plotted as a function of wind speed plotted at 1 m s^{-1} intervals in Fig. 3.4c. These data originate from the field study of Sutherland and Melville (2015) from direct measurements of oceanic subsurface turbulence, the breaking wave field (including both micro-breakers and whitecaps) and the wind field.

The combined four S_{wcap}/S_{in} datasets, namely TLS, HP99, C18 and BM18, are plotted as a function of wind speed in figure 4c. Of these datasets, it is important to note that the BM18 is the most direct estimate. At wind speeds above 10 m s^{-1}, the average values of S_{wcap}/S_{in} fall very close to a value of unity, regardless of the origin of the dataset, albeit with the HP99 dataset showing larger fluctuations. This provides strong evidence supporting the data in Sutherland and Melville (2015) and the conclusions in Banner and Morison (2018), that at sufficiently large wind speeds

(i.e. $u_{10} \gtrsim 10$ m s^{-1}), when the wave field is less likely to be swell-dominated, whitecaps largely balance the wind energy input to the wave field and upper ocean. It is worth pointing out that the agreement between all four datasets at these wind speeds is excellent given that the S_{wcap} values of TLS, HP99 and C18 are derived from remote sensing of whitecaps from different studies, in different locations and using non-standardised image acquisition and analysis techniques.

The agreement in values of S_{wcap}/S_{in} at wind speeds greater than 10 m s^{-1}, mirrors the reduction in variability between whitecap coverage parameterisations where digital image analysis was used. As pointed out in Brumer et al. (2017) (see their Figure 1), there is much closer agreement between wind speed parameterisation of W above wind speeds of 10 m s^{-1} developed since 2007, when compared to datasets collected prior to this. This increase in agreement between wind speed parameterisations may reflect a move to more standardised image analysis techniques as suggested by Brumer et al. (2017). It may also be related to the larger image datasets that digital image analysis can enable, thereby decreasing uncertainty in whitecap coverage estimates at larger wind speeds where fewer data points have been collected.

As seen in Fig. 3.4c, agreement between the four datasets diminishes at lower wind speeds, accompanied by a decreasing trend in S_{wcap}/S_{in} values with decreasing wind speed. There is still a large degree of overlap between several of the studies, most notably BM18, TLS and C18, but the values of S_{wcap}/S_{in} from the different studies diverge as the wind speed drops. This is presumably a reflection of the different sea states between the studies at these low wind speeds. Indeed, at lower wind speeds, the presence of swell waves can have a much larger influence on the local wave field. Moreover, from *in-situ* measurements, Sutherland and Melville (2015) conclude that the dissipative contribution from whitecaps diminishes with increasing wave age characteristic of older swell-dominated seas.

Wind speed independent variability in wave age at low wind speeds is likely an important factor influencing wave breaking patterns which can drive large variability in values of S_{wcap}/S_{in}. One way in which variability in wave breaking patterns can be quantified at low wind speeds is by identifying the minimum wind speed at which whitecaps are first measured via photographic remote sensing of the ocean surface. This idea of a critical wind speed above which whitecaps can be recorded in images of the sea surface is encapsulated in terms of the Beaufort velocity (u_B) introduced by Monahan and O'Muircheartaigh (1986). As defined, the Beaufort velocity quantifies the wind speed at which there is a 50% chance of observing a whitecap in a set of images of the sea surface. Monahan and O'Muircheartaigh (1986) conclude that u_B is dependent on a range of factors, with water temperature and the stability of the lower atmosphere being of particular importance. For example, their Figure 2 suggests that u_B may extend from approximately 2 m s^{-1} to 7.5 m s^{-1} for a water-air temperature difference of +4 °C to −8 °C. In other words, whitecapping begins at lower wind speeds in conditions of unstable atmospheric stability. This view is supported qualitatively by Kraan et al. (1996) who commented that in their whitecap observations, there were "....two situations where no whitecaps were visible, though the wind speed was in the range 7-8 m s^{-1}". One of these instances occurred

in very stable atmospheric conditions, and the other in a neutrally stratified lower atmosphere. They also note that these observations occurred at times of strong tidal currents reaching magnitudes of 1 m s^{-1} which may have played a contributing role.

In addition to the Beaufort velocity set out in Monahan and O'Muircheartaigh (1986), previous studies have reported values of the critical wind speed above which whitecap coverage is non-zero. Estimates of this critical wind speed are found by fitting a model of the form $W = a(u_{10} - b)^n$ to a dataset of whitecap coverage and wind speed measurements. The value of the coefficient b represents the speed at which whitecapping is expected to begin. Values for this wind speed range between 2.56 m s^{-1} (Scanlon and Ward 2016) and to 6.33 m s^{-1} (Stramska and Petelski 2003) which are similar in magnitude to those reported in Monahan and O'Muircheartaigh (1986). The physical causes for the variation in this minimum critical wind speed are not entirely clear, but Stramska and Petelski (2003) suggest it is related to wave field development. Their data suggests that the onset of whitecapping is delayed in undeveloped or younger seas. In any case, it is evident from previous studies that a large degree of variability in wave breaking activity, and hence whitecap-driven energy dissipation can occur at wind speeds below about 8 m s^{-1}, in agreement with the data presented in Fig. 3.4 here.

3.4 Summary and Conclusions

The photographic observation of whitecaps at the ocean surface remains the most straightforward above-water method to detect the occurrence and scale of breaking waves in the ocean. The high reflectance of the aerated two-phase flow allows digital image remote sensing and subsequent image analysis techniques to return information on the properties of individual whitecaps, and populations of whitecaps, which can be used to estimate energy dissipation rates associated with breaking wave whitecaps.

This study has presented estimates of the energy dissipation rate of breaking wave whitecaps via the results of image analysis of sea surface images following the model presented in Callaghan (2018). The datasets used consisted of observations of both whitecap coverage and stage A, or growth phase, whitecap coverage, along with coincident measurements of wind and wave properties. To implement the model, the whitecap coverage measurements were combined with estimates of the average bubble plume penetration depth estimated from the wind speed parameterisation presented in Callaghan (2018). The wave measurements were used to calculate the dissipation rate of wave energy. The assumption of a stationary wave field was made such that total wave energy dissipation rate balanced the rate of wind energy input to the upper ocean and wave field. The estimates of the whitecap energy dissipation rate were then compared to coincident estimates of the wind energy input rate. This was used to determine the fraction of wind energy that is dissipated by whitecaps, and how this fraction varied as a function of wind speed.

These data were then compared to the results of Sutherland and Melville (2015), as presented by Banner and Morison (2018).

Under the constraints of the assumptions made here, as well as the assumptions inherent in the Callaghan (2018) model, the analysis in this study suggests that, on average in an equilibrium sea state, the fraction of the wind energy input to the wave field that is balanced by energy dissipation in whitecaps is not constant and typically increases with wind speed, approaching unity for wind speeds above 10 m s^{-1}. In other words, almost all of the wind energy input to the wave field is dissipated by whitecaps, with other dissipative processes playing a minor role at these wind speeds. This conclusion was found to be consistent across several different datasets, one of which was derived from direct oceanic turbulence and wave field measurements, with the others derived from remote sensing measurements of whitecaps and *in situ* wave field measurements. At lower wind speeds, below about 10 m s^{-1}, there is a large degree of variability in the energy flux ratio which ranged by up to two orders of magnitude from 1 to approximately 0.01for individual data points.

The results presented have implications for how either wind energy input models and energy dissipation rate in spectral wave models may be used to estimate air-sea bubble-mediated fluxes of gas and aerosol production, especially at low wind speeds. The analysis suggests, in line with the general conclusions of Sutherland and Melville (2015) and Banner and Morison (2018), that wave breaking whitecaps are not always the dominant mechanism balancing the wind energy input into the wave field at low wind speeds. It is speculated that variations in sea state at these low wind speeds, and in particular the presence or absence of swell, is responsible for this large variation. Further work is needed to constrain this variability in terms of wave field parameters. It should also be said that variability in how well wind energy input rate is estimated may also be important, but examining this in detail was beyond the scope of this study.

Finally, the estimates of the energy dissipation rate of whitecaps in this study provided an upper bound to the values of wind energy input. That provides further support that the model developed in Callaghan (2018), which was in part derived from a series of laboratory breaking wave experiments, is applicable to oceanic conditions. A key element of this model is the recognition that both the average bubble plume penetration depth and the surface whitecap coverage are needed to estimate the dissipation rate associated with whitecaps. Presently, the bubble plume penetration depth values used have been parameterised in terms of the wind speed raised to the power of 2. This functional form suggests that bubble plume penetration depth is proportional to the significant wave height of wind-forced waves, which has also been found to follow a similar wind speed dependence (Hanson and Phillips 1999). Further work is needed to develop a sea-state dependent parameterisation of bubble plume penetration depth, preferentially based on data from direct *in-situ* measurements.

Acknowledgements AHC gratefully acknowledges the provision of data from several studies by Paul Hwang. Funding for this study came from a Royal Society International Shooter Fellowship awarded to AHC. The author wishes to express his gratitude to E.C. Monahan for many helpful discussions on whitecaps.

References

Andreas, E. L., & Monahan, E. C. (2000). The role of whitecap bubbles in air–sea heat and moisture exchange. *Journal of Physical Oceanography, 30*(2), 433–442. https://doi.org/10.1175/1520-0485(2000)030<0433:Trowbi>2.0.Co;2.

Anguelova, M. D., & Hwang, P. A. (2016). Using energy dissipation rate to obtain active whitecap fraction. *Journal of Physical Oceanography, 46*(2), 461–481.

Banner, M. L., & Morison, R. P. (2018). On the upper ocean turbulent dissipation rate due to microscale breakers and small whitecaps. *Ocean Modelling, 126*, 63–76. https://doi.org/10.1016/j.ocemod.2018.04.004.

Blenkinsopp, C., & Chaplin, J. (2007). *Void fraction measurements in breaking waves*. Paper presented at proceedings of the Royal Society of London A: Mathematical, Physical and Engineering Sciences, The Royal Society.

Brumer, S. E., Zappa, C. J., Brooks, I. M., Tamura, H., Brown, S. M., Blomquist, B. W., Fairall, C. W., & Cifuentes-Lorenzen, A. (2017). Whitecap coverage dependence on wind and wave statistics as observed during SO GasEx and HiWinGS. *Journal of Physical Oceanography, 47*(9), 2211–2235. https://doi.org/10.1175/jpo-d-17-0005.1.

Callaghan, A. H. (2018). On the relationship between the energy dissipation rate of surface-breaking waves and oceanic whitecap coverage. *Journal of Physical Oceanography, 48*(11), 2609–2626. https://doi.org/10.1175/jpo-d-17-0124.1.

Callaghan, A., de Leeuw, G., Cohen, L., & O'Dowd, C. D. (2008a). Relationship of oceanic whitecap coverage to wind speed and wind history. *Geophysical Research Letters, 35*(23), n/a–n/a. https://doi.org/10.1029/2008GL036165.

Callaghan, A. H., Deane, G. B., & Stokes, M. D. (2008b). Observed physical and environmental causes of scatter in whitecap coverage values in a fetch-limited coastal zone. *Journal of Geophysical Research: Oceans, 113*(C5). https://doi.org/10.1029/2007JC004453.

Callaghan, A. H., Deane, G. B., & Stokes, M. D. (2013). Two regimes of laboratory whitecap foam decay: Bubble-plume controlled and surfactant stabilized. *Journal of Physical Oceanography, 43*(6), 1114–1126.

Callaghan, A. H., Deane, G. B., & Stokes, M. D. (2016). Laboratory air-entraining breaking waves: Imaging visible foam signatures to estimate energy dissipation. *Geophysical Research Letters, 43*(21), 11320–11328.

Callaghan, A. H., Deane, G. B., & Stokes, M. D. (2017). On the imprint of surfactant-driven stabilization of laboratory breaking wave foam with comparison to oceanic whitecaps. *Journal of Geophysical Research: Oceans, 122*(8), 6110–6128. https://doi.org/10.1002/2017JC012809.

Chen, S., Qiao, F., Huang, C. J., & Zhao, B. (2018). Deviation of wind stress from wind direction under low wind conditions. *Journal of Geophysical Research: Oceans, 0*(0). https://doi.org/10.1029/2018JC014137.

Duncan, J. (1981). *An experimental investigation of breaking waves produced by a towed hydrofoil*. Paper presented at proceedings of the Royal Society of London A: Mathematical, Physical and Engineering Sciences, The Royal Society.

Hanson, J. L., & Phillips, O. M. (1999). Wind sea growth and dissipation in the open ocean. *Journal of Physical Oceanography, 29*(8), 1633–1648.

Holthuijsen, L. H., Powell, M. D., & Pietrzak, J. D. (2012). Wind and waves in extreme hurricanes. *Journal of Geophysical Research: Oceans, 117*(C9), 1–15.

Hwang, P. A., & Sletten, M. A. (2008). Energy dissipation of wind-generated waves and whitecap coverage. *Journal of Geophysical Research: Oceans, 113*(C2), C02003.

Kraan, G., Oost, W., & Janssen, P. (1996). Wave energy dissipation by whitecaps. *Journal of Atmospheric and Oceanic Technology, 13*(1), 262–267.

Lafon, C., Piazzola, J., Forget, P., Le Calve, O., & Despiau, S. (2004). Analysis of the variations of the whitecap fraction as measured in a coastal zone. *Boundary-Layer Meteorology, 111*(2), 339–360.

Lafon, C., Piazzola, J., Forget, P., & Despiau, S. (2007). Whitecap coverage in coastal environment for steady and unsteady wave field conditions. *Journal of Marine Systems, 66*(1–4), 38–46.

Lamarre, E., & Melville, W. (1991). Air entrainment and dissipation in breaking waves. *Nature, 351*(6326), 469.

Melville, W. K., & Matusov, P. (2002). Distribution of breaking waves at the ocean surface. *Nature, 417*, 58. https://doi.org/10.1038/417058a.

Monahan, E. C. (1971). Oceanic whitecaps. *Journal of Physical Oceanography, 1*(2), 139–144.

Monahan, E. C., & Callaghan, A. H. (2015). *The discrete whitecap method for estimating sea salt aerosol generation: A reassessment*. Paper presented at 17th conference on atmospheric chemistry.

Monahan, E. C., & Dam, H. G. (2001). Bubbles: An estimate of their role in the global oceanic flux of carbon. *Journal of Geophysical Research: Oceans, 106*(C5), 9377–9383. https://doi.org/10.1029/2000JC000295.

Monahan, E. C., & Lu, M. (1990). Acoustically relevant bubble assemblages and their dependence on meteorological parameters. *IEEE Journal of Oceanic Engineering, 15*(4), 340–349.

Monahan, E. C., & O'Muircheartaigh, I. (1980). Optimal power-law description of oceanic whitecap coverage dependence on wind speed. *Journal of Physical Oceanography, 10*(12), 2094–2099. https://doi.org/10.1175/1520-0485(1980)010<2094:Opldoo>2.0.Co;2.

Monahan, E. C., & O'Muircheartaigh, I. G. (1986). Whitecaps and the passive remote sensing of the ocean surface. *International Journal of Remote Sensing, 7*(5), 627–642.

Monahan, E. C., & Spillane, M. C. (1984). The role of oceanic whitecaps in air-sea gas exchange. In W. Brutsaert & G. H. Jirka (Eds.), *Gas transfer at water surfaces* (pp. 495–503). Boston: Reidel.

Monahan, E. C., & Wilson, M. (1993). *Whitecap measurements. Critical Sea Test 7, Phase 2: Principal investigators' results*. The Johns Hopkins University Applied Physics Laboratory Tech. Rep. STD-R-2258, (808p, F. T. Erskine, & J. L. Hanson (Eds.)).

Monahan, E. C., & Woolf, D. K. (1989). Comments on variations of whitecap coverage with wind stress and water temperature. *Journal of Physical Oceanography, 19*(5), 706–709.

Monahan, E., Davidson, K., & Spiel, D. (1982). Whitecap aerosol productivity deduced from simulation tank measurements. *Journal of Geophysical Research: Oceans, 87*(C11), 8898–8904.

Monahan, E. C., Spiel, D. E., & Davidson, K. L. (1986). A model of marine aerosol generation via whitecaps and wave disruption. In *Oceanic whitecaps* (pp. 167–174). Dordrecht: Springer.

Phillips, O. (1985). Spectral and statistical properties of the equilibrium range in wind-generated gravity waves. *Journal of Fluid Mechanics, 156*, 505–531.

Ross, D. B., & Cardone, V. (1974). Observations of oceanic whitecaps and their relation to remote measurements of surface wind speed. *Journal of Geophysical Research, 79*(3), 444–452.

Scanlon, B., & Ward, B. (2016). The influence of environmental parameters on active and maturing oceanic whitecaps. *Journal of Geophysical Research: Oceans, 121*(5), 3325–3336. https://doi.org/10.1002/2015JC011230.

Scanlon, B., Breivik, Ø., Bidlot, J.-R., Janssen, P. A., Callaghan, A. H., & Ward, B. (2016). Modeling whitecap fraction with a wave model. *Journal of Physical Oceanography, 46*(3), 887–894.

Schwendeman, M., Thomson, J., & Gemmrich, J. R. (2014). Wave breaking dissipation in a young wind sea. *Journal of Physical Oceanography, 44*(1), 104–127. https://doi.org/10.1175/jpo-d-12-0237.1.

Stramska, M., & Petelski, T. (2003). Observations of oceanic whitecaps in the north polar waters of the Atlantic. *Journal of Geophysical Research: Oceans, 108*(C3), 3086.

Sugihara, Y., Tsumori, H., Ohga, T., Yoshioka, H., & Serizawa, S. (2007). Variation of whitecap coverage with wave-field conditions. *Journal of Marine Systems, 66*(1–4), 47–60.

Sutherland, P., & Melville, W. K. (2013). Field measurements and scaling of ocean surface wave-breaking statistics. *Geophysical Research Letters, 40*(12), 3074–3079.

Sutherland, P., & Melville, W. K. (2015). Field measurements of surface and near-surface turbulence in the presence of breaking waves. *Journal of Physical Oceanography, 45*(4), 943–965.

Toba, Y., and M. Chaen (1973), Quantitative expression of the breaking of wind waves on the sea surface, Rec. Oceanogr. Works Jpn., 12, 1–11

Xu, D., Liu, X., & Yu, D. (2000). Probability of wave breaking and whitecap coverage in a fetch-limited sea. *Journal of Geophysical Research: Oceans, 105*(C6), 14253–14259.

Chapter 4
Inferences to Be Drawn from a Consideration of Power-Law Descriptions of Multiple Data Sets Each Comprised of Whitecap Coverage, W_B, and 10-m Elevation Wind Speed Measurements (U_{10})

Giles Hooker, Sophia E. Brumer, Christopher J. Zappa, and Edward C. Monahan

Abstract Using an aggregate of 17 whitecap data sets collected over the past 50 years, it has been possible to confirm that the exponent, n, in the traditional simple power-law expression used to express the dependence of whitecap coverage, W_B, on 10 m-elevation wind speed, U_{10}, increases significantly as the sea surface temperature (SST) increases. Via several statistical approaches, it has been demonstrated that the stability of the lower marine atmosphere, represented by SST- T_A, has a significant influence on the $W_B(U_{10})$ power-law. Previous analyses using only the 12 whitecap data sets that included the geographical co-ordinates where each observation was made, did not confirm a statistically significant dependence of n on latitude. While this study benefited from the size of the whitecap data set available, future studies can achieve even more significant conclusions with more extensive whitecap data sets, that, in addition to W_B and U_{10} values, include the geographical coordinates, and T_A and SST values, associated with each whitecap observation.

G. Hooker (✉)
Department of Statistics and Data Science, Cornell University, Ithaca, NY, USA
e-mail: gjh27@cornell.edu

S. E. Brumer
Laboratoire d'Océanographie Physique et Spatiale (LOPS), University of Brest, CNRS, IRD, Ifremer, IUEM, Brest, France

C. J. Zappa
Lamont-Doherty Earth Observatory, Columbia University, Palisades, NY, USA

E. C. Monahan
Department of Marine Sciences, University of Connecticut, Groton, CT, USA

P. Vlahos (ed.), *Recent Advances in the Study of Oceanic Whitecaps*,
https://doi.org/10.1007/978-3-030-36371-0_4

4.1 Introduction

The first analytical expression describing whitecap coverage (W_B) as a function of the 10 m-elevation wind speed (U_{10}) can be found in Blanchard (1963). Blanchard used a power-law to describe $W_B(U_{10})$. In the current paper we use the power-law expression found in Eq. 4.1

$$W_B = C\, U_{10}{}^n \tag{4.1}$$

where W_B represents the fraction of the sea surface covered at any instant by oceanic whitecaps, or, in some cases, the fraction of the sea surface covered by decaying foam (i.e., Stage B whitecaps). The total fraction of the ocean surface at any instant covered by whitecaps, W_T, is the sum of Stage B and Stage A (i.e., spilling wave crest) fractions (see also Bortkovskii 1987a), but since typically for any sea state the Stage A coverage is approximately 10% of the Stage B coverage (see, e.g., Monahan 1989; Monahan and Lu 1990), henceforth we will use W_B interchangeably to represent the total, or the decaying foam portion, of the whitecap coverage. Note that W_B is an average computed over 5 min to 1 h and while early studies only considered smalls set of images, technological advances including digitization, storage and detection automatisation now allow for W_B estimates from substantially larger sets such as acquired from high frequency video recordings.

From theoretical considerations Wu (1979, 1982) came to the conclusion that n, the power-law exponent should be 3.75, while Monahan and O'Muircheartaigh (1980, 1982) undertook to determine n by applying statistical methods to each of the accumulating whitecap data sets.

Spillane and Doyle (1983), using the four whitecap W_B data sets S, J, BB1 and BB2 (see Table 4.1) demonstrated that n appeared to increase as the sea surface temperature, SST, increases from cold, to moderate, to warm. This was reinforced by the initial findings of Monahan and O'Muircheartaigh (1986) who, using just the combined BOMEX W_B data set (i.e. BB1 + BB2) and the C data set, i.e. the two "warm water" data sets then available, found that n increased with increasing SST, as illustrated in their Fig. 4.9. When these same authors plotted the n's they found for 5 W_B data sets, i.e. S, M83, J, C, and (BB1 + BB2), against the mean SST for each of these sets, they again found that n increased as SST increased, as shown in their Fig. 4.11.

While these authors discussed two physical-chemical factors that could contribute to this increase in n with SST, they homed in on the observation that both the typical duration of high wind events and the mean SST vary latitudinally, i.e. they both tend to increase as one moves Equator-ward.

They reasoned that if the typical high wind event duration is insufficient in a region to produce the fully developed sea associated with that high wind velocity, but the typical duration of lower wind events in that same region is sufficient to produce the fully developed sea associated with that low wind velocity, then the inevitable result is a reduced n compared to the n in a region where the high wind event durations are sufficient to produce a fully developed sea at all wind speeds for which one has observations of W_B.

Table 4.1 List of the data sets available for this study, ordered alphabetically by acronym (column 1)

Data set	Experiment/cruise	# of data points	U range ($m\ s^{-1}$)	SST range (°C)	T_A range (°C)	Reference	Link to repository
BB1	BOMEX-only	38	4.1–10	19.1–28.8	26.3–30.85	Monahan (1971)	
BB2	BOMEX-PLUS	16	2.4–17.4	17.4–30.55	17.0–30.55	Monahan (1971)	
BO	BOHAI	40	5.34–14.57	2.6–10.5	−5.1– −0.3	Wang et al. (1990)	
Bu∗	Bugaev	23	9–23.3	5.9–10.5	0.9–9.8	Bortkovskii (1987b)	
C	East China Sea and Pasific	36	3.5–20.9	16.6–29	21.1–29.8	Toba and Chaen (1973)	
G98	GASEX'98	186	3.12–15.98	14.79 16.18	13.71–17.5	Asher et al. 2002	
G08	SO GASEX'08	91	4.4–18.5	2.65–14.98	1.82–17.04	Brumer et al. (2017)	
HW	HiWinGS	139	6.32–26.45	6.26–20.76	2.47–19.52	Brumer et al. (2017)	
J	JASIN	50	3–15.3	12.5–29.3	10.5–14.4	Monahan and O'Muircheartaigh (1981)	
M77∗	MONSOON-77	24	9.2–19.2	16.5–29.3	18.8–29.7	Bortkovskii (1987b)	
M83	MIZEX83	21	4.7–14	3.9–14.4	−1.0–16.0	Monahan et al. (1984)	
M84	MIZEX84	38	2.6–13.1	−1.2–4.4	−2.5–9.5	Monahan and Woolf (1986)	
Pr	Priliv 1983	30	9–20	7.6–28.4	−2.7–28.5	Novak (1991)	
S	STREX	84	2.7–17.2	5.1–11.1	3.5–10.2	Doyle (1984)	
STa∗	2012 N. Pacific	41	5.24–12.78	12.48–19.55	13.09–18.92	Schwendeman and Thomson (2015b)	http://hdl.handle.net/1773/42596
STb	2015 N. Pacific (port)	44	6.24–15.98	7.66–10.9	6.54–11.79	Schwendeman and Thomson (2015b)	http://hdl.handle.net/1773/42596
STc	2015 N. Pacific (starboard)	34	6.24–15.98	7.71–10.93	6.77–11.79	Schwendeman and Thomson (2015b)	http://hdl.handle.net/1773/42596
T75	TYPHOON-75	45	5.8–14.2	27.1–29.5	26.1–29.4	Bortkovskii (1987b)	

(continued)

Table 4.1 (continued)

Data set	Experiment/cruise	# of data points	U range (m s^{-1})	SST range (°C)	T_A range (°C)	Reference	Link to repository
T78	TYPHOON-78	15	4.8–12.9	26.8–29.7	26.5–29.2	Bortkovskii (1987b)	
Zu	ZUBOV'81–2	57	7.3–18.8	−0.7–22.8	−1.6–20.9	Bortkovskii (1987b)	

The number of data points available where both W_B and SST measurements exists and are non-zero is given in column 3, the ranges of 10 m wind speeds, sea surface temperature and air temperatures are given in columns 4, 5, and 6 respectively. The reference to the original works reporting the data sets is listed in column 7 and the link to existing data repository in column 8. Data sets whose acronyms are followed by ∗ are discarded from the statistical analysis, see reasons in Sect. 4.2

The Bu, M77, Pr, T75, T76, and Zu whitecap data sets as used in this chapter were kindly provided to one of the authors (ECM) in the form of manually typed sheets by the late R.S. Bortkovskii (personal communication) when the Monahan et al. (1990) paper was being prepared. Some of these data appear in graphical form in Bortkovskii (1987b) and in tabular form in Bortkovskii and Novak (1993)

Figure 4.1 of the current paper, generated by using the same S, M83, J, and C data sets as used by Monahan and O'Muircheartaigh (1986), but including the BOMEX data sets differentiated into BB1 and BB2, and also including the M84 data set, shows a less pronounced increase in n with SST than found by Monahan and O'Muircheartaigh (1986).

As noted in the Fig. 4.1 caption, the dashed horizontal line associated with each of the seven n-points on this figure represents the range of SSTs associated with the W_B observations, which upon analysis, yielded that n-value. These dashed horizontal lines vary markedly in length, i.e. the SST ranges over which the observations in those W_B sets were taken vary greatly. For example, the horizontal line through point BB1 is short, as all the BB1 W_B observations were taken during the BOMEX experiment from two vessels on station within a limited, near-constant-temperature area to the east of Barbados. In contrast, the horizontal line through point BB2 is extremely long, reflecting the broad temperature range encountered during the BB2 measurements, many of which were taken from a ship-of-opportunity (a banana boat) on a round trip cruise from New Jersey to Honduras and back. A sample of the W_B observation stations, color-coded to reflect the SST readings along the associated cruise tracks, are shown in Fig. 4.2 below. For a more detailed review of the early studies of oceanic whitecaps, such as those that generated the data used in producing Fig. 1, the reader is referred to Monahan (Chap. 14) which appears in this same volume.

In a more recent brief paper Monahan et al. (2015) found, using the W_B data sets BB1, BB2, J, S, M83, M84, C, Bu, M77, Pr, T75, T78, Zu, BO, and G08 (the third GasEx experiment) as their data base, that when they sorted all of these W_B(U,SST) observations into those where the SST was greater than 15 °C and those where the SST was less than 15 °C, and calculated the n's for each of these two sub-sets, the n for the warmer observations, 3.53, was significantly higher than the n for the cooler observations, 2.89. The probability that a difference of this magnitude would be observed by chance is recorded by the p-value of 0.01625.

4.2 The Data Base for the Current Study

The current study benefits from the addition to our omnibus W_B data base of five relatively recent data sets, i.e. STa, STb, STc, HW, and G98. We therefore now have all 20 of the W_B data sets listed, with relevant citations, in Table 4.1, and each W_B, U couplet in each such data set is accompanied by SST, and in most cases by the air temperature T_A. But we must address the vexing question of whether or not we should set aside from further consideration one or more of these data sets based on one or more objective criteria. Not all of these W_B,U_{10} sets are characterized by a sufficiently broad range of wind speeds, nor in all cases are the wind speeds spread somewhat uniformly over the range of wind speeds that are encompassed by the set. A case in point: Bortkovskii's W_B,U_{10} data set M77 is characterized by having 75% of its data couplets associated with the wind speed 15 ± 0.5 m s^{-1}. In fact only one

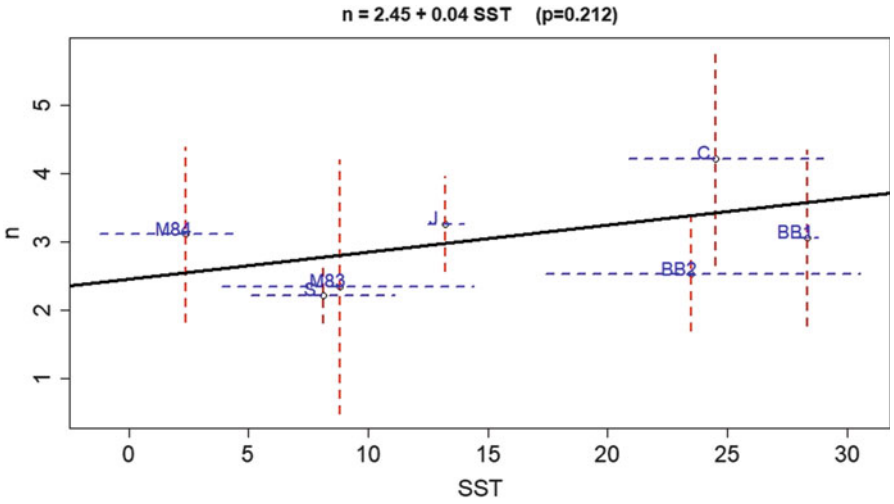

Fig. 4.1 Plot of power-law exponent, n, versus sea surface temperature, SST, for first 7 W_B data sets. Vertical lines indicate confidence intervals for n estimated for each data set; horizontal lines give the range of SST values in each. S Table 4.1 for key to data sets alpha-numeric designations

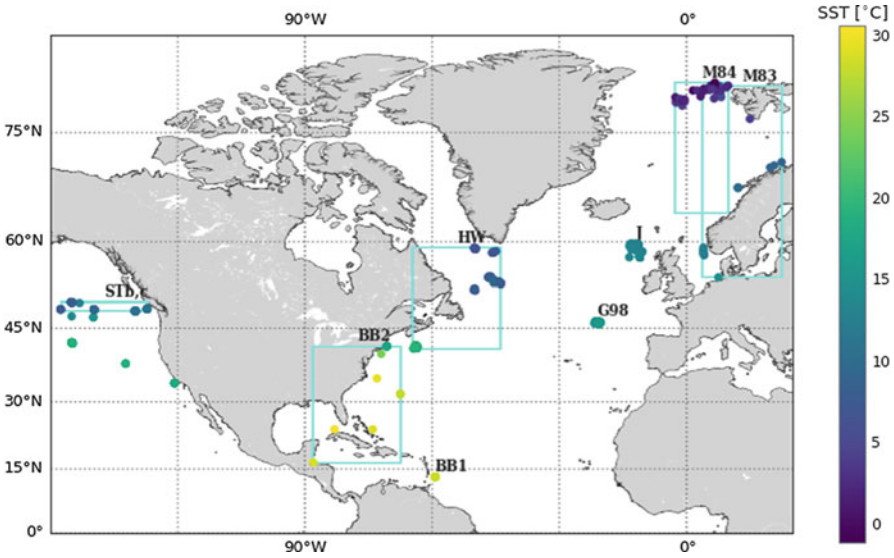

Fig. 4.2 Map showing the location of W_B measurements of a subset of the data sets considered here. The color coding reflects measured SST and the cyan boxes roughly delimit the area where each experiment took place. The points in the east pacific outside of the cyan box correspond to STa which are excluded from later analysis, see Sect. 4.2. Note that observations taken in close geographic proximity are overlaid when graphed and may thus be hidden by others

observation was recorded at a wind speed less than 10 m s^{-1} and likewise only one observation was made at a wind speed greater than 15.5 m s^{-1}. Thus the M77 data set does not represent a sufficiently robust set from which to deduce a stable value for n, and the current authors feel justified in omitting it from further consideration. Bortkovskii's W_B,U data set Bu fares only slightly better, with 74% of the observations that make up this data set having been recorded between wind speeds of 10.4–18 m s^{-1}, with only one observation having been made below 10.4 m s^{-1}, and likewise only one whitecap observation recorded for winds above 19.8 m s^{-1}. These considerations, combined with the observation that Bu and M77 are respectively the fourth and fifth smallest of the twenty sets in Table 4.1, have led the current authors to feel justified in setting aside both the M77 and BU data sets from further consideration.

Wu (1979, 1982) reached the conclusion, mentioned previously, that for steady state conditions n should equal 3.75 from the reasonable assumption that the fraction of the surface at any moment covered by decaying whitecaps should just be proportional to the rate at which energy from the wind was being transferred to the sea surface (see Monahan Chap. 14, this volume, for more details). And earlier Cardone (1969), using the fresh water whitecap data that Monahan (1969) had recorded on the Laurentian Great Lakes (supplemented by data that author had provided on the fetch associated with each of these observations), concluded that the fraction of instantaneous whitecap coverage "is directly related to the rate of energy transfer from the air flow to the fully developed spectral components (of the waves) through a combined Miles-Phillips type instability mechanism". This in turn led to the conclusion (see Monahan 1971, for details) that n would equal 3.3, Eq. 4.2, for a fully developed sea and neutral atmospheric stability. We thus conclude, that for stationary conditions, n should certainly fall between 3 and 4.

$$W_B = C_{FD} U_{10}^{3.3} \tag{4.2}$$

Using the conventional power-law description of $W_B(U_{10})$, we find that only one of the data sets considered here has a power law exponent, n, greater than 4, i.e. STa where n = 6. STa, which was obtained with a video system aboard the R/V New Horizon in 2012 that was able to resolve individual whitecaps as small as 0.012 m^2 area, might possibly be biased by this limited resolution of small whitecaps (Schwendeman and Thomson 2015a, b). We should note that whitecap coverage increases markedly with increase in wind speed due to two factors: (1) as wind speed increases the number of whitecaps per unit area of sea surface increases significantly, and likewise (2) as wind speed increases the average size of the individual whitecap also increases. Thus if a recording method is incapable of detecting a significant fraction of the individual whitecaps at low wind speeds, but is capable of detecting most of the whitecaps at higher wind speeds, the apparent increase in whitecap coverage with wind speed will be greater than if the recording system were able to resolve essentially all whitecaps that appear on the sea surface at any wind speed. This suggests that if this circumstance pertains we can expect an analysis to yield an n of even greater than 4.

Schwendeman and Thomson (2015b) addressed the detection resolution concern by collecting video data aboard the R/V Thomas G. Thompson in 2015 using two new video systems, one with same resolution as the system used in 2012, and the other with the ability to resolve whitecaps as small in area as 0.0015 m^2. From a log-log comparison of the fractional whitecap coverage determined from their 2015 wide field of view/lesser resolution measurements to their fractional whitecap coverage determined from their 2015 narrow field of view/greater resolution measurements (their Fig. 5) they concluded there was "little difference" in average whitecap coverage determined by using their two new video systems, and henceforth used the 2015 results from the wide FOV/lower resolution video system.

The power-law exponents determined from the Schwendeman and Thomson Wide FOV 2015 data sets STb and STc are in the range of 3.5–4.0, consistent with many of other W_B whitecap data sets herein analyzed, and compatible with the inferences drawn from the theoretical approaches of Cardone (1969) and Wu (1979). We are left with the suggestion that the discrepancy between the two sets of measurements obtained with the different video systems having the same effective resolution is due to a different effective range and distribution of wind speeds under which these authors' 2012 and 2015 W_B observations were made. We will none-the-less not consider further the Schwendeman et al. (2014) data set STa, as the n-value associated with this set is some 50% higher than the n-values found for the remaining W_B data sets, and well beyond the range of n-values derived from the theoretical approaches described above.

Henceforth our statistical investigation of how the n values in Eq. 4.1 vary with SST will be based on a consideration of the remaining 17 W_B data sets listed in Table 4.1. Each of these 17 data sets includes, in addition to W_B and U, SST, T_A, and hence ΔT, which is equal to $SST - T_A$, and which is a measure of the stability of the marine atmospheric boundary layer. (If T_A is measured at an elevation of 10 m above the sea surface, then we will consider the atmospheric stability to be near neutral if $-0.4\ ^\circ C < \Delta T < 0.6\ ^\circ C$, stable if ΔT is $<-0.4\ ^\circ C$, and unstable is $\Delta T > 0.6\ ^\circ C$.) It is to be noted that 12 of these 17 W_B data sets also include the Latitude (lat) at which each of the observations in these data sets were made, and these 12 W_B data sets will thus be used in an attempt to determine to what extend the n values for these data sets vary with the absolute Latitude of the observations.

4.3 The Apparent Variation of the Power-Law Exponent, n, with Changes in SST

We are now in a position to consider how expansions in our W_B data base alter, or confirm, our initial understanding of how the power-law exponent, n, varies with alterations in sea surface temperature. When Bortkovskii's data sets Pr, Zu, T75, and T78 are added to seven data sets considered in the preparation of Fig. 4.1, we arrive at Fig. 4.3. In comparing these two figures, we note that the slope of the best fit line, i.e. the coefficient of SST in the equation at the top of these figures, has increased

modestly from 0.04 to 0.05 from Figs. 4.1, 4.2, and 4.3, but more importantly the probability of observing this slope, were the underlying relationship to be zero, i.e. were there no SST dependence of n, has decreased almost four-fold, from 0.212 to 0.056, in going from Figs. 4.1, 4.2, and 4.3.

The final version of this particular n(SST) plot, based on all 17 W_B data sets, is Fig. 4.4.

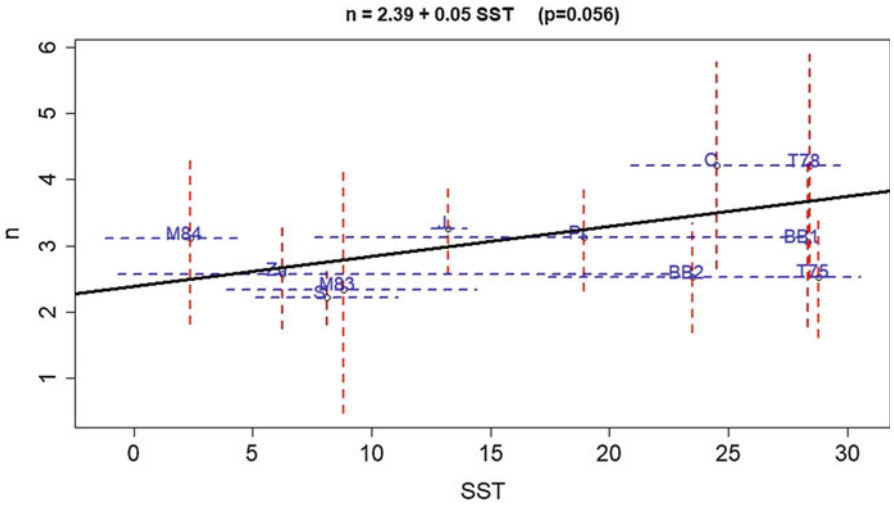

Fig. 4.3 Plot of power-law exponent, n, versus sea surface temperature, SST, for first 11 W_B data sets, (see Table 4.1 for key to data sets alpha-numeric designations)

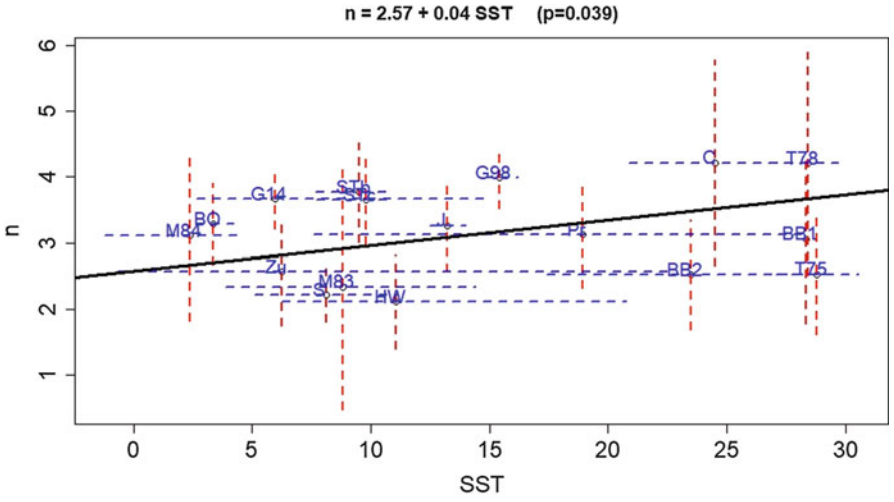

Fig. 4.4 Plot of power-law exponent, n, versus sea surface temperature, SST, for all 17 W_B data sets, see Table 4.1 for key to data sets alpha-numeric designations

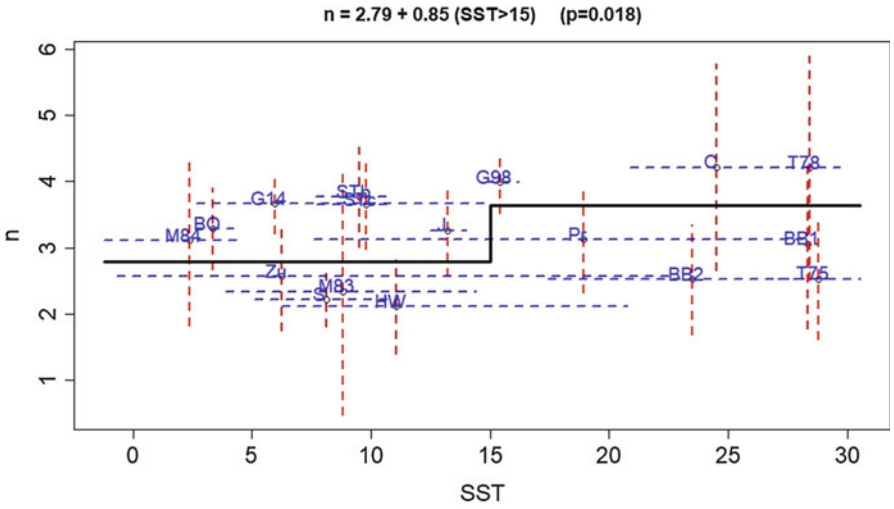

Fig. 4.5 Step function of n, fitted to 10 W_B data sets where SST <15 °C, and separately to 7 data sets where SST >15 °C, see text for details

We note that the slope of the best fit line has decreased only slightly, from 0.05 back to 0.04 as ones goes from Figs. 4.3 and 4.4, but that the probability that this slope is zero has again decreased markedly, from 0.056 to 0.039, from the 11 data set figure (Fig. 4.3) to the 17 data set figure (Fig. 4.4).

Noticing that these 17 W_B data sets are comprised of observations taken over a range of SSTs varying from just below 0 °C to just above 30 °C, it was decided to divide these data sets into those where the average SST was under 15 °C (10 sets) and those where the average SST was above 15 °C (7 sets). Using these two distinct groups of W_B data sets, a further test was undertaken to ascertain if SST was a statistically significant determinant of n. This test is one that we will illustrate with the "step-function plot" of Fig. 4.5.

This model, which essentially constrains each of the two groups to be associated with one n, yields for the 10 SST < 15 °C W_B data sets a group n of 2.79, and for the 7 SST > 15 °C W_B data sets a group n of 3.64. But more importantly this model indicates that the probability of observing this difference between the sets if they were not different is 0.018.

A second model arose when we decided to again use 15 °C as the discriminating temperature, not as the basis for binning the W_B data sets by their average SSTs, but rather as the basis for binning all of the individual W_B data points by their associated SSTs. The result of this exercise is summarized in Fig. 4.6.

As can be seen from this figure the Eq. 4.1 fit to the warm water (SST > 15 °C) data points yields a higher n (3.61) than the fit to the cold water (SST < 15 °C) data points which yields a n-value of 2.99. It is to be noted that the cold water n determined from the "step function" analysis was 2.79 compared to the "all data

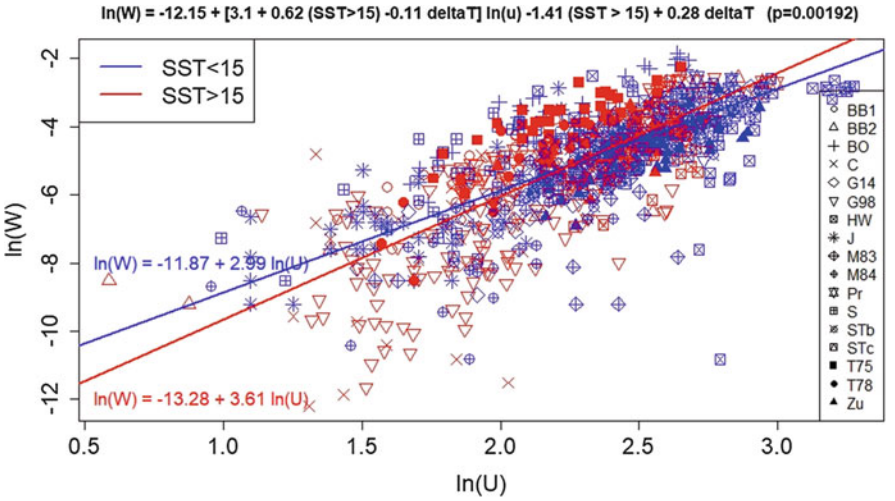

Fig. 4.6 Plot, in ln-ln space, of each W_B,U_{10}–observation where the SST < 15 °C (in blue), and each W_B,U_{10}–observation where the SST > 15 °C (in red), with power-law expressions for best fits to each of the data sets taken separately. See text for details

points" analysis for which the cold water n was 2.99, while the warm water n from the "step function" analysis was 3.64 while the "all data points" analysis yielded a warm water n of 3.61.

Before we consider the possible dependence of n upon latitude, it is timely that we consider the statistical approaches used so far in this Chapter, and those that will be used in the latter sections.

4.4 Statistical Methods

The analysis of data from multiple sources is collected under the term *meta-analysis* (see Borenstein et al. 2009, for example). For this study we take two approaches. We first present a two-stage method based on computing individual analyses for each data set and combining these to obtain greater precision and, in this case, broader coverage of sea surface temperatures. The results of these analyses are presented in Figs. 4.1, 4.3, 4.4 and 4.5. We also consider a joint model in which all the data are combined and data set-specific effects due to data processing or experimental apparatus are accounted for via a random effect structure. That these analyses produce very similar conclusions provides a validation of those conclusion's robustness to specific statistical methods. We also examine a moving window model to obtain a more detailed representation of the effect of sea surface temperature. All analyses were carried out using the R statistical language version 3.5.0 and the lme4 mixed effect package version 1.1-19 (Bates et al. 2015).

We take as a basic model the log-transformed whitecap measurement model, Eq. 4.3, from O'Muircheartaigh and Monahan (1983, 1986) in which parameters (C) land n appear as the intercept and slope of a simple linear regression and are obtained by minimizing the sum of squared differences of the above equation in the data. The use of log-transformed data both enables an explicit minimization of the least-square criterion and stabilizes the observable heteroscedasticity in which the spread of observed W values as well as their level increases with U. The ε in Eq. 4.3 represents observation-specific deviations from the logarithm of Eq. 4.1, and are assumed to be random, independent with the same distribution for all observations. Different fitting criteria will produce different numerical estimates for these parameters; e.g., O'Muircheartaigh and Monahan (1983, 1992) examined several fitting criteria and found broad agreement between their conclusions. We have elected to use linear regression on logged data here because of its stability, particularly within the mixed models applied below, and because the agreement of these data with the linear regression assumptions.

$$ln\,(W) = ln\,(C) + nln(U) + \varepsilon \tag{4.3}$$

Monahan and O'Muircheartaigh (1986) have suggested further modifications to this equation to include effects for ΔT and for SST either as additional linear terms in the model above, or used to modulate n. We account for both of these naturally within the mixed model framework. In particular we examine the effect of the threshold T15 = (SST > 15 °C). This is motivated from the observed behavior of the moving windows analysis with the 15 °C threshold chosen as the (rounded) median value of SST in our data set.

4.4.1 Two-Stage Analysis

A first analysis examines each data set individually. We obtain estimates $(\log(C)_i, n_i)$ for each of the $i = 1,\ldots,17$ data sets that we examine by minimizing the squared error of the logged observations. Linear regression also provides uncertainties in the form of standard errors (s_{Ci}, s_{ni}) for each of these parameters that account for both the amount of data and the spread of $\ln(U_{10})$ in each data set. We also obtain average values of SST, denoted T_i. Using these results, we develop an initial analysis based on a further regression, Eq. 4.4,

$$n_i = \beta_0 + \beta_1 T_i + \delta \tag{4.4}$$

in which we obtain parameters by minimizing the weighted sum of squared criterion, Eq. 4.5,

Table 4.2 Statistical results from a two-stage analysis of n as a function of SST

	Estimate	Std. Error	t value	Pr(>|t|)
β_0	2.57158	0.33374	7.705	1.36e-06
β_1	0.03848	0.01697	2.268	0.0385

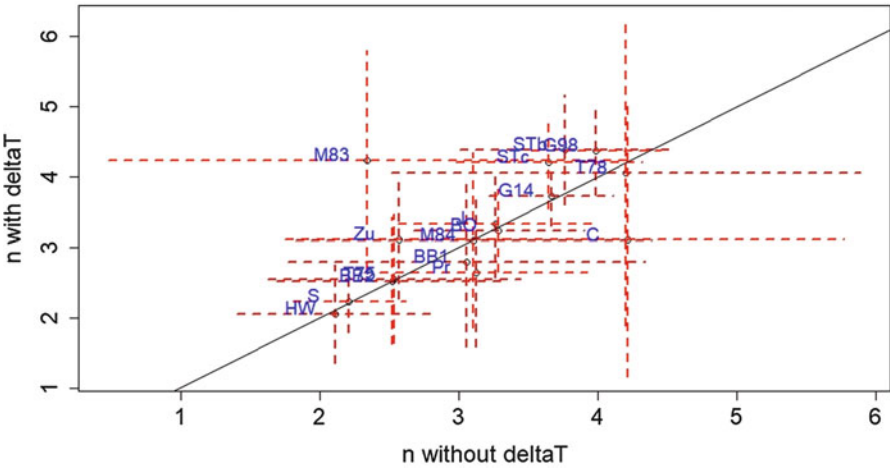

Fig. 4.7 A comparison of estimated n for each data set with and without accounting for ΔT. The diagonal indicates the line giving equal estimates; horizontal lines indicate confidence intervals for each

$$\sum_{i=1}^{17} s_i^2 (n_i - \beta_0 - \beta_1 T_i)^2 \tag{4.5}$$

which accounts for the differing precision of the n_i from each data set. We similarly incorporate this precision into our statistical uncertainty yielding the result in Table 4.2, which we also report graphically in Fig. 4.4. There we plot the n and T values along with vertical confidence intervals for each n and horizontal intervals indicating the range of SST in that data set. The statistical significance of β_1 in this model suggests a direct modulation of the U-W relationship by SST.

We note that we have not accounted for influences other than U on W in our estimates of n and ln(C), which may distort our analysis. Figure 4.7 reports the values of n from this analysis and a model, Eq. 4.6, in which the estimates for n are little changed, indicating robustness to the inclusion of further effects.

$$ln\,(W) = ln\,(C_0) + nln(U10) + C_2 \Delta T + \varepsilon \tag{4.6}$$

4.4.2 Combined Analysis

While the analysis above provides evidence that SST changes the *U*-*W* relationship, we here provide a detailed examination that results from pooling all the data sources. Here we use a model, Eq. 4.7, for the *i*th observation from the *j*th data set:

$$ln\left(W_{ij}\right) = ln\left(C_0\right) + C_1 T15 + C_2 \Delta T + \left(n_0 + n_1 T15 + n_2 \Delta T\right) ln\left(U\right) + S_j + \varepsilon_{ij} \tag{4.7}$$

within this model, the term n_0+n_1T15+$n_2\Delta T$ allows the effective exponent of U to change with both T15 and ΔT. C_1 and C_2 allow a similar modulation of the multiplier and S_j accounts for the ways in with the *j*th data set may differ systematically in the observation of W. ε_{ij} provides observation-specific deviations from this relationship. We treat the values of S_j as having been drawn at random from a normally-distributed population of potential data set biases (corresponding to differing instrumentation or image processing methods) yielding what is described as longitudinal mixed model (Verbeke and Molenberghs 2000). The collected parameters for this model, ($\ln(C_0)$,C_1,C_2,n_0,n_1,n_2) are chosen to maximize the probability of observing the data that we have and yield the results in Table 4.3.

As a means of visualizing these results, in Fig. 4.6 we plot the combined data set colored by the T15 threshold along with the relationship estimated each side of the threshold with ΔT held fixed at the approximate median value of 1 °C. Since T15 takes values either 0 or 1, for SST < 15 the slope of the line is simply n_0 while for SST > 15 it is $n_0 + n_1$. Our analysis here yields a slightly more strongly significant value for n_1, borrowing strength from the spread of SST values within each data set.

We note that we could have replaced T15 in the above analysis with SST. Doing so does not yield a value of n_1 that is statistically different from zero. We conjecture that this may be due to a nonlinear relationship between n and SST. To examine this possibility, we estimated the mixed model above without n_1 (ie, ignoring SST) using only those data points which fall in a window of 10 °C. Moving this window over the range of SST in the combined data sets allows us to trace the estimated value of n as the window covers different portions of the data. In the results plotted in Fig. 4.8 we see threshold- like behavior when the middle of the window crosses 10 °C, or when

Table 4.3 Results of a longitudinal mixed model estimated on the combined values in 17 data sets accounting for the effect of SST (C_1), ΔT (C_2) and their interaction with log(U) (n_1 and n_2 respectively)

	Estimate	Std. Error	df	t value	Pr(>|t|)
$\log(C_0)$	−12.14578	0.41964	289.91433	−28.944	<2e-16
C_1	−1.41206	0.51600	838.97788	−2.737	0.00634
C_2	0.27788	0.10930	955.38054	2.542	0.01117
n_0	3.09984	0.15496	955.03283	20.004	<2e-16
n_1	0.62495	0.20089	944.67515	3.111	0.00192
n_2	−0.10636	0.04352	954.40736	−2.444	0.01470

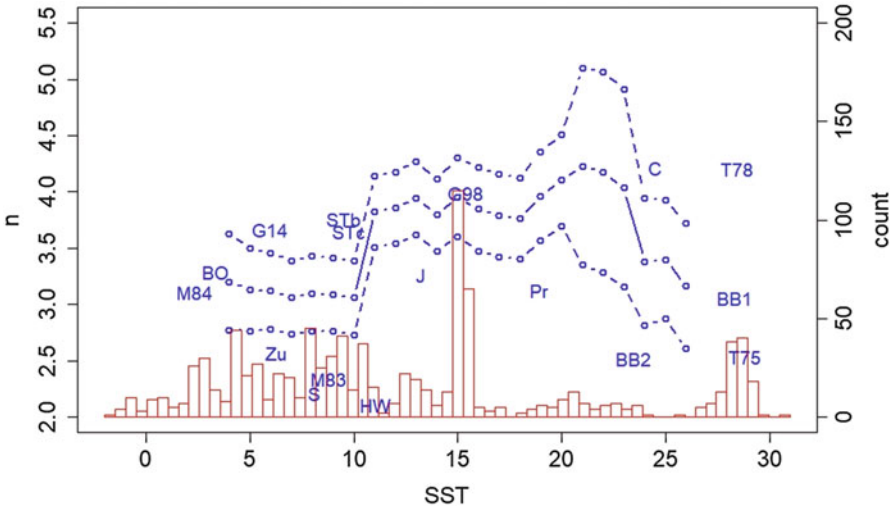

Fig. 4.8 Moving windows estimate of *n* over different ranges of SST. Blue points and confidence bands give the values of *n* estimated from a mixed model using only those data points within 5 °C of the point. Red histogram indicates the distribution of SST values in the combined data set. Text indicates the value of n obtained for each data set located at the corresponding average SST

the right-hand edge of the window starts to include data over our SST > 15 value for T15. We emphasize that the value of 15 °C was chosen prior to examining this plot based on the distribution of SST values in the combined data set and we are thus not biasing our statistical significance.

4.4.3 The Potential Dependence of n on the Absolute Latitude

The suggestion was raised in Monahan and O'Muircheartaigh (1986), and again in Monahan et al. (2015) that, at least to some degree, the apparent dependence of n on SST might be a reflection of a dependence of n on Latitude. Making use of the 12 W_B data sets for which we have the Latitudes at which observations were taken (i.e., sets BB1, BB2, C, G14, G98, HW, J, M83, M84, S, STb, and STc, see Table 4.1), Fig. 4.9 was generated. As can be seen from this figure the probability that the best fit line describing n(lat) would be this large if there is no dependence of n upon Latitude, is 0.118. This can be compared to Fig. 4.3, an n(SST) plot generated using one fewer number of W_B data sets (only 7 of these 11 data sets were included in the 12 sets used to produce Fig. 4.9). From Fig. 4.3 we found that the p-value for the slope of the best-fit line describing n(SST) was 0.056. Thus, from this imperfect comparison of these two analyses, the dependence of n upon Latitude appears not as clear as its dependence on SST.

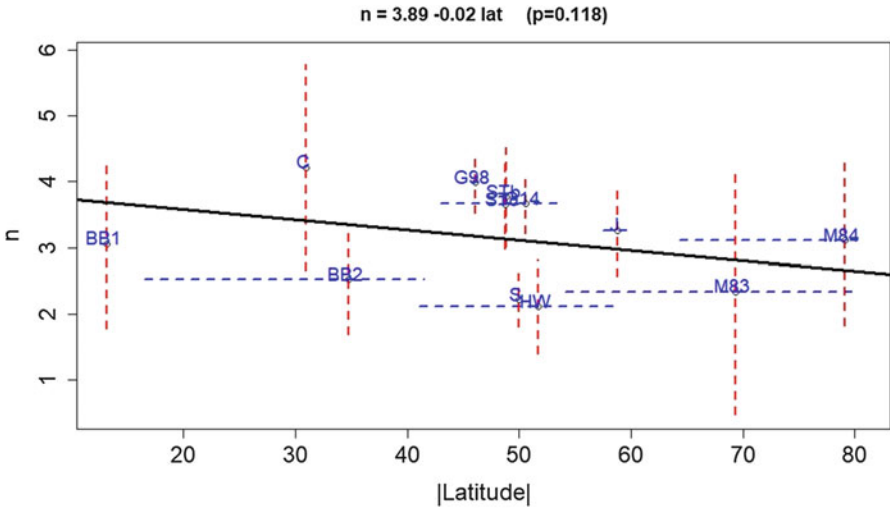

Fig. 4.9 This plot of n, the simple power-law exponent, versus the absolute (i.e. no algebraic sign is assigned to hemisphere) latitude, suggests that n deceases with distance from the equator. Vertical lines give confidence intervals for each estimated n, while horizontal lines indicate the range of latitudes associated with each data set

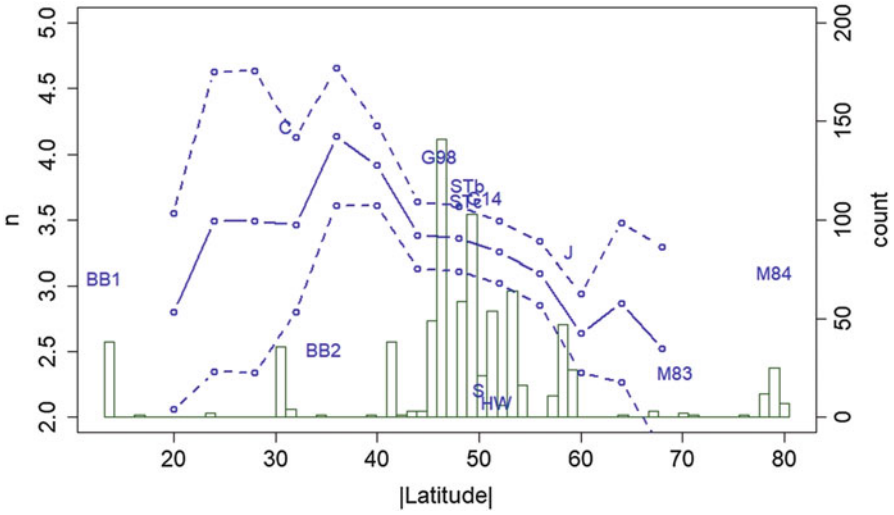

Fig. 4.10 Moving windows analysis of the relationship of n and absolute latitude based on estimates from a mixed model using data include within 10° of each blue circle. Green histogram indicates the distribution of latitudes in the data set

A similar moving-windows estimate can also be performed substituting absolute latitude for SST this time using bands of width 20° and this is reported in Fig. 4.10

where a strong decrease in *n* is observed when latitude increases. Note that latitude is not available for many of the older data sets so these results are based on a smaller sample of observations. Because of the strong relationship between latitude and SST, it is unlikely that we can distinguish between the two effects using these data.

4.5 Conclusions

All of the statistical assessments in this Chapter support the contention that n, the exponent in the power-law description of oceanic whitecap coverage (Eq. 4.1) varies positively with sea surface temperature, SST. If one were to assume that the coefficient C in Eq. 4.1 is a constant as regards SST, then using the n-values from Fig. 4.6 for warm (>15 °C) water and cold (<15 °C) water one might conclude that for winds of 7 m s^{-1} (just a few meters per second above the threshold for whitecapping) a warm ocean would have 3.34 times the whitecap coverage as a cold ocean, and at a wind speed of 10 m s^{-1} a warm ocean would have 4.17 times the whitecap coverage as a cold ocean. This conclusion would be incorrect as the assumption that C does not vary with SST, and hence with n, is invalid. Figure 4.11 clearly shows that ln(C), and hence C, varies strongly with changes in n, and hence with changes in SST. The coefficient C gets smaller as n becomes larger, and hence as SST increases. This is also observable in the value of C_1 in Table 4.3.

While we acknowledged that from the limited collection of data sets that included the Latitude at which the whitecap observations were made, we could not conclude

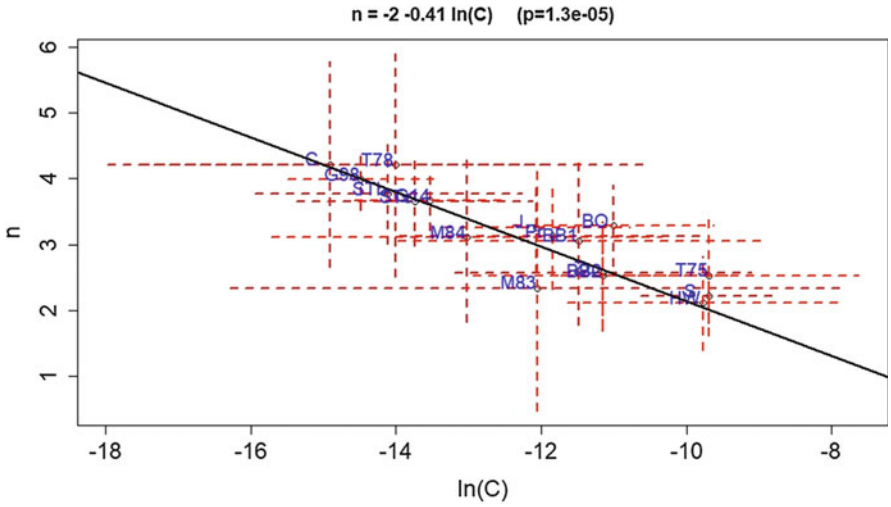

Fig. 4.11 This plot of n, the power-law exponent, versus ln C, shows the strong inverse relationship between these two quantities. Vertical and horizontal lines indicate confidence intervals for each estimated n and ln(C) respectively. See text for details

that the relative influence on n of Latitude was equal to, or greater than, the influence of SST, we note that Salisbury et al. (2014) have tested the *in situ* derived expression of Monahan and O'Muircheartaigh (1980), Eq. 4.8, against their satellite-derived W expressions, based on enhanced microwave brightness temperatures, in particular, their 37 GHz radiometer data which reflect the presence of sea foam "whitecaps" as thin as 1 mm.

$$W = 3.84 \times 10^{-6} U_{10}{}^{3.41} \tag{4.8}$$

It should be noted here that Eq. 4.8 was derived using solely the whitecap data from Monahan (1971) and from Toba and Chaen (1973). Now the largest component of this aggregate data set was what we in this Chapter refer to as the BB1 (BOMEX) set, comprised of 38 non-zero observations taken at a Latitude of 12.5°N. The second largest component of this aggregate set, C (Toba and Chaen 1973), contains 36 non-zero observations obtained on a cruise from Tokyo to the East China Sea and "the southern region off Japan" before returning to Tokyo (the SST for all of these observations is recorded as being between 20.9 °C – 29.0 °C reflecting the "southern" nature of this cruise). The last and smallest component of this aggregate set is 16 non-zero observations referred to in the Chapter as BB2 ("BOMEX Plus") consisting of observations made between the Gulf of Honduras on the south to Cape Cod on the north. We conclude that Eq. 4.8 reflects the $W(U_{10})$ relationship that pertains in the Trade Wind regions of the Northern Hemisphere.

Salisbury et al. (2014) document in their Fig. 3, lower left panel, that while their 37 GHz algorithm over estimates, compared to Eq. 4.8, the foam cover in lower- and mid-latitude regions, their algorithm tends to under estimate foam cover at high northern and southern latitudes. It is clear from their paper that if our $W(U_{10})$ expression allowed for a decrease in the magnitude of n with an increase in absolute latitude, our thus-modified expression would more closely agree with their satellite estimates global foam cover.

We will now return to the matter of the role of atmospheric stability in affecting the relationship between U_{10}, the 10 m-elevation wind speed, and W_B, the fractional whitecap coverage of the sea surface. In this Chapter we have adopted ΔT, which here is the notation for SST-T_A, as a measure of the stability of the lower marine atmospheric boundary layer. The more positive the value of ΔT the more unstable the marine atmospheric boundary layer (MABL), likewise the more negative the value of ΔT the more stable the MABL. And the more unstable the MABL the more effective is U_{10} at transferring horizontal momentum to the sea surface, and the greater the rate at which the wind transfers momentum to the sea surface the greater is W_B, the fraction of the sea surface covered by whitecaps. In Monahan et al. (1981a), using the W_B data sets BB1, BB2, C, and J, obtained Eq. 4.9.

$$U_{10} = 23.81 W_B{}^{0.19} T_A{}^{0.84} SST^{-0.88} \tag{4.9}$$

For a fixed U and T_A, as SST increases, so does W_B, i.e. as the atmosphere becomes less stable, whitecap coverage increases. And for a fixed U and SST, as T_A increases W_B decreases, i.e. as the atmosphere becomes more stable, whitecap coverage decreases.

Using u∗, where the effect of ΔT, i.e. stability, is taken care of, should result in $W_B(u*)$ being a better fit, smaller RMSE, than $W_B(U_{10})$, where "noise" due to stability effects should be apparent for data sets with relatively large and variable ΔT values. This can be significant for large ΔT, although Schwendeman and Thomson (2015b) found (their Table 3) that when it came to the Statistics of the Threshold Power Law Best Fit, they obtained a better fit (smaller RMSE and smaller R^2) using U_{10} as opposed to u^*.

A caveat in closing: When for remote sensing applications a $U_{10}(W_B)$ expression is needed, note that the simple inverse of a statistically optimal $W_B(U10)$ expression determined from a W_B,U_{10} data set is not as good as, i.e. has a greater mean square error than, the optimal $U(W_B)$ expression obtained by applying the same statistical approach directly to the W_B,U data set (Monahan and O'Muircheartaigh 1981; Monahan et al. 1981b).

Acknowledgments GH is partially supported by National Science Foundation grants DMS-1712554 and DEB-1353039. SEB is supported by a postdoctoral grant by Centre National d'Etudes Spatiales (CNES). CJZ was supported by the National Science Foundation (Grants OCE-0647667, OCE-1537890, and OCE-1756839) and the National Oceanic and Atmospheric Administration (Grant NA07OAR4310094). ECM's recent research has been supported by the National Science Foundation via awards AGS-1356541 and NSF-1630846. ECM would like to acknowledge the generosity of the late Roman S. Bortkovskii in providing typed listings of the 8 Russian whitecap data sets listed in Table 4.1.

References

Asher, W. E., Edson, J., McGillis, W., Wanninkhof, R., Ho, D. T., Litchendorf, T., Donelan, M., Drennan, W., Saltzman, E., & Wanninkhof, R. (Eds.). (2002). *Fractional area whitecap coverage and air-sea gas transfer velocities measured during gas Ex-98 gas transfer at water surfaces* (Geophysical monograph) (Vol. 127, pp. 199–205). Washington, DC: AGU.

Bates, D., Maechler, M., Bloker, B., & Walker, S. (2015). Fitting linear mixed-effects models using lme4. *Journal of Statistical Software, 67*(1), 1–48.

Blanchard, D. C. (1963). The electrification of the atmosphere by particles from bubbles in the sea. *Progress in Oceanography, 1*, 71–202.

Borenstein, M., Larry, V. H., Julian, H., & Hannah, R. W. (2009). *Introduction to meta-analysis*. London: John Wiley and Sons, Ltd.

Bortkovskii, R. S. (1987a). *Air-sea exchange of heat and moisture during storms, revised English edition*. Dordrecht: Springer, 194 pp.

Bortkovskii, R. S. (1987b). Time-space characteristics of whitecaps and foam patches formed by wave breaking. *Meteorologiya i Gidrologiya, 5*, 68–75. (in Russian).

Bortkovskii, R. S., & Novak, V. A. (1993). Statistical dependencies of sea state characteristics on water temperature and wind age. *Journal of Marine Systems, 4*, 161–169.

Brumer, S. E., Zappa, C. J., Brooks, I. M., Tamura, H., Brown, S. M., Blomquist, B. W., Fairall, C. W., & Cifuentes-Lorenzen, A. (2017). Whitecap coverage dependence on wind and wave

statistics as observed during SO GasEx and HiWinGS. *Journal of Physical Oceanography, 47*, 2211–2235. https://doi.org/10.1175/JPO-D-17-0005.1.

Cardone, V. J. (1969). *Specification of the wind distribution in the marine boundary layer for wave forecasting, Technical Report GSL-69-1*. New York University, 131 pp., available from the Defense Documentation Center.

Doyle, D. M. (1984). *Marine aerosol research in the Gulf of Alaska and on the Irish West Coast (Inishmore)*. M.Sc. Thesis, Department of Oceanography, University College, Galway, 140 pp.

Monahan, E. C. (1969). Fresh water whitecaps. *Journal of the Atmospheric Sciences, 25*, 1026–1029.

Monahan, E. C. (1971). Oceanic whitecaps. *Journal of Physical Oceanography, 1*, 139–144.

Monahan, E. C. (1989). From the laboratory tank to the Global ocean. In E. C. Monahan & M. A. Van Patten (Eds.), *Climate and health implications of bubble-mediated sea-air exchange* (pp. 43–63). Groton: Connecticut Sea Grant College Program.

Monahan, E. C. (this volume). Twixt wind and waves, a first-person account of the early years of the study of oceanic whitecaps. In P. Vlahos & E. C. Monahan (Eds.), *Recent advances in the study of oceanic whitecaps*. Switzerland: Springer.

Monahan, E. C., & Lu, M. (1990). Acoustically relevant bubble assemblages and their dependence on meteorological parameters. *IEEE Journal of Oceanic Engineering, 15*, 340–349.

Monahan, E. C., & O'Muircheartaigh, I. G. (1980). Optimal power-law description of oceanic whitecap dependence on wind speed. *Journal of Physical Oceanography, 10*, 2094–2099.

Monahan, E. C., & O'Muircheartaigh, I. G. (1981). Improved statement of the relationship between surface wind speed and oceanic whitecap coverage as required for the interpretation of satellite data. In J. F. R. Gower (Ed.), *Oceanography from space* (pp. 751–755). New York: Plenum Publication.

Monahan, E. C., & O'Muircheartaigh, I. G. (1982). Reply. *Journal of Physical Oceanography, 12*, 751–752.

Monahan, E. C., & O'Muircheartaigh, I. G. (1986). Whitecaps and the passive remote sensing of the ocean surface. *International Journal of Remote Sensing, 7*, 627–642.

Monahan, E. C., & Woolf, D. K. (1986). Oceanic whitecaps, their contribution to air-sea exchange, and their influence on the MABL, whitecap report no. 1, to ONR from MSI, University of Connecticut, 135pp.

Monahan, E. C., O'Muircheartaigh, I. G., & FitzGerald, M. P. (1981a). *Oceanic whitecap coverage as a function of wind speed and air-water temperature difference; A physical basis for wind retrieval algorithm development, program and abstracts.* In IAMAP third scientific assembly, Hamburg, 17–28 August 1981, I.R.C. Volume, p. 41.

Monahan, E. C., O'Muircheartaigh, I. G., & FitzGerald, M. P. (1981b). Determination of surface wind speed from remotely measured whitecap coverage, a feasibility assessment. *Proceedings of an EARSeL-ESA Symposium, Applications of Remote Sensing Data on the Continental Shelf, Voss, Norway, European Space Agency, SP-167*, 103–109.

Monahan, E. C., Spillane, M. C., Bowyer, P. A., Higgins, M. R., & Stabeno, P. J. (1984). Whitecaps and the marine atmosphere, report no. 7, to the Office of Naval Research from University College, Galway, 103pp.

Monahan, E. C., Bortkovskii, R. S., & O'Muircheartaigh, I. G. (1990). The influence of wind speed and surface water temperature on oceanic whitecapping, with particular reference to the onset of wave breaking. *EOS, Transactions, American Geophysical Union, 71*, 73.

Monahan, E. C., Hooker G. J., & Zappa, C. J. (2015). *The latitudinal variation in the wind-speed parameterization of ocean whitecap coverage: Implications for global modelling of air-sea gas flux and sea surface aerosol generation*. In Paper 14.5, 19th conference on air-sea interaction, American Meteorological Society, Phoenix, AZ, e-posted to AMS Confex Website, 7pp.

Novak, V. A. (1991). Dependence of sea surface fractions covered by whitecaps and foam patches on determining parameters. Deponir. IC VNIIGMI-MCD, 05.06.91, No. 1080-GM91:159-187 (in Russian).

O'Muirchearthaigh, I. G., & Monahan, E. C. (1983). *Use of the box-cox transformation in determining the functional form of the dependence of oceanic whitecap coverage on several environmental factors*. In preprint volume: Eighth conference on probability and statistics in

atmospheric sciences, November 16–18, 1983, Hot Springs, Arkansas, publication by American Meteorological Society, pp. 55–58.

O'Muirchearthaigh, I. G., & Monahan, E. C. (1986). Statistical aspects of the relationship between oceanic whitecap coverage, wind speed and other environmental factors, pp. 125–128, in Monahan and MacNiocaill (1986).

O'Muircheartaigh, I. G., & Monahan, E. C. (1992). *Modeling the dependence of whitecap on wind speed: Hierarchicals models, and shrunken parameter estimation*. In Preprints, fifth international meeting on statistical climatology, 22–26 June, 1992, Toronto, Canada, pp. 553–556.

Salisbury, D. J., Anguelova, M. D., & Brooks, I. M. (2014). Global distribution and seasonal dependence of satellite-based whitecap fraction. *Geophysical Research Letters, 41*, 1616–1623. https://doi.org/10.1002/2014GL059246.

Schwendeman, M., & Thomson, J. (2015a). A horizontal-tracking method for shipboard video stabilization and rectification. *Journal of Atmospheric and Oceanic Technology, 32*, 164–176. https://doi.org/10.1175/JTECH-D-14-00047.1.

Schwendeman, M., & Thomson, J. (2015b). Observations of whitecap coverage and the relation to wind stress, wave slope, and turbulent dissipation. *Journal of Geophysical Research, Oceans, 120*, 8346–8363. https://doi.org/10.1002/2015JC011196.

Schwendeman, M., Thomson, J., & Gemmrich, J. R. (2014). Wave breaking dissipation in a young wind sea. *Journal of Physical Oceanography, 44*, 104–127. https://doi.org/10.1175/JPO-D-12-0237.1.

Spillane, M. C., & Doyle, D. M. (1983). Final results for STREX and JASIN photo-analysis with preliminary search for whitecap algorithm, pp. 8–27, in Monahan, Spillane, Bowyer, Doyle, and Stabeno (1983).

Toba, Y., & Chaen, M. (1973). Quantitative expression of the breaking of wind waves on the sea surface. *Records of Oceanographic Works in Japan, 12*, 1–11.

Verbeke, G., & Molenberghs, G. (2000). *Linear mixed models for longitudinal data*. New York: Springer.

Wang, W., Xu, D., & Lou, S. (1990). Directly synchronization measurement and results analysis of ocean whitecap and friction velocity. *Acta Oceanologica Sinica, 12*, 638–647. (in Chinese).

Wu, J. (1979). Oceanic whitecaps and sea state. *Journal of Physical Oceanography, 9*, 1064–1068.

Wu, J. (1982). Comments on "Optimal power-law description of oceanic whitecap dependence on wind speed". *Journal of Physical Oceanography, 12*, 750–751.

Chapter 5
Rain, Wave Breaking and Spray

Luigi Cavaleri

Abstract Starting from a quick historical perspective, I frame the present situation among meteorologists and oceanographers, joined by the crucial role of the sea surface interface. Hinting to its dynamics, I then focus on the key process of white-capping. I stress how much we still have to learn, discussing in particular the relevance of rain as an example of a process whose implications, for white-capping hence spray, are practically ignored. I frame the related situation, also with practical examples and applications.

5.1 A Picture of the Situation

Meteorology and oceanography developed along obviously connected, but mostly one-way and largely independent, paths. As humans mostly living on land, our interest has been focused on the overlying atmosphere in which we live. Interest in oceanography, basically on waves and currents, arose when man started navigating, first the coastal environment and then progressively the oceans. It was only in recent times, and satellite images were very effective in this respect, that we started realizing how the thin layer of fluids surrounding, and relative to, our planet had to be considered, hence modeled, as a whole body. The contemporary understanding of the key processes relevant for short term forecasting and climate prediction pushed much in this direction.

Within this polarized, but integral view, a key role is played by the sea surface, the dynamical boundary between the atmosphere and the ocean. One of the most, if not the most, important performers in this play is wave breaking (henceforth w-c for white-capping). With an implied orders of magnitude increase of the contact surface between the two layers (air and water) and with its very dynamical conditions, w-c, with on average 15–20% of the ocean surface under stormy conditions at any given time, is controlling the evolution of storms and Earth's climate.

L. Cavaleri (✉)
CNR-ISMAR, Institute of Marine Sciences, Venice, Italy
e-mail: luigi.cavaleri@ismar.cnr.it

P. Vlahos (ed.), *Recent Advances in the Study of Oceanic Whitecaps*,
https://doi.org/10.1007/978-3-030-36371-0_5

Given this crucial role (truly understood only a short while ago), it is somehow surprising that we still know relatively little about its detailed physics. We know that w-c, bubbles in water and spray are the most evident reality, but, notwithstanding the large literature on the subject (of course see, among others, the extensive literature by E.C. Monahan), we still have very large uncertainties. Reviewing the literature in time, it is interesting that repetitive claims of "big progresses in recent years" have been issued. My opinion, both from direct experience on the sea and as a wave modeller, is that this can be true with respect to the past, but there remains a long way to go. Suffice it to say that w-c is still the tuning knob of any wave model and it is conveniently ignored in most circulation models.

The dichotomy among aerosol and wave modellers is a good example. Historically the formers have estimated w-c on the ocean as a function of wind speed, typically U_{10}. The latter base their estimate of the corresponding source function on only the wave spectrum. The truth stays in the middle, as I have repeatedly witnessed in the open sea measuring wind and waves from the ISMAR oceanographic tower (Cavaleri and Zecchetto 1987, and Cavaleri 2000). The spectrum of course counts, but the w-c coverage extent changes almost instantaneously with the wind speed.

In the recent years I have been working on a meteorological parameter hardly considered in oceanography: rain. Also in meteorology rain has almost a passive role granted the implied heat transfers as rain can condense, evaporate and fall. Only recently in the meteorological model of the European Centre for Medium-Range Weather Forecasts (Reading, U.K., henceforth ECMWF) has a different falling speed according to drop dimensions been considered. However, direct experience at sea (and I stress its importance with respect to working only on paper or computer oceanography) shows its significance. In this paper I report some recent work, both modelling and in the field, concerning the implications of rain on w-c. In Sect. 5.2 I give a brief picture of the present situation in wave modelling, with its good and not so good aspects. Section 5.3 describes an enlightening experience on the ISMAR oceanographic tower. In Sect. 5.4 I discuss the derived implications for physics, including w-c and the consequent spray and aerosol. In 5.5 I move to a practical aspect showing how the above may affect the development and modelling of storms, in particular hurricanes and typhoons. Section 5.6 provides another aspect relating rain and spray. I close the paper (Sect. 5.7) with a summarizing view.

5.2 How Good Wave Models Are

Something we all agree upon is the high quality of the present wave model results. Focusing on the most difficult aspect, i.e. operational forecasts, it is sufficient to check the statistics of ECMWF at http://www.ecmwf.int/en/forecasts/charts/obstat/?facets=Parameter,Wave%20Height, and of the National Center for Environmental Prediction (NOAA-NCEP, Maryland, USA) at http://polar.ncep.noaa.gov/nwps/ to

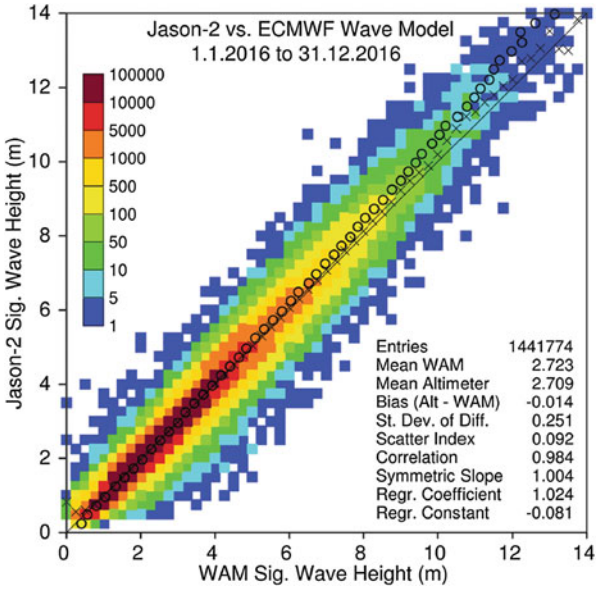

Fig. 5.1 Comparison between Jason-2 altimeter wave height data and the ECMWF analysis

see that one can indeed wonder if and how much better we will ever be able to do. The scatter plot in Fig. 5.1 summarizes well the situation. Taking this for granted, two things need to be specified. First, a large part of these improvements are due to the improvement of the forcing wind fields. Then problems still exist, particularly in extreme situations. Here both the logical (spectral) approach (Pierson and Marks 1952) and the physics we use are pushed to their limit. This is true particularly for w-c that, as the least known source function, is characterized by a lot of parameterizations, and in any case it is the tuning knob of the system. Many users are content with this situation, but as scientists we should never forget what George Bernard Shaw said: "science becomes dangerous only when it imagines it has reached its goal". So we need to be severe with ourselves, looking with critical attitude at our results, trying to understand why, even if just a little, we are wrong.

Not surprising, breaking due to w-c is almost always the main suspect. Sections 5.3 and 5.5 offer good examples of this. W-c is a strongly non-linear process surely requiring a good mathematical background, but also a direct perception of what is actually going on in the sea during a storm. Therefore to improve our computer oceanography (e.g., the forecast modelling) it is often useful (I strongly recommend) to spend some time observing the ocean and its waves. At ISMAR we are lucky for the availability of a habitable oceanographic tower (Fig. 5.2) located 15 km off the coastline of the Venice lagoon (see Fig. 5.3) on 16 meters of depth. Here I had the privilege and the possibility of being on board during mild and severe storms, and I learnt a lot from these experiences. In particular I was lucky to be on board during a peculiar event. Witnessing it was like breaking the veil covering the truth. This is what I describe in the next section.

Fig. 5.2 The ISMAR oceanographic tower "Acqua Alta", located in the Northern Adriatic Sea, 15 km offshore the Venice lagoon

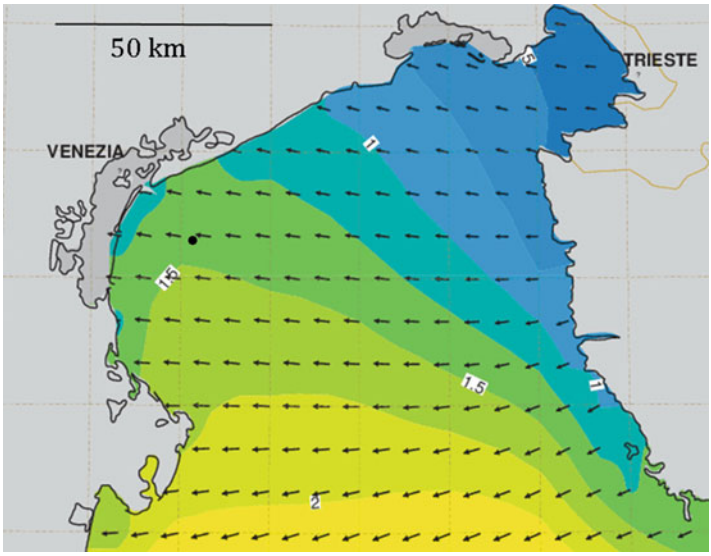

Fig. 5.3 Wave conditions (significant wave height) in the Northern Adriatic Sea on 12 November 2014. The dot shows the position of the ISMAR oceanographic tower (see Fig. 5.2)

5.3 A Witnessed Event

In November 2014 I was on board the tower running an experiment involving both wind and wave measurements. Wind was oscillating between 8 and 10 ms^{-1} with a limited gustiness (see the later Fig. 5.5). The significant wave height H_s was close to 1.5 m. The wind was blowing from North-East with frequent breakers on the sea surface. Figure 5.3 provides an overall view of the wave distribution. With all of the instruments at work, all of a sudden there was a tremendous downpour (close to 80 mmh^{-1}, from the local rain gauge) lasting between 2 and 3 min. As it had started, the shower suddenly stopped. It was a pure local phenomenon in space and time because just before the shower and soon after I looked around the tower and there was no rain on sight.

The crucial point is that, as soon as the rain began, the white-caps practically disappeared from the sea surface. Figure 5.4 shows its appearance just before and during the shower. Videos are available as well at https://youtu.be/irMzXZ4WwnE and https://youtu.be/dK-XwOF0aTk. An approximate count of the number of breakers visible in the 20 s of each video supports 140 w-c before, and 20 during, the rain. Most of all, as visible in the pictures and better so in the videos, it is the appearance of the sea surface that changed, passing from the usual rough surface typical of an active wind sea to a still wavy but smooth one, only roughened by the presence of the rain drops. Interesting as the event is in itself, the most important aspects are the physical implications of what I saw, implications that I describe in the next Sect. 5.4.

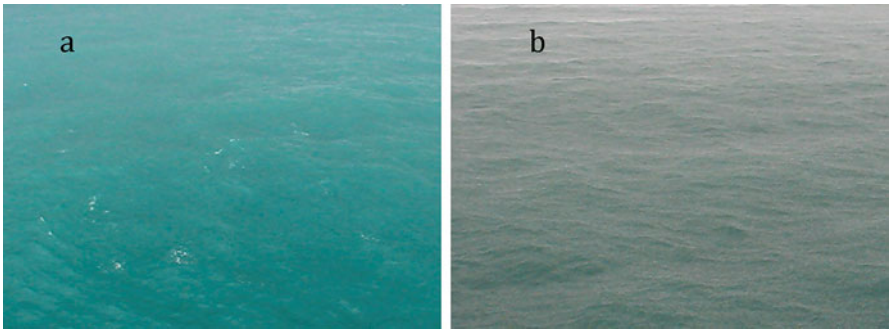

Fig. 5.4 Wave conditions at the time of Fig. 5.3 (**a**) before the rain, (**b**) 3 min later under a strong rain. Note the smoother surface and the (almost) absence of white-caps during the rain. (After Cavaleri et al. 2018)

5.4 The Physical Implications

I start with the detailed measured data that provide a clear idea of how things evolved. Figure 5.5, panel a, shows the evolution of the wind speed. The reported section covers 10 min (data scanned at 10 Hz). In both the panels the two vertical dashed lines identify the shower. Panel b shows the corresponding waving of the surface as measured by a pressure transducer at 3 m depth. Note the decreasing amplitude of the wave groups during the rain, summarized in Fig. 5.6 by the sequential values of the significant wave height H_s. Note that the rapidly changing situation implied the analysis to be done on only short sections, hence the large confidence limits that I have purposely not drawn to provide a clear and

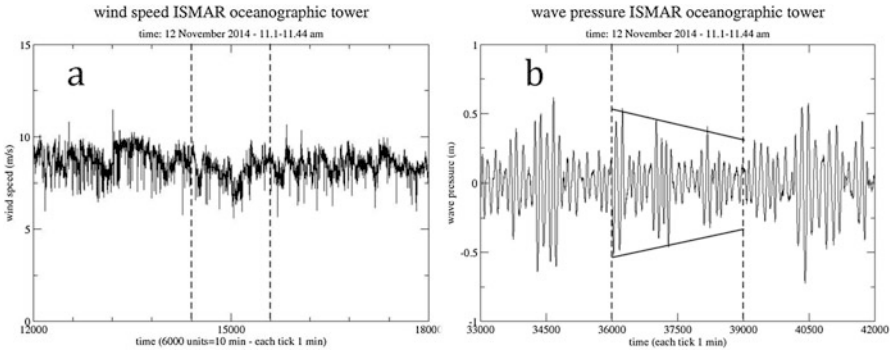

Fig. 5.5 (**a**) Wind speed history before, during and after the downpour. Sampling at 10 Hz. (**b**) Pressure record at 3.2 m depth. Sampling at 25 Hz. In both the panels the downpour is limited by the two dashed vertical lines. (After Cavaleri et al. 2018)

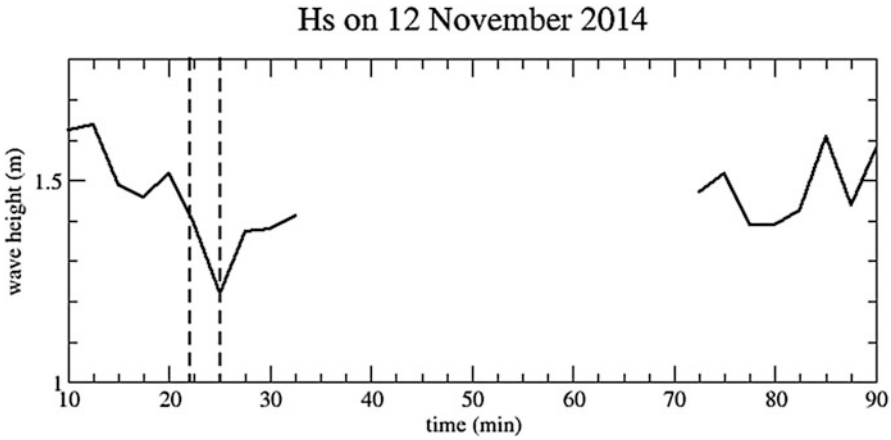

Fig. 5.6 Variation of the significant wave height across the downpour period, marked by the two dashed vertical lines. (After Cavaleri et al. 2018)

straightforward understanding. Again the dotted lines identify the shower. The record stops soon after as had been previously planned according to the original reasons of the experiment.

Now let us see the implications. A wind sea is a dynamical equilibrium between input by wind and loss by w-c. In practice wind keeps inputting energy and momentum (if faster than waves) into the wave field while waves lose (more or less) 90% of them to the sea via w-c. By and large only 10% of the input remains to lead to wave growth. For a more complete description of the overall process see the classical book by Komen et al. (1994) and the beautiful one by Holthuijsen (2007). For our present purpose the key point is that w-c virtually disappeared during the rain. Had the input by wind been still active, a quick estimate of the energies involved shows that H_s would have grown substantially, order of magnitude between 10 and 20%. This did not happen. On the contrary wave height decreased (see Figs. 5.5 and 5.6). The only logical conclusion is that during the rain, the input by wind was practically absent.

The crucial point is that in these conditions, following the present theory, all the models say waves should grow. Actually they ignore both the effects (lack of input by wind). Cavaleri et al. (2015) tried "to tell" to the computer system that rain smooths the sea surface. This was done flattening, at each time step, the tail of the spectrum proportionally to the local, in space and time, rain rate. The results was the opposite of what has been described because the lower surface roughness implied higher wind speeds, hence, following the unaffected (in the model) generation process, higher wave heights resulted.

Section 5.7 discusses how to frame the whole process. For the time being I illustrate with two examples the influence of breaking and spray in practical applications and how, especially in hurricanes and typhoons, we manage to get correct results making two errors that compensate each other.

5.5 How Rain Affects Hurricanes and Typhoons

Hurricanes and typhoons are energy fed by the underlying warm ocean. It is amazing that this process is not yet sufficiently well parameterized in the operational models. Similarly, the two effects of rain cited above, (a) reduction of input by wind, (b) reduction of breaking, imply large variations in the field and in the output of the storm. I illustrate this with two examples.

Haiyan, 2013, has been one of the most powerful and destructive typhoons ever (6000 fatalities in the Philippines). For a while modellers struggled to achieve the correct intensity of the storm. Figure 5.7 shows the results of the simulations by Zhao et al. (2017), first with a standard coupled model, and then with a proper formulation of spray and rain (and related heat transfer) following the formulation by Andreas et al. (2015). The comparison with the best track pressure history is enlightening. Note the abrupt increase of pressure around 100 h when the typhoon came ashore and was interacting with land.

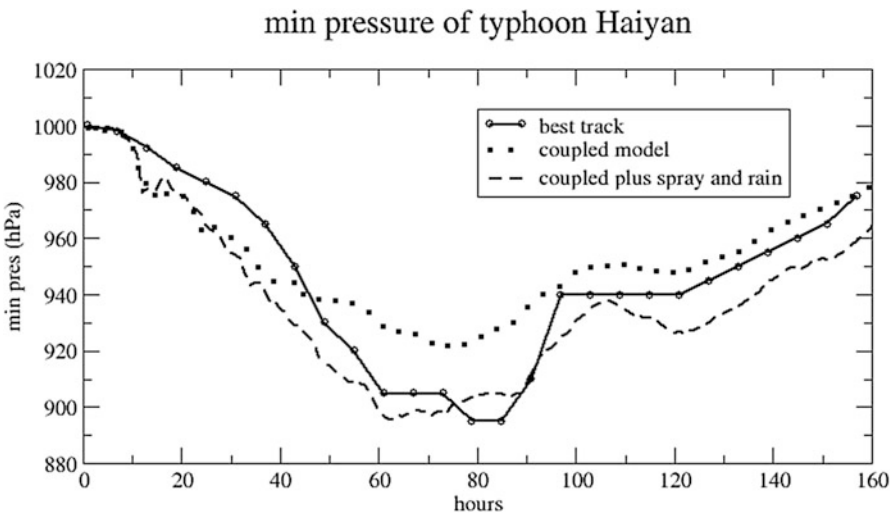

Fig. 5.7 Evolution of the minimum pressure in typhoon Haiyan according to best-track, coupled model and coupled model with the effects of spray and rain

On a different (not meteorological) front, i.e. exploring the influence of rain on wind input and w-c, Cavaleri and Bertotti (2018) have shown how the final results, in their case the maximum significant wave height H_s in the related field, vary modifying the two source functions according to the local (in space and time) rain rate. Figure 5.8 summarizes the results. The already exceptional (in some place close to 21 m) maximum H_s increased of almost five extra meters when rain modulated the input. On the contrary this H_s extra amount almost disappeared when, taking into account the push of the strong winds towards w-c, they blindly introduced the modulation of wind input according to the local rain (in space and time). What is emerging is that in some conditions, in practice when it is raining, models do provide good results, but this is because the opposite errors due to w-c (too much dissipation) and wind input (too much input) compensate each other.

5.6 Rain and Spray

Most of the marine aerosol is produced when in a growing sea, especially under the action of a strong wind, waves frequently break. Each single breaker produces an enormous number of water particles of different sizes. Monahan (e.g., 1986) spent a large part of his career parameterizing this production as a function of, mostly, the white-cap coverage and implicitly of the wind speed. This is still a matter of very active debate, but this is not where I want to focus (I have no doubt there will be many contributions in this direction). My point is again rain. We have seen in

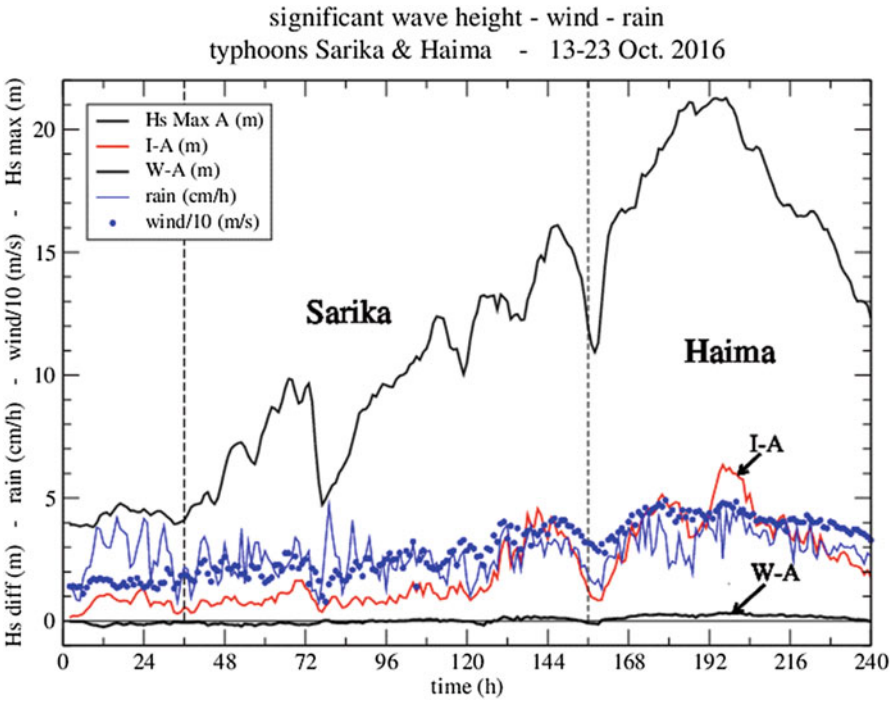

Fig. 5.8 Two sequential typhoons, Sarika and Haima, in the Philippines. For each hour of the considered period we show the maximum significant wave height H_s in the field, the corresponding rain rate and wind speed, the extra H_s (I-A) gained by the model when the modulation of white-caps by wind is considered, the corresponding reduced gain (W-A) when also the modulation of wind input is considered

Sect. 4.3 that rain kills the breakers. It follows at once that rain affects also the aerosol (and spray) production, the more intense the rain the lower the number and intensity of breakers, hence the reduced spray production on the sea surface.

This is partly compensated for by another effect of rain on the sea surface. Falling on it, each drop of rain tends to produce a small bubble of air just below it (there are limits on the size of the drop). After a delay that depends on its size, the bubble reaches the surface, its bursting producing tiny droplets of water that then move with the wind. The size of the bubble, hence of the droplets, depends on the size (and implicitly the falling speed) of the rain drop. Medwin et al. (1992) and Oliveira et al. (2003) provide an estimate of the number of rain drops and when they produce bubbles in water. Besides the diameter and speed, the effects of a rain drop depends also on the local wind. Given that the rain falling velocity is typically lower than 10 ms^{-1}, it is clear that in most of the cases rain falls obliquely. This is a less explored area for bubble formation, simply because most of the experimental data have been obtained under laboratory conditions in absence of rain. There are suggestions (see Medwin et al., 1990) that an oblique impact is less likely to lead

to bubbles in water. In any case it is mandatory to point out that, however intense the rain, the associated production of aerosol is orders of magnitude smaller than that produced by w-c. The only area where rain becomes the dominant producer (relatively speaking) is under convective zones in the absence of any wind.

5.7 What We Have Learnt

Breakers in deep water, mostly referred to as white-caps, have a crucial role in the exchange of energy, momentum, heat, aerosol, gas, etc. between the ocean and the atmosphere. Given that the 15–20% of the oceans that is steadily in stormy conditions is in effect controlling the exchanges at the interface, it is in so doing also controlling the climate. Notwithstanding this crucial role, it is relatively surprising that we cannot frame well the physics of the process, both for the conditions that lead to it, and for its dynamics that we can describe only in statistical terms.

People have parameterized w-c as a function of wave conditions, wind speed and water temperature. Surprisingly, rain has not been considered. This is not the case among mariners, for whom "the rain calms the sea" is an accepted truth derived from their direct experience. I was lucky enough to witness such an event, and it was enlightening. Of course in "calming the sea", more precisely cancelling the breakers of a storm, rain strongly affects also the related aerosol and spray production. Implicitly, and at a more fundamental level not strictly related to aerosol, the evident truth derived from the field has shed new light on the process of input by wind, more generally, wave generation by wind. The truth I see unfolding in front of us during a stormy and rainy event is that these processes, rain, wind input and white-capping, which for many decades have been considered as separate and independent processes, are coupled, synchronously present or absent, and as such they will have to be considered in the future.

References

Andreas, E. L., Mahrt, L., & Vickers, D. (2015). An improved bulk air-sea surface flux algorithm, including spray-mediated transfer, Q.J.R. *Meteorological Society, 141*(686), 642–654. https://doi.org/10.1002/qj.2424.

Cavaleri, L. (2000). The oceanographic tower Acqua Alta – Activity and prediction of sea states at Venice. *Coastal Engineering, 39*, 29–70.

Cavaleri, L., & Bertotti, L. (2018). Rain on generative seas. *Geophysical Research Letters, 45*, 7049–7056. https://doi.org/10.1029/2018GL078006.

Cavaleri, L., & Zecchetto, S. (1987). Reynolds stresses under wind waves. *Journal of Geophysical Research, 92*(C4), 3894–3904.

Cavaleri, L., Baldock, T., Bertotti, L., Langodan, S., Olfateh, M., & Pezzutto, P. (2018). What a sudden downpour reveals about wind wave generation. *Procedia IUTAM*, 26, 70–80.

Cavaleri, L., Bertotti, L., & Bidlot, J.-R. (2015). Waving in the rain. *Journal of Geophysical Research*. https://doi.org/10.1002/2014JCO10348. 18 pp.

Holthuijsen, L. H. (2007). *Waves in oceanic and coastal waters* (p. 387). Cambridge: Cambridge University Press.

Komen, G. J., Cavaleri, L., Donelan, M., Hasselmann, K., Hasselmann, S., & Janssen, P. A. E. M. (1994). *Dynamics and modelling of ocean waves* (p. 532). Cambridge: Cambridge University Press.

Medwin, H., Kurgan, A., & Nystuen, J. A. (1990). Impact and bubble sound from raindrops at normal and oblique incidence. *The Journal of the Acoustical Society of America, 88*(1), 413–418.

Medwin, H., Nystuen, J. A., Jacobus, P. W., Ostwald, L. H., & Snyder, D. E. (1992). The anatomy of underwater rain noise. *The Journal of the Acoustical Society of America, 92*(3), 1613–1623.

Monahan, E. C., Davidson, K. L., & Spiel, D. E. (1986). A model of marine aerosol generation via whitecaps and waves disruption. In E. C. Monahan & G. Mac Niocaill (Eds.), *Oceanic whitecaps and their role in Air-Sea exchange processes* (pp. 167–174). Dordrecht: Reidel. https://doi.org/10.1007/978-94-009-4668-2_16.

Oliveira, M. S. N., Fitch, A. W., & Ni, X. (2003). A study of bubble velocity and bubble residence time in a gassed oscillatory baffled column, ICHEM, trans. *ICHEM, 81*., Part A, 233–242.

Pierson, W. J., & Marks, W. (1952). The power spectrum analysis of ocean-wave records. *Transactions, American Geophysical Union 33*(6), 834

Zhao, B., Qiao, F., Cavaleri, L., Wang, G., Bertotti, L., & Liu, L. (2017). Sensitivity of typhoon modeling to surface waves and rainfall. *Journal of Geophysical Research Oceans, 122*. https://doi.org/10.1002/2016JC012262.

Chapter 6
Measurements of Airside Shear- and Wave-Induced Viscous Stresses over Strongly Forced Wind Waves

Kianoosh Yousefi, Fabrice Veron, and Marc P. Buckley

Abstract Detailed knowledge of the airflow over the surface of the ocean is paramount to evaluate and predict air-sea fluxes. The flux of momentum is of particular interest because it involves phenomena over a large spectrum of length and temporal scales from aerodynamic drag in large storm systems, down to the wind-wave generation problem at sub-centimeter scales. At the smaller scales, while there is a body of theoretical and experimental work which suggests that the wind-wave generation process is linked to the instability of the coupled air-water surface flow, progress has been hindered by the difficulties associated with making reliable measurements or simulations near the air-water interface at scales at which viscosity plays a role. In this paper, we present recent measurements of the two-dimensional velocity field in the turbulent airflow above wind waves. Improvements in measuring techniques have allowed us to detect the viscous sublayer in the airflow near the interface and make direct measurements of the airside viscous tangential stress (analogous to those made by (Banner ML, Peirson WL, J Fluid Mech 364:115–145, 1998) on the water side). Furthermore, we were able to separate mean, turbulent, and wave-coherent motions, and this decomposition yielded wave-coherent flow measurements as well as wave-phase averages of several flow field variables. We present the relationship of the varying surface viscous stress with the dominant wave phase. Also, to the authors' knowledge, we present the first measurements of airside wave-induced viscous stresses. We conclude that at low wind speed, surface viscous effects are substantial and likely need to be accounted for in the early stages of the wind-wave generation process.

K. Yousefi (✉)
Department of Mechanical Engineering, University of Delaware, Newark, DE, USA
School of Marine Science and Policy, University of Delaware, Newark, DE, USA
e-mail: kyousefi@udel.edu

F. Veron
School of Marine Science and Policy, University of Delaware, Newark, DE, USA
e-mail: fveron@udel.edu

M. P. Buckley
Institute of Coastal Research, Helmholtz-Zentrum Geesthacht, Geesthacht, Germany
e-mail: mbuckley@udel.edu

P. Vlahos (ed.), *Recent Advances in the Study of Oceanic Whitecaps*,
https://doi.org/10.1007/978-3-030-36371-0_6

6.1 Introduction

The exchanges of momentum between the atmosphere and the ocean are strongly contingent on small-scale interfacial dynamics, particularly in low to moderate wind forcing conditions. These microphysical processes at the air-sea interface have important effects on the exchanges of momentum between the atmosphere and the ocean. However, relatively less attention has been paid to the tangential viscous stress and its contribution to the total air-sea momentum exchanges. This is in part because of the challenges associated with acquiring data close to the water surface (where viscosity is important) either in the open ocean or in the laboratory (Banner and Peirson 1998). In recent years, however, increased efforts have been made to examine the importance of viscous stress at the interface (e.g., Banner and Peirson 1998; Veron et al. 2007; Grare et al. 2013b; Peirson et al. 2014).

Several theoretical, numerical, and laboratory studies have investigated the tangential viscous stress over surface waves (e.g., Longuet-Higgins 1969; Okuda et al. 1977; Banner and Peirson 1998; Peirson and Banner 2003; Veron et al. 2007; Reul et al. 2008; Grare et al. 2013b; Peirson et al. 2014). These efforts were, in part, motivated by the need to better understand the early stages of the wave generation process. The early laboratory measurements of Okuda et al. (1977) estimated the shear stress at the air-sea interface from the aqueous boundary layer below water waves and concluded that the tangential stress predominantly supports the total wind stress for waves in strongly wind-forced conditions. In contrast, Banner and Peirson (1998) determined through a particle image velocimetry (PIV) technique at short fetches that the tangential stress does not contribute significantly to the total stress over very young wind-generated waves, though it is a non-zero fraction of the wind stress (see also Peirson 1997). Further works by Grare et al. (2013b) and Peirson et al. (2014) also determined that the contribution of the viscous stress to the total momentum flux is not negligible for low wind speeds but is possibly trivial at high wind speeds even close to the surface.

The airflow separation events over wind-driven waves significantly influence the distribution of the tangential viscous stress along the wave crest. The first studies measuring the viscous stress at the interface of surface waves in a laboratory, first performed by McLeish and Putland (1975) and Okuda et al. (1977) and furthered by Csanady (1985, 1990) and Kawamura and Toba (1988), qualitatively revealed that the tangential stress suddenly decreases to an almost zero value just past wave crests. Okuda et al. (1977) attributed the reduction of the viscous stress past the wave crest to the occurrence of airflow separation. More recently, Veron et al. (2007) also observed, through quantitative measurements of the velocity field on the airside of the water waves, that the tangential viscous stress is significantly reduced at the point of separation thereby leading to abrupt and dramatic along-wave variations in the viscous stress at the water surface (see also Reul et al. 2008). The tangential viscous stress increases again past the wave trough and reaches its peak value close to the wave crest.

As a general trend, the tangential stress over surface waves shows reductions compared to the flat or smooth water surfaces (Banner and Peirson 1998;

Kudryavtsev and Makin 2001). This can be partly explained by the fact that a portion of the total wind stress is carried by wave-coherent components when waves are present on the water surface. Moreover, the tangential viscous stress exhibits a phase-locked distribution over surface waves. Over both separating and non-separating wind waves, viscous stress presents a pattern of along-wave asymmetry close to the water interface in which it is highest (lowest) on the windward (leeward) side of waves (see Veron et al. 2007; Peirson et al. 2014). This is qualitatively consistent with predictions by Gent and Taylor (1976, 1977).

In recent years, there has been growing interest in evaluating the influences of the ocean surface waves on the turbulent flow structure above the water interface, and therefore, in the fundamental processes of wind-wave couplings. Although the primary features of the turbulent and wave-coherent momentum fluxes across the air-sea interface have received much attention over the last two decades (e.g., Hsu et al. 1981; Sullivan et al. 2000; Shen et al. 2003; Hara and Belcher 2004; Kihara et al. 2007; Yang and Shen 2010; Grare et al. 2013a; Hara and Sullivan 2015; Buckley and Veron 2016, 2019; Husain et al. 2019), the role of the tangential viscous stress in the air-sea momentum transfer is less well understood. In the current study, we present detailed measurements of the viscous stress within the viscous sublayer on the airside of the wind-driven surface waves and provide an estimation of its contribution to the total interfacial wind stress for low to strong wind forcing conditions. These measurements were acquired in the large wind-wave tunnel facility at the Air-Sea Interaction Laboratory of the University of Delaware using a combined PIV and laser-induced fluorescence (LIF) techniques (Buckley and Veron 2017). The paper is organized in the following fashion. In Sect. 6.2, the experimental setup and configurations are briefly described, along with the coordinate transformation and wave-turbulence decomposition. The results are discussed in Sect. 6.3 wherein the measurements of the mean and wave-induced tangential viscous stresses are presented in detail. Finally, a summary of the conclusions is offered in Sect. 6.4.

6.2 Experimental Configurations

6.2.1 Experimental Setup

The experimental measurements presented in the current study are based on the existing raw data obtained in the large wind-wave tunnel facility at the Air-Sea Interaction Laboratory of the University of Delaware (Buckley 2015; Buckley and Veron 2017). As schematically shown in Fig. 6.1, the wave tank has dimensions of 42 m length, 1 m width, and 1.25 m height of which 0.7 m filled with water to ensure sufficient airflow space above the water surface. A permeable absorbing beach was located at the end of the tank to dissipate the wave energy and eliminate the wave reflections. A honeycomb airflow straightener was also employed at the location of zero fetch to ensure uniform airflow across the tank and provide a smooth transition

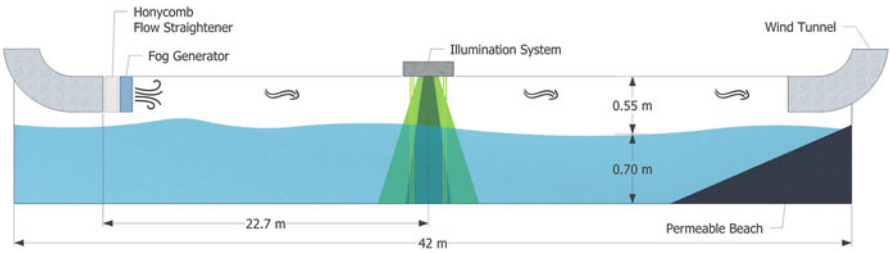

Fig. 6.1 Schematic representation of the large wind-wave tunnel facility at the Air-Sea Interaction Laboratory of the University of Delaware. The imaging data collection was located at a fetch of 22.7 m, and the airflow was seeded (fog particles) at the location of zero fetch. Airside velocity fields and wave properties were measured by PIV and LIF techniques, respectively. The flow is directed from left to right

from the wind tunnel inlet to the water surface. The flow visualization instruments were positioned at a fetch of 22.7 m. For the experiments presented here, various wind forcing conditions were considered with wind speeds ranging from 2.25 m s^{-1} to 16.59 m s^{-1}. The complete experimental conditions with corresponding wave properties are summarized in Table 6.1.

The quantitative velocity measurements were acquired using a combination of PIV and LIF techniques on the airside of surface wind waves within the viscous sublayer, on average, within 100 μm to the air-water interface. The PIV technique was employed to acquire along-channel two-dimensional airflow velocity fields above the wind waves. Water droplet particles (8–12 μm), used to seed the airflow, were illuminated with a high-intensity laser sheet and imaged by two adjacent digital cameras (Jai RM-4200, 2048 × 2048 pixels) at a frame rate of 14.4 fps. The two captured PIV frames were concatenated to produce a high-resolution 18.7 × 9.6 cm PIV image with a pixel resolution of 47 μm per pixel. An adaptive PIV algorithm similar to that described by Thomas et al. (2005) was applied to the concatenated PIV images, yielding a velocity vector measurement every 188 μm^2. Further, the LIF technique was utilized to accurately detect the surface profiles within the PIV field of view. To that end, high-resolution LIF images were simultaneously acquired with the PIV images using an identical digital camera (Jai RM-4200, 2048 × 2048 pixels) providing a high-resolution 20.48 × 20.48 cm image with a pixel resolution of 100 μm per pixel. In addition, large along-channel surface profiles of waves were obtained through the LIF technique and using a large field of view digital camera (Jai RM-4200, 2048 × 2048 pixel, 7.2 fps) equipped with a large field of view lens such that the final image spanned 51.20 × 51.20 cm with a resolution of 250 μm per pixel. An example of a raw large field of view (LFV) image along with the instantaneous horizontal velocity field estimated with the PIV is presented in Fig. 6.2. The reader is referred to Buckley (2015) and Buckley and Veron (2017) for the complete details of these experiments, including wind-wave facility, experimental setup, image acquisition, and processing procedures.

Table 6.1 Summary of experimental and flow conditions

U_{10} $(m\ s^{-1})$	u_* $(m\ s^{-1})$	C_p $(m\ s^{-1})$	C_p/u_*	ζ_0 (mm)	δ_0 (mm)	a_p (cm)	k_p (m^{-1})	$\delta_0 k_p$	$a_p k_p$	f_p (Hz)
2.25	0.075	0.47	6.27	0.063	2.00	0.15	44.88	0.0876	0.07	3.3
5.08	0.168	0.62	3.69	0.056	0.89	0.50	25.13	0.0225	0.13	2.5
9.57	0.318	0.78	2.46	0.043	0.49	1.20	16.11	0.0079	0.19	2.0
14.82	0.567	0.87	1.53	0.290	0.26	1.96	13.09	0.0034	0.26	1.8
16.59	0.663	0.92	1.39	0.449	0.23	2.29	11.64	0.0026	0.27	1.7

The friction velocity, roughness height, and 10-m extrapolated velocity were calculated by fitting the logarithmic part of the mean wind velocity profile. The viscous sublayer thickness is estimated by $\delta_0 u_*/\nu = 10$ (Phillips 1977). The peak wave frequencies, f_p, obtained from frequency spectra of single point elevation measurements, and other parameters with subscript p derived by applying linear wave theory. The peak amplitude is $a_p = \sqrt{2} a_{rms}$ in which a_{rms} is the root-mean-square amplitude calculated from wave gauge time series.

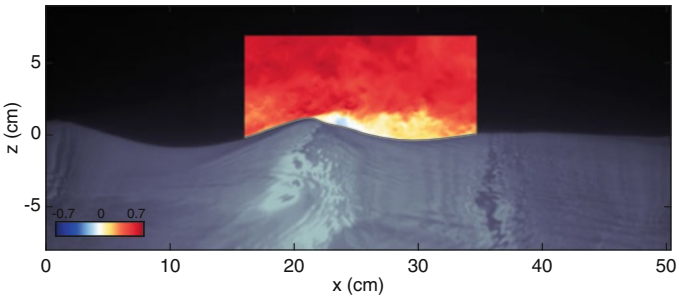

Fig. 6.2 Example of a raw large field of view (LFV) image plotted along with the measured instantaneous horizontal velocity field acquired with the PIV. The colorbar shows u/U_{10}, the horizontal velocity normalized with the 10-m equivalent wind speed; here U = 5.08 m s^{-1}

6.3 Coordinate Transformation and Triple Decomposition

In order to study the mean, wave, and turbulence contributions to the mean flow and air-sea momentum fluxes, it is necessary to separate mean, wave, and turbulent motions. Therefore, mean and phase averages need to be performed on the airside velocity field obtained experimentally, and to so requires a coordinate system that follows the wave motion, at least near the interface. By using surface elevation profiles $\eta(x)$ detected by the LIF camera, we were able to decompose the wave profiles within the PIV image into corresponding spatial Fourier components,

$$\eta(x) = \sum_n \eta_n = \sum_n a_n e^{i(k_n x + \varphi_n)} \tag{6.1}$$

where a_n, k_n, and φ_n are the amplitude, wavenumber, and phase of the n^{th} mode in the Fourier decomposition of the surface $\eta(x)$, respectively. From there, it is relatively straightforward to derive a coordinate system that follows the water surface near the interface and tends toward a laboratory-attached Cartesian coordinate system far away from the surface. Thus, we define a wave-following coordinate system that relates to the Cartesian coordinates using the following expressions,

$$\begin{aligned} \xi(x,z) &= x - i\sum_n \eta_n e^{-k_n \zeta} \\ \zeta(x,z) &= z - \sum_n \eta_n e^{-k_n \zeta} \end{aligned} \tag{6.2}$$

Here, lines of constant ζ are pseudo-horizontal in that $\zeta = 0$ gives $z = \eta(x)$, which is exactly the location of the wavy interface. Far from the influence of the waves (proportional here to the surface wave wavenumbers) lines of constant ζ tend toward Cartesian horizontal lines of constant z.

Accordingly, the ensemble mean velocity profiles $\bar{u}(\zeta)$ are obtained by simply averaging velocity profiles following these pseudo-horizontal ζ lines. Alternatively, by using the phase of the peak wave component (from the Fourier decomposition), each velocity profiles measured above the surface can be associated with the phase of the underlying wave, and phase-dependent velocity profiles $\langle u \rangle(\varphi, \zeta)$ can be obtained. Therefore, measured velocity fields can be decomposed into a phase-averaged component and a residual, which by definition is a turbulent component, i.e., $u(\xi, \zeta, t) = \langle u \rangle(\varphi, \zeta) + u'(\xi, \zeta, t)$. The phase-averaged velocity fields can be further decomposed into the mean and wave-induced components leading to the so-called triple decomposition of a velocity field (Hussain and Reynolds 1970),

$$u(\xi, \zeta, t) = \bar{u}(\zeta) + \tilde{u}(\varphi, \zeta) + u'(\xi, \zeta, t) \tag{6.3}$$

The general properties of the time and phase averages can be found in reports by Hussain and Reynolds (1970) and Reynolds and Hussain (1972).

6.4 Results

6.4.1 Governing Equations

In order to express the governing equations of fluid motion, we consider the Cartesian coordinate system in which (x, y, z) are respectively streamwise, spanwise, and vertical coordinates. The airflow is assumed to have a constant density and kinematic viscosity with the velocity components (u, v, w) in (x, y, z) directions, respectively. The equations of motion including continuity, momentum, and energy can be decomposed into the mean, wave-induced, and turbulent fluctuation components by applying the triple decomposition technique briefly described above. The starting point is substituting the decomposed variables into the governing equations, and then averaging; the time averaging is applied first and then the phase averaging. The mean, wave-induced, and turbulent momentum equations in a Cartesian coordinate system can be then expressed as,

$$\frac{\partial \bar{u}_i}{\partial t} + \frac{\partial}{\partial x_j}(\bar{u}_i \bar{u}_j) = -\frac{1}{\rho}\frac{\partial \bar{p}}{\partial x_i} + \frac{1}{\rho}\frac{\partial \bar{\tau}_{ij}}{\partial x_j} - \frac{\partial}{\partial x_j}(\overline{u_i' u_j'} + \overline{\tilde{u}_i \tilde{u}_j}) \tag{6.4}$$

$$\frac{\partial \tilde{u}_i}{\partial t} + \frac{\partial}{\partial x_j}(\bar{u}_i \tilde{u}_j) + \frac{\partial}{\partial x_j}(\tilde{u}_i \bar{u}_j) = -\frac{1}{\rho}\frac{\partial \tilde{p}}{\partial x_i} + \frac{1}{\rho}\frac{\partial \tilde{\tau}_{ij}}{\partial x_j} + \frac{\partial}{\partial x_j}(\overline{\tilde{u}_i \tilde{u}_j} - \tilde{u}_i \tilde{u}_j) - \frac{\partial \tilde{r}_{ij}}{\partial x_j} \tag{6.5}$$

$$\frac{\partial u_i'}{\partial t} + \frac{\partial}{\partial x_j}(u_i'\bar{u}_j) + \frac{\partial}{\partial x_j}(u_i'\tilde{u}_j) + \frac{\partial}{\partial x_j}(\bar{u}_i u_j') + \frac{\partial}{\partial x_j}(\tilde{u}_i u_j')$$
$$= -\frac{1}{\rho}\frac{\partial p'}{\partial x_i} + \frac{1}{\rho}\frac{\partial \tau_{ij}'}{\partial x_j} + \frac{\partial}{\partial x_j}(\langle u_i' u_j' \rangle - u_i' u_j') \tag{6.6}$$

where $\tilde{r}_{ij} = \langle u_i' u_j' \rangle - \overline{u_i' u_j'}$ is the wave-induced turbulent stress, $-\overline{u_i' u_j'}$ is the Reynolds stress, and $-\overline{\tilde{u}_i \tilde{u}_j}$ is the wave-induced stress. Moreover, in these equations, the mean, wave-induced, and turbulent tangential viscous stresses can be respectively expressed as,

$$\bar{\tau}_{ij} = 2\mu \bar{S}_{ij} = \mu\left(\frac{\partial \bar{u}_i}{\partial x_j} + \frac{\partial \bar{u}_j}{\partial x_i}\right) \tag{6.7}$$

$$\tilde{\tau}_{ij} = 2\mu \tilde{S}_{ij} = \mu\left(\frac{\partial \tilde{u}_i}{\partial x_j} + \frac{\partial \tilde{u}_j}{\partial x_i}\right) \tag{6.8}$$

$$\tau_{ij}' = 2\mu S_{ij}' = \mu\left(\frac{\partial u_i'}{\partial x_j} + \frac{\partial u_j'}{\partial x_i}\right) \tag{6.9}$$

where $\bar{S}_{ij}$, $\tilde{S}_{ij}$, and S_{ij}' are the mean, wave-induced, and turbulent strain rate tensors, respectively. In this paper, we are interested in examining the effects of wind waves on the tangential viscous stress terms. Specifically, the off-diagonal components of the viscous stress tensors are of importance in the turbulent boundary layer over surface waves.

6.4.2 Mean Tangential Viscous Stress

The phase-averaged distribution of tangential viscous stress measurements normalized by the total wind stress is presented in Fig. 6.3 for experimental conditions with 10-m wind speeds varying from 2.25 m s^{-1} to 16.59 m s^{-1}. The right panels of Fig. 6.3 show the corresponding profiles of the mean tangential stress. The tangential viscous stress is computed from Eq. (6.7) for a two-dimensional flow field as,

$$\bar{\tau}_{13} = \mu\left(\frac{\partial \bar{u}}{\partial z} + \frac{\partial \bar{w}}{\partial x}\right) \tag{6.10}$$

The surface waves are inducing a phase-locked variability in the viscous stress consistent with the results of, for example, Banner and Peirson (1998) and Veron et al. (2007). In general, the along wave distributions of the phase-averaged tangential viscous stress present an asymmetric pattern close to the surface; the viscous stress is intense upwind of wave crests with its maximum value about the wave crests, and less intense downwind of wave crests with its minimum in the middle of

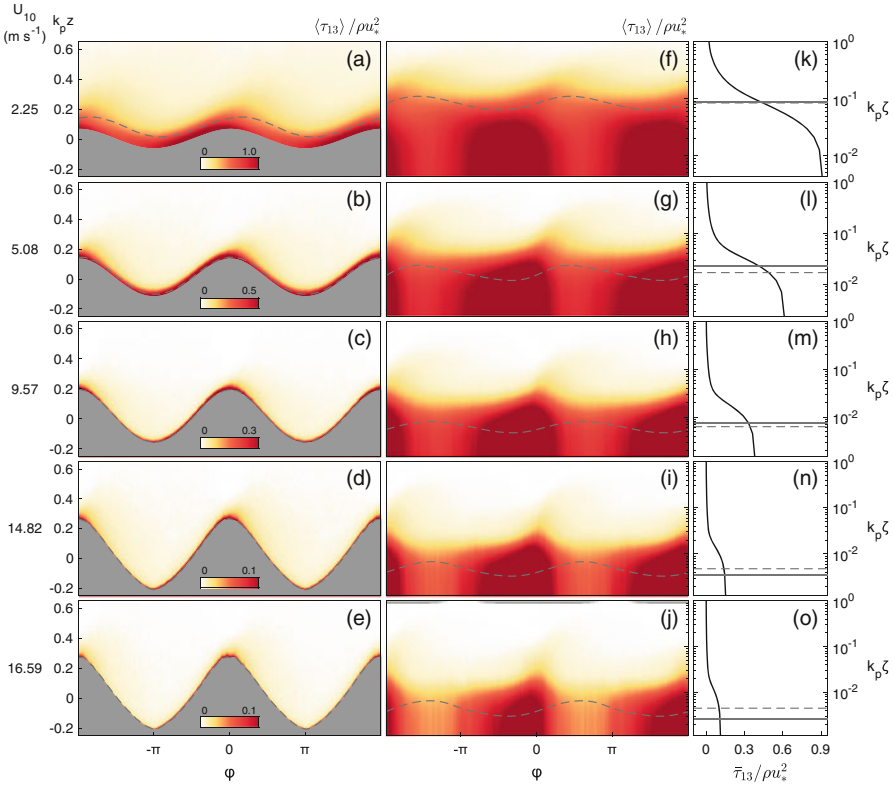

Fig. 6.3 Phase-averaged distributions of the tangential viscous stress measurements (defined in Eq. 6.10) normalized with the total wind stress for all wind speed cases plotted on the (**a-e**) linear and (**f-j**) logarithmic scales. The corresponding vertical mean profiles of the tangential viscous stresses are also presented in the last column (panels **k-o**). The logarithmic phase-averaged and mean profile fields are plotted above the mean water surface as a function of dimensionless height $k_p\zeta$, while the linear vertical scale uses Cartesian coordinates k_pz. The dashed, grey lines indicate the location of the critical layer, i.e., the height at which $\langle u \rangle = C_p$, and the solid, grey lines indicate the height of the viscous sublayer. The 10-m wind speeds corresponding to each experimental condition are indicated on the left

the leeward side of waves. With increasing wind speed, the peak values of the normalized viscous stress reduce and shift downward. The magnitude of the peak viscous stress near the surface decreases from $\langle \tau_{13} \rangle / \tau = 1.20$ for $U_{10} = 2.25$ m s^{-1} to $\langle \tau_{13} \rangle / \tau = 0.19$ for $U_{10} = 16.59$ m s^{-1}, where $\tau = \rho u_*^2$ is the total wind stress. For the lowest wind speed, an enhanced viscous stress was observed at/near the water surface for almost the entire upwind face of the wave from $\varphi = -3\pi/4$ to $\varphi = 0$ in which the viscous stress was greater than the total stress. This is the region that the wave-coherent and turbulence are greatly suppressed. Close to the surface (at the height of $\zeta = 284$ μm), the normalized tangential viscous stress, averaged over the whole upwind side of the wave, is $\overline{(\langle \tau_{13} \rangle / \tau)}_{[-\pi,0]} = 1.05$, while it is

$\overline{(\langle\tau_{13}\rangle/\tau)}_{[0,\pi]} = 0.75$ averaged over the leeward side, for the wind speed of $U_{10} = 2.25$ m s^{-1}. We note that the phase-locked variations in tangential viscous stress exert important influences on the wave growth and the boundary layer thickness on the windward and leeward side of the waves. Finally, while the viscous stress is significant close to the surface, even for higher wind speed cases, it rapidly vanishes, as expected, farther from the interface outside of the viscous sublayer.

To further examine the near-surface viscous stresses, the mean tangential stress profiles are presented in the wall-layer coordinates in Fig. 6.4a on a logarithmic scale. The height of the critical layer is also indicated with cross symbols for each experimental case. As a general trend, the contribution of the viscous stress to the total momentum flux decreases with increasing wind speed consistent with the literature (e.g., Banner and Peirson 1998; Peirson et al. 2014). At the surface, however, the tangential viscous stress remains a considerable portion of the total wind stress, particularly at low to moderate wind forcing conditions. For the low wind speed of $U_{10} = 2.25$ m s^{-1}, the mean tangential viscous stress supports more than 90% of the total momentum flux at the interface and remains significant up to a dimensionless height of $\zeta^+ = 10$ with approximately a 40% contribution to the wind stress. Although the mean normalized tangential stress reduces with increasing wind speed, it still contributes more than 60% and 35% to the total stress for wind speeds of $U_{10} = 5.08$ m s^{-1} and $U_{10} = 9.57$ m s^{-1}, respectively. For strongly forced wind waves, the normalized mean viscous stress remains a non-zero portion of the total wind stress; it is approximately 15% and 11% of the total wind stress for the cases with $U_{10} = 14.82$ m s^{-1} and $U_{10} = 16.59$ m s^{-1}, respectively. Again, outside the

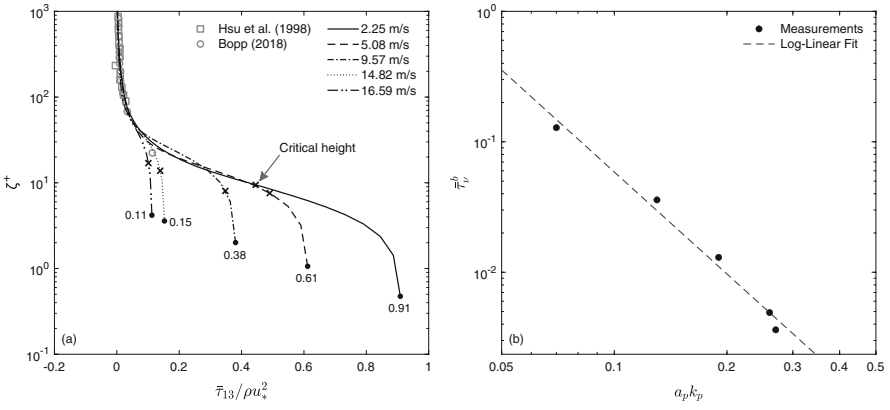

Fig. 6.4 (**a**) Vertical profiles of the mean tangential viscous stress (defined in Eq. 6.10) normalized by the total wind stress for different experimental conditions plotted as a function of dimensionless law-of-the-wall height, i.e., $\zeta^+ = \zeta u_*/\nu$, on the logarithmic scale. The results of Hsu et al. (1981) for mechanically generated water waves with $U_{10} = 2.4$ m s^{-1} and $C_p/u_* = 18.2$ and Bopp (2018) for wind waves with $U_{10} = 12$ m s^{-1} and $C_p/u_* = 1.7$ are also indicated by square and circle symbols, respectively, for comparison purposes. The location of the critical layer is also denoted by cross symbols. (**b**) Height-integrated tangential viscous stress $\bar{\tau}_\nu^b$ (defined in Eq. 6.11) as a function of wave slope. The dashed line is the best fit through the data and shows $\bar{\tau}_\nu^b \propto (a_p k_p)^{-2.6}$

viscous sublayer farther above the surface, the viscous stress rapidly drops to zero, and consequently, the influences of viscosity become trivial.

The normalized tangential viscous stress profiles integrated within the wave boundary layer (i.e., up to $\zeta = k_p$) are defined as,

$$\bar{\tau}_\nu^b = \frac{k_p}{\rho u_*^2} \int_0^1 |\bar{\tau}_{13}| \, d\zeta \tag{6.11}$$

and displayed in Fig. 6.4b as a function of wave slope. They represent the average contribution of the viscous stress to the wind stress. As expected, the height-integrated contribution of the viscous stress decreases with the wave slope (or equivalently in these single fetch experiments, with the 10-m wind speed).

6.4.3 Wave-Induced Tangential Viscous Stress

In this section, we investigate the wave-induced tangential viscous stress in the wave boundary layer. The wave-induced tangential viscous stress, for these two-dimensional experimental data, can be estimated using Eq. (6.8) and reduces to,

$$\tilde{\tau}_{13} = \mu\left(\frac{\partial \tilde{u}}{\partial z} + \frac{\partial \tilde{w}}{\partial x}\right) \tag{6.12}$$

In Fig. 6.5, we first present the phase-averaged distributions of wave-induced viscous stress. The streamwise-averaged (average across all phases) profiles of the absolute value of $\tilde{\tau}_{13}$ fields, i.e., $\overline{|\tilde{\tau}_{13}|}$ where $|\tilde{\tau}_{13}|$ is the absolute value, are also plotted on the right panels (k-o). All the terms are normalized by the total wind stress. Over the lowest wind speed, the wave-induced tangential stress was positive (negative) upwind (downwind) side of wave crests below the critical height with its positive and negative peaks located about the middle of the windward and leeward face of the waves (see Fig. 6.5 panels a and f). Above the critical height, this positive-negative pattern in the wave viscous stress was substantially shifted in the downstream direction by almost $3\pi/4$. In high winds, the pattern of positive-negative asymmetry in the wave-induced tangential stress can also be observed very close to the interface (see Fig. 6.5 panels b-e and g-j). With increasing wind speed, the region of positive wave-induced viscous stress on the windward side of waves moves downwind, while the negative stress on the leeward side of waves slightly extends up to the windward face of the next wave. The location of extrema in the wave viscous stress also moves downwind with increasing wind speed. The positive extremum was located at a phase of approximately $-85°$, $-60°$, $-30°$, $-25°$ for the wind speeds of $U_{10} = 2.25$ m s^{-1}, $U_{10} = 5.08$ m s^{-1}, $U_{10} = 9.57$ m s^{-1}, and $U_{10} = 14.82$ m s^{-1}, respectively. The negative extremum was also shifted from a phase of 95° for $U_{10} = 5.08$ m s^{-1} to a phase of about 115° for $U_{10} = 16.59$ m s^{-1}.

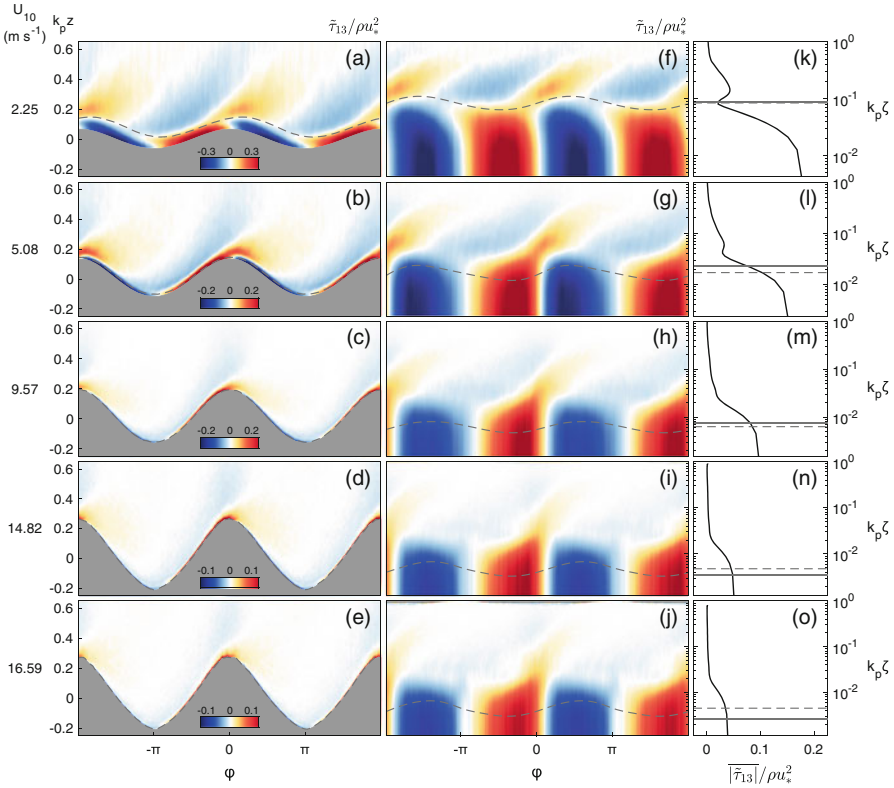

Fig. 6.5 Phase-averaged distributions of the wave-induced tangential viscous stress (see Eq. 6.12) for all wind-wave experiments plotted on the (**a–e**) linear and (**f–j**) logarithmic scales. The corresponding streamwise-averaged profiles of the absolute value of $\tilde{\tau}_{13}$ fields, i.e., $\overline{|\tilde{\tau}_{13}|}$ where $|\tilde{\tau}_{13}|$ is the absolute value, are also presented on the right panels (**k-o**). All fields are normalized by the total wind stress, i.e., ρu_*^2. The logarithmic phase-averaged and streamwise-averaged fields are plotted above the mean water surface as a function of dimensionless height $k_p\zeta$, while the linear vertical scale uses Cartesian coordinates k_pz. The dashed and solid lines denote the location of the critical layer and viscous sublayer, respectively. The 10-m wind speeds corresponding to each experimental case are indicated on the left

At the lowest wind speed, however, the negative peak was positioned closer to the wave trough at a phase of approximately 110°. Moreover, farther above the surface, the wave viscous stress forms a negative-positive pattern along the wave crest. In general, the wave-induced viscous stress quickly reduces away from the surface. To the author's knowledge, these are the first measurements of airside wave-induced viscous stresses.

The streamwise-averaged profiles of wave-induced tangential viscous stress are also shown in Fig. 6.5 panels k-o. As expected, the variations of $\overline{|\tilde{\tau}_{13}|}$ are mainly constrained in the vicinity of the water surface and rapidly tends toward zero farther above the surface. The magnitude of streamwise-averaged wave viscous

stress decreases as the wind speed increases, which is consistent with the behavior of the mean viscous stress. In general, the wave-induced viscous stresses are smaller than the mean tangential viscous stresses by almost an order of magnitude but still can be, on average, 10% of the total wind stress for low to moderate wind forcing conditions. The wave-induced tangential viscous stress supports about 17%, 10%, and 7% of the total wind stress for wind speeds of 2.25 m s^{-1}, 5.08 m s^{-1}, and 9.57 m s^{-1}, respectively. It is, however, trivial for higher wind speeds. The wave-induced tangential viscous stress, in fact, represents viscous forces due to the wave motion and equals the rate of momentum loss of waves through the viscosity.

The streamwise-averaged profiles of wave-induced viscous stresses are next plotted in Fig. 6.6a as a function of dimensionless wave viscous layer height, i.e., $\zeta^{\omega} = \zeta\sqrt{\omega/\nu}$, on a logarithmic scale as we are interested in small scale processes very close to the water interface. Here, all the profiles are appropriately normalized by the orbital velocities $\rho(a\omega)^2$ where ω is the angular frequency and $\omega^2 = gk$ is the dispersion relationship for propagating deep water waves. It can be observed that the (streamwise-averaged) wave tangential stress decreases with wind speed; it was $\overline{|\tilde{\tau}_{13}|}/\rho(a\omega)^2 = 1.03$ for wind speed of $U_{10} = 2.25$ m s^{-1} and reduced to approximately $\overline{|\tilde{\tau}_{13}|}/\rho(a\omega)^2 = 0.3$ for the wind speed of $U_{10} = 16.59$ m s^{-1}. The wave-induced viscous stress remains significant up to a height of about $\zeta^{\omega} = 1$ for all experimental conditions, even the highest wind speed cases, and then falls to zero farther outside the wave viscous layer. As for the viscous tangential stress, close to the surface, the streamwise-averaged wave tangential stresses are nearly constant, showing a constant behavior in the wave

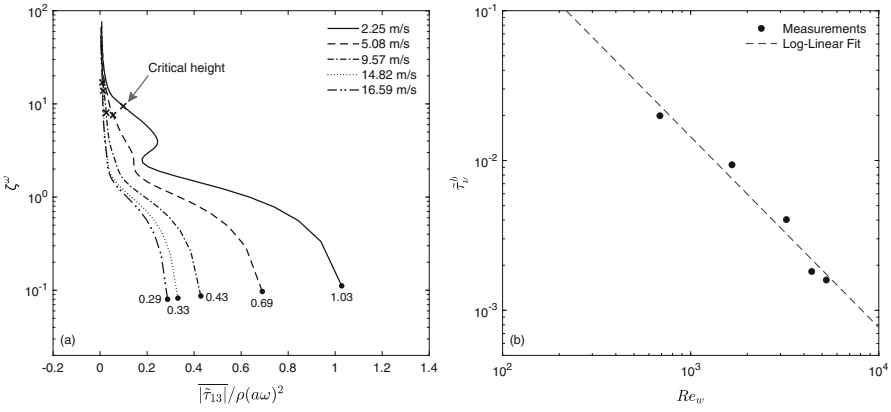

Fig. 6.6 (**a**) Vertical profiles of the streamwise-averaged wave-induced viscous stress, i.e., $\overline{|\tilde{\tau}_{13}|}$ where $|\tilde{\tau}_{13}|$ is the absolute value, plotted against the height of the wave viscous, i.e., $\zeta^{\omega} = \zeta\sqrt{\omega/\nu}$, on a logarithmic scale for all wind speed cases. Note that these stress profiles are normalized by $\rho(a\omega)^2$. The cross symbols are the height of the critical layer. (**b**) Height-integrated wave-induced viscous stress $\tilde{\tau}_{\nu}^{b}$ (defined in Eq. 6.13) as a function of wave Reynolds number, i.e., $Re_w = \omega/\nu k^2$. The dashed line shows $\tilde{\tau}_{\nu}^{b} \propto (Re_w)^{-1.3}$ (or $\tilde{\tau}_{\nu}^{b} \propto (a_p k_p)^{-1.85}$)

boundary layer. This is somewhat unexpected since, in theory, there should be some weak shear in the wave-coherent velocity fields near the interface. The height-integrated of the streamwise-averaged wave-induced viscous stress profiles (i.e., bulk representation) are also defined as,

$$\tilde{\tau}_{\nu}^{b} = \frac{k_p}{\rho u_*^2} \int_0^1 \overline{|\tilde{\tau}_{13}|}\, d\zeta \tag{6.13}$$

and shown in Fig. 6.6b against the wave Reynolds number $Re_w = \omega/\nu k^2$. The height-integrated wave-induced viscous stress represents the average contribution of the wave-induced viscous stress to the total wind stress. The height-integrated contribution of wave-induced viscous stress decreases with the wave Reynolds number, or equivalently, wind speed. This observed trend is consistent with the variations of the height-integrated tangential viscous stress (see Fig. 6.4b).

Finally, in Fig. 6.7, we show along-wave surface distributions of the wave-induced viscous stress for all experimental conditions. These near-surface data were calculated by taking averages within the viscous sublayer and normalized by

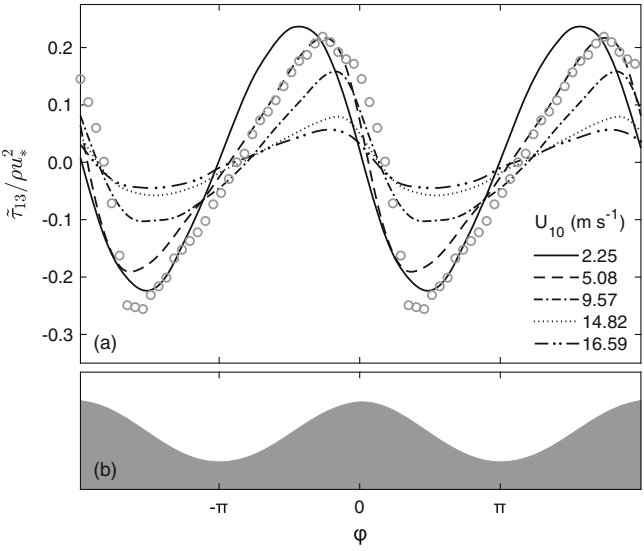

Fig. 6.7 (**a**) Along-wave surface profiles of the wave-induced viscous stress (whiten the viscous sublayer) normalized by the total wind stress ρu_*^2 for all experimental conditions. The results of Banner and Peirson (1998), which is for $U_{10} = 12.8$ m s^{-1} and fetch of 4.35 m, are also shown by circle symbols for comparison. It should be noted here that no reliable data could be collected by Banner and Peirson (1998) for some locations along the leeward side of the waves such as the spilling regions and trough regions, and thus, the data are interpolated for the leeward side of the waves. The bottom of the figure (*panel b*) shows a sketch of the mean wave profile to visualize the wave phase

the total wind stress. For comparison, the data from Banner and Peirson (1998) for $U_{10} = 12.8$ m s^{-1} at a fetch of 4.35 m are also shown with grey circles. The wave-induced viscous stress is compiled from Banner and Peirson (1998) data by subtracting the mean tangential stress from phase-averaged fields, so that $\tilde{\tau}_{13} = \langle \tau_{13} \rangle - \bar{\tau}_{13}$. It should be noted here that no reliable data could be collected by Banner and Peirson (1998) for locations along the leeward side of the waves such as the spilling and trough regions, and thus, they interpolated their data for the leeward side of the waves. It can be observed from Fig. 6.7 that the wave-induced tangential stresses, on average, exhibits important along-wave variations in all wind forcing conditions. In all cases, the wave-induced tangential stress data indicate a peak upwind of the wave crest ($\varphi \sim -\pi/4$) and a dip at approximately the middle of the leeward face of waves ($\varphi \sim \pi/2$). This is in complete agreement with the measurements of Banner and Peirson (1998) for microscale breaking wind waves. As wind speed increases, the peak value of the normalized wave viscous stress decreases from 0.24 for $U_{10} = 2.25$ m s^{-1} to 0.06 for $U_{10} = 16.59$ m s^{-1}, while the minimum value increases from -0.22 for $U_{10} = 2.25$ m s^{-1} to -0.04 for $U_{10} = 16.59$ m s^{-1}.

6.5 Conclusions

In this paper, we presented high-resolution viscous tangential measurements in the airflow above wind-generated surface waves within the viscous sublayer for different wind-wave conditions at a fetch of 22.7 m and with a range of 10-m wind speed varying from 2.25 to 16.59 m s^{-1}. To this end, two-dimensional velocity fields in the turbulent airflow above the waves were acquired in the laboratory using a combination of PIV and LIF techniques. Upon separating the mean, wave-coherent, and turbulence motions, we were further able to examine the mean and wave phase-coherent tangential viscous stress fields separately.

The surface waves are inducing a phase-locked variability in the viscous stress. As a general trend, the phase-averaged distribution of the viscous stress forms a pattern of along-wave asymmetry near the surface; it is highest on the upwind face of wave crest with its peak value close to the wave crest and its minimum about the middle of the leeward side of waves. Although the contribution of the viscous stress to the total momentum flux decreases with increasing wind speed, it is not negligible for low to moderate wind speeds. Close to the water interface, the mean tangential stress supported more than 90% of the wind stress for the low wind speed of $U_{10} = 2.25$ m s^{-1} and remained considerable up to a dimensionless height of $\zeta^+ = 10$ with approximately a 40% contribution to the total wind stress. With increasing wind speed, the surface contribution, however, reduced (exponentially) to almost 60% and 35% of the total stress for wind speeds of $U_{10} = 5.08$ m s^{-1} and $U_{10} = 9.57$ m s^{-1}, respectively. The viscous stress is always a non-zero fraction of the total momentum flux, even for strong wind forcing conditions.

Close to the surface, the phase-averaged distributions of the wave-induced tangential stress are positive (negative) upwind (downwind) side of wave crests below the critical height with their positive and negative extrema located about the middle of the windward and leeward face of the waves. Farther above the surface, this positive-negative pattern in the wave viscous stress is substantially shifted in the downstream direction above the critical height. Moreover, the wave-induced viscous stress quickly reduces to a zero value away from the surface. The streamwise-averaged profiles of wave-induced tangential stress are also shown to be mainly constrained in the vicinity of the water surface, and consistent with the mean viscous stress, their magnitude decreases as wind speed increases. In general, the wave-induced viscous stresses are smaller than the mean viscous stresses by almost an order of magnitude, but still can be on average 10% of the total wind stress for low to moderate wind speeds; it was about 17%, 10%, and 7% of the total wind stress for wind speeds of $U_{10} = 2.25$ m s^{-1}, $U_{10} = 5.08$ m s^{-1}, and $U_{10} = 9.57$ m s^{-1}, respectively.

Overall, mean tangential and wave-coherent viscous stresses carry a substantial fraction of the total air-sea stress, particularly at low wind speeds. Thus, we postulate that the viscous tangential stress in the airflow at the interface is likely to be an integral part of the wave generation process, but detailed experiments, simulations, and theoretical investigations of the early stages of the wind-wave generation mechanisms are still needed.

Acknowledgements We wish to sincerely thank Ed Monahan for inviting us to participate, with this modest contribution, in the Festschrift celebrating his 83rd birthday. Ed has had a long, remarkable, and distinguished career, greatly influencing the field of air-sea interaction, and providing landmark contributions on many challenging problems through innovative ideas and keen physical interpretations. In particular, he is probably most well-known for his seminal work on white cap coverage, and on the generation of sea spray. His work has had indeed a profound influence on the field, opening new research avenues, and inspiring generations of scientists. We are truly honored to be invited to celebrate Ed's birthday. Ed, we wish you a happy birthday!

This research was supported by the National Science Foundation (NSF) through grant numbers OCE 0748767, OCE-1458977, and OCE-1634051.

References

Banner, M. L., & Peirson, W. L. (1998). Tangential stress beneath wind-driven air-water interfaces. *Journal of Fluid Mechanics, 364*, 115–145.

Bopp, M. (2018). *Air-flow and stress partitioning over wind waves in a linear wind-wave facility* (Doctoral dissertation), Heidelberg: Heidelberg University.

Buckley, M. P., (2015). *Structure of the airflow above surface waves*. (Doctoral dissertation), Newark: University of Delaware.

Buckley, M. P., & Veron, F. (2016). Structure of the airflow above surface waves. *Journal of Physical Oceanography, 46*(5), 1377–1397.

Buckley, M. P., & Veron, F. (2017). Airflow measurements at a wavy air–water interface using PIV and LIF. *Experiments in Fluids, 58*(11), 161.

Buckley, M. P., & Veron, F. (2019). The turbulent airflow over wind generated surface waves. *European Journal of Mechanics - B/Fluids, 73*, 132–143.

Csanady, G. (1985). Air-sea momentum transfer by means of short-crested wavelets. *Journal of Physical Oceanography, 15*(11), 1486–1501.

Csanady, G. (1990). Momentum flux in breaking wavelets. *Journal of Geophysical Research: Oceans, 95*(C8), 13289–13299.

Gent, P. R., & Taylor, P. A. (1976). A numerical model of the air flow above water waves. *Journal of Fluid Mechanics, 77*, 105–128.

Gent, P. R., & Taylor, P. A. (1977). A note on separation over short wind waves. *Boundary-Layer Meteorology, 11*(1), 65–87.

Grare, L., Lenain, L., & Melville, W. K. (2013a). Wave-coherent airflow and critical layers over ocean waves. *Journal of Physical Oceanography, 43*(10), 2156–2172.

Grare, L., Peirson, W. L., Branger, H., Walker, J. W., Giovanangeli, J. P., & Makin, V. (2013b). Growth and dissipation of wind-forced, deep-water waves. *Journal of Fluid Mechanics, 722*, 5–50.

Hara, T., & Belcher, S. E. (2004). Wind profile and drag coefficient over mature ocean surface wave spectra. *Journal of Physical Oceanography, 34*(11), 2345–2358.

Hara, T., & Sullivan, P. P. (2015). Wave boundary layer turbulence over surface waves in a strongly forced condition. *Journal of Physical Oceanography, 45*(3), 868–883.

Hsu, C. T., Hsu, E. Y., & Street, R. L. (1981). On the structure of turbulent flow over a progressive water wave: Theory and experiment in a transformed, wave-following coordinate system. *Journal of Fluid Mechanics, 105*, 87–117.

Hussain, A. K. M. F., & Reynolds, W. C. (1970). The mechanics of an organized wave in turbulent shear flow. *Journal of Fluid Mechanics, 41*, 241–258.

Husain, N. T., Hara, T., Buckley, M. P., Yousefi, K., Veron, F., & Sullivan, P. P. (2019). Boundary layer turbulence over surface waves in a strongly forced condition: LES and observation. *Journal of Physical Oceanography, 49*(8), 1997–2015.

Kawamura, H., & Toba, Y. (1988). Ordered motion in the turbulent boundary layer over wind waves. *Journal of Fluid Mechanics, 197*, 105–138.

Kihara, N., Hanazaki, H., Mizuya, T., & Ueda, H. (2007). Relationship between airflow at the critical height and momentum transfer to the traveling waves. *Physics of Fluids, 19*(1), 015102.

Kudryavtsev, V. N., & Makin, V. K. (2001). The impact of air-flow separation on the drag of the sea surface. *Boundary-Layer Meteorology, 98*(1), 155–171.

Longuet-Higgins, M. S. (1969). Action of a variable stress at the surface of water waves. *Physics of Fluids, 12*(4), 737–740.

McLeish, W., & Putland, G. E. (1975). Measurements of wind-driven flow profiles in the top millimeter of water. *Journal of Physical Oceanography, 5*(3), 516–518.

Okuda, K., Kawai, S., & Toba, Y. (1977). Measurement of skin friction distribution along the surface of wind waves. *Journal of Oceanography, 33*(4), 190–198.

Peirson, W. L. (1997). Measurement of surface velocities and shears at a wavy air–water interface using particle image velocimetry. *Experiments in Fluids, 23*(5), 427–437.

Peirson, W. L., & Banner, M. L. (2003). Aqueous surface layer flows induced by microscale breaking wind waves. *Journal of Fluid Mechanics, 479*, 1–38.

Peirson, W. L., Walker, J. W., & Banner, M. L. (2014). On the microphysical behavior of wind-forced water surfaces and consequent re-aeration. *Journal of Fluid Mechanics., 743*, 399–447.

Phillips, O. M. (1977). *The dynamics of the upper ocean* (2nd ed.). Cambridge/London/New York/Melbourne: Cambridge University Press.

Reul, N., Branger, H., & Giovanangeli, J. P. (2008). Air flow structure over short-gravity breaking water waves. *Boundary-Layer Meteorology, 126*(3), 477–505.

Reynolds, W. C., & Hussain, A. K. M. F. (1972). The mechanics of an organized wave in turbulent shear flow. Part 3. Theoretical models and comparisons with experiments. *Journal of Fluid Mechanics, 54*, 263–288.

Shen, L., Zhang, X., Yue, D. K. P., & Triantafyllou, M. S. (2003). Turbulent flow over a flexible wall undergoing a streamwise travelling wave motion. *Journal of Fluid Mechanics, 484*, 197–221.

Sullivan, P. P., McWilliams, J. C., & Moeng, C. H. (2000). Simulation of turbulent flow over idealized water waves. *Journal of Fluid Mechanics, 404*, 47–85.

Thomas, M., Misra, S., Kambhamettu, C., & Kirby, J. T. (2005). A robust motion estimation algorithm for PIV. *Measurement Science and Technology, 16*(3), 865.

Veron, F., Saxena, G., & Misra, S. K. (2007). Measurements of the viscous tangential stress in the airflow above wind waves. *Geophysical Research Letters, 34*(19), L19603.

Yang, D. I., & Shen, L. (2010). Direct-simulation-based study of turbulent flow over various waving boundaries. *Journal of Fluid Mechanics, 650*, 131–180.

Part II
Whitecaps and Gas Transfer

Chapter 7
The Role of Physical Chemical Properties of Gases in Whitecap Facilitated Gas Transfer

Penny Vlahos and Edward C. Monahan

Abstract Air-sea gas exchange is one of the most important processes that controls both biogeochemical cycles and the earth's climate. The need to accurately quantifying gas exchange under the range of temperatures, wind speeds and gases has been recognized as a priority over the last three decades and parameterizations have improved over this period. To date however, there remains a concern of applying parameterizations tuned to a subset of gases broadly to many gases. Here we present some of the physical chemical differences across gases that when considered could lead to better gas flux estimates and improve the margins of error in air-sea gas exchange.

7.1 Introduction

The ocean-atmosphere boundary layer has a crucial role in regulating earth's climate, however currently, global climate models are unable to capture many key physical and chemical processes in the ocean-atmospheric system (Rosenfeld et al. 2014). Significant improvements have been made over the last 30 years though much work is still needed to shift from empirically to theoretically based models.

Gas transfer across the air-sea interface is proportional to the concentration gradient of a gas i in air (C_{ia}) and water (C_{iw}) and a transfer velocity k

$$F = k\Delta C_{iaw} \tag{7.1}$$

The transfer velocity depends on the gas in question, the media it is moving through and the thickness of the boundary layer. The exact expression for k has case specific forms that include

P. Vlahos (✉) · E. C. Monahan
Department of Marine Sciences, University of Connecticut, Mansfield, USA
e-mail: Penny.vlahos@uconn.edu

P. Vlahos (ed.), *Recent Advances in the Study of Oceanic Whitecaps*,
https://doi.org/10.1007/978-3-030-36371-0_7

$$k = D_i/z \tag{7.2}$$

the diffusion coefficient of i in water D_i and boundary layer thickness z which applies well to continuous quiescent (flat) interfaces where wind speeds (u) are <3 m/s. The most commonly used expression in air-ocean transfer is based on a k that is proportional to the water-side friction velocity u_* and the dimensionless Schmidt number $Sc = \nu/ D_i$ where ν is the kinematic viscosity of water wherein

$$k = u * Sc^{-n} \tag{7.3}$$

In this expression the exponent n depends on the sea state where n = 2/3 for a continuous but wavy water surface and n = 1/2 for a discontinuous rough surface.

By rearranging these expressions for k we find that

$$z = Di^{(1-n)}v^n/u* \tag{7.4}$$

and therefore u_* and z are inversely proportional. The values for D_i and ν are based on certain assumptions, that is, for a given temperature and pressure, assuming ideal solutions where i is the gas and w is a homogeneous solution of water (or seawater) and i and w do not interact with one another.

Over the past century investigators have modeled gas exchange in both experimental and field settings and have produced several versions of Eq. 7.3 such that

$$k = \alpha U^b \tag{7.5}$$

The values for a and b are usually derived from direct observation of a specific gas and the Sc number is absorbed in the proportionality constant α (Table 7.1).

Table 7.1 Frequently cited parameterizations that have been applied to gas exchange studies over the last 40 years (U_{10} is the wind speed or wind speed equivalent, measured 10 m above the sea surface)

	Parameterization k(cmh^{-1})	Gases	Source
Freshwater	$k = 0.36(4.1 + 0.417\ U^2_{10})^{0.5}U_{10}$	CO_2	Kanwisher (1963)
Freshwater	$k = 0.63(6.1 + 0.63\ U_{10})^{0.5}U_{10}$	O_2	Mackay and Yeun (1983)
Seawater	$k = 0.17\ U_{10}$ if $U_{10} < 3.6\ ms^{-1}$ $k = 2.85\ U_{10}–9.65$ if $3.6 < U_{10} < 13\ ms^{-1}$ $k = 5.9\ U_{10}–49.3$ if $U_{10} > 13\ ms^{-1}$	CO_2	Liss and Merlivat (1986)
Freshwater	$k = 1.024^{(Tw-10C)}(4.2 \times 10^{-6}\ U_{10}^{0.5})$ if $U_{10} < 5.5\ ms^{-1}$ $k = 1.024^{(Tw-10C)}(0.32 \times 10^{-6}\ U_{10}^2)$ if $U_{10} > 5.5\ ms^{-1}$	O_2	Banks (1975)
Seawater	$k = 0.31\ U_{10}^2(Sc/660)^{-1/2}$	CO_2	Wanninkhof (1992)
Seawater	$k = (0.029\ U_{10}^3 + 5.4)(660/Sc)^{0.5}$	CO_2	Edson (2011)
Seawater	$k = 0.251\ U_{10}^2(Sc/660)^{-1/2}$	CO_2	Wanninkhof (2014)

Generally, these dependencies have evolved from lab to field-based concentration gradients to eddy diffusivity methods (Fairall et al. 2000) and will continue to evolve with improved higher resolution measurements as they emerge. What is evident in these parameterizations is that they are primarily governed by the physical field (wind speed) and chemical differences among diffusing gases are absorbed in parameterization constants.

7.2 Chemical Properties

Investigators have long recognized that utilizing parameterizations derived for specific gases does not account for chemical enhancement effects including the direct reaction of ammonia and carbon dioxide gases with water to produce ammonium and carbonic acid (Johnson 2010). These chemical reactions should be considered on an individual gas basis. There are also physical-chemical differences among gases that may impact their air-water gas exchange relative to other gases. Some of these include:

7.2.1 Size and Geometry

The larger the molecule, the larger the diffusional cross section and therefore the more water or air that needs to be displaced. This is largely accounted for in D_i. The geometry of a molecule greatly impacts it effective radius as it diffuses and the more irregular the geometry, the more orientation can impact exchange and is less constrained in D_i. Table 7.2 summarizes a representative list of diffusion coefficients for common gases in seawater.

Table 7.2 Diffusion coefficients for common gases in water at 25 °C in seawater

Gas	Molecular weight (g/mol)	Approximate diameter (10^{-10}m)	$D_i(cm^2s^{-1})$	Source
He	4.002	0.62	8.03×10^{-5}	Jahne et al. (1987)
H_2	2.016	1.24	4.91×10^{-5}	Jahne et al. (1987)
N_2	14.01	2.38	2.00×10^{-5}	Jahne et al. (1987)
O_2	32.00	2.28	2.42×10^{-5}	Jahne et al. (1987)
Ar	39.95	2.00	2.50×10^{-5}	Jahne et al. (1987)
CO_2	44.01	2.36	1.91×10^{-5}	Zeebe et al. (2011)
DMS	62.13	3.08	1.34×10^{-5}	Saltzman et al. (1993)

7.2.2 Polarity

Whether a molecule is polar, non-polar or as is often the case amphiphilic (has both polar and non-polar parts) will have significant impact on its mobility in water. Polar-molecules may interact with surrounding water molecules and ions and therefore do not acting as an "ideal" non-interacting mixture would assume. Non-polar molecules are less interactive with their surrounding media but require more energy to be dissolved in water and displace existing hydrogen bonds between water molecules. Often these molecules tend to seek "lower" energy environments such as the air sea boundary layer where fewer water molecules require displacement.

7.2.3 Solubility & Vapor Pressure

Similarly, solubility is extremely important in air water exchange. Gases that are highly soluble will tend to remain in solution and less likely to move into air whereas gases that are less soluble will tend to seek a phase where less energy is required to accommodate it. Each gas has a unique solubility dependence in water with respect to changes in temperature and salinity and this is well described in Wanninkhof (1992) for several common gases.

7.2.4 Henry's Law Constant

Ultimately it is the ratio of preference in air to preference in water (vapor pressure/solubility) that determines a gas's likelihood to remain in or evade bulk seawater. For example, a substance may have both low solubility and low vapor pressure but the ratio of the two determines the relative preferred state. Table 7.3 summarizes these parameters for common gases at 25 °C. Note, all of these gases have very low solubilities relative to vapor pressure and therefore encounter the majority of their resistence to air-sea gas transfer in the water phase. These gases are "water-side controlled".

Table 7.3 Henry's Law Constants for common gases at 25 °C (Sander 2015)

Gas	$K_H(mol/(m^3Pa))$
H_2	7.7×10^{-6}
O_2	1.3×10^{-5}
N_2	6.4×10^{-6}
CO_2	3.4×10^{-5}
He	3.8×10^{-6}
Ar	1.4×10^{-5}

7.3 The Altered Sea State

At high wind speeds (ie >15 m/s) the sea state is altered sufficiently that there is a regular discontinuity in the surface resulting in whitecaps and bubbles and a surface ocean that has a corresponding steady state concentration of bubbles, particularly in the top 10 m. These discontinuities markedly increase the air-water surface area through both bubbles on the water side and sea spray on the air side. The extent of surface area of the air-water interface has been constrained as both a bubble surface area (Vlahos and Monahan, 2009) and sea spray surface area (Monahan et al. 2017). The increase in the air water boundary layer can be estimated by Eq. 7.6 for entrained bubbles (Φ_B).

$$\Phi_B = 0.090 \times (U_{10}/10)^3 \qquad \text{in } m^2 \text{per } m^2 \text{sea surface} \qquad (7.6)$$

At a given wind speed (U_{10}, ms^{-1}), the total air-water surface area added by bubbles is Φ_B. Therefore the at wind speeds of 10 ms^{-1}, average aggregate bubble area beneath a square meter of sea surface is estimated to be 0.090 m^2 and the total air-water surface area is 1.09 m^2. At wind speeds of 18 ms^{-1} Φ_B is 0.52 and the air-water boundary surface area beneath 1 m^2 of ocean surface reaches 52%. The total air-water surface area A becomes 1 + 0.52 or 1.52 m^2 per m^2 sea surface. Therefore it is at high wind speeds where data is curently severley lacking, that these phenomena are expected to become significant.

Vlahos and Monahan (2009) argue that this altered sea state (>18 ms^{-1}) significantly changes the effective solubility of a dissolved compound, particularly if it is bipolar or amphiphilic and is likely to adhere to, and be more impacted by, the air-water interface (Fig. 7.1). To account for this influence on gas exchange they

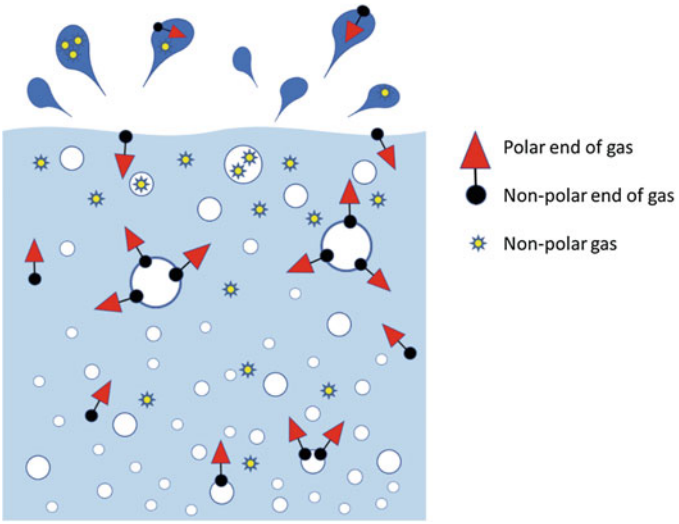

Fig. 7.1 Schematic of how bubbles and sea spray extent the air-water boundary layer and offer an extended interface for molecules to diffuse through and adsorb to

suggest using an effective solubility that considers sorption to the interface. Therefore, for surface active gases this alters the apparent solubility and would attenuate gas exchange (see eqs. 11 and 12 in Vlahos and Monahan (2009)). This shift in gas exchange would be as long lived as the sustained wind events.

Sea spray surface area is a secondary process that extents the air-sea boundary layer which becomes significant above 15 ms^{-1} as is inferred from Fig. 2 in Monahan et al. (2017). See in particular the curve on this figure derived from Anguelova et al. (2019). The volume fluxes of sea spray are reasonably constrained in terms of winds speed however the actual surface area of the droplets is dependent on the time aloft and net evaporation that may occur (primarily driven by relative humidity) and more work is needed to establish a relationship for sea spray that is equivalent to Eq. 7.6. The role of sea spray in gas transfer is expended upon in Chap. 9 by Staniec et al.

In addition to the formation of entrained air and spray, it is also important to know the actual residence time of these phenomena in order to properly constrain their impact.

7.4 NOAA COARE Model

The Coupled Ocean-Atmosphere Response Experiment (COARE) (Fairall et al. 2011) is one of the most comprehensive gas exchange models to date and has been tuned to 79 gases. The algorithm has high accuracy between wind speeds of 2-18 ms^{-1} and is less certain at higher windspeeds primarily due to a lack of field data. The algorithm includes bubble driven transfer from Woolf (1997) though sea spray is not currently included. The model is based on CO_2 parameterizations but has been extended to include reactive species in eq. 18 of Fairall et al. (2011) and chemical parameterizations of Johnson (2010) and Rowe et al. (2011) that consider gas solubility and diffusivities. Though these inclusions present an important first step in improving gas specific gas transfer rates, there remains a need to consider polarity and surface activity (i.e. an affinity for interfaces), particularly for volatile organic compounds, which changes the effective solubility of a molecule in turbulent bubble containing waters (Vlahos and Monahan 2009).

7.5 Field Data

Field studies have compared CO_2 (non-polar) and DMS (polar) gas exchange in several regions. Bell et al. (2013) performed measurements in the North Atlantic and found that although DMS transfer velocities varied linearly with wind speed up to 11 ms^{-1}, at high wind speeds fluxes were lower than predicted and the linear relationship failed. Interestingly, the heat transfer coefficient did not have this trend but rather continued to increase linearly. The authors attribute this to the

interfacial control of DMS gas transfer. Figure 7.2 below appears as Figures 3 and 7 in Bell et al. (2013) and shows that DMS fluxes diverge most under conditions of high significant wave height and % whitecap coverage (a proxy for bubbles). The figures also show significant departures between CO_2 and DMS at high wind speeds (Fig. 7.2c) and clear consensus across DMS studies (Fig. 7.2d).

In the Southern Ocean Yang et al. (2011) also found lower transfer velocities for DMS than those predicted and reported in warmer regions. The authors found that normalizing to temperature could account for some of these regional differences though this was not pronounced for other gases such as CO_2. Here too the increased solubility of DMS was considered the primary factor controlling this attenuation of

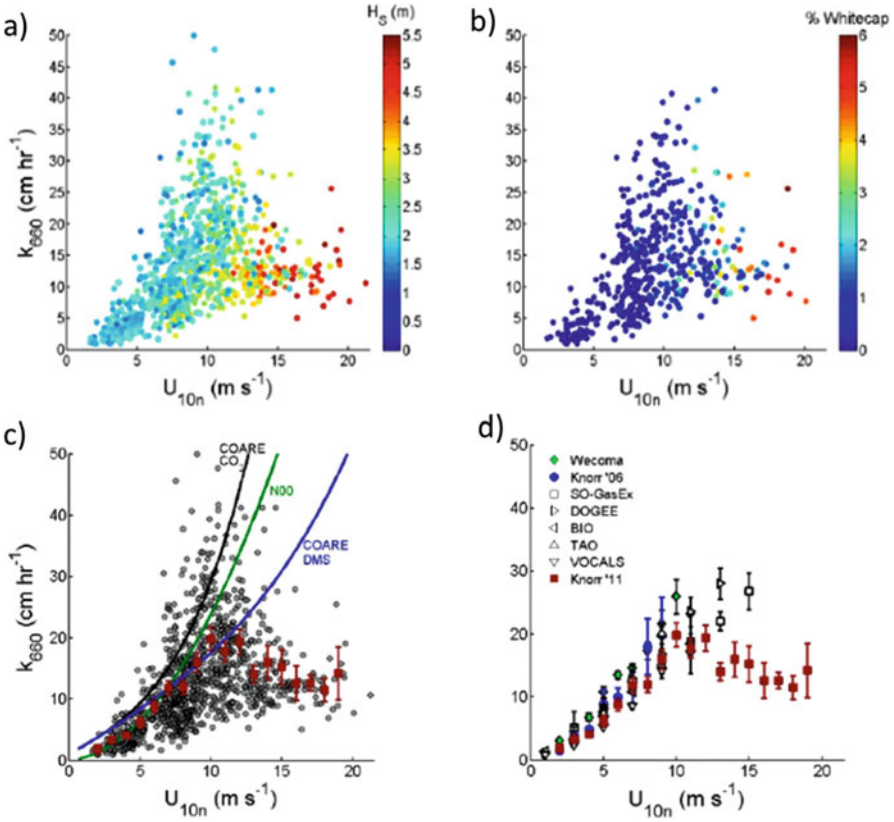

Fig. 7.2 From Bell et al. (2013): Gas transfer coefficient of DMS plotted as a function of wind speed (**a**) symbol color indicates significant wave height (**b**) color indicates % whitecap coverage (**c**) mean DMS transfer coefficients (red squares) and ± std. error compared to predicted values using NOAA COARE model for CO_2, DMS and the Nightingale et al. (2000) parameterization (NOO) (**d**) average transfer coefficients across other DMS eddy covariance methods (Wecoma – Marandino et al. 2007; Knorr_06 – Marandino et al. 2008; SO-Gas-Ex – Yang et al. 2011; DOGEE – Huebert et al. 2010; BIO – Blomquist et al. 2006; TAO – Huebert et al. 2004; VOCALS – Yang et al. 2011)

DMS gas exchange. This regional difference is consistent with white capping and therefore bubble plume differences in colder versus warmer latitudes at a given wind speed, addressed in Chap. 4 of this book.

Finally, satellite-based retrievals of air-sea gas transfer velocities are emerging and offer promise for capturing remote and high wind gas exchange. Frew et al. (2007) developed a scatterometer-based algorithm from QuikSCAT normalized radar backscatter to estimate gas transfer velocity via remotely sensed sea surface roughness. Goddijn-Murphy et al. (2012) compared satellite altimeter backscattering with eddy covariance measurements taken in the field to predict DMS gas transfer. Their results were comparable to those obtained from wind speed over the wind ranges studied. It is reasonable to expect that these remote sensing applications will lead to advances in air sea gas exchange.

7.6 Conclusions

As our sampling ability improves, so does our understanding of air sea gas exchange and the differences among gases. To date the most comprehensive model is the NOAA COARE model in its most recent form as described above. It is likely that over the next two decades, highly resolved measurements will lead to gas exchange parameterizations that are based on physical-chemical properties of gases. In addition, the role of sea spray and other turbulent phenomena at high wind speeds should be prioritized as these are currently not well constrained and observations are severely lacking.

Acknowledgements The authors would like to acknowledge funding from the National Science Foundation grant numbers 1356541 and 1630846.

References

Anguelova, M., Barber, R. P., Jr., & Wu, J. (2019). Spume drops produced by the wind tearing of wave crests. *Journal of Physical Oceanography, 29*, 1156–1165.

Banks, R. B. (1975). Some features on wind action on shallow lakes. *Proceedings of the American Society of Civil Engineers, 101*, 813.

Bell, T., Bruyn, W., Miller, S., Ward, B., Christensen, K., & Saltzman, E. (2013). Air/sea DMS gas transfer in the North Atlantic: Evidence for limited interfacial gas exchange at high wind speed. *Atmospheric Chemistry and Physics, 13*, 11073–11087. https://doi.org/10.5194/acp-13-11073-2013.

Blomquist, B. W., Fairall, C. W., Huebert, B. J., Kieber, D. J., & Westby, G. R. (2006). DMS Sea-air transfer velocity: Direct measurements by eddy covariance and parameterization based on the NOAA/COARE gas transfer model. *Geophysical Research Letters, 33*, L07601. https://doi.org/10.1029/2006gl025735.

Edson, J., Fairall, C., Bariteau, L., Zappa, C., Cifuentes-Lorenzen, A., McGillis, W. M., Pezoa, S., Hare, J., & Helmig, D. (2011). Eddy-covariance measurement of CO2 gas transfer velocity

during the 2008 Southern Ocean gas exchange experiment: Wind speed dependency. *Journal of Geophysical Research, 161*. https://doi.org/10.1029/2011JC007022.

Fairall, C. W., Hare, J. E., Edson, J. B., & McGillis, W. (2000). Parameterization and micrometeorological measurements of air-sea gas transfer. *Boundary-Layer Meteorology, 96*, 63–106. https://doi.org/10.1023/A:1002662826020.

Fairall, C. W., Yang, M., Bariteau, L., Edson, J. B., Helmig, D., McGillis, W., Pezoa, S., Hare, J. E., Huebert, B., & Blomquist, B. (2011). Implementation of the coupled ocean-atmosphere response experiment flux algorithm with CO2, dimethyl sulfide, and O3. *Journal of Geophysical Research, 116*, C00F09. https://doi.org/10.1029/2010JC006884.

Frew, N. M., Glover, D. M., Bock, E. J., & McCue, S. J. (2007). A new approach to estimation of global air-sea gas transfer velocity fields using dual-frequency altimeter backscatter. *Journal of Geophysical Research, 112*, C11003. https://doi.org/10.1029/2006JC003819.

Goddijn-Murphy, L., Woolf, D. K., & Marandino, C. (2012). Space-based retrievals of air-sea gas transfer velocities using altimeters: Calibration for dimethyl sulfide. *Journal of Geophysical Research, 117*, C08028. https://doi.org/10.1029/2011JC007535.

Huebert, B. J., Blomquist, B. W., Hare, J. E., Fairall, C. W., Johnson, J. E., & Bates, T. S. (2004). Measurement of the sea-air DMS flux and transfer velocity using eddy correlation. *Geophysical Research Letters, 31*, L23113. https://doi.org/10.1029/2004GL021567.

Huebert, B. J., Blomquist, B. W., Yang, M. X., Archer, S. D., Nightingale, P. D., Yelland, M. J., Stephens, J., Pascal, R. W., & Moat, B. I. (2010). Linearity of DMS transfer coefficient with both friction velocity and wind speed in the moderate wind speed range. *Geophysical Research Letters, 37*, L01605. https://doi.org/10.1029/2009gl041203.

Jahne, B., Heinz, G., & Dietrich, W. (1987). Measurement of the diffusion coefficients of sparingly soluble gases in water. *Journal of Geophysical Research: Oceans, 92*, 10767–10776. https://doi.org/10.1029/JC092iC10p10767.

Johnson, M. T. (2010). A numerical scheme to calculate temperature and salinity dependent air-water transfer velocities for any gas. *Ocean Science, 6*, 913–932. https://doi.org/10.5194/os-6-913-2010.

Kanwisher, J. (1963). On the exchange of gases between the atmosphere and the sea. *Deep Sea Research, 10*, 195–207.

Liss, P. S., & Merlivat, L. (1986). Air-sea gas exchange rates: Introduction and synthesis. In P. Buat-Menard (Ed.), *The role of air-sea exchange geochemical cycling* (pp. 113–127). Dordrecht: D. Reidel.

Mackay, D., & Yeun, A. T. K. (1983). Mass transfer coefficients for volatilization of organic solutes from water. *Environmental Science & Technology, 17*, 211–233.

Marandino, C. A., De Bruyn, W. J., Miller, S. D., & Saltzman, E. S. (2007). Eddy correlation measurements of the air/sea flux of dimethylsulfide over the North Pacific Ocean. *Journal of Geophysical Research-Atmospheres, 112*, D03301. https://doi.org/10.1029/2006JD007293.

Monahan, E. C., Staniec, A., & Vlahos, P. (2017). Spume drops: Their potential role in Air-Sea gas exchange. *Journal of Geophysical Research-Oceans, 122*. https://doi.org/10.1002/2017JC013203.

Marandino, C. A., De Bruyn, W. J., Miller, S. D., & Saltzman, E. S. (2008). DMS air/sea flux and gas transfer coefficients from the North Atlantic summertime coccolithophore bloom. *Geophysical Research Letters, 35*, L23812. https://doi.org/10.1029/2006JD007293.

Nightingale, P. D., Malin, G., Law, C. S., Watson, A. J., Liddicoat, M. I., Boutin, J., Upstill-Goddard, R. C. (2000). In situ evaluation of air-sea gas exchange parameterizations using novel conservative and volatile tracers. *Global Biogeochemical Cycles, 14*(1), 373–387. https://doi.org/10.1029/1999GB900091.

Rosenfeld, D., Sherwood, S., Wood, R., & Donner, L. (2014). Climate effects of aerosol-cloud interactions. *Science, 343*, 379–380. https://doi.org/10.1126/science.1247490.

Rowe, M. D., Fairall, C. W., & Perlinger, J. A. (2011). Chemical sensor resolution requirements for near-surface measurements of turbulent fluxes. *Atmospheric Chemistry and Physics, 11*, 5263–5275. https://doi.org/10.5194/acp-11-52632011.

Saltzman, E. S., King, D. B., Holmen, K., & Leck, C. (1993). Experimental-determination of the diffusion-coefficient of Dimethylsulfide in water. *Journal of Geophysical Research Oceans, 98*, 16481–16486.

Sander, R. (2015). Compilation of Henry's law constants (version 4.0) for water as solvent. *Atmospheric Chemistry and Physics, 15*(8), 4399–4981. https://doi.org/10.5194/acp-15-4399-2015.

Vlahos, P., & Monahan, E. C. (2009). A generalized model for the air-sea transfer of dimethylsulfide at high wind speeds. *Geophysical Research Letters, 36*, L21605. https://doi.org/10.1029/2009GL0400695.

Wanninkhof, R. (1992). Relationship between gas exchange and wind speed over the ocean. *Journal of Geophysical Research, 97*, 7373–7381. https://doi.org/10.1029/92JC00188.

Wanninkhof, R. (2014). Relationship between wind speed and gas exchange over the ocean revisited. *Limnology and Oceanography-Methods, 12*, 351–362. https://doi.org/10.4319/lom.2014.12.351.

Woolf, D. K. (1997). Bubbles and their role in gas exchange. In P. S. Liss & R. A. Duce (Eds.), *The sea surface and global change* (pp. 173–206). Cambridge, U. K.: Cambridge University Press. https://doi.org/10.1017/CBO9780511525025.007.

Yang, M., Blomquist, B. W., Fairall, C. W., Archer, S. D., & Huebert, B. J. (2011). Air-sea exchange of dimethylsulfide in the Southern Ocean: Measurements from SO GasEx compared to temperate and tropical regions. *Journal of Geophysical Research-Oceans, 116*, C00F05. https://doi.org/10.1029/2010jc006526.

Zeebe, R. E. (2011). On the molecular diffusion coefficients of dissolved CO_2, HCO_3^- and CO_3^{2-}, and their dependence on isotopic mass. *Geochimica et Cosmochimica Acta, 75*(2011), 2483–2498. https://doi.org/10.1016/j.gca.2011.02.010.

Chapter 8
Studying the Role of Gas Bubbles on Air-Sea Gas Transfer Using Computer Models

Jun-Hong Liang

Abstract Oceanic gas bubbles, the building blocks of whitecaps, play important roles in air-sea gas transfer at moderate to high wind speed when wave breaking and bubble formation are frequent. This review focuses on the development of computer models, usually constrained by laboratory and field observation, to improve the qualitative and quantitative understanding of bubble-mediated air-sea gas transfer. The construction of bubble models, the coupling of bubble models with other ocean models, examples of their application and major findings from existing bubble modeling studies are discussed and summarized.

8.1 Introduction

Oceanic gas bubbles, visually identified as whitecap at the ocean surface because of their distinctly different optical property from seawater, influences the properties of both sides of the ocean-atmosphere interface. One of the disciplines that bubbles play an important role in is air-sea gas transfer. Air-sea gas transfer modulates dissolved gas concentration in the ocean surface mixed layer and the cycling of chemical elements between the ocean and the atmosphere (e.g., Hamme et al. 2019). Air-sea gas transfer at low wind speeds ($U_{10} < \sim 7$ m/s) is relatively well understood thanks to a series of theoretical (e.g., Liss and Slater 1974), laboratory (e.g., Broecker et al. 1978) and in situ studies (e.g., Wanninkhof et al. 1993; Asher 1997). The ocean under these wind speeds is unbroken though possibly wavy, and gases diffuse in and out of the ocean through the ocean-atmosphere interface. The gas transfer rate for this regime is proportional to wind speed. In contrast, air-sea gas exchange at moderate to extreme wind speeds ($U_{10} > \sim 7$ m/s) is more challenging to quantify. At these wind speeds, ocean surface gravity waves break and the breaking waves entrain air bubbles into the ocean (e.g., Monahan and Torgersen 1991; Farmer et al. 1993). Gas transfer occurs not only at the ocean surface, but also

J.-H. Liang (✉)
Department of Oceanography and Coastal Sciences & Center for Computation and Technology, Louisiana State University, Baton Rouge, LA, USA
e-mail: Jliang@lsu.edu

P. Vlahos (ed.), *Recent Advances in the Study of Oceanic Whitecaps*,
https://doi.org/10.1007/978-3-030-36371-0_8

between gas bubbles inside the ocean surface mixed layer and the surrounding water. The significance of gas bubbles in air-sea gas transfer generally increases with wind speed since wave breaking occurs more frequently and turbulence that traps bubbles becomes more energetic. Under hurricane winds, the contribution from bubbles is dominant (D'Asaro and McNeil 2007; McNeil and D'Asaro 2007). Bubbles contribute to the total air-sea gas flux for most gases in two ways (e.g., Woolf 1997): (1) the enhancement of the total gas transfer rate and (2) surface bubble-induced equilibrium supersaturation. Bubbles provide a pathway in addition to the ocean surface for air-sea gas transfer; gas transfer rate is, therefore, larger with bubbles than without bubbles. Gases can dissolve from bubbles at supersaturated conditions, caused by the surface tension and hydrostatic pressure on bubbles. Intuitively, gases can dissolve into water that is 200% saturated when a bubble is deeper than 10 m. When the total gas flux is zero, the surface ocean is supersaturated with surface outgassing balanced by interior dissolution through bubbles. For polar gases such as DMS that are more prone to stay at the bubble-water interface than the aqueous or gas phase alone, bubbles enhance their effective solubility (Vlahos and Monahan 2009; Vlahos et al. 2011). Besides directly transferring gases through their interface, bubbles also enhance surface transfer rate when they burst by disrupting the diffusive sublayer.

Mathematically, the total air-sea gas flux F, including the contribution from bubbles, is expressed as (e.g., Woolf 1997),

$$F = (k_s + k_b)[SP_{atm}(1 + \Delta_b) - C_w] \tag{8.1}$$

where k_s and k_b are the gas transfer rate at the ocean surface and bubble-water interface, respectively; S is gas solubility; P_{atm} is atmospheric pressure; Δ_b is bubble-induced equilibrium supersaturation defined as the relative deviation of dissolved gas concentration from saturation concentration due to bubbles; C_w is dissolved gas concentration. The bubble-enhanced gas transfer rate is either explicitly or implicitly in many widely used gas flux parameterizations (e.g., Wanninkhof et al. 2009; Fairall et al. 2011). Bubble-induced equilibrium supersaturation Δ_b, however, is not commonly included. Recently, the importance of Δ_b has been realized as saturation anomaly influences the estimate of other biogeochemical processes, such as biological production and denitrification, using dissolved gas measurements (e.g., Emerson and Bushinsky 2016; Nicholson et al. 2016). Quantification of Δ_b is very challenging as direct measurement of gas flux across bubble-water interface in the ocean is impossible. Currently, two approaches are used to estimate Δ_b. The first approach utilizes observations of the dissolved gas saturation anomaly (e.g., Stanley et al. 2009; Vagle et al. 2010). By subtracting the contribution to the gas saturation anomaly by processes other than bubbles, the effect by bubble-mediated gas flux is quantified. The second approach directly calculates the gas flux through bubbles using bubble fields. Quantitative observation of bubbles in the ocean surface boundary layer is very limited (e.g., Farmer et al. 1998), and it is particularly challenging at high wind speed when bubble-mediated gas transfer is important. The approach is therefore achieved by using calculated bubble fields, usually constrained by the

limited observations (e.g., Woolf and Thorpe 1991). This review focuses on the use of a computer model that generates subsurface bubble fields to derive bubble-mediated air-sea gas flux.

8.2 Bubble Modelling

8.2.1 Bubble Processes

A bubble model needs to simulate all important bubble processes that are reviewed in this subsection. The majority of gas bubbles form during the breaking of surface gravity waves, although they can also be generated by the impact of raindrops at the ocean surface, from seafloor gas vents, and through biological processes such as photosynthesis that releases gases. After their formation, gas bubbles rise due to their own buoyancy. At the same time, the energetic turbulent ocean surface boundary layer currents compete with the buoyancy of bubbles to keep them suspended in the water column. While in the water column, gas bubbles exchange gases with the surrounding water. They also change size when they exchange gas with the surrounding water and when they move up and down in the water column leading to the change in hydrostatic pressure. Large, fast-rising bubbles have a relatively short life in the water column and eventually burst at the ocean surface. Small, slow-rising bubbles are able to suspend in the water for a long period so that gases in them completely dissolve in the water. The fate of bubbles is important for the purpose of bubble-mediated air-sea gas transfer. Intuitively, the amount of gas dissolving from completely dissolved bubble equals to the amount of gases in those bubbles, while the amount gas dissolving from partially dissolved bubbles are controlled by a number of factors such as gas solubility, gas diffusivity, and the life span of those bubbles, in addition to the amount of gas in those bubbles. Theoretically, it can be shown that k_b is only determined by flux through the relatively large, partially dissolved bubbles, while Δ_b is controlled by flux through all bubbles including both the completely and partially dissolved bubbles (e.g., Liang et al. 2013) (Fig. 8.1).

8.2.2 Construction of a Bubble Model

There are two types of bubble models: an Eulerian bubble concentration model and a Lagrangian bubble model. In the Eulerian bubble concentration model, bubble concentrations at each spatial location (computational grids) are calculated. In a Lagrangian bubble model, a large amount of Lagrangian particles, each representing a certain number of actual bubbles, are traced. The two types of models are separately reviewed:

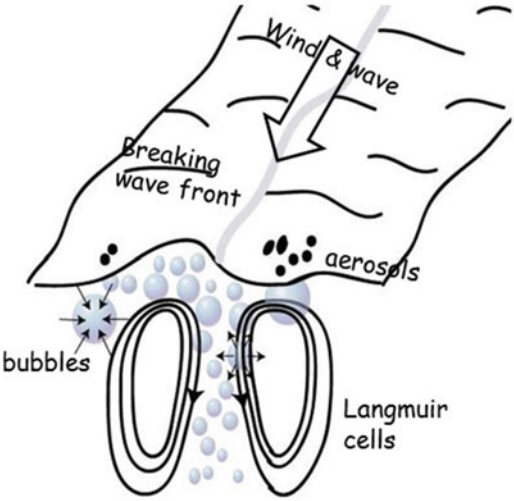

Fig. 8.1 A schematic showing processes related to oceanic bubbles

8.2.2.1 Eulerian Model

For the accurate calculation of gas flux through bubbles, bubble concentration field is modeled as,

$$\begin{aligned}\frac{\partial n_j(\mathbf{x}, r, t)}{dt} = & advection + diffusion \\ & + buoyant\ \ rising \\ & + gas\ exchange\ with\ \ surrounding\ water \\ & + bubble\ size\ change \\ & + bubble\ formation\ \ under\ breaking\ waves \\ & + bubble\ \ bursting\end{aligned} \tag{8.2}$$

where n_i is the concentration density of gas i in bubbles of radius r at spatial location $\mathbf{x}$ and time t. Bubble number density is diagnosed from n_i using the ideal gas law. The detailed mathematical expressions for the right-hand-side RHS terms can be found in Equations (1) to (5) in Liang et al. (2011). The first two terms, i.e., turbulent advection and diffusion, are based on fluid dynamical principles. The rest of the RHS terms related to bubble physics and dynamics come from many theoretical and experimental studies (e.g., Thorpe 1982; Lamarre and Melville 1991; Deane and Stokes 2002). The equation requires inputs of water velocity, dissolved gas concentrations in the surrounding water, and other parameters related to gases such as diffusivity and solubility.

There are here a couple of differences from bubble models used to study bubbles in the surf zone or in a laboratory flume (e.g., Shi et al. 2010). First, gas dissolution included in Eq. (8.2) is neglected in surf zone bubble models. It is shown in Liang

et al. (2012) that gas dissolution is the dominant factor shaping the distribution of bubbles in an oceanic surface boundary layer except very close to the surface where breaking waves actively entrain bubbles. Secondly, the amount of individual gases in bubbles is explicitly prognostic in Eq. (8.2) while bubble number density is modeled in surf zone bubble models. The gas fraction in bubbles dynamically evolves using Eq. (8.2). This is important to accurately diagnose gas flux through bubbles. Because different gases have different solubility, the fraction of a gas differs from the atmospheric fraction of the gases after bubble formation. It is demonstrated in Liang et al. (2012) that the averaged fraction of O_2 goes from approximately 0.21 at the surface to about 0.15 at 15 m depth under a 10-m wind speed of 20 m/s. Assuming a constant gas fraction based on atmospheric gas composition would lead to an underestimate of gas flux from the less soluble gas N_2 and overestimate of gas flux for more soluble O_2.

The biggest appeal of an Eulerian bubble model is the relatively straightforward coupling with a hydrodynamic model. Equation (8.2) can be discretized and solved in the same spatial computing grid as for the hydrodynamic model and n_j is conveniently added as an additional tracer in the model. There are a few limitations associated with the numerical solution of an Eulerian bubble model. First, Eq. (8.2) includes an advection term and its numerical solution cannot avoid the inherent, spurious diffusive (smoothing) and dispersive (oscillating) errors. Secondly, Eq. (8.2) has to be solved for different gas components in different size bins. For example, 3 gases and 200 size bins are used in Liang et al. (2011) to simulate bubbles under an individual breaking wave, implying that Eq. (8.2) is solved 600 times at each spatial location $\mathbf{x}$. Furthermore, when bubbles are simulated in the ocean surface boundary layer, the vertical extent of the computing grid has to be 2 to 3 times the boundary layer depth and is usually greater than 100 m although bubbles are only in the upper 10 or 20 m of the water column. In Liang et al. (2013), 2 gases and 17 size bins are used and the authors were able to carry out bubble flow simulations for about a half day. Finally, the separation of completely and partially dissolved bubbles is ambiguous in an Eulerian bubble model because we are not able to follow individual bubbles in an Eulerian bubble concentration model. Since the separation is crucial in a model for gas flux through bubbles based on first principles, the ratio of the two types of bubbles is diagnosed using the gas flux ratio in Liang et al. (2013).

8.2.2.2 Lagrangian Bubble Model

In a Lagrangian bubble model, the location ($\mathbf{x}$), gas contents (n_j with subscript j indicates gas type, e.g., j = 1 for N_2, and j = 2 for O_2), and size (r) of each Lagrangian particle are solved,

$$\frac{d\mathbf{x}}{dt} = \mathbf{u} \tag{8.3a}$$

$$\frac{dn_j}{dt} = f\left(r, z, c_j, S_j, D_j\right) \tag{8.3b}$$

$$\frac{dr}{dt} = f\left(\frac{dn_j}{dt}, w\right) \tag{8.3c}$$

In Eq. (8.3b), z is the vertical location of the Lagrangian particle; c_j, S_j, and D_j, is the dissolved concentration in the surrounding water, the solubility, and the diffusivity of gas j, respectively. Particle velocity (**u**) includes the effect of current, wave, and its own buoyancy that is size dependent. Ideally, each Lagrangian particle represents one gas bubble, but that is currently impossible because there are numerous bubbles in the ocean and computing power is limited. In actual simulations, each Lagrangian particle represents a large number of actual bubbles. Following the tradition in Lagrangian modeling of atmospheric cloud droplets where a Lagrangian particle is called a "super-droplet", the Lagrangian particles are called "superbubbles" in Liang et al. (2017). In Woolf and Thorpe (1991) where Langmuir circulations are represented by steady circulation cells, 5000 superbubbles were used. In Liang et al. (2017) where the ambient current is fully turbulent and unsteady, 8 million superbubbles were used.

A Lagrangian bubble model has the following advantages over an Eulerian bubble concentration model. Physically, a Lagrangian model allows straightforward separation of completely and partially dissolved bubbles since the fate of individual bubbles is tracked. Numerically, the Lagrangian model is a set of ordinary differential equations, whose numerical solutions are straightforward, without nonphysical effects associated with the dispersive and diffusive errors inherent to the numerical solutions of advection-diffusion equations in an Eulerian model. Computationally, computing power is allocated only to locations where bubbles are abundant, while bubble concentrations are calculated at each grid point for each size in an Eulerian coordinate system, even at depths where bubbles seldom reach and for sizes of few bubbles. The processor to compute a Lagrangian particle is the one that computes turbulent flow at the location of the particle. Buoyant particles are unevenly distributed in space, particularly in wave-driven Langmuir circulations, therefore computing loads are also unevenly distributed among processors. Our experience is that this increase in computing time due to heterogeneity is moderate and we are able to simulate bubbly flows for a two-week period in Liang et al. (2017). However, a Lagrangian model is less straightforward to implement in a parallel computing framework. A large number of Lagrangian particles are required to represent a field in the space.

8.2.2.3 Coupling with Hydrodynamic Model and Dissolved Gas Model

Bubble models require information about ambient current, temperature, and dissolved gas concentration. In early bubble modeling studies, due to insufficient knowledge of turbulent flows in the ocean surface boundary layer and limited

computing power, the effect of turbulence on bubbles is either neglected (Memery and Merlivat 1985), or by a pair of steady counter-rotating circulation cells mimicking Langmuir circulation (e.g., Woolf and Thorpe 1991). Dissolved gas concentration is set to a constant in those studies. In the past two decades when computation-expensive data-intensive parallelized computer models are able to resolve water turbulence, the concurrent simulation of turbulent flow and bubble fields becomes possible. Direct numerical simulation (DNS), where all water motions are resolved, has been used to simulate the evolution of bubbly flows under breaking waves in surf zones (e.g., Derakhti and Kirby 2014; Deike et al. 2016). However, DNS of the ocean surface boundary layer which is much deeper than the surf zone is still formidable in the foreseeable future because the ocean surface boundary layer is highly turbulent requiring a large number of grid points to resolve motions at all scales. Large eddy simulation (LES), where the majority of the energetic turbulent flows is simulated and the unresolved motions have little effect on resolved motions, is the popular approach to simulate boundary layer turbulence.

In the past few years, we coupled bubble models, first an Eulerian bubble concentration model (Liang et al. 2012) and later a Lagrangian bubble model (Liang et al. 2017) in a paralleled LES model for ocean surface boundary layer flows. The LES model we used is the National Center for Atmospheric Research Large Eddy Simulation (NCAR-LES) model (e.g., McWilliams et al. 1997). It is considered a state-of-the-art model for turbulent flows in the ocean surface boundary layer, and has been applied to study ocean turbulent flows under a variety of surface meteorological conditions and lateral forcing (See Sullivan and McWilliams 2010 and references therein). In a recent study (Liang et al. 2017), we demonstrated the use of the model to reproduce the observed concurrent evolution of the hydrodynamics, bubbles, and dissolved gases. The coupling between different models is illustrated in Fig. 8.2.

8.3 Studying Bubble-Mediated Gas Transfer Using a Computer Model

Four studies using numerical models to study bubble-mediated gas transfer are reviewed in this section in chronological order.

8.3.1 The Study of Merlivat and Memery (Memery and Merlivat 1985) (Hereafter MM85)

In MM85, bubbles are modeled as Lagrangian particles (superbubbles). In an era without advanced knowledge of boundary layer currents, superbubbles of diameter from 50 μm to 2000 μm are assumed to rise at their terminal velocity in quiescent

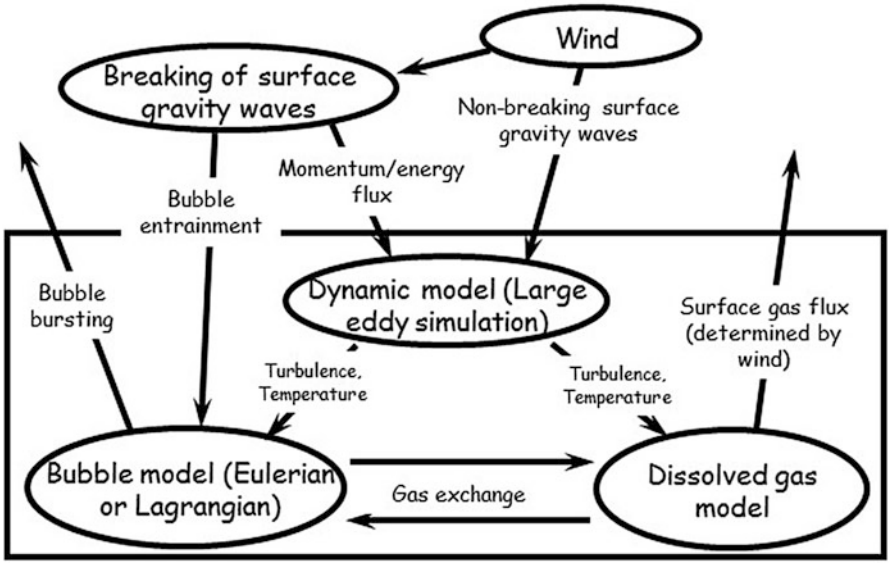

Fig. 8.2 A schematic showing the coupled hydrodynamic-bubble-gas model

water after their release in the ocean. Gas flux from each superbubble during its whole life in the water column ($q(r_0, z_0)$ with r_0 the initial size and z_0 the depth of entrainment by breaking wave) is computed. Because the evolution of each superbubble is deterministic, the gas flux through bubbles (F_b) is then calculated as,

$$F_b = \iint S(r_0, z_0) q(r_0, z_0) dr dz \tag{8.4}$$

where $S(r_0, z_0)$ is the bubble source function and the mean observed subsurface bubble distribution function was used by the authors. The use of mean subsurface bubble distribution as a bubble source function is not accurate, but was the best the authors could do at that time. The study draws some useful qualitative conclusions and new insights on how bubble-mediated gas transfer is influenced by gas solubility, gas diffusivity, and surfactants.

8.3.2 *The Study of Woolf and Thorpe (1991) (Hearafter WT91)*

Woolf and Thorpe (1991) also utilized a Lagrangian bubble model, similar to MM85, but made a few important improvements to the approach. In WT91, Langmuir circulations were included, as steady and counter-rotating circulation cells and background turbulence were modeled as isotropic random displacement determined

by diffusivity that is assumed uniform in the water column. The mean observed subsurface bubble distribution was used to tune the initial bubble size distribution. Furthermore, updated formulas for bubble and gas physics were used. Since bubble evolution is no longer deterministic due to turbulence, bubble gas flux is computed using simulated equilibrium bubble fields ($\Phi(r,\mathbf{x})$ with r the bubble size and $\mathbf{x}$ the bubble location) as,

$$F_b = \iint \frac{dn_j}{dt} \Phi(r, \mathbf{x}) dr d\mathbf{x} \tag{8.5}$$

Using the simulated bubble solutions, the authors are the first to propose parameterization for bubble-induced supersaturation and the parameterization has been shown to produce a reasonable agreement with dissolved gas measurements in a global model (Liang et al. 2013). They also suggested that gas flux depends on the saturation level of the most abundant gases including O_2 and N_2.

8.3.3 The Study of Liang et al. (2013) (Hearafter L13)

L13 fitted a parameterization for bubble gas flux based on simulated bubble fields in Langmuir turbulence driven by waves in equilibrium with the wind. The bubble fields were simulated with an Eulerian bubble concentration model (Eq. 8.2) and the bubble-mediated gas flux (F_b) is calculated the same way as in WT91 (Eq. (8.5)). Similar to some previous parameterization derived from observations (e.g., Stanley et al. 2009; Nicholson et al. 2011), the parameterization by L13 separates completely and partially dissolved bubbles indirectly through analyzing the gas flux ratio between O_2 and N_2. It was also demonstrated that bubble-induced equilibrium supersaturation (Δ_b) is temperature dependent and is larger at lower temperatures because diffusive gas flux at the ocean surface that offsets gas injection through bubbles is slower at lower temperatures. The authors also compared existing parameterizations that include Δ_b and show that huge uncertainty exists in those parameterizations. For example, bubble-induced supersaturation for N_2 spans the range from ~ 2% to more than 12% among different parameterizations.

The parameterizations were then tested in a global ocean transport model. Although bubbles only stay in the upper ocean for a short period of time, they set the near-surface dissolved gas concentration as a boundary for ocean ventilation and have non-negligible effects in the deep ocean. For example, L13 showed that bubbles at the near-surface ocean contribute more than 1% of the saturation level for Argon in the abyssal ocean and are crucial for accurately simulating deep-water gas concentration.

8.3.4 The Study of Liang et al. (2017) (Hearafter L17)

L17 applied a coupled hydrodynamic-bubble-dissolved gas model to study the evolution of the ocean environment and dissolved gases under a winter storm with wind speeds up to 20 m/s at ocean station Papa, where concurrent, relatively high-resolution (hourly or three-hourly), observations at both sides of the ocean-atmosphere interface including wind, buoyancy fluxes, wave, temperature, salinity, and dissolved gas concentrations are available. While the model-data comparison in L13 is for long-term means, the model-data comparison in L17 is for a transient synoptic event.

An instantaneous snapshot of subsurface bubble distribution (Fig. 8.3) shows that bubbles are mixed to more than 20 m during the peak wind of 20 m/s or so. The model reproduces the transient evolution of both observed O_2 and N_2 in the mixed layer when bubbles are considered. Without bubbles, the dissolved concentrations of both gases are underestimated. L17 also showed that sea state is an important parameter for bubble-mediated air-sea gas transfer, consistent with some other recent studies (e.g., Brumer et al. 2017; Deike and Melville 2018). When waves are less developed, there are fewer but larger breaking waves, leading to deeper bubble entrainment and larger gas fluxes through bubbles. At the same wind speed, gas flux through bubbles when the wind is strengthening, and the wave is less developed, can be twice as large as that when the wind is weakening.

8.4 Outlook

Computer models have improved our quantitative and qualitative understanding of bubble-mediated air-sea gas transfer. With the many data obtained recently and in the near future (see other chapters of this book), and the continued advancement in supercomputers, bubble models can be further improved by more detailed simulations of bubble and gas processes, such as entrainment under breaking waves and gas dissolution that are currently highly parameterized. Furthermore, existing bubble modeling studies are all for bubbles under the exclusive influence of boundary layer turbulence. Bubbles have been observed to reach tens of meters (Baschek et al. 2006) and are expected to contribute to the aeration of the water column in those scenarios that deserve more studies.

In addition to their significant role in air-sea gas transfer, bubbles also play important roles in other disciplines in oceanography, ocean sensing and earth science. For example, their optical and passive acoustical footprints are used to study and quantify dynamic processes, such as breaking waves (e.g. Melville and Matusov 2002) and turbulent mixing (e.g., Wang et al. 2016) in the upper ocean. Active noise levels during bubble formation were used to infer strong wind speeds (e.g., Zhao et al. 2014). In addition to gas transfer in the surface ocean, bubbles carry gases such as methane from the seafloor through the water column to the atmosphere

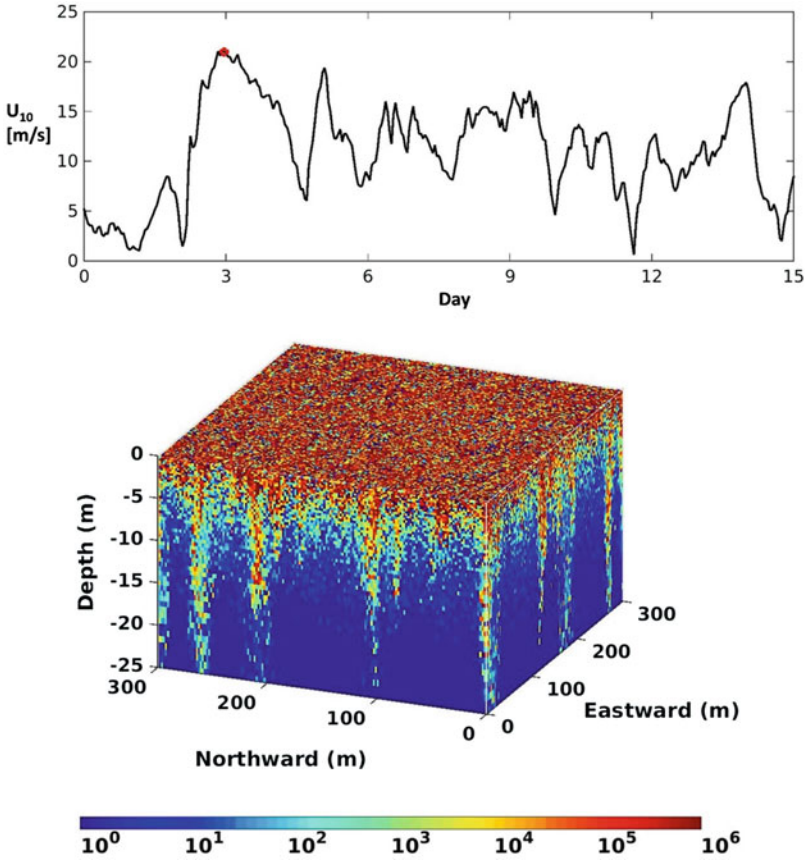

Fig. 8.3 Time series of wind speed during the period of simulation with day 0 corresponding to the start of Nov. 14th 2011 GMT (upper panel), and simulated bubble number density during peak wind denoted by a red circle in the upper panel. See Liang et al. (2017) for detailed description of the model configuration and other model results

(e.g., Leifer and Patro 2002). When bubbles burst, they contribute to aerosol production (Monahan et al. 1986) that leads to the formation of marine clouds. Finally, artificially generated bubbles have been proposed as a geoengineering approach to reduce night-time bottom water acidification in shallow water (Koweek et al. 2016). The use of bubble models is expected to improve the qualitative and quantitative understanding of these subjects.

Acknowledgement The author would like to acknowledge funding support from the National Science Foundation through grant OCE-1521018 and OCE-1558317. Computation in this study was carried out on high-performance supercomputing facilities at Louisiana State University and at the National Center for Atmospheric Research.

References

Asher, W. (1997). The sea-surface microlayer and its effect on global air-sea transfer. In P. S. Liss & R. Duce (Eds.), *The sea surface and global change* (pp. 251–285). A: Cambridge University Press.

Baschek, B., Farmer, D. M., & Garrett, C. (2006). Tidal fronts and their role in air-sea gas exchange. *Journal of Marine Research, 64*, 483–515.

Broecker, H. C., Petermann, J., & Siems, W. (1978). Influence of wind on CO2 exchange in a wind-wave tunnel, including effects of monolayers. *Journal of Marine Research, 36*(4), 595–610.

Brumer, S., Zappa, C., Blomquist, B., Fairall, C., Cifuentes-Lorenzen, A., Edson, J., et al. (2017). Wave-related Reynolds number parameterizations of CO2 and DMS transfer velocities. *Geophysical Research Letters, 44*, 9865–9875.

D'Asaro, E., & McNeil, C. (2007). Air-sea gas exchange at extreme wind speeds measured by autonomous oceanographic floats. *Journal of Marine Systems, 66*, 92–109.

Deane, G. B., & Stokes, M. D. (2002). Scale dependence of bubble creation mechanisms in breaking waves. *Nature, 418*, 839–844.

Deike, L., & Melville, W. K. (2018). Gas transfer by breaking waves. *Geophysical Research Letters, 45*, 10482–10492.

Deike, L., Melville, W. K., & Popineta, S. (2016). Air entrainment and bubble statistics in breaking waves. *Journal of Fluid Mechanics, 801*, 91–129.

Derakhti, M., & Kirby, J. T. (2014). Bubble entrainment and liquid-bubble interaction under unsteady breaking waves. *Journal of Fluid Mechanics, 761*, 464–506.

Emerson, S., & Bushinsky, S. (2016). The role of bubbles during air-sea gas exchange. *Journal of Geophysical Research, Oceans, 121*, 4360–4376.

Fairall, C. W., Yang, M., Bariteau, L., Edson, J. B., Helmig, D., McGillis, W., Pezoa, S., Hare, J. E., Huebert, B., & Blomquist, B. (2011). Implementation of the Coupled Ocean-Atmosphere Response Experiment flux algorithm with CO2, dimethyl sulfide, and O3. *Journal of Geophysical Research, 116*, C00F09.

Farmer, D. M., McNeil, C. L., & Johnson, B. D. (1993). Evidence for the importance of bubbles in increasing air-sea gas flux. *Nature, 361*, 620–623.

Farmer, D. M., Vagle, S., & Booth, A. D. (1998). A free-flooding acoustical resonator for measurement of bubble size distributions. *Journal of Atmospheric and Oceanic Technology, 15*, 1132–1146.

Hamme, R. C., Nicholson, D. P., Jenkins, W. J., & Emerson, S. R. (2019). Using noble gases to assess the ocean's carbon pumps. *Annual Review of Marine Science, 11*, 75–103.

Koweek, D. A., Mucciarone, D. A., & Dunbar, R. B. (2016). Bubble stripping as a tool to reduce high dissolved CO2 in coastal marine ecosystems. *Environmental Science & Technology, 50*(7), 3790–3797.

Lamarre, E., & Melville, W. K. (1991). Air entrainment and dissipation in breaking waves. *Nature, 351*, 469–472.

Leifer, I., & Patro, R. K. (2002). The bubble mechanism for methane transport from the shallow sea bed to the surface: A review and sensitivity study. *Continental Shelf Research, 22*, 2409–2428.

Liang, J.-H., McWilliams, J. C., Sullivan, P. P., & Baschek, B. (2011). Modeling bubbles and dissolved gases in the ocean. *Journal of Geophysical Research, 116*, C03015.

Liang, J.-H., McWilliams, J. C., Sullivan, P. P., & Baschek, B. (2012). Large eddy simulation of the bubbly ocean: New insights on subsurface bubble distribution and bubble-mediated gas transfer. *Journal of Geophysical Research, 117*, C04002. https://doi.org/10.1029/2011JC007766.

Liang, J.-H., Deutsch, C., McWilliams, J. C., Baschek, B., Sullivan, P. P., & Chiba, D. (2013). Parameterizing bubble-mediated air-sea gas exchange and its effect on ocean ventilation. *Global Biogeochemical Cycles, 27*, 894–905. https://doi.org/10.1002/gbc.20080.

Liang, J.-H., Emerson, S. R., D'Asaro, E. A., McNeil, C. L., Harcourt, R. R., Sullivan, P. P., Yang, B., & Cronin, M. F. (2017). On the role of sea-state in bubble-mediated air-sea gas flux during a winter storm. *Journal of Geophysical Research, Oceans, 122*, 2671–2685. https://doi.org/10.1002/2016JC012408.

Liss, P. S., & Slater, P. G. (1974). Flux of gases across the air-sea interface. *Nature, 247*, 181–184.

McNeil, C., & Asaro, E. D. (2007). Parameterization of air-sea gas fluxes at extreme wind speeds. *Journal of Marine Systems, 66*, 110–121.

McWilliams, J. C., Sullivan, P. P., & Moeng, C.-H. (1997). Langmuir turbulence in the ocean. *Journal of Fluid Mechanics, 334*, 1–30.

Melville, W. K., & Matusov, P. (2002). Distribution of breaking waves at the ocean surface. *Nature, 417*, 58–63.

Memery, L., & Merlivat, L. (1985). Modelling of gas flux through bubbles at the air-water interface. *Tellus B, 37*, 272–285.

Monahan, E. C., Spiel, D. E., & Davidson, K. L. (1986). A model of marine aerosol generation via whitecaps and wave disruption. In E. C. Monahan and G. Mac Niocaill, (Eds.), *Oceanic Whitecaps* (pp. 167–174). D. Reidel.

Monahan, E. C., & Torgersen, T. (1991). Enhancement of air-sea gas exchange by oceanic whitecapping. In S. C. Wilhelms & J. S. Gulliver (Eds.), *Air-water mass transfer: Selected papers from the second international symposium on gas transfer at water surfaces* (pp. 608–617). New York: American Society of Civil Engineers.

Nicholson, D. P., Emerson, S. R., Khatiwala, S., and Hamme, R. C. (2011). An inverse approach to estimate bubble-mediated air-sea gas flux from inert gas measurements. In *The 6th international symposium on gas transfer at water surfaces* (pp. 223–237). Kyoto University Press.

Nicholson, D. P., Khatiwala, S., & Heimbach, P. (2016). Noble gas tracers of ventilation during deep-water formation in the Weddell Sea. *IOP Conference Series: Earth and Environmental Science, 35*(1), 012019.

Shi, F., Kirby, J. T., & Ma, G. (2010). Modeling quiescent phase transport of air bubbles induced by breaking waves. *Ocean Modell, 35*, 105–117. https://doi.org/10.1016/j.ocemod.2010.07.002.

Stanley, R. H. R., W. J. Jenkins, D. E. Lott III, & S. C. Doney (2009) Noble gas constraints on air-sea gas exchange and bubble fluxes, Journal of Geophysical Research, 114, C11020.

Sullivan, P. P., & McWilliams, J. C. (2010). Dynamics of winds and currents coupled to surface waves. *Annual Review of Fluid Mechanics, 42*, 19–42.

Thorpe, S. A. (1982). On the clouds of bubbles formed by breaking wind-waves in deep water, and their role in air-sea gas transfer. *Philosophical Transaction of the Royal Society London A, 304*, 155–210.

Vagle, S., McNeil, C., & Steiner, N. (2010). Upper ocean bubble measurements from the NE pacific and estimates of their role in air-sea gas transfer of the weakly soluble gases nitrogen and oxygen. *Journal of Geophysical Research, 115*, C12054.

Vlahos, P., & Monahan, E. C. (2009). A generalized model for the air-sea transfer of dimethyl sulfide at high wind speeds. *Geophysical Research Letters, 36*, L21605.

Vlahos, P., Monahan, E. C., Huebert, B. J., & Edson, J. B. (2011). Wind-dependence of dms transfer velocity: Comparison of model with recent southern ocean observations. In *The 6th international symposium on gas transfer at water surfaces* (pp. 455–463). Kyoto University Press.

Wang, D. W., Wijesekera, H. W., Jarosz, E., Teague, W. J., & Pegau, W. S. (2016). Turbulent diffusivity under high winds from acoustic measurements of bubbles. *Journal of Physical Oceanography, 46*, 1593–1613.

Wanninkhof, R., Asher, W. E., Ho, D. T., Sweeney, C., & McGillis, W. R. (2009). Advances in quantifying air-sea gas exchange and environmental forcing. *Annual Review of Marine Science, 1*, 213–244.

Wanninkhof, R., Asher, W., Weppernig, R., Chen, H., Schlosser, P., Langdon, C., & Sambrotto, R. (1993). Gas transfer experiment on Georges Bank using two volatile deliberate tracers. *Journal of Geophysical Research, 98*, 20237–20248.

Woolf, D. K. (1997). Bubbles and their role in gas exchange. In P. S. Liss & R. A. Duce (Eds.), *The Sea Surface and Global Change* (pp. 173–206). Cambridge: Cambridge Univ. Press.

Woolf, D. K., & Thorpe, S. A. (1991). Bubbles and the air-sea exchange of gases in near-saturation conditions. *Journal of Marine Research, 49*, 435–466.

Zhao, Z., D'Asaro, E. A., & Nystuen, J. A. (2014). The sound of tropical cyclones. *Journal of Physical Oceanography, 44*, 2763–2778.

Chapter 9
Sea Spray and Gas Transfer

A. Staniec, P. Vlahos, and E. C. Monahan

Abstract In this Chapter we investigate the natural complement of bubble plumes (air entrained in water), sea spray (water entrained in air). As air is entrained in the surface ocean under breaking waves, sea spray is generated from the bubble plumes and the breaking waves themselves. In the same way as bubble plumes, the size distribution and volume flux of sea spray is related to wind speed. The work involving sea spray has been modest relative to its counterpart though significant strides have been made. The momentum and heat flux transfer associated with spray droplets has been reasonably characterized, though the role of sea spray in gas exchange has not. We introduce the Andreas Gas Exchange Sea Spray model (AGES) as an effort to advance our knowledge of sea spray-mediated exchange and present a case study of the role sea spray may serve in gas exchange of the North and South Atlantic Ocean.

9.1 Introduction

Sea spray is uniquely suited to transport energy and matter across the ocean atmosphere interface. Understanding the pivotal role that sea spray plays began in the 1960s, including E.C. Monahan's pioneering work in sea spray observations, which recognized that the production of sea spray was non-linearly related to wind speed (Monahan 1968). Since then, sporadic efforts have attempted to characterize the nature, size, and distribution of sea spray across different sea states and wind speeds, followed by efforts to elucidate their role in transporting heat, moisture, and momentum (Andreas et al. 1995, 2015; Boa et al. 2011). Most spray studies in the 1970s were laboratory based and, in 1979, Wu presented a review of these efforts, identifying that bubbles bursting at the ocean surface were the primary generation mechanism of sea spray (Wu 1979). Detailed studies revealed that sea spray has a bimodal distribution (Andreas 1992) that is derived from two separate mechanisms of formation. The first mechanism is bubble-mediated, as recognized by Wu, which

A. Staniec (✉) · P. Vlahos · E. C. Monahan
Department of Marine Sciences, University of Connecticut, Groton, CT, USA
e-mail: Allison.staniec@uconn.edu; Penny.vlahos@uconn.edu; Edward.monahan@uconn.edu

P. Vlahos (ed.), *Recent Advances in the Study of Oceanic Whitecaps*,
https://doi.org/10.1007/978-3-030-36371-0_9

results in smaller film and jet droplets, as was documented earlier (Blanchard 1963). Bubble-mediated droplets are formed when a bubble rises to the surface of the water and bursts. The film of water at the top of the bubble shatters into film droplets and the collapse of the resulting cavity forms a jet of water which breaks apart into several jet droplets. This is the dominant sea spray source at wind speeds above 3–4 ms^{-1} and below 12 ms^{-1} as breaking waves entrain the air required to make these bubble plumes (O'Dowd et al. 1997). The second sea spray source emerges at wind speeds of 7–11 ms^{-1} (Spiel 1996; Andreas 1998) and is composed of larger spray droplets generated from shear and tearing at the crests of breaking waves. Splash and spume droplets, collectively referred to here as wave-mediated droplets, form when a wave has instabilities or intersections which splash up water (splash drops) and when a wave crest is torn off by the wind (spume drops).

Sea spray is endlessly renewed by wind and wave action, constantly moving between the ocean surface and the marine boundary layer of the atmosphere. This makes it an important vessel for the transport of both energy and matter. Many aerosols which carry heat, momentum, and dissolved and particulate compounds act as irreversible transports, remaining in the ocean once deposited there, such as the iron deposition of desert dust aerosols and the raining out of organics and soot particles. Sea spray droplets, however, are the first step in an evolution, with the ability to transform in terms of size, temperature, salinity. These droplets may complete their transformation into sea salt and organic aerosols or be partially transformed. Their changing properties act as measurements of the storage capacity of a sea spray droplet, with shifts in temperature, salinity, and size determining their capacity to hold or transfer heat, momentum, and gases (Andreas et al. 1995, 2015; Bao et al. 2011).

9.1.1 Sea Spray Generation Functions

One of the major barriers to understanding spray is the uncertainty associated with sea spray generation functions. The most common parameterizations of sea spray generation correlate wind speed with water volume lifted. Size spectrums at different wind speeds are also variable and dependent on the methods used to obtain them. Laboratory experiments usually use falling water jets or glass frits to create rising bubble plumes (a noted exception being the studies of Monahan et al. (1986)). Wave-mediated droplets remain the purview of empirical observations and wind-wave tunnels.

Multiple sea spray generation functions exist although there are a few that are considered staples which can and have been modified to expand beyond their original size ranges and applications. Among these is the Monahan et al. 1986 model. Several reviews of these various functions exist and choosing a single function is informed by looking at the application for which it is intended. For example, various models of sea spray aerosol effects use different generation functions depending on region, wind speed, and size range (Barthel et al. 2019).

Concern for this uncertainty led Monahan et al. (2017) to complete a review of sea spray generation functions and identify the advantages and limitations of each. Fourteen spray generation volume fluxes were evaluated, covering research from 1986 to 2016. The most obvious observation was that the volume fluxes, while generally based on wind speed, covered 2–3 orders of magnitude and represented a wide range of functions (different exponential expressions). High wind speeds also represent an area of uncertainty, with many of the higher wind speed estimates representing an extrapolation rather than a direct measurement. The functions are derived from many sources ranging from direct measurement to experimental wind-wave tunnels to theoretical considerations. Some of the fluxes were rejected on theoretical or experimental considerations (i.e insufficient energy sources, observations at elevations that would not support spume production or droplets that are too small.) However, a consensus was reached on upper and lower bound expressions (Bortkovskii (1987) and Fairall et al. (1994) respectively).

9.1.2 The Role of Sea Spray

Understanding aerosols, a regulator of climate through irradiance and cloud cover, necessitates an understanding of sea spray. The ocean is considered to be the most prolific natural source of aerosol particulates and the sea salt aerosol mass flux is estimated in petagrams per year ($1–3*10^{16}$ g $year^{-1}$) (Blanchard and Woodcock 1980; O'Dowd and de Leeuw 2007). Sea spray affects almost all aspects of atmospheric and climatic science; from visibility, remote sensing, and air quality to indirect and direct radiative forcing (Lewis and Schwartz 2004). This is particularly important when we consider that natural aerosols, including sea spray, are the source of most of the uncertainty in understanding indirect radiative forcings (Carslaw et al. 2013). Sea spray is one of the dominant scatterers of surface irradiance and is produced over 70% of the earth. It influences trace gases, cloud condensation nuclei, and cloud microphysics as well as the optical properties of the marine atmosphere and represents 44% of the optical aerosol depth (de Leeuw et al. 2003; O'Dowd and de Leeuw 2007). Sea spray is a major component of our atmospheric aerosol; both directly, as sea salt particles, and indirectly, as it accumulates and carries both organic and inorganic material across the ocean atmosphere boundary.

Sea spray emissions have been shown to contribute significantly to particulate organic matter in the atmosphere but the amount of that contribution remains uncertain, with estimates ranging from 7.5–76 Tg $year^{-1}$ (Vignati et al. 2010; Tsigaridis et al. 2013). Organic matter that concentrates at the air-sea boundary layer is in the direct vicinity of breaking waves and rising bubbles. Bubbles generated by breaking waves create air-sea interfaces which scavenge hydrophobic organic molecules and surfactants (Monahan and Dam 2001). Those bubbles break at the surface to form sea spray droplets enriched in organics. In addition, wave-mediated droplets are also created at the air- sea interface on the surfaces of waves. This process is enhanced seasonally, with the increased biological activity in the

summer increasing the organic payload of individual droplets and acting to stabilize larger droplets (Yoon et al. 2007; O'Dowd et al. 2008). Winter results in a higher sea salt fraction and cleaner aerosols (Yoon et al. 2007). Parameterizations which investigate the proportion of organic material in sea spray droplets lead to a more constrained emission estimates of 2.8–5.6 Tg C $year^{-1}$ (Gantt et al. 2011) with the majority of emissions occurring in calmer waters where the surface microlayer of organic material is intact.

Sea spray also has the potential to influence the heat and energy budgets directly, with droplets acting as sources and sinks of moisture, sensible, and latent heat (Wang and Street 1978). Modeling efforts in the 1990s showed that sea spray, in high wind conditions, had the potential to contribute latent and sensible heat fluxes on the order of 150 and 15 Wm^{-2}, respectively (Andreas et al. 1995). Momentum and surface stress are also impacted by sea spray, with sea spray redistributing the wind momentum as it leaves the sea surface and is accelerated to the near surface wind speed. This acceleration removes momentum from the near surface wind and acts as a dampener on the speed of that near surface wind (Andreas 2004). These droplets act as stress on the sea surface upon re-entry, with high wind speed conditions allowing them to support 10–100% of sea surface stress (Andreas 2004). For heat fluxes, sea spray has been found to contribute most to the latent heat flux, with 20 ms^{-1} wind giving a spray generated latent heat flux on the same order of magnitude as the interfacial heat flux. Sensible heat flux is only an appreciable contributor when the interfacial sensible heat flux is very small and models show that the sea spray generated sensible heat flux is usually 10% or less of the interfacial flux (Andreas 1992).

9.2 The Role of Sea Spray in the Transfer of Gases

While much work has been done on the heat, moisture, and organic material fluxes inherent to sea spray, we now look to understand the potential for sea spray droplets to carry gases into and out of the ocean and the seasonality of those fluxes. This transport is reliant on the way that sea spray droplets evolve after they are injected into the atmosphere; whether that injection is a result of bubbles rising to the surface or wind tearing off parts of wave crests.

Larger wave-mediated droplets, because they contain a larger volume of water, can carry more gases. However, their size also means that they don't stay in the air for very long and this acts as a limit to the amount of gas they can transfer. Bubble-mediated droplets, which are smaller, carry less gas but remain aloft longer, often allowing them to transfer all the gas they carry.

The evolution of sea spray droplets upon injection to the marine boundary layer can be portrayed as a two-step process (Fig. 9.1).

The first step depends upon the difference between the temperature of the droplet (derived from the sea surface) and the temperature of the air into which the droplet is

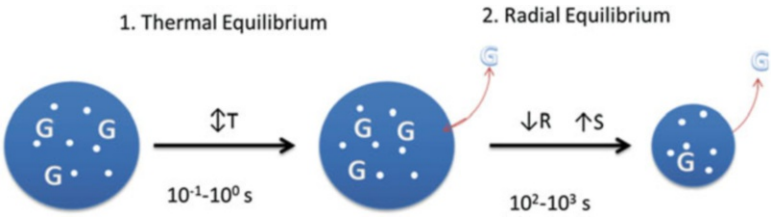

Fig. 9.1 The two step equilibration of a sea spray droplet to the marine boundary layer conditions with accompanying gas invasion or evasion

moving. The droplet generally cools unless the air is approximately >2 °C warmer than the water (Staniec et al. 2020 under review). This initial temperature change is referred to as reaching the initial thermal equilibrium and occurs because the droplet transfers internal energy to latent heat upon surface evaporation associated with injection into the air (Andreas 1995). A secondary evaporation occurs at a rate that is inversely proportional to the relative humidity until the spray drop reaches radial equilibration. As this occurs, the droplet becomes both smaller and saltier.

The first step is relatively quick, taking less than a couple of seconds for most droplets (50-500 μm). This shift in temperature, usually cooling, means that the droplet generally acquires gas in this first step, as gases are more soluble in cooler water and the droplets capacity for dissolved gas increases. If the droplet falls back to the sea surface at this point, it carries gas from the atmosphere to the ocean. This is only reversed if the air temperature is >2° warmer than the water. In this case the droplet does not experience net cooling, instead pulling energy from the warmer air to evaporate and warming in the process. Warming droplets will tend to evade gas and thus act to transfer gas from the sea surface and into the atmosphere. This latter condition occurs sporadically and does not represent the average state of the ocean. Average sea and air temperatures lead to consistent in-gassing to the droplet during the initial thermal equilibrium. However it is likely that warming droplets occur on occasion.

The second step, radial equilibration, takes much longer, on the order of hundreds to thousands of seconds and depends on the initial radius, the temperature of water and surrounding air and, most importantly, the relative humidity of the surrounding air. This step is reserved for smaller droplets ($\leq$50 μm) or situations with very high winds (>20 ms^{-1}) that hold larger droplets aloft (Mueller and Veron 2014). In this step the droplet evaporates, as the atmosphere has a lower relative humidity than the sea surface. This evaporation removes water, but not salt, from the droplet causing the droplet to shrink in size and increase in salinity. It also generally approaches the temperature of the air as it completes this evaporation. The shrinking size drives gas evasion through the salting out effect into the atmosphere. Any droplet which remains aloft long enough for this step inevitably moves gases completely or partially from the sea surface into the atmosphere.

9.2.1 The AGES Model

The gas exchanges presented here are the result of a modified version of Edgar Andreas' microphysical sea spray model (2013) which models the thermal and radial evolution of a sea spray droplet. Using Henry's Law constants, Setchenow constants, and solubility, the thermal and radial changes undergone by the droplet were used to inform the gas carrying capacity of the droplet at each step in the aforementioned evolution. This modified model is referred to as the Andreas Gas Exchange Spray model or AGES model (Staniec et al. 2020, under review). The AGES model highlights the importance of understanding sea spray fluxes, especially at high wind speeds, by indicating that not only does sea spray enhance heat and moisture exchange, but it also enhances gas exchange. In particular, at high wind speeds, sea spray has the potential to contribute significantly to air-sea fluxes (Andreas et al. 1995).

The AGES model treats the equilibration of gases as instantaneous as compared to the temperature and radial shifts associated with the drops evolution. This assumption has been shown to be valid by Andreas et al. (2017) who calculated the diffusional time scales of the gases moving through the droplet and across the drop-atmosphere barrier. Both these diffusional timescales are shown to be much less than the thermal and radial equilibration timescales. This is a valid assumption for gases which are non-reactive to dissolution. Other gases, like CO_2, which readily react with water may have additional time constraints through their reaction rates.

While we understand the physical processes that drive this exchange in individual droplets, formulating an overall estimate for the contribution of sea spray to gas exchange is confounded by the uncertainties in the total amounts of sea spray generated, as discussed above. Sea spray is relatively chaotic in its generation, affected by wind speeds, wave action, fetch, and roughness. Collecting sea spray data is difficult due to its inherent reliance on high wind speeds and rough seas which preclude direct observation except with the use of wind-wave tunnels and via satellite. Satellite data is promising though it also is confounded by cloud cover and albedo. Even wind-wave tunnels must be used with caution as they do not exactly simulate open ocean conditions due to their constrained water volumes and wind fetch.

Currently the AGES model is constrained to the calculation of single droplet gas exchange potential which is scaled to ocean regions by multiplying the single droplet potential by the volume of water lifted at different wind speeds. However, the AGES model still gives us preliminary insight into the seasonality and spatial variation of sea spray mediated gas exchange. One region, the Atlantic Ocean, is of particular interest in determining the seasonal effect of sea spray droplets.

9.3 Application of AGES to the Atlantic Ocean

As discussed above, the two step sea spray evolution is particularly driven by the air-sea temperature difference, especially in the first, thermal equilibrium step. The secondary radial equilibrium is driven by the salting out and evaporative

processes and thus remains relatively unchanged by the temperature differentials that indicate seasonality. Significant differences emerge in the characteristics of the North and South Atlantic Oceans. The northern hemisphere shows a very distinct seasonality in its air-water temperature differentials with larger differentials occurring in the winter (January) versus the summer (July). This larger differential drives differences in the gas exchange as well. Droplets in January experience a larger influx of gas (1.4–1.7× larger).

The southern hemisphere, on the other hand, shows a smaller temperature differential overall, generally less than 1 °C and consequently has a smaller influx of gas. The seasonality of the northern hemisphere is replicated albeit on a smaller scale with a slightly larger gas influx in the winter (July) and a slightly smaller influx in the summer (January). This gas exchange may be further compounded by the seasonal wind patterns. The Atlantic Ocean has generally higher wind speeds in winter vs summer for both hemispheres. (The equatorial Atlantic, as we might expect, does not experience this seasonality.) Average wind speeds for the Northern Atlantic peak around 17.5 ms^{-1} in January and have a low in July of around 2.5–5 ms^{-1} (Young 1999). The Southern Atlantic doesn't experience quite this range of change but varies from a lowest average of 2.5 ms^{-1} to about 10 ms^{-1} over the course of a year. (Note that this analysis excludes the Southern and Arctic Oceans). This means that sea spray mediated gas exchange likely also experiences a seasonal change. In lower wind speeds (i.e. summer) drops are less likely to be kept aloft and therefore only experience thermal equilibration which is on the order of single seconds. Summer temperature differentials also tend to be lower, minimizing the amount of gas exchange facilitated by thermal equilibration. Thermal equilibrium gas exchange is linearly correlated with the difference between the air and water temperatures ($\Delta T_{air\text{-}water}$). Plotting the change in temperature against the change in gas concentration for the thermal equilibrium gives a linear correlation (Fig. 9.2).

Winter months generally show higher wind speeds, increasing both the production of sea spray and the amount of time the drops are likely to be held aloft. Winter temperature differentials also tend to be larger, facilitating more gas exchange due to thermal equilibration. The longer residence time in the atmosphere could lead to more drops reaching radial equilibrium as well, a step which results in mass evasion of gas from the droplet due to salting out and loss of water content. In winter we would expect that droplets which reach thermal equilibrium would absorb larger amounts of gas (approximately 50% more than would be absorbed in summer). This could be offset by an increase in droplets reaching radial equilibrium and thus evading most of their gases.

Relative humidity may also play a role in determining what type of gas flux occurs. We can examine this more closely in the Atlantic Ocean where relative humidity has a range of about 10%, with values generally around 75–85% RH (Dai 2006). Relative humidity affects the evaporative potential of droplets; any parameter affected by evaporation will be impacted by a change in relative humidity. Increases in RH lead to increased time needed to reach radial equilibrium, slowing the evasion of gas from the droplet. The effects of RH increases are nonlinear, particularly as you approach saturation of the air. Overall impacts of relative humidity increases show

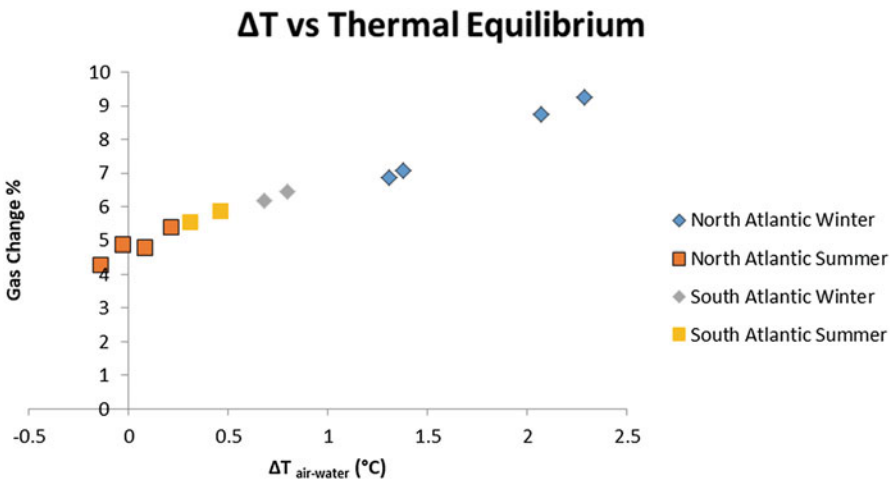

Fig. 9.2 Change in gas concentration for a single 100 μm radius droplet is plotted against $\Delta T_{air\text{-}water}$. Increases in $\Delta T_{air\text{-}water}$ lead to linear increases in gas exchange into the droplet. January (diamond) and July (square) average temperature differences for 6 year averages from 1981–2010 across the Atlantic Ocean are displayed

an increase in the time needed to reach radial equilibrium, an increase in the radius at radial equilibrium and slight increases in the temperature associated with thermal equilibrium. This is due to the change in energy needed for evaporation, the cause of the initial temperature change. The final droplet also shows a decrease in the final salinity of the droplet. This makes sense as increased relative humidity should lead to less evaporation from the droplet and indeed this is reflected in the amount of change in the gas concentration at final radial equilibrium, which decreases as relative humidity increases.

9.4 Conclusions

Presented here is a brief overview of the study of sea spray: both to elucidate the ways in which it is generated and the ways in which it influences the ocean atmosphere interface. Sea spray has been the subject of a variety of techniques and, as such, represents advances in experimental, theoretical, modeling, and in situ practices. Its history includes forays into chemistry, physics, and biology. We present a look at one specific aspect of sea spray, through the combination of chemical principles and a microphysical model, to examine the seasonality of gas exchange via sea spray droplets in the Atlantic Ocean. We find that the winter months enhance the influx of gas into sea spray droplets during their initial thermal equilibration and postulate that this may be augmented or mitigated by the higher wind speeds which impact the size of droplets held aloft as well as their time aloft.

This effect is dependent on how far the droplets get in their evolution with in-gassing to the spray droplet expected in the case of initial thermal equilibrium and outgassing when the droplet approaches final radial equilibrium. We do not expect seasonality to be reflected in the final radial equilibration as the gas exchange during that part of their evolution is due to the salting out process associated with evaporation. Examining relative humidity effects shows that relative humidity changes have the greatest effect on the final radial equilibrium. Thus, we see that seasonality should primarily be reflected in larger droplets with less time aloft and that, overall, droplets which reach final radial equilibrium have the potential to act as a negative feedback to the supersaturation of the surface ocean through bubble entrainment.

Acknowledgements The first two authors (AS and PV) would like to acknowledge that this work would not have been possible without the great amount of foundational sea spray work pioneered by Edward C. Monahan and thank him for the mentorship and support. Work for the model which prompted this exploration of sea spray gas exchange was funded through NSF Grants #13-56541 and 16-30846.

The first two authors (AS and PV) wish to note that the AGES model is a continuation of work pioneered by Edward Monahan and Edgar Andreas whose contribution to understanding the heat and moisture fluxes attributable to sea spray form the basis of the calculations performed here to estimate the potential gas exchange flux. The work includes the bubble/whitecap mediated droplets which inform much of Ed Monahan's early work but places a special emphasis on larger spume droplets which constitute the more recent and continuing focus of Ed Monahan's scientific career.

This model and these calculations of the gas exchange inherent to sea spray droplets is present in this Festschrift as the logical expansion and continuation of work that Edward Monahan has pioneered and had a hand in throughout his career. The first author (AS) is deeply grateful for his expertise, wisdom, and guidance in working on this project.

References

Original Andreas model: Andreas, E. An algorithm for making fast calculations of the microphysical properties of evolving saline droplets. 2013. www.nwra.com/resumes/andreas/software.php

Andreas, E. L. (1992). Sea spray and the turbulent air-sea heat fluxes. *Journal of Geophysical Research, 97*(C7), 11,429–11,441.

Andreas, E. L. (1995). The temperature of evaporating sea spray droplets. *Journal of the Atmospheric Sciences, 52*, 852–862. https://doi.org/10.1175/1520-0469(1995)052<0852:TTOESS>2.0.CO;2.

Andreas, E. L. (1998). A new sea spray generation function for wind speeds up to 32 m s-1. *Journal of Physical Oceanography., 28*, 2175–2184.

Andreas, E. L. (2004). Spray stress revisited. *Journal of Physical Oceanography, 34*, 1429–1440.

Andreas, E. L., Edson, J. B., Monahan, E. C., Rouault, M. R., & Smith, S. D. (1995). The spray contribution to net evaporation from the sea: A review of recent Progress. *Boundary-Layer Meteorology, 72*, 3–52.

Andreas, E. L., Mahrt, L., & Vickers, D. (2015). An improved bulk air–sea surface flux algorithm, including spray-mediated transfer. *Quarterly Journal of the Royal Meteorological Society, 141*, 642–654. https://doi.org/10.1002/qj.2424.

Andreas, E. L., Vlahos, P., & Monahan, E. C. (2017). Spray-mediated air-sea gas exchange: The governing time scales. *Journal of Marine Science and Engineering, 5*(4), 60.

Bao, J., Fairall, C. W., Michelson, S. A., & Bianco, L. (2011). Parameterizations of sea-spray impact on the Air–Sea momentum and heat fluxes. *Mon. Wea. Rev., 139*, 3781–3797. https://doi.org/10.1175/MWR-D-11-00007.1.

Barthel, S., Tegen, I., & Wolke, R. (2019). Do new sea spray aerosol source functions improve the results of a regional aerosol model? *Atmospheric Environment, 198*, 265–278. https://doi.org/10.1016/j.atmosenv.2018.10.016.

Blanchard, D. C. (1963). The electrification of the atmosphere by particles from bubbles in the sea. *Progress in Oceanography, 1*, 71–202.

Blanchard, D. C., & Woodcock, A. H. (1980). The production, concentration, and vertical distribution of the sea-salt aerosol∗. *Annals of the New York Academy of Sciences, 338*, 330–347. https://doi.org/10.1111/j.1749-6632.1980.tb17130.x.

Bortkovskii, R. S. (1987). *Air-sea exchange of heat and moisture during storms* (p. 194). Berlin: Springer.

Carslaw, K. S., et al. (2013). Large contribution of natural aerosols to uncertainty in indirect forcing. *Nature, 503*, 67–71.

Dai, A. (2006). Recent climatology, variability, and trends in global surface humidity. *Journal of Climate, 19*, 3589–3606. https://doi.org/10.1175/JCLI3816.1.

DeLeeuw, G., Moerman, M., Cohen, L., Brooks, B., Smith, M., & Vignatti, E. (2003). Aerosols, bubbles and sea spray production studies during the RED experiments. Extended Abstract. 12th Conference on Interactions of the Sea and Atmosphere.

Fairall, C. W., Kepert, J. D., & Holland, G. J. (1994). The effect of sea spray on surface energy transports over the ocean. *Global Atmosphere-Ocean System, 2*, 121–142.

Gantt, B., Meskhidze, N., Facchini, M. C., Rinaldi, M., Ceburnis, D., & O'Dowd, C. D. (2011. www.atmos-chem-phys.net/11/8777/2011/). Wind speed dependent size-resolved parameterization for the organic mass fraction of sea spray aerosol. *Atmospheric Chemistry and Physics, 11*, 8777–8790. https://doi.org/10.5194/acp-11-8777-2011.

Lewis, E. R., & Schwartz, S. E. (2004). *Sea salt aerosol production: Mechanisms, methods, measurements and models a critical review*. Washington, DC: American Geophysical Union.

Monahan, E. C. (1968). Sea spray as a function of low elevation wind speed. *Journal of Geophysical Research, 73*(4), 1127–1137. https://doi.org/10.1029/JB073i004p01127.

Monahan, E. C., & Dam, H. G. (2001). Bubbles: An estimate of their role in the global oceanic flux of carbon. *Journal of Geophysical Research, 106*, 9377–9383.

Monahan, E. C., Spiel, D. E., & Davidson, K. L. (1986). A model of marine aerosol generation via whitecaps and wave disruption. In E. C. Monahan & G. MacNiocaill (Eds.), *Oceanic whitecaps, and their role in air-sea exchange processes* (pp. 167–174). Springer Nature.

Monahan, E. C., Staniec, A., & Vlahos, P. (2017). Spume drops: Their potential role in air-sea gas exchange. *Journal of Geophysical Research: Oceans, 122*, 9500–9517. https://doi.org/10.1002/2017JC013293.

Mueller, J. A., & Veron, F. (2014). Impact of sea spray on air–sea fluxes. Part I: Results from stochastic simulations of sea spray drops over the ocean. *Journal of Physical Oceanography, 44*, 2817–2834. https://doi.org/10.1175/JPO-D-13-0245.1.

O'Dowd, C. D., Smith, M. H., Consterdine, I. E., & Lowe, J. E. (1997). Marine aerosol, sea-salt, and the marine SULPHUR cycle: A short review. *Atmospheric Enuironmenr, 31*(1), 73–80.

O'Dowd, C. D., & de Leeuw, G. (2007). Marine aerosol production: A review of the current knowledge. *Philosophical Transactions of the Royal Society A, 365*, 1753–1774. https://doi.org/10.1098/rsta.2007.2043.

O'Dowd, C. D., Langmann, B., Varghese, S., Scannell, C., Ceburnis, D., & Facchini, M. C. (2008). A combined organic-inorganic sea-spray source function. *Geophysical Research Letters, 35*, L01801. https://doi.org/10.1029/2007GL030331.

Spiel, D. E. (1996). Formation and production of sea spray aerosol. *Journal of Aerosol Science, 27* (Suppl. 1), S65–S66.

Staniec, A., Vlahos, P., & Monahan, E. C. (2020). Sea spray gas transfer: The role of sea spray in atmosphere-ocean exchange. *Nature Geoscience*. Under Review.

Tsigaridis, K., Koch, D., & Menon, S. (2013). Uncertainties and importance of sea spray composition on aerosol direct and indirect effects. *Journal of Geophysical Research – Atmospheres, 118*, 220–235. https://doi.org/10.1029/2012JD018165.

Vignati, E., et al. (2010). Global scale emission and distribution of sea-spray aerosol: Sea-salt and organic enrichment. *Atmospheric Environment, 44*, 670–677.

Wang, S. C., & Street, R. L. (1978). Transfers across an air-water Interface at high wind speeds: The effect of spray. *Journal of Geophysical Research, 83*, 2959–2969.

Wu, J. (1979). Spray in the atmospheric surface layer: Review and analysis of laboratory and oceanic results. *Journal of Geophysical Research, 84*, 1693–1704.

Yoon, Y. J., et al. (2007). Seasonal characteristics of the physicochemical properties of North Atlantic marine atmospheric aerosols. *Journal of Geophysical Research, 112*, D04206. https://doi.org/10.1029/2005JD007044.

Young, I. R. (1999). Seasonal variability of the Global Ocean wind and wave climate. *International Journal of Climatology, 19*, 931–950.

Chapter 10
What Controls Air-Sea Gas Exchange at Extreme Wind Speeds? Evidence from Laboratory Experiments

Bernd Jähne

Abstract In 1983 Ed Monahan presented the paper "The role of oceanic whitecaps in air-sea gas exchange" at the first International Symposium on Gas Transfer at Water Surfaces. He predicted a steep increase in the gas transfer velocities once the whitecaps can act as low impedance vents. He also postulated that the main role of bubbles is not their additional surface for exchange but that bubbles act as "stirring devices". In 1983 no suitable experimental data was available to test this simple but keen and visionary idea. Now more than 30 years later laboratory measurements in high wind speed facilities show that a new regime is established at wind speeds beyond 35 m/s, in which the gas transfer increases very steeply with wind speed. This steep increase is independent of the additional flux across bubble surfaces, because it was also observed for gases with moderate solubility including DMS. In fresh water bubble-induced gas transfer is not dominant even at hurricane wind speeds. For low solubility gases such as SF_6 and He, an enhancement of at most 25% was found. In sea water transfer across bubble surfaces contributes at most 2/3 of the flux.

10.1 Introduction: State-of-the-Art 1983

Ed and I met for the first time at Cornell University on the First International Symposium "Gas Transfer at Water Surfaces "(Brutsaert and Jirka 1984) in June 1983. At this time air-sea gas exchange was an emerging research topic still in its infancy. Ed presented a paper on "The role of oceanic whitecaps in air-sea gas exchange" (Monahan and Spillane 1984) to make the research community aware of the important role of whitecaps for air-sea gas exchange. At the beginning of this paper, he sketched the essential idea (Monahan and Spillane 1984):

B. Jähne (✉)
HCI and IWR at Institute of Environmental Physics, Heidelberg University, Heidelberg, Germany
e-mail: Bernd.jaehne@iwr.uni-heidelberg.de

P. Vlahos (ed.), *Recent Advances in the Study of Oceanic Whitecaps*,
https://doi.org/10.1007/978-3-030-36371-0_10

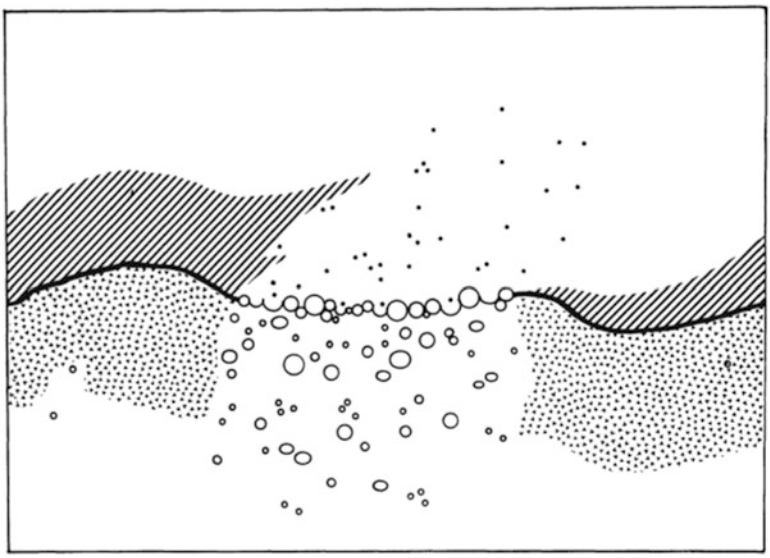

Fig. 10.1 From [36, Fig. 1] with the original caption: "Vertical section through a portion of the sea surface containing a whitecap. Note bubbles rising towards, and momentarily resting at, the sea surface. Dots represent spray particles produced by the bursting of the whitecap bubbles. Stippled zones correspond to portions of the undisturbed viscous ocean surface sub-layer through which gas transfer is solely by molecular diffusion. Hatching delineates regions where undisturbed laminar boundary layer is present in the atmosphere"

> When the meteorological conditions are such that whitecaps are present, then each such whitecap is perceived to act as a low impedance vent which has been punched through the laminar surface layer. The low impedance nature of the whitecap patch is due to the strong turbulence present in such an area which destroys the laminar surface layer.

Ed illustrated this basic idea with Figure 10.1 and continued:

> It should be noted that we perceive the bubbles primarily as stirring devices, recognizing that the potential energy released as they float towards the surface sustains the turbulent mixing induced in the first instance by the plunging or spilling wave that produced the whitecap.

From these basic arguments, Ed derived a simple quantitative model by defining transfer velocities for the whitecap vents (k_t) and the rest of the water surface (k_m). Then he could relate the effective transfer velocity k_e to the whitecap coverage W [36, Eq. 10.1]:

$$k_e = k_m(1 - W) + k_t W. \tag{10.1}$$

It was already well known that whitecap coverage increased strongly with wind speed. Using the then available data, Ed found by regression analysis that whitecap coverage is increasing stronger than with wind speed cubed:

$$W = 3.84 \cdot 10^{-6} U^{3.41}. \tag{10.2}$$

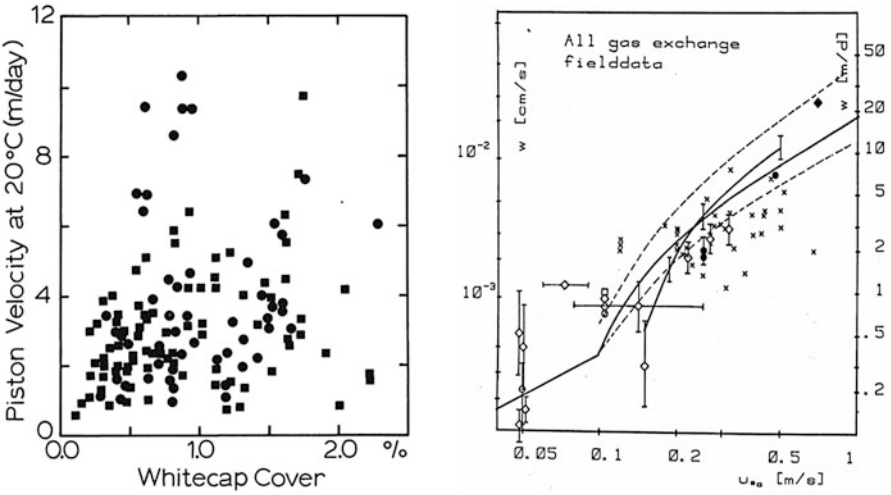

Fig. 10.2 Left: Correlation between gas transfer velocity k with the whitecap coverage W (Monahan and Spillane 1984, Fig. 7.1); Right: Collection of field data together with the parametrization using the Schmidt number Sc and the friction velocity u_{*a} as suggested by the author in 1982 (solid line). The two dashed lines indicate the range of gas transfer velocities measured in wind/wave facilities (Jähne 1982)

He then took the transfer velocities obtained during the GEOSECS and TTO expeditions by the radon deficit method (Peng et al. 1979) and found that a relation with the wind speed cubed gave the best correlation:

$$k_e\,[\mathrm{m/day}] = 2.3 + 1.25 \cdot 10^{-3} U^3, U \text{ in}[\mathrm{m/s}]. \tag{10.3}$$

Ed also estimated the transfer velocity in whitecap vents, $k_t = 114 \pm 66$ m/day, within a confidence band of 95%. According to Eq. 10.1 this means, of course, that the cubed increase of the transfer velocity cannot go on forever. It is rather capped to a maximum value of $k_e = 114 \pm 66$ m/day (or $\approx 500 \pm 300$ cm/h) when the whitecap coverage becomes 100%. The measured transfer velocities shown in Figure 10.2 are still an order of magnitude lower than this limit because there were no measurements available at sufficiently high wind speeds.

As Figure 10.2 (left) shows, however, that the correlation between whitecap coverage and the gas transfer velocity is quite poor. The correlation coefficient is only 0.162. Thus other parametrizations may be possible. In one of my contributions at the Cornell Symposium (Jähne et al. 1984a), I pointed out that a stronger than linear increase of the gas transfer velocity with the friction velocity (as a better measure for the wind shear than the wind speed itself), is caused by the transition of a smooth regime to a wavy regime due to two effects: (a) the decrease of the Schmidt number exponent from $-2/3$ to $-1/2$ and (b) the increase of the turbulence level. From simultaneous measurements of bubbles and He and Rn gas exchange in the

large Marseille wind/wave facility, also reported at the Cornell Symposium (Jähne et al. 1984b), we knew that up to the maximum wind speeds in this facility (reference wind speed 13.8 m/s), the influence of bubbles by wave breaking was negligible.

Already a year before the Cornell Symposium in a report for the Battelle Institute in Frankfurt (Jähne 1982), I used a careful selection of field experiments (Fig. 10.2, right) and the knowledge about Schmidt number dependency from the laboratory experiments to establish a first semi-empirical relation between the gas transfer velocity and the friction velocity in air, u_{*a}, four years before the well-known Liss-Merlivat relation (Liss and Merlivat 1986):

$$k = \begin{cases} 2.9 \cdot 10^{-3} Sc^{-2/3} u_{*a} & u_{*a} < u_{*c} \\ 2.9 \cdot 10^{-3} Sc^{-2/3} u_{*a} + 5.5 \cdot 10^{-3} Sc^{-1/2} \left(u_{*a} - u_{*c}\right) \end{cases} \tag{10.4}$$

with $u_{*c} = 0.1$ m/s.

Ed was well aware of the wind/wave facility results, but argued that it is better to use field data:

> It is our contention that the laboratory results are not directly applicable to the open ocean, and thus do not rule out the whitecap vent model for gas exchange... The marked difficulty encountered in achieving with a particular air speed in these flumes the sea state or "wave age" that would characterize the open sea at the same wind speed is well known... We have concluded therefore that open ocean piston velocity measurements, in spite of their experimental shortcomings, represent the most suitable data base for the testing of gas exchange models such as the whitecap vent one.

These arguments are to be considered carefully, although it is surprising to see how close the laboratory results are to the field results in Figure 10.2 (right). They even lie in the upper range of the field data. Therefore, it is harder to argue that the wind/wave tunnel data miss the influence of whitecaps.

On the other side: In the early days, the difficulties to measure correct gas transfer velocities in the field have been underestimated. My colleagues Roether and Kromer from the Institute of Environmental Physics at Heidelberg showed also in Cornell (Roether and Kromer 1984) that the simple approach for the GEOSECS radon deficit measurements is inappropriate under most circumstances and caused biased gas transfer values.

Ed was again aware of these difficulties:

> The nature of the currently available radon measurements and associated meteorological data are such that it cannot yet be determined whether the open ocean piston velocity is approximately proportional to a + bU^3 as the whitecap vent model (Eq. 10.3) would suggest, or shows a lesser functional dependence upon wind speed as has been inferred by a number of workers from a variety of laboratory tank measurements.

Ed's proposed model for the influence of whitecaps on air-sea gas exchange was certainly an oversimplification, incorrect in many details. But this was not the point in these early days of gas exchange research. The essential keen and visionary idea was that there should be a strong increase of the gas transfer towards high wind speeds due to the highly turbulent processes in whitecaps. This model could not be

Table 10.1 International symposia on "Gas Transfer at Water Surfaces"

Date	Place	Chairs [reference proceedings]
1st June 13–15, 1983	Ithaca, USA	W Brutsaert and G H Jirka (1984)
2nd Sept. 11–14, 1990	Minneapolis, USA	S C Wilhelms and J S Gulliver (1991)
3rd July 24–27, 1995	Heidelberg, Germany	B Jähne and E C Monahan (1995)
4th June 5–8, 2000	Miami, USA	M A Donelan et al. (2002)
5th May 2–6, 2005	Liege, Belgium	A V Borges and R Wanninkhof (2007)
6th May 17–21, 2010	Kyoto, Japan	S Komori and W McGillis (2011)
7th May 18–21, 2015	Seattle, USA	A T Jessup and W E Asher (2016)
8th May 19–22, 2020	Plymouth, UK	

tested at that time because simply no measurements at high enough wind speeds were available.

The First International Symposium on Gas Transfer at Water Surfaces at Cornell University in 1983 triggered an intensive research period which lasts until today. A regular series of symposia every five years was established (Table 10.1). Ed and I chaired the third symposium at Heidelberg University in 1995. Ed continues to make important contributions until today to almost every symposium.

Here I will try to shed more light on what controls air-sea gas exchange at high wind speeds and therefore to give an answer whether Ed's early keen idea of whitecap venting is correct. First, progress in field experiments will be reviewed (Sect. 10.2). Only recently, suitable laboratory facilities became available to perform gas exchange measurements at high wind speeds. In Sect. 10.3 I will report measurements and a preliminary analysis of the results from four different wind/wave facilities which my group has undertaken in recent years. Some of the results are already contained in the article on Air-Sea Gas Transfer in the third edition of the Encyclopedia of Ocean Science (Jähne 2019). A more detailed analysis can be found in Krall et al. (2019).

10.2 Review of Field Experiments

A collection of field data together with some of the empirical k (U_{10})-relationship shows several interesting points (Fig. 10.3). Almost all measurements were performed only in a narrow wind speed range between 4 and 15 m/s. Even in this range, the measured transfer velocity may deviate from any of the relationships by more than a factor 1.7 in both directions. Outside of this wind speed range, there is almost no experimental data. This also means that the empirical parametrizations are very uncertain — if not even invalid — outside the 4 to 15 m/s wind speed range.

This is not surprising for high wind speeds larger than 15 m/s up to hurricane wind speeds of 70 m/s, because field experiments are very difficult under these conditions. The only available field measurements were made during hurricane Frances in 2004. At wind speeds larger than 25 m/s, three transfer velocities of O2

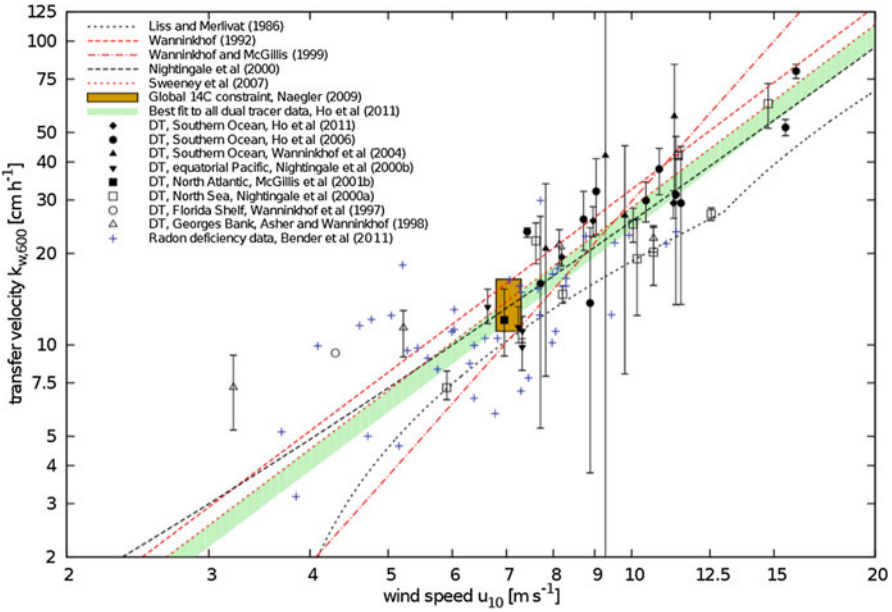

Fig. 10.3 Gas transfer velocity as a function of the wind speed from many recent gas transfer field experiments including the dual tracer technique (DT) (Asher and Wanninkhof 1998; Ho et al. 2006, 2011; McGillis et al. 2001; Nightingale et al. 2000a; Nightingale et al. 2000b; Wanninkhof et al. 1997; Wanninkhof et al. 2004), the radon deficit technique (Bender et al. 2011) and the global ^{14}C constraint (Naegler 2009) together with some of the empirical gas transfer velocity / wind speed relations as indicated (Ho et al. 2011; Liss and Merlivat 1986; Nightingale et al. 2000b; Sweeney et al. 2007; Wanninkhof 1992; Wanninkhof and McGillis 1999). (From Kunz and Jähne 2018)

were estimated using unmanned floats, with the highest wind speed being 50.4 m/s, yielding the highest ever measured transfer velocity in the field of $k660 = (725 \pm 485)$ cm/h (McNeil and D'Asaro 2007). This is already beyond the maximum value of Ed's 1983 whitecap model of 500 ± 300 cm/h (Sect. 10.1). Thus field experiments could so far not give much new insight for gas exchange at high wind speeds. Just three data points beyond 25 m/s are not enough. Therefore, Wanninkhof et al. (Wanninkhof et al. 2009) concluded in their most recent review article: "there are not yet any reliable estimates possible about gas exchange at very high wind speeds". Five years later in 2014, another review paper drew the same conclusion (Garbe et al. 2014).

10.3 Laboratory Measurements at Extreme Wind Speeds

Other experimental setups were designed which could at least partly simulate the conditions at higher wind speeds. The famous WABEX-93 experiment (Asher et al. 1995) used a freshwater surf pool without wind but with heavily breaking waves.

At a fractional whitecap coverage of 0.067 a gas transfer velocity of $k600 = 450$ cm/h was measured (Wanninkhof et al. 1995). Another sophisticated large-scale experiment, named LUMINY, was performed by a European research consortium in the large wind/wave facility at the IRPHE-IOA of Marseilles University, France, (de Leeuw et al. 1999; de Leeuw et al. 2002; Woolf et al. 2007) in spring 1997. The conditions at higher wind speeds were simulated by superimposing mechanically generated waves with wind waves to reach heavy wave breaking and by producing high bubble densities with submerged aerators. Gas transfer velocities were measured with 4 tracers. These conditions, however, do not adequately simulate high wind speeds.

Only in the recent years, suitable wind/wave flumes became available to conduct gas exchange measurements at high wind speeds. After first success pilot experiments in the High Wind Speed Facility of Kyoto University by our Japanese colleagues and my research group (Iwano et al. 2013; Iwano et al. 2014; Krall and Jähne 2014), we conducted an extensive experimental program in the Kyoto facility (fall 2015) and the Surge-Structure-Atmosphere-Interaction Facility (SUSTAIN) at the Rosenstiehl School of Marine and Atmospheric Science (RSMAS) of the University of Miami (spring 2017).

10.3.1 Experimental Setup

The solubilities of the tracers used spans more than four decades (Table 10.2). In the limit of low values (SF6 and He), the gas concentration in a bubble does not come into equilibrium with the water during the bubble's lifetime, so that the bubble surface is actively involved in the gas transfer during its whole lifetime. In the limit of high solubility, bubbles quickly come into equilibrium with the surrounding water and thus do not significantly contribute to gas exchange. In this limit, the bubble-induced transfer velocity is much smaller, no longer depends on the diffusion coefficient and is proportional to the volume flux of the bubbles and inversely proportional to the solubility. In this way a wide range of tracer solubilities is the key to determine the fraction of bubble-induced gas transfer.

Wind speed, flow characteristics, and friction velocities were measured in close cooperation with the respective local cooperation partners. Drag coefficients are shown in Figure 10.4. Figure 10.5 together with the links to videos give an impression of the conditions at the water interface at hurricane wind speeds.

A high-speed imaging system (Kiefhaber et al. 2014) was used to characterize the water surface conditions at high wind speeds. The system was used to measure wave slopes with 1500 frames/s. In cooperation with Y. Troitskaya from the Institute of Applied Physics (Russian Academy of Science, Nizhny Novgorod) the system was modified to measure wave breaking, surface detachment at wave crests, and spray generation with more than 10000 frames/s.

Table 10.2 Selection of gases and volatile species measured simultaneously by membrane inlet mass spectrometry (MIMS) in the different facilities. The table contains the molecular weight MG, dimensionless solubility α (partition coefficient in cm^3 /cm^3), diffusion coefficient D in water, Schmidt number Sc, and in which facilities the tracer were used: Kyoto, SUSTAIN Miami. All values at 25 °C, order: increasing solubility

Species	MG g/Mol	α	D, (10^{-5} cm^2 / s)	Sc	Usage
CF4	88.00	0.0052	1.42	629	Kyoto
SF6	146.06	0.0060	1.20	745	Kyoto, SUSTAIN
^{4} He	4.00	0.0095	7.22	122	Kyoto, SUSTAIN
Ne[a]	20.18	0.0110	4.16	215	Kyoto
Ar[b]	39.95	0.034	2.5	357	Kyoto, SUSTAIN
Kr	83.80	0.061	1.84	486	SUSTAIN
Xe	131.29	0.107	1.47	608	Kyoto
Pentafluorethane	120.02	0.184	1.12	798	Kyoto, SUSTAIN
Acetylene	26.04	0.97	1.68	532	SUSTAIN
Hexafluorobenzene (HFB)	186.05	1.0	0.86	1040	Kyoto, SUSTAIN
Difluoromethane	50.49	2.55	2.55	638	Kyoto
1,4-Difluorobenzene (DFB)	114.09	3.2	0.94	951	Kyoto
Dimethyl sulfide (DMS)	62.13	12.7	1.35	662	Kyoto, SUSTAIN
Methyl acetate (MA)	74.08	110	1.09	820	Kyoto, SUSTAIN

[a]Measurement accuracy not high enough because of too high background
[b]Reference for stability of system
Sources: (Jähne et al. 1987; Sander 2015; Yaws 1995)

10.3.2 Fresh Water Results

The first measuring campaign at Kyoto revealed surprising results. Up to about 35 m/s (U_{10}) or a friction velocity in water of about 7 cm/s, the gas transfer velocity in fresh water increases about linearly with friction velocity. Beyond this threshold, the gas transfer velocity increases at least with the friction velocity cubed (Fig. 10.6). Therefore, the gas transfer velocity scaled to a Schmidt number of 600 increases from about 200 cm/h to about 1500 cm/h, or by about an order of magnitude in a range, in which the friction velocity just doubles. This is in stark contrast to the effect that in the same facility momentum transfer does not show this strong increase. The drag coefficient remains almost constant, see Fig. 10.4 and (Takagaki et al. 2012).

The strong increase in the high wind speed regime is not caused by bubble-induced gas exchange. This is evident from the fact that the transfer velocities are

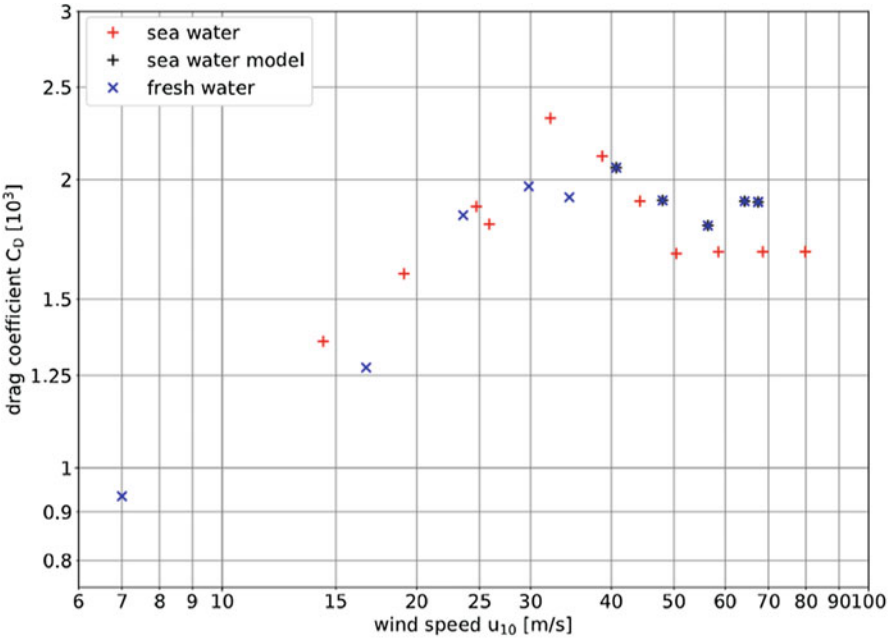

Fig. 10.4 Drag coefficient measured under different conditions: fresh water in the Kyoto facility (blue x), modeled sea water in the Kyoto facility (black +), and seawater in the SUSTAIN facility (red +)

Fig. 10.5 SUSTAIN facility in operation at hurricane wind speeds, here with fresh water. Video impression from the wind ramp up to the highest wind speeds in the Kyoto and SUSTAIN facilities are in these videos: https://www.youtube.com/watch?v=KDcAzL01LT0 and https://www.youtube.com/watch?v=DUrP-rRnRxU

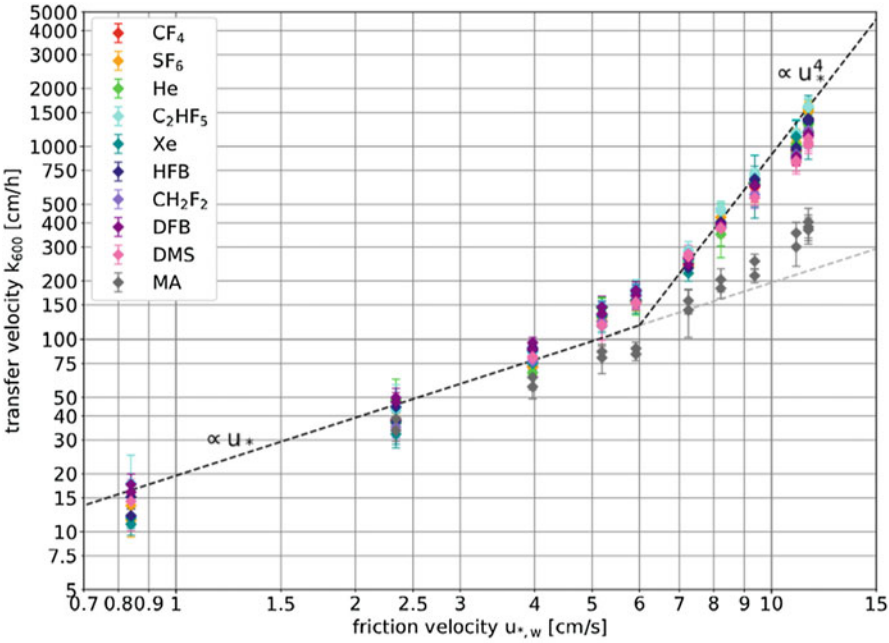

Fig. 10.6 Gas exchange results from the Kyoto facility in fresh water, partly published (Krall et al. 2016; Krall and Jähne 2014): Transfer velocities scaled to a Schmidt number of 600 as a function of friction velocity in water (*HFB* hexafluorobenzene, *DFB* 1,4-difluorobenzene, *MA* methyl acetate)

almost independent of the solubility (Fig. 10.6). Up to wind speed of 48 m/s the enhancement is below 20%, while it reaches up to 50% at the highest wind speeds. This means that even at the highest wind speed bubble-induced gas transfer in fresh water is not dominant. Even for gases with very low solubilities, it contributes at most 1/3 to the total transfer. Consequently, a new regime for mass exchange is in effect, which in not primarily caused by bubbles. Bubbles are rather a secondary effect in fresh water.

10.3.3 Air Phase Controlled Gas Transfer

The only volatile species that deviates from the transfer velocities of the other gases is methyl acetate (MA) (Fig. 10.6). This is because of the non-negligible air phase resistance for the high solubility of methyl acetate ($\alpha = 110$), see Table 10.2. The lower transfer velocities of methyl acetate at the high wind speeds indicates that the equal partitioning of the transfer resistance between air and water has reduced to a solubility of below 100, while it is between 750 and 450 for wind speeds below 15 m/s, as measurements in the Heidelberg Aeolotron showed (Kräuter 2011; Kräuter et al. 2012).

10.3.4 Sea Water Results

In seawater, bubble concentrations are expected to be higher. Therefore, the effect of bubbles should be more significant. Unfortunately, seawater could not be used in the Kyoto facility. But by adding traces of 1-butanol (0.5 L in 13 700 L of water) to fresh water, the bubble spectrum changes to resembles that of seawater, an effect which was used for measurements of bubble-induced gas exchange in a special bubble tank (Mischler 2014; Mischler and Jähne 2012). With the modeled seawater, the gas exchange rates for low solubility gases such as SF_6 and He are significantly enhanced (Fig. 10.7). For these two gases, the enhancement was threefold at the highest wind speeds. Thus the highest ever measured gas transfer velocities of about 4000 cm/h—scaled to a Schmidt number of 600—were obtained, more than six (!) times higher than the highest ever measured value in the field (McNeil and D'Asaro 2007). However, for moderately soluble gases, most notably carbon dioxide, the bubble effect is not significant at all (Krall et al. 2019).

Because of the uncertainty in the bubble effect for simulated seawater, high wind speed gas exchange experiments in true seawater became very important. Fortunately, the opportunity arose to perform the very first air-sea gas exchange measurements in the new SUSTAIN facility at RSMAS, University of Miami in spring 2017. Preliminary results agree very well with the butanol experiments in the Kyoto facility, both in the wind speed dependency and in the relative contribution of the bubbles.

10.3.5 DMS Gas Exchange

Another interesting result could be gained for DMS. While recent field measurements (Bell et al. 2015; Bell et al. 2013) showed a leveling off or even a decrease of the DMS transfer velocity with wind speed, such an effect could not be observed in our measurements (Fig. 10.8). DMS behaves like all other volatile species. Its solubility of 12.7 is not large enough to cause a significant transfer resistance in the gas phase. In good approximation DMS can be regarded as water phase controlled species for gas transfer. The decrease of the DMS transfer velocity as measured by eddy-covariance in the field can therefore very questionable. It could be caused by unknown other source/sink terms, problems in estimating the air-sea concentration difference or other systematic errors in the eddy covariance measuring technique at high wind speeds. And the theory that DMS gas transfer is diminished by an apparently higher solubility due to accumulation of DMS at the surface of bubbles (Vlahos et al. 2011; Vlahos and Monahan 2009) is obviously also not correct.

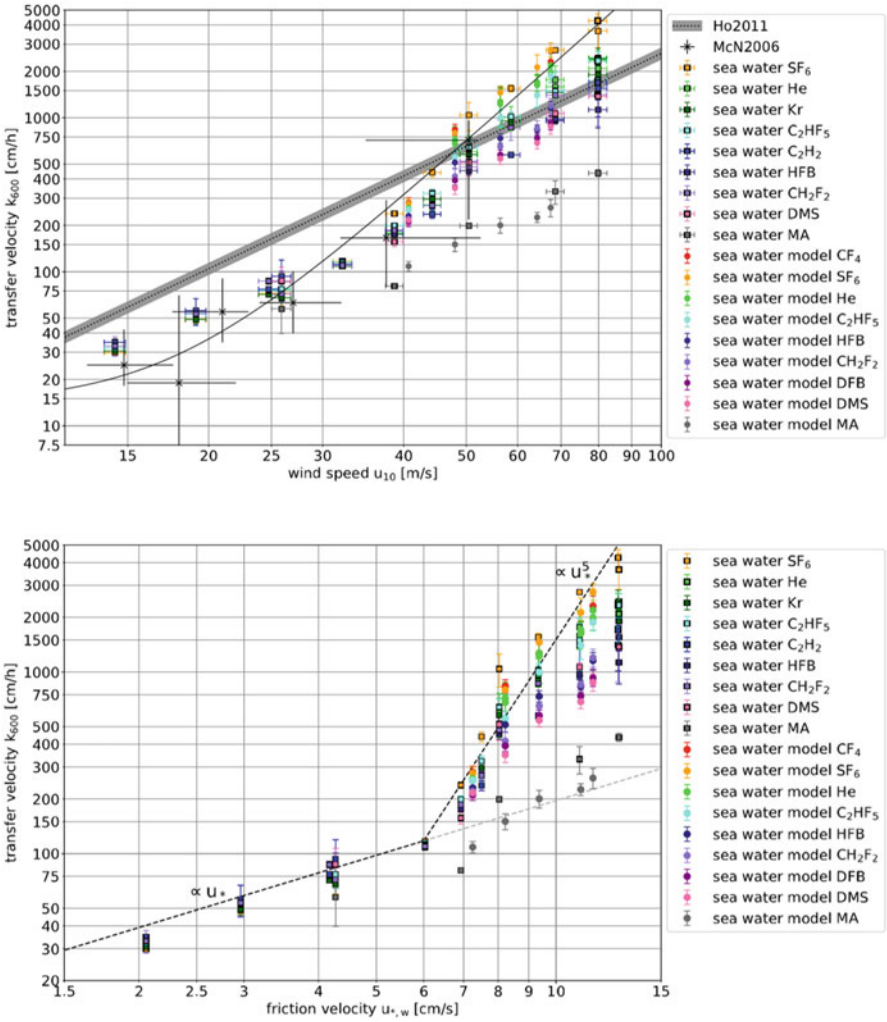

Fig. 10.7 Gas transfer velocities measured at high wind speeds in modeled sea water (Kyoto facility) and seawater (SUSTAIN facility) as a function of the wind speed at 10 m height (top) and the friction velocity in water (bottom)

10.3.6 Bubble Concentrations

Bubble concentrations depend not only on the wind speed but also on the fetch or wave age (Fig. 10.9, (Flothow 2017)). At the same wind speed, the fractional area, i.e., the surface area of bubbles versus the free water surface area, increases with fetch. It is at least an order of magnitude higher in the Heidelberg Aeolotron with infinite fetch than in the short-fetch Kyoto and Marseille Luminy facilities. The same

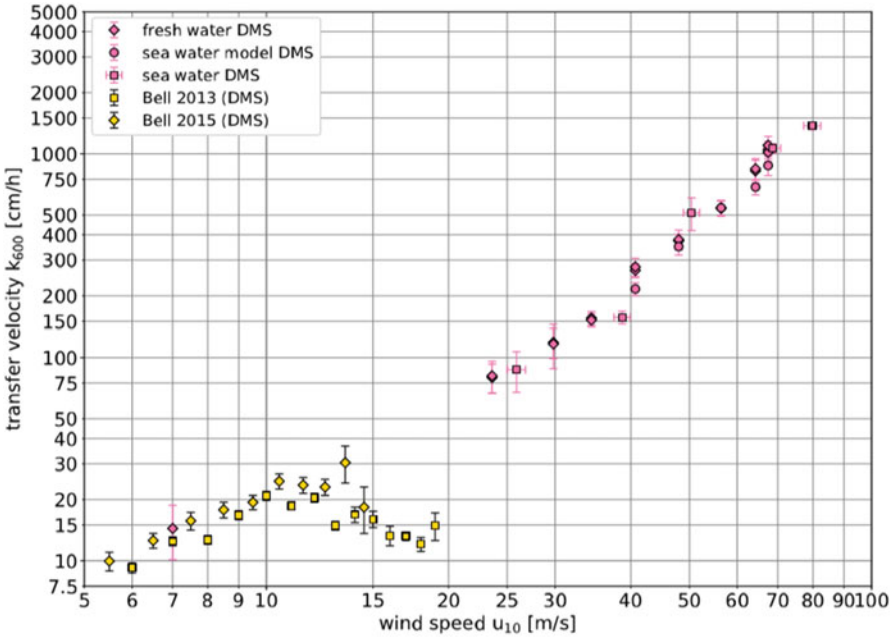

Fig. 10.8 Comparison of DMS gas transfer velocities measured in the field and in high-wind speed laboratory facilities

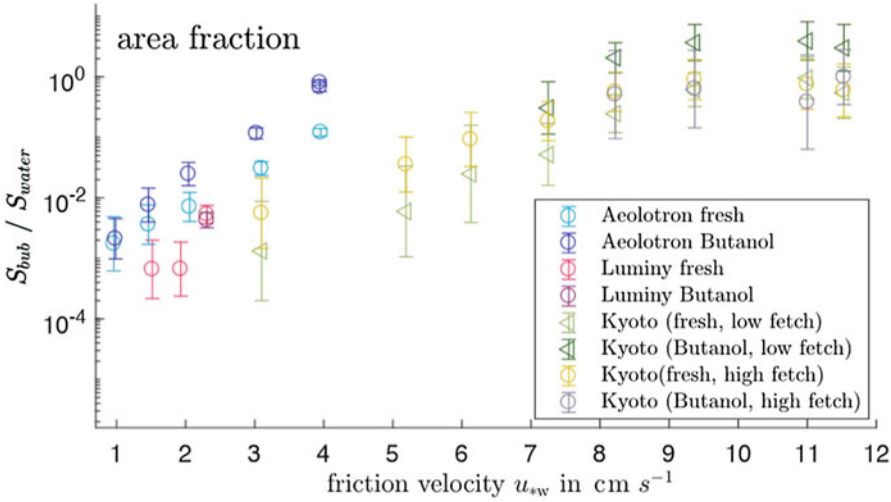

Fig. 10.9 Bubble area per water surface area measured in fresh water and modeled seawater by adding butanol to fresh water: Kyoto: 4 and 8 m fetch, Marseille Luminy: 28 m fetch, Aeolotron Heidelberg: infinite fetch. (From Flothow 2017)

fractional area of bubbles is reached in the Aeolotron at about half the friction velocity than in the Kyoto facility. This could mean that at larger fetches the influence of bubbles is larger. In any way, this clearly indicates that laboratory results must not simply be extrapolated to field conditions, as pointed out by Ed already in 1983 (Monahan and Spillane 1984). It is, however, difficult to simulate all relevant fetch conditions in laboratory facilities. New experimental approaches are urgently required.

Generally bubble concentrations in modeled seawater are four to six times larger than in fresh water. The saturation of the fractional bubble area at high wind speeds in the Kyoto facility is probably caused by a bias in the measurements, because bubble-induced gas exchange is still increasing. The only explanation for this effect is that the bubble measurements performed at a depth of 30 cm come to a saturation, whereas short-lived bubbles very close to the water surface—which could not be measured—still increase. This effect is an indication that bubble generation and bubble bursting taking place in the vicinity of the surface may contribute more to the gas transfer than the bubbles submerged into the depth.

10.4 Conclusions and Outlook

Gas exchange measurements in two different wind/wave facilities at high wind speeds clearly show a steep increase of the gas transfer velocities beyond a critical wind speed of 35 m/s or a friction velocity in water of 7 cm/s. The measured gas transfer velocities are in surprisingly good agreement with the only available field data set (Fig. 10.7). This does not mean that laboratory results can be used for field conditions. Firstly, the agreement is not very significant because of the large error bars of the field measurements. Secondly, the fetch dependency of the small-scale air sea interaction processes needs to be resolved before a reliable estimate of gas transfer velocities at high wind speeds can be estimated from laboratory results for field conditions.

A new regime is established, which is governed by the intense turbulent mixing and permanent rapid disruption of the surface in whitecaps. Thus more than thirty year after the keen and visionary idea of Ed about the low impedence vents in whitecaps could finally be verified experimentally, the detailed mechanisms causing the steep increase of the gas transfer velocity at high wind speeds are still unclear and require further research. Because this effect is clearly not primarily caused by bubbles, it can be either significantly enhanced turbulence at the water surface, or a significantly enlarged surface area for the exchange processes, or a combination of both. Many processes must be considered including the generation of steep small-scale surface waves, the defragmentation of wave crests including the formation of bags (Troitskaya et al. 2017) and spray, the effects of high-speed spray droplets plunging into the water surface again and the effects of bursting bubbles.

Acknowledgements The author would like to thank all members of his research group at Heidelberg University who participated in the realization of the laboratory experiments or the evaluation of the data: Kerstin Krall, Sonja Friman, Angelika Klein, Leonie Flothow, Maximilian Bopp, and Wolfgang Mischler. He is equally grateful for the help of all cooperation partners, who made the measurements at the facilities in Kyoto, Marseille, and Miami facilities possible, among others Satoru Komori from Kyoto University, Brian Haus from RSMAS, Miami, Guillemette Caulliez from MIO, Marseille and Yuliya Troitskaya from the Applied Physics Institute in Nizhny Novgorod. Partial financial support for this research by the German Science Foundation (DFG), projects JA395/17-1 and JA395/17-2 "Air-Sea Gas Exchange at High Wind Speeds" is gratefully acknowledged.

References

Asher, W., & Wanninkhof, R. (1998). The effect of bubble-mediated gas transfer on purposeful dual- gaseous tracer experiments. *Journal of Geophysical Research, 103*. https://doi.org/10.1029/98JC00245.

Asher, W. E., Higgins, B. J., Karle, L. M., Farley, P. J., Sherwood, C. R., Gardiner, W. W., Wan-ninkhof, R., Chen, H., Lantry, T., Steckley, M., Monahan, E. C., Wang, Q., & Smith, P. M. (1995). Measurement of gas transfer, whitecap coverage, and brightness temperature in a surf pool: An overview of WABEX-93. In B. Jähne & E. Monahan (Eds.), *Air-water gas transfer, selected papers, 3rd international symposium On air-water gas transfer* (pp. 205–216). Hanau: AEON. https://doi.org/10.5281/zenodo.10571.

Bell, T. G., Bruyn, W. D., Miller, S. D., Ward, B., Christensen, K. H., & Saltzman, E. S. (2013). Air-sea dimethylsulfide (dms) gas transfer in the North Atlantic: Evidence for limited interfacial gas exchange at high wind speed. *Atmospheric Chemistry and Physics, 13*, 11073–11087. https://doi.org/10.5194/acp-13-11073-2013.

Bell, T. G., Bruyn, W. D., Marandino, C. A., Miller, S. D., Law, C. S., Smith, M. J., & Saltzman, E. S. (2015). Dimethylsulfide gas transfer coefficients from algal blooms in the southern ocean. *Atmospheric Chemistry and Physics, 15*, 1783–1794. https://doi.org/10.5194/acp-15-1783-2015.

Bender, M. L., Kinter, S., Cassar, N., & Wanninkhof, R. (2011). Evaluating gas transfer velocity param- eterizations using upper ocean radon distributions. *Journal of Geophysical Research, 116*(C2), C02010. https://doi.org/10.1029/2009JC005805.

Borges, A.V., Wanninkhof, R. (eds.): 5th international symposium on gas transfer at water surfaces, Journal of marine systems,Amsterdam : Elsevier vol. 66, 1–4 (2007).

Brutsaert, W., & Jirka, G. H. (Eds.). (1984). *Gas transfer at water surfaces*. Dordrecht: Reidel. https://doi.org/10.1007/978-94-017-1660-4.

de Leeuw, G., Kunz, G.J., Caulliez, G., Jaouen, L., Badulin, S., Woolf, D.K., Bowyer, P., Leifer, I. A., Nightingale, P., Liddicoat, M., Rhee, T. S., Andreae, M. O., Larsen, S., Hansen, F. A., & Lund, S. W. (1999). Breaking waves and air-sea gas transfer (LUMINY). *Final report. Tech. Rep. FEL-98-C122*, TNO FEL – Netherlands Organisation for Applied Scientific Research – Physics and Electronics Laboratory.

de Leeuw, G., Kunz, G. J., Caulliez, G., Woolf, D. K., Bowver, P., Leifer, I., Nightingale, P., Liddicoat, M., Rhee, T., Andreae, M. O., Larsen, S., Hansen, F. A., & Lun, S. (2002). LUMINY - an overview. In E. Saltzman, M. Donelan, W. Drennan, & R. Wanninkhof (Eds.), *Gas transfer at water surfaces, geophysical monograph* (Vol. 127, pp. 291–294). American Geophysical Union. https://doi.org/10.1029/GM127p0291.

Donelan, M. A., Drennan, W. M., Saltzman, E. S., & Wanninkhof, R. (Eds.). (2002). *Gas Transfer at Water Surfaces*. American Geophysical Union. https://doi.org/10.1029/GM127.

Flothow, L. (2017). Bubble characteristics from breaking waves in fresh water and simulated seawater. Master's thesis, Institut für Umweltphysik, Universität Heidelberg, Germany. https://doi.org/10.11588/heidok.00023754

Garbe, C. S., Rutgersson, A., Boutin, J., Delille, B., Fairall, C. W., Gruber, N., Hare, J., Ho, D., Johnson, M., de Leeuw, G., Nightingale, P., Pettersson, H., Piskozub, J., Sahlee, E., Tsai, W., Ward, B., Woolf, D. K., & Zappa, C. (2014). Transfer across the air-sea interface. In P. S. Liss & M. T. Johnson (Eds.), *Ocean-atmosphere interactions of gases and particles* (pp. 55–112). Springer. https://doi.org/10.1007/978-3-642-25643-1_2.

Ho, D. T., Law, C. S., Smith, M. J., Schlosser, P., Harville, M., & Hill, P. (2006). Measurements of air-sea gas exchange at high wind speeds in the southern ocean: Implications for global parameteriza- tions. *Geophysical Research Letters, 33*, 16611–16616. https://doi.org/10.1029/2006GL026817.

Ho, D. T., Wanninkhof, R., Schlosser, P., Ullman, D. S., Hebert, D., & Sullivan, K. F. (2011). Toward a universal relationship between wind speed and gas exchange: Gas transfer velocities measured with ^{3} He/SF6 during the Southern Ocean Gas Exchange Experiment. *Journal of Geophysical Research, 116*, C00F04. https://doi.org/10.1029/2010JC006854.

Iwano, K., Takagaki, N., Kurose, R., & Komori, S. (2013). Mass transfer velocity across the breaking air-water interface at extremely high wind speeds. *Tellus B, 65*, 21341. https://doi.org/10.3402/tellusb.v65i0.21341.

Iwano, K., Takagaki, N., Kurose, R., & Komori, S. (2014). Erratum: Mass transfer velocity across the breaking air-water interface at extremely high wind speeds. *Tellus B, 66*, 25233. https://doi.org/10.3402/tellusb.v66.25233.

Jähne, B. (1982). Trockene Deposition von Gasen über Wasser (Gasaustausch). In D. Flothmann (Ed.), *Austausch von Luftverunreinigungen an der Grenzfläche Atmosphäre/Erdoberfläche, Zwischenbericht für das Umweltbundesamt zum Teilprojekt 1: Deposition von Gasen, BleV-R-64.284-2*. Frankfurt: Battelle Institut. https://doi.org/10.5281/zenodo.10278.

Jähne, B. (2019). Air-sea gas exchange. In *Encyclopedia of ocean sciences* (3rd ed.). Academic Press. URL: https://www.elsevier.com/books/encyclopedia-of-ocean-sciences/cochran/978-0-12-813081-0. In press.

Jähne, B., & Monahan, E. C. (1995). *Air-water gas transfer — selected papers from the third international symposium on air-water gas transfer*. Hanau: AEON. https://doi.org/10.11588/heidok.00017063.

Jähne, B., Huber, W., Dutzi, A., Wais, T., & Ilmberger, J. (1984a). Wind/wave-tunnel experiments on the Schmidt number and wave field dependence of air-water gas exchange. In W. Brutsaert & G. H. Jirka (Eds.), *Gas transfer at water surfaces* (pp. 303–309). Hingham: Reidel. https://doi.org/10.1007/978-94-017-1660-4_28.

Jähne, B., Wais, T., & Barabas, M. (1984b). A new optical bubble measuring device; a simple model for bubble contribution to gas exchange. In W. Brutsaert & G. H. Jirka (Eds.), *Gas transfer at water surfaces* (pp. 237–246). Hingham: Reidel. https://doi.org/10.1007/978-94-017-1660-4_22.

Jähne, B., Heinz, G., & Dietrich, W. (1987). Measurement of the diffusion coefficients of sparingly soluble gases in water. *Journal of Geophysical Research, 92*(C10), 10,767–10,776. https://doi.org/10.1029/JC092iC10p10767.

Jessup, A. T., & Asher, W. E. (Eds.). (2016). *7th international symposium on gas transfer at water surfaces* (Vol. 35). IOP Publishing. https://doi.org/10.1088/1755-1315/35/1/011001.

Kiefhaber, D., Reith, S., Rocholz, R., & Jähne, B. (2014). High-speed imaging of short wind waves by shape from refraction. *Journal of the European Optical Society-Rapid Publications, 9*, 14015. https://doi.org/10.2971/jeos.2014.14015.

Komori, S., McGillis, W., & Kurose, R. (Eds.). (2011). *Gas transfer at water surfaces 2010*. Kyoto: Kyoto Univ Press. URL: http://hdl.handle.net/2433/156156.

Krall, K. E., & Jähne, B. (2014). First laboratory study of air-sea gas exchange at hurricane wind speeds. *Ocean Science, 10*, 257–265. https://doi.org/10.5194/os-10-257-2014.

Krall, K., Takagaki, N., Mischler, W., Klein, A., Flothow, L., Komori, S., & Jähne, B. (2016). Investigating the mechanisms of air-sea gas exchange at hurricane wind-speeds in wind-wave tunnel experiemnts. In *Air-sea gas flux; progress and future prospects, IFREMER, Brest, September 6–9, 2016*. https://doi.org/10.5281/zenodo.321372

Krall, K. E., Smith, A. W., Takagaki, N., & Jähne, B. (2019). Air-sea gas exchange at wind speeds up to 85 m s^{-1}. *Ocean Science, 15*, 1783–1799, https://doi.org/10.5194/os-15-1783-2019

Kräuter, C. (2011). Aufteilung des Transferwiderstands zwischen Luft und Wasser beim Austausch flüchtiger Substanzen mittlerer Löslichkeit zwischen Ozean und Atmosphäre. Diplomarbeit, Institut für Umweltphysik, Fakultät für Physik und Astronomie, Univ. Heidelberg. https://doi.org/10.11588/heidok.00013010

Kräuter, C., Richter, K. E., Mesarchaki, E., Rocholz, R., Williams, J., & Jähne, B. (2012). Partitioning of the trasfer resistance between air and water. In *SOLAS open science conference, Washington State, USA*. https://doi.org/10.5281/zenodo.12328

Kunz, J., & Jähne, B. (2018). Investigating small scale air-sea exchange processes via thermography. *Frontiers of Mechanical Engineering, 4*. https://doi.org/10.3389/fmech.2018.00004.

Liss, P. S., & Merlivat, L. (1986). Air-sea gas exchange rates: Introduction and synthesis. In P. Buat-Menard (Ed.), *The role of air-sea exchange in geochemical cycling* (pp. 113–129). Boston: Reidel. https://doi.org/10.1007/978-94-009-4738-2_5.

McGillis, W. R., Edson, J. B., Hare, J. E., & Fairall, C. W. (2001). Direct covariance air-sea CO2 fluxes. *Journal of Geophysical Research, 106*(C8), 16729–16745. https://doi.org/10.1029/2000JC000506.

McNeil, C., & D'Asaro, E. (2007). Parameterization of air sea gas fluxes at extreme wind speeds. *Journal of Marine Systems, 66*, 110–121. https://doi.org/10.1016/j.jmarsys.2006.05.013.

Mischler, W. (2014). Systematic measurements of bubble induced gas exchange for trace gases with low solubilities. Dissertation, Institut für Umweltphysik, Fakultät für Physik und Astronomie, Univ. Heidelberg. https://doi.org/10.11588/heidok.00017720

Mischler, W., & Jähne, B. (2012). Optical measurements of bubbles and spray in wind/water facilities at high wind speeds. In *12th international triennial conference on liquid atomization and spray systems 2012, Heidelberg (ICLASS 2012)*. https://doi.org/10.5281/zenodo.10957

Monahan, E. C., & Spillane, M. C. (1984). The role of oceanic whitecaps in air-sea gas exchange. In W. Brutsaert & G. H. Jirka (Eds.), *Gas transfer at water surfaces* (pp. 495–503). Hingham: Reidel. https://doi.org/10.1007/978-94-017-1660-4_45.

Naegler, T. (2009). Reconciliation of excess ^{14}C-constrained global CO2 piston velocity estimates. *Tellus B, 61*(2), 372–384. https://doi.org/10.1111/j.1600-0889.2008.00408.x.

Nightingale, P. D., Liss, P. S., & Schlosser, P. (2000a). Measurements of air-sea gas transfer during an open ocean algal bloom. *Geophysical Research Letters, 27*, 2117–2120. https://doi.org/10.1029/2000GL011541.

Nightingale, P. D., Malin, G., Law, C. S., Watson, A. J., Liss, P. S., Liddicoat, M. I., Boutin, J., & Upstill-Goddard, R. C. (2000b). In situ evaluation of air-sea gas exchange parameterization using novel conservation and volatile tracers. *Global Biogeochemical Cycles, 14*, 373–387. https://doi.org/10.1029/1999GB900091.

Peng, T. H., Broecker, W. S., Mathieu, G. G., Li, Y. H., & Bainbridge, A. (1979). Radon evasion rates in the Atlantic and Pacific oceans as determined during the geosecs program. *Journal of Geophysical Research, 84*(C5), 2471–2487. https://doi.org/10.1029/JC084iC05p02471.

Roether, W., & Kromer, B. (1984). Optimum application of the radon deficit method to obtain air–sea gas exchange rates. In W. Brutsaert & G. H. Jirka (Eds.), *Gas transfer at water surfaces* (pp. 447–457). Hingham: Reidel. https://doi.org/10.1007/978-94-017-1660-4_41.

Sander, R. (2015). Compilation of henry's law constants (version 4.0) for water as solvent. *Atmospheric Chemistry and Physics, 15*, 4399–4981. https://doi.org/10.5194/acp-15-4399-2015.

Sweeney, C., Gloor, E., Jacobson, A. R., Key, R. M., McKinley, G., Sarmiento, J. L., & Wanninkhof, R. (2007). Constraining global air-sea gas exchange for CO2 with recent bomb ^{14} C measurements. *Global Biogeochemical Cycles, 21*, B2015. https://doi.org/10.1029/2006GB002784.

Takagaki, N., Komori, S., Suzuki, N., Iwano, K., Kuramoto, T., Shimada, S., Kurose, R., & Takahashi, K. (2012). Strong correlation between the drag coefficient and the shape of the wind sea spectrum over a broad range of wind speeds. *Geophysical Research Letters, 39*. https://doi.org/10.1029/2012GL053988.

Troitskaya, Y., Kandaurov, A., Ermakova, O., Kozlov, D., Sergeev, D., & Zilitinkevich, S. (2017). Bag-breakup fragmentation as the dominant mechanism of sea-spray production in high winds. *Scientific Reports, 7*, 1614. https://doi.org/10.1038/s41598-017-01673-9.

Vlahos, P., & Monahan, E. C. (2009). A generalized model for the air-sea transfer of dimethyl sul-fide at high wind speeds. *Geophysical Research Letters, 36*(21), 0094–8276. https://doi.org/10.1029/2009GL040695.

Vlahos, P., Monahan, E., Huebert, B., & Edson, J. (2011). Wind-dependence of DMS transfer velocity: Comparison of model with recent southern ocean observations. In S. Komori, W. McGillis, & R. Kurose (Eds.), *Gas transfer at water surfaces 2010* (pp. 313–321). URL: http://hdl.handle.net/2433/156156.

Wanninkhof, R. (1992). Relationship between wind speed and gas exchange over the ocean. *Journal of Geophysical Research, 97*, 7373–7382. https://doi.org/10.1029/92JC00188.

Wanninkhof, R., & McGillis, W. R. (1999). A cubic relationship between gas transfer and wind speed. *Geophysical Research Letters, 26*, 1889–1892. https://doi.org/10.1029/1999GL900363.

Wanninkhof, R., Asher, W., & Monahan, E. (1995). The influence of bubbles on air-water gas exchange: Results from gas transfer experiments during WABEX-93. In B. Jähne & E. Monahan (Eds.), *Air-water gas transfer, selected papers, 3rd international symposium on air-water gas transfer* (pp. 239–254). Hanau: AEON. https://doi.org/10.5281/zenodo.10571.

Wanninkhof, R., Hitchcock, G., Wiseman, W. J., Vargo, G., Ortner, P. B., Asher, W., Ho, D. T., Schlosser, P., Dickson, M., Masserini, R., Fanning, K., & Zhang, J. (1997). Exchange, dispersion, and biological productivity on the West Florida shelf: Results from a lagrangian tracer study. *Geophysical Research Letters, 24*(14), 1767–1770. https://doi.org/10.1029/97GL01757.

Wanninkhof, R., Sullivan, K. F., & Top, Z. (2004). Air-sea gas transfer in the southern ocean. *Journal of Geophysical Research, 109*, C08S19. https://doi.org/10.1029/2003JC001767.

Wanninkhof, R., Asher, W. E., Ho, D. T., Sweeney, C., & McGillis, W. R. (2009). Advances in quantifying air-sea gas exchange and environmental forcing. *Annual Review of Marine Science, 1*, 213–244. https://doi.org/10.1146/annurev.marine.010908.163742.

Wilhelms, S.C., Gulliver, J.S. (eds.): Air-water mass transfer—Selected papers from the 2nd international symposium on gas transfer at water surfaces, Minneapolis Minnesota, Sept. 11–14, 1990. American Society of Civil Engineers, New York (1991).

Woolf, D., Leifer, I., Nightingale, P., Rhee, T., Bowyer, P., Caulliez, G., de Leeuw, G., Larsen, S., Liddicoat, M., Baker, J., & Andreae, M. (2007). Modelling of bubble-mediated gas transfer: Fundamental principles and a laboratory test. *Journal of Marine Systems, 66*, 71–91. https://doi.org/10.1016/j.jmarsys.2006.02.011.

Yaws, C. L. (1995). *Handbook of transport property data*. Houston: Gulf Publishing Company.

Part III
Whitecaps and Remote Sensing

Chapter 11
Global Whitecap Coverage from Satellite Remote Sensing and Wave Modelling

Magdalena D. Anguelova

Abstract For decades, photographic measurements of whitecap coverage W have been the workhorse for characterizing oceanic whitecaps and parameterizing air-sea processes associated with them. The detail that in situ W data provide is now complemented with the possibilities offered by long-term, consistent determination of W on a global scale from passive microwave remote sensing and from third generation wave modelling. This chapter gives an overview of the development and present status of obtaining the whitecap fraction with remote sensing and wave models.

11.1 Introduction

Global whitecap fraction (or coverage) W can be useful to evaluate more accurately the air-sea surface fluxes of momentum, mass, and energy under a variety of environmental conditions. Reliable assessment of air-sea fluxes is necessary to reproduce more realistically the coupling between the ocean and the atmosphere in numerical weather prediction, chemical transport, and climate models. Usually, computations of global surface fluxes use maps of global whitecap fraction obtained with parameterizations of W as a function of wind speed at a reference height of 10 m above the surface, U_{10}. Numerous $W(U_{10})$ parameterizations exist (Anguelova and Webster 2006; Goddijn-Murphy et al. 2011; Brumer et al. 2017). These are based on in situ (most often shipboard) measurements of U_{10} collected together with photographs of the sea state. Image processing algorithms, involving the choice of an intensity threshold, have been used to extract W from such sea state photographs; see Chap. 2 for details on the photographic method of measuring W.

The exponents of the wind speed dependences in existing $W(U_{10})$ parameterizations vary widely, reflecting local meteorological and oceanographic (hereafter metoc) conditions. Predictions of W with such in situ $W(U_{10})$ parameterizations differ when using U_{10} values from either shipboard data sets, or satellite retrievals, or

M. D. Anguelova (✉)
Remote Sensing Division, Naval Research Laboratory, Washington, DC, USA
e-mail: maggie.anguelova@nrl.navy.mil

P. Vlahos (ed.), *Recent Advances in the Study of Oceanic Whitecaps*,
https://doi.org/10.1007/978-3-030-36371-0_11

numerical models (Goddijn-Murphy et al. 2011; Paget et al. 2015). This implies that the accuracy of global surface fluxes would depend on the choice of the $W(U_{10})$ expression and the source of the U_{10} values.

In addition, individual in situ data sets are not sufficient to support the development of parameterizations predicting the natural variability of whitecap formation, whitecap spatial extent, and whitecap temporal evolution. Each in situ data set represents a limited range of metoc conditions, which hinders the quantification of whitecap dependences beyond that on the wind speed. Compilations of in situ data sets, representative of different experimental sites, had partially alleviated this situation in the past. For example, Monahan and O'Muirchaertaigh (1980) used two data sets to develop the widely used expression $W(U_{10})$ with wind exponent of 3.41. Five in situ data sets enabled Monahan and O'Muirchaertaigh (1986) to clearly demonstrate the dependence of whitecap inception on the sea surface temperature (SST) T and to quantify W in terms of both U_{10} and atmospheric stability ΔT (defined as the difference between SST and air temperature T_a, $\Delta T = T - T_a$). The inclusion of additional dependences in W parametrizations—e.g., those of the wave field and/or the influence of salinity and surface active materials (surfactants)—can help to predict the spread of the W data due to the natural whitecap variability.

However, differences caused by equipment, measuring protocols, and subsequent image processing continue to contribute to the spread of measured or predicted W values based on a medley of photographic data sets (Paget et al. 2015). In short, while in situ field campaigns provide valuable data for detail studies of air-sea processes in different metoc environments, the in situ W data are not sufficient to develop new $W(U_{10}, etc.)$ parameterizations applicable on a global scale.

The desire to minimize the spread of W data associated with difficulties of the photographic method, and the need to predict adequately the natural whitecap variability, led to efforts in the last 15 or so years to develop different methods for measuring whitecap fraction. These methods involve remote sensing and wave models. Both methods have the potential to provide consistent, long-term W data sets covering the global range of metoc conditions. Compiling a database of global W data and additional metoc variables can supply sufficient data to study and quantify the natural whitecap variability. This chapter gives an overview of the development and present status of obtaining whitecap fraction with remote sensing and wave models.

11.2 Satellite Remote Sensing of Whitecap Fraction

Satellite remote sensing is an obvious choice for obtaining global whitecap fraction. Satellite-based observations can provide longstanding daily measurements of whitecaps and controlling (forcing) metoc variables such as wind speed U_{10}, significant wave height H_s, SST T, air temperature T_a, salinity S, and surfactant proxies (e.g., ocean color or primary production). Especially valuable are routine observations from a single satellite platform because simultaneous, collocated measurements of

W and other variables would minimize the spread among data points caused by spatial and temporal mismatch.

Oceanic whitecaps have distinct remote sensing signatures in different regions of the electromagnetic (EM) spectrum, each with specific pros and cons; refer to de Leeuw et al. (2011) for a brief review. The high reflectivity of the sea foam is the basis for whitecap observations at visible wavelengths, including the use of still photographs and video images (Monahan 1971; Bobak et al. 2011). Only recently the photographic method was complimented with a novel method inferring whitecap fraction from the total upwelling radiance measured with a radiometer at visible (411 nm) wavelengths (Randolph et al. 2017).

Observations of breaking waves and surface renewal at infrared (IR) wavelengths have been available for some time (Jessup et al. 1997). Observing and quantifying whitecap properties at IR wavelengths is a recent development. Potter et al. (2015) demonstrated the unique use of IR cameras for whitecap observations. The presence of relatively strong signals in the IR region of the EM spectrum from both actively breaking waves and decaying foam patches allows to quantify the lifetimes of stage A (active, young) and stage B (residual, mature) whitecaps (as defined by Monahan and Lu 1990).

Microwave radiometry is a suitable observational tool of whitecaps due to the high, black-body-like emissivity of sea foam at microwave wavelengths with frequencies of 1–37 GHz (Anguelova and Gaiser 2012). The tractability of removing the atmospheric influence on the signals emanated from whitecaps on the ocean surface is a good justification for satellite-based radiometric observations of W. The relatively low spatial resolution of the satellite observations at microwave frequencies is somewhat compensated by the consideration that microwave radiometers provide statistical (spatially averaged) measure of whitecap fraction, a provision fitting well the stochastic nature of breaking waves (Bondur and Sharkov 1982; Melville and Matusov 2002; Mironov and Dulov 2008). This section summarizes the status of using microwave radiometry to obtain the whitecap fraction from satellite observations.

11.2.1 Microwave Ocean Emissivity and Whitecaps

The microwave remote sensing signature of the whitecaps is related to variations of the natural ocean thermal emission e occurring when wind waves break and produce sea foam. Brightness temperature $T_B = eT$ quantifies the natural ocean thermal emission at microwave frequencies for a given SST. The strong relationship between T_B and the sea foam emissivity is the physical basis for estimating W from satellite microwave observations. The relationship $T_B(W)$ has been established by a long history of passive microwave measurements (see Bobak et al. 2011 and the references there-in). Williams (1969) first measured T_B variations in presence of foam (along with T_B of flat and rough surfaces) and proposed explanation of the high foam emissivity. Subsequent measurements at different microwave frequencies confirmed

the high foam emissivity leading to large variations of T_B (Nordberg et al. 1971; Ross and Cardone 1974; Militskii et al. 1978; Smith 1988; Rose et al. 2002; Padmanabhan et al. 2006).

The remote sensing community saw great opportunity in using the effect of sea foam (and roughness) on T_B for microwave sensing of the ocean, especially for retrieving wind speed U_{10}. The development of geophysical retrieval algorithms required modeling of the emissivity e and T_B of rough (Stogryn 1967; Wentz 1975) and foamy (Droppleman 1970; Stogryn 1972) surfaces. These efforts yielded the first inference of whitecap fraction W using T_B data from the Scanning Multichannel Microwave Radiometer (SMMR) (Pandey and Kakar 1982; Wentz 1983). As the geophysical retrieval algorithms matured, it became clear that it is sufficient to include the sea foam signal only implicitly in wind-induced terms (Wentz 1997; Bettenhausen et al. 2006; Meissner and Wentz 2012). Such representation of sea foam contribution to the T_B registered by a satellite radiometer is valid when we do not seek to retrieve whitecap fraction.

The seminal paper of Monahan and O'Muircheartaigh (1986) introduced the connection between W and the passive remote sensing of the ocean surface to the air-sea interaction community. The Monahan and O'Muircheartaigh (1986) analysis clearly justified the need to account for additional variables when relating T_B, U_{10}, and W. Measurements of T_B and W in a surf pool during the Wave Basin Experiment in October 1993 (WABEX-93) were the first to quantify an air-sea process (namely, air-water gas transfer) using microwave radiometry (Asher et al. 1995). The observed correlation between W and T_B at horizontal (H) and vertical (V) polarizations enabled the derivation of empirical expressions for the gas transfer velocity in terms of measured T_B (Wang et al. 1995). Further analysis by Asher et al. (1998) showed that microwave radiometric data have the necessary precision to obtain gas transfer velocities.

Building on these previous efforts from both the remote sensing and the air-sea interaction communities, Anguelova and Webster (2006) renewed attempts to infer whitecap fraction W from satellite T_B observations. They proved the feasibility of satellite remote sensing of W by using T_Bs from the Special Sensor Microwave Imager (SSM/I).

11.2.2 Passive Remote Sensing of Whitecaps

The concept of an algorithm obtaining whitecap fraction W from satellite measurements of ocean brightness temperature T_B, hereafter referred to as $W(T_B)$ algorithm, has been given in detail by Anguelova and Webster (2006) and Anguelova and Bettenhausen (2019). It is briefly summarized here.

We seek to develop a physical $W(T_B)$ algorithm because it allows to account for processes associated with breaking waves and whitecaps better than empirical expressions do. Physical $W(T_B)$ algorithm must be based on a radiative transfer model (RTM) in order to properly couple air-sea processes with atmospheric

propagation effects. The RTM gives the T_B at the top of the atmosphere (TOA) with four terms:

$$T_{Bp}^{\mathrm{TOA}} = \tau e_p T + T_{BU} + \tau \Omega_{Dp} r_p T_{BD} + \tau^2 \Omega_{Cp} r_p T_C \tag{11.1}$$

where p refers to polarization (H or V) (hereafter omitted for simplicity). The first term in (11.1) is the brightness temperature of a sea surface with emissivity e at SST T. The remaining three terms represent contributions from the atmosphere, namely upwelling and downwelling atmospheric radiation, T_{BU} and T_{BD}, and cosmic background radiation T_C. Reflectivity $r = 1 - e$ represents the reflection of T_{BD} and T_C from the ocean surface back to space. The atmospheric transmissivity τ accounts for the attenuation of the microwave radiation as it propagates up and down through the atmosphere. The Ω factors in the T_{BD} and T_C terms account for their non-specular (diffuse) reflection from a rough sea surface.

Variables e and r in (11.1) carry the information for whitecap fraction W. The surface emissivity e comprises two contributions: emissivity of rough surface e_r and emissivity of whitecaps e_W. Whitecap fraction W controls the relative contributions of terms e_r and e_W to T_B^{TOA} in (11.1). The following equation expresses this premise:

$$e = e_r + e_W = (1 - W)E_r + WE_f \tag{11.2}$$

with E_r being the emissivity of rough, foam-free sea surface and E_f the emissivity of 100% foam-covered sea surface.

Equation (11.2) offers different approaches to obtaining W. Anguelova and Webster (2006) obtained whitecap fraction by solving (11.2) for variable W:

$$W = \frac{e - E_r}{E_f - E_r} \tag{11.3}$$

Anguelova and Bettenhausen (2019) solve (11.2) for the whitecap term:

$$e_W = e - e_r = e - (1 - W)E_r = WE_f. \tag{11.4}$$

From (11.4), Anguelova and Bettenhausen (2019) obtain W as:

$$W = e_W / E_f = (e - e_r)/E_f. \tag{11.5}$$

The composite (roughness + foam) and the roughness-only emissivity terms e and e_r in (11.2, 11.3, 11.4 and 11.5) are obtained by solving (11.1) for the respective sea surface emissivity:

$$e = \left(T_B^{\mathrm{TOA}} - B\right)/A \tag{11.6a}$$

$$e_r = \left(T_{Br}^{\mathrm{TOA}} - B\right)/A \tag{11.6b}$$

where

$$A = \tau(T - \Omega_D T_{BD} - \tau\Omega_C T_C) \tag{11.7a}$$

$$B = T_{BU} + \tau\Omega_D T_{BD} + \tau^2\Omega_C T_C. \tag{11.7b}$$

In (11.3) and (11.5), terms e and e_r are corrected for the atmospheric signal with factors A and B, thus providing W at the surface. Both measured and modeled data are necessary to obtain W with (11.3) or (11.5). The specific choices of data and models lead to different implementations of the $W(T_B)$ algorithm.

11.2.3 Implementations of the $\mathbf{W(T_B)}$ *Algorithm*

Several models are necessary to calculate T_B^{TOA} and T_{Br}^{TOA} in (11.6) with (11.1) and (11.2). An atmospheric model provides the atmospheric variables τ, T_{BU}, and T_{BD}. Models for surface roughness and wave spectrum are necessary for e_r or E_r. A model for the foam emissivity is needed for E_f . We need both instrumental (sensor) and geophysical variables to run these models. The sensor variables include the radiometer frequency f, polarization p, and Earth incidence angle θ. The geophysical variables necessary for the atmospheric model are water vapor V, cloud liquid water L, and SST T. The model for the foam emissivity needs data for T and S. The roughness model, through the wave spectrum, needs data for T, θ, U_{10}, and wind direction. The input variables forcing the models can be geophysical retrievals from different satellites and/or data from numerical models.

Anguelova and Webster (2006) combined simple and empirical models with satellite data to calculate the emissivities in (11.3). They simplified the RTM by assuming specular reflection of T_B from a flat sea surface and setting the Ω factors in (11.1) to 1. Empirical expressions were used to calculate E_r. Foam emissivity E_f was computed from foam reflectivity R_f, which, in turn, was computed with the Fresnel formula using foam permittivity ε_f calculated from the Maxwell Garnett formula (Anguelova 2008) with a constant void fraction. The composite surface emissivity e, corrected for the atmospheric signal as in (11.6a), was obtained from SSM/I observations of T_B at 19.35 GHz. SSM/I retrievals of U_{10}, V, and L were used as input to the chosen models. Anguelova and Webster (2006) suggested two major improvements to further develop the $W(T_B)$ algorithm. These were: (i) Use of physical (instead of empirical and simple) models for rough and foam-covered sea surfaces; and (ii) Use of independent data as input to those models. The decoupling of the sources for T_B and the model inputs aims to avoid intrinsic correlations between the emissivities in (11.3) or (11.5).

Anguelova and Bettenhausen (2019) realized these two suggestions within the framework of the WindSat mission (Gaiser et al. 2004). In pursuing the use of

physical models, Anguelova and Bettenhausen (2019) implemented the $W(T_B)$ algorithm with (11.5) using three notable changes in the modeling. First, they accounted for the non-specular reflections from the ocean surface by including the Ω factors in the RTM (11.1). Second, they used the so-called 2-scale model for the roughness-only term e_r instead of empirical expressions (Bettenhausen et al. 2006). Third, a dedicated foam emissivity RTM was developed for E_f (Anguelova and Gaiser 2013). In pursuing the use of independent data sets as inputs to those models, Anguelova and Bettenhausen (2019) combined WindSat T_B observations for the composite term e with independent geophysical variables (matched in time and space with WinSat T_Bs) to force the roughness and foam models. Specifically, an early (interim) version of the $W(T_B)$ algorithm used wind vector (speed and direction) from QuikSCAT, V and L from SSM/I on platform f13, and SST from NCEP/GDAS (Global Data Assimilation System of the National Centers for Environmental Prediction).

Anguelova and Bettenhausen (2019) show that the interim version of the $W(T_B)$ algorithm produced noisy satellite-based W data mostly due to space-time mismatch of WindSat and external data. Efforts to minimize the spread of the W data yielded a modified version of the interim algorithm, which did not use the WindSat T_Bs observations directly for the composite term e. Rather, the $W(T_B)$ algorithm employed a semi-empirical model for e, which was developed on the basis of WinSat T_Bs (Bettenhausen et al. 2006). This trade-off between W computations using either independent data (to avoid intrinsic correlations of emissivity terms) or direct Windat T_B observations (to avoid spread of W data from collocation) prompted the consideration of an algorithm version with fewer data sources. Disruptions in the availability of external data (e.g., SSM/I on f13 and QuikSCAT failed in 2009) further supported this idea. As a result, an updated (and currently the latest) version of the $W(T_B)$ algorithm uses the WindSat T_Bs for term e in (11.5) and the WindSat geophysical retrievals (T, V, L, U_{10}, and wind direction) for the terms e_r and e_W.

11.2.4 Satellite Whitecap Fraction

The latest (updated) version of the $W(T_B)$ algorithm (Sect. 11.2.3) retrieves whitecap fraction W at four WindSat frequencies, from 10 to 37 GHz, and H and V polarizations. Figure 11.1 shows W retrievals as a function of wind speed U_{10}. Panel a shows W from T_B at 18 GHz, H and V polarizations (squares and asterisks, respectively) in logarithmic scale along the y-axis. The W values at V polarization are lower than the W values at H polarization by a factor of 2–3 depending on the frequency. Panel b shows the wind speed dependence of W retrievals for H polarization at frequencies of 10, 18, and 37 GHz (triangles, squares, and diamonds, respectively) in linear scales. In contrast to the W retrievals at H polarization (Fig. 11.1b), the W values at V polarization differ little for different frequencies (not shown). The satellite W values are compared in Fig. 11.1 to W values from the $W(U_{10})$ parametrization of Monahan and O'Muirchaertaigh (1980) (gray symbols).

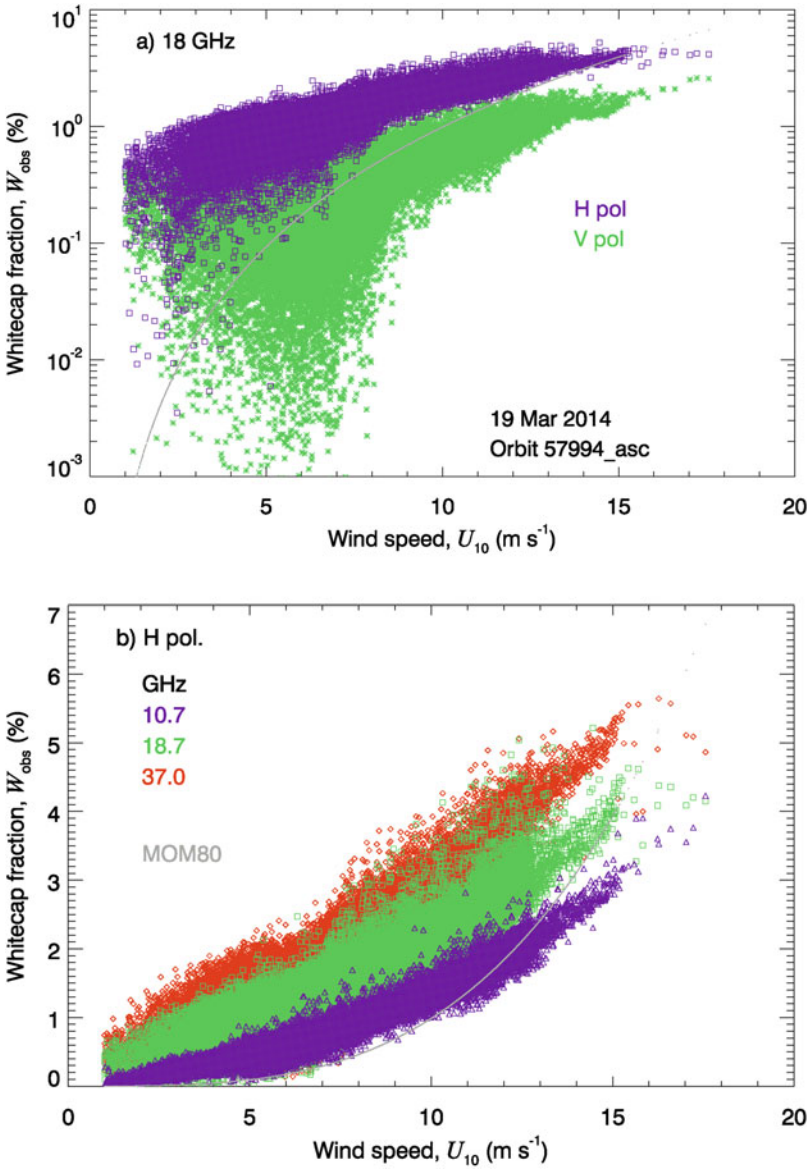

Fig. 11.1 Whitecap fraction W as a function of wind speed U_{10} obtained with the updated (latest) version of the $W(T_B)$ algorithm using WindSat retrievals as input data to models. a) W in logarithmic scale for 18 GHz, H (squares) and V (asterisks) polarizations; b) W for 10 (triangles), 18 (squares), and 37 (diamonds) GHz, H polarization in linear scale. The data are for WindSat orbit 57,994, ascending pass on 19 March 2014. The gray symbols (forming a line) are for the $W(U_{10})$ parameterization of Monahan and O'Muircheartaigh (1980, MOM80 in the legend)

The frequency and polarization variations of the radiometric W values seen in Fig. 11.1 are consistent with both measurements (Rose et al. 2002) and models (Chen et al. 2003). The frequency variations of W arise from the sensitivity of the different frequencies to the thicknesses of the foam layers (Anguelova and Gaiser 2011). Foam layers with different thicknesses provide different skin depths for emission of EM radiation, yielding different foam emissivity, thus varying T_B. These differences provide a crude way to represent whitecaps at different lifetime stages, actively breaking crests (stage A) and residual foam patches (stage B). The polarization variations (at a given frequency) are caused by different polarization sensitivity to surface roughness. The EM signals at H polarization are sensitive to both roughness and foam, and thus vary stronger with U_{10}. Conversely, the signals at V polarization are caused (presumably) mainly by the foam (V polarization is the least sensitive to roughness at $\theta \cong 53°$). These polarization differences can be helpful for tuning the $W(T_B)$ algorithm to minimize the contribution from roughness, thus to improve the retrievals of whitecap coverage.

Figure 11.2 shows global maps of W retrievals at 18 GHz (top panel) and W values obtained with the $W(U_{10})$ parametrization of Monahan and O'Muirchaertaigh (1980) (bottom panel). The data are for 19 March 2014. The comparison of the global maps shows more uniform distribution of the satellite W data from low to high latitudes compared to the one based on photographic data. This reflects the expected change of wind speed dependence due to influences of different environmental factors (Anguelova and Webster 2006; Monahan et al. 2015). The validation of the satellite W data is ongoing work (Anguelova and Bettenhausen 2019).

11.3 Whitecap Fraction Inferred from Wave Models

Until recently, the air-sea interaction community has been underutilizing wave modelling regarding whitecap fraction W. Wave modeling has been mostly called for to provide wave field characteristics for inclusion in W parameterizations. Early works proposed parameterizations of W in terms of wave spectrum (Ross and Cardone 1974; Snyder and Kennedy 1983) and wave age (Kraan et al. 1996). Numerous studies argued for explicit inclusion of wave field characteristics in the roughness length z_0 for better representation of friction velocity u_* (Donelan et al. 1993; Fairall et al. 2000; Taylor and Yelland 2001; Bourassa 2004). Accounting for the wave field via z_0 has the potential to improve $W(u_*)$ parameterizations. Parameterizations of W in terms of a (dimensionless) breaking wave parameter explicitly combine u_* with wave field characteristics such as the peak angular velocity of the wave spectrum ω_p (Zhao and Toba 2001) or H_s (Woolf 2005). Modified existing or new $W(U_{10}, etc.)$ parametrizations have used both measured or modeled data to account for the wave field (Sugihara et al. 2007; Salisbury et al. 2013; Brumer et al. 2017).

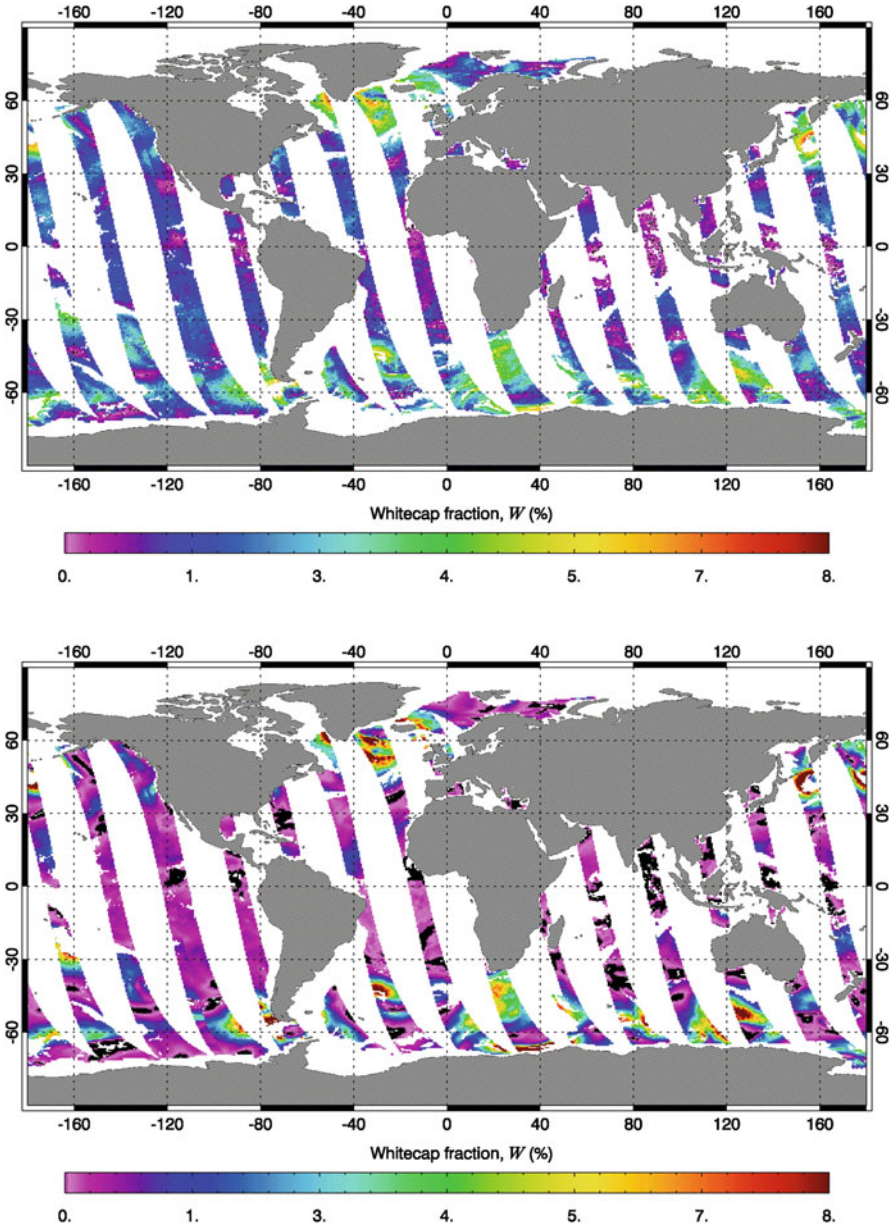

Fig. 11.2 Daily maps of whitecap fraction (19 Mar 2014): (top panel) W at 18 GHz, H polarization, obtained with the updated (latest) version of the $W(T_B)$ algorithm; (bottom panel) W from the $W(U_{10})$ parametrization of Monahan and O'Muirchaertaigh (1980) calculated with WindSat retrieval of U_{10}

Inferring (not parameterizing) W directly from wave models is a recent development. The long-standing work on including the effect of breaking wave in wave models (Komen et al. 1994; WISE Group 2007) has paved the way to this new capability. The physical basis for inferring W from wave models is the strong relationship between whitecap fraction W and the rate of energy dissipation ε. This section highlights the development and status of using wave modelling to determine whitecap fraction.

11.3.1 Breaking Waves, Energy Dissipation, and Whitecaps

Breaking waves dissipate the energy transferred from the wind to the waves. Whitecaps are the most direct, visual expression of wave breaking with air entrainment in the ocean. It is thus only logical that the two quantities that characterize the wave breaking phenomenon—namely, the rate of energy dissipation ε and the whitecap fraction W—are related. In fact, even the ubiquitous $W(U_{10})$ parameterizations originate from this $W(\varepsilon)$ relationship following the reasoning (Wu 1979, 1988, 1992):

$$W \propto \varepsilon = \tau V_c \propto \tau u_* \propto \left(C_{10}U_{10}^2\right)\left(C_{10}^{1/2}U_{10}\right) \propto U_{10}^{3.75} \tag{11.8}$$

where τ this time denotes the wind stress (not the atmospheric transmissivity as in Sect. 11.2.2), V_c is surface drift current, and C_{10} is the wind stress (or drag) coefficient.

Equation (11.8) builds on the assumption that whitecaps manifest the dissipation of excessive energy transferred from the air flow to the fully developed spectral components of the wave spectrum (Cardone 1969). This assumption contains two important notions. First, wave breaking with air entrainment is the main dissipative mechanism, thus ignoring other dissipation pathways such as microscale breaking and bottom friction (Banner and Peregrine 1993). Second, the spectral energy dissipation $S_{ds}(\omega,\theta)$ balances the spectral energy input $S_{in}(\omega,\theta)$ in the equilibrium range of the wave spectrum (Phillips 1985). This basis allows determining the total energy dissipation rate $\langle S_{ds}\rangle$ (also denoted Φ_{oc} or ε_t) of the wave field by integrating the dissipation (or the wind input) functions over wave spectrum frequency ω and direction θ (the meaning of notation θ here differs from that in Sect. 11.2.3):

$$\langle S_{ds}\rangle = \rho_w g \int_0^{2\pi}\int_0^{\infty} S_{ds}(\omega,\theta)d\omega\, d\theta \tag{11.9}$$

where ρ_w is the density of water and g is the acceleration due to gravity. Spectral wave models provide $S_{ds}(\omega,\theta)$. Using field data, Hwang and Sletten (2008) prove

this expected balance for the spectrally averaged terms of wind energy input $\langle S_{in} \rangle$ and wave energy dissipation $\langle S_{ds} \rangle$:

$$\langle S_{in} \rangle \cong \langle S_{ds} \rangle \tag{11.10}$$

Ross and Cardone (1974) first derived a linear expression for $W(\varepsilon)$ by combining aircraft observations of whitecaps and a simple model describing the growth of the wave spectrum due to energy transferred from a turbulent wind profile. Kraan et al. (1996) first compared W observations with W estimates from a wave model. Hanson and Phillips (1999) employed W from video records and ε computed from measured wave spectra to demonstrate that using $W(\varepsilon)$ expression reduces the range of W data scatter by 2–3 orders of magnitude compared to using $W(U_{10})$ parameterizations.

Phillips (1985) developed a theoretical framework to express W and ε in terms of breaking wave statistical properties. Phillips (1985) defined a statistical variable called breaking crest length distribution $\Lambda(\boldsymbol{c})d\boldsymbol{c}$, which quantifies the total length of breaking crests per unit area moving with a velocity in the range ($\boldsymbol{c}$, $\boldsymbol{c}$ + $d\boldsymbol{c}$) (bold letters denote vector variable). Phillips (1985) uses moments of the Λ distribution to define various breaking wave statistics. Combining the first moment of $\Lambda(\boldsymbol{c})d\boldsymbol{c}$ with the persistence time of the bubbles T_{bub}, gives the active whitecap fraction:

$$W_A = \int_c T_{bub} c \Lambda(\boldsymbol{c}) d\boldsymbol{c} \tag{11.11}$$

The fifth moment of the Λ distribution determines the energy dissipation rate:

$$\varepsilon(\boldsymbol{c})d\boldsymbol{c} \propto c^5 \Lambda(\boldsymbol{c})d\boldsymbol{c} \tag{11.12}$$

Expressions (11.10, 11.11 and 11.12) allow inferring whitecap fraction W from wave models.

11.3.2 Whitecaps from Wave Models

A full-spectral third-generation wind-wave model (WW3) uses the directional wavenumber (k) spectrum (or wave spectral energy) $F(k, \theta)$ to calculate various quantities of the wave field (WAMDI Group 1988; Komen et al. 1994; Tolman et al. 2002). Used also is the action density spectrum $N(k, \theta) = F(k, \theta)/\sigma$, where $\sigma = 2\pi f_r$ is the intrinsic radian frequency corresponding to relative frequency f_r. The wave model gives the evolution of the spectral energy in space (x, y) and time t, $F(k, \theta,$

x, y, t), using the wave energy balance equation:

$$\frac{DF}{Dt} = S_{in} + S_{nl} + S_{ds} \tag{11.13}$$

where D/Dt is the total (material) derivative and terms S are the various source and sink terms, which drive the evolution and propagation of the spectral energy F. In addition to the terms of energy input from the wind S_{in} and energy dissipation S_{ds}, the wave field is shaped by the non-linear wave-wave interaction term S_{nl}, which transfers the input energy from large to small scales.

Different wave models use different functional representations for the dissipation term S_{ds}. The spectral wave model developed by the European Center for Medium range Weather Forecasting (ECMWF), referred to as ECWAM, uses the dissipation source term of Hasselmann (1974) adjusted by Janssen et al. (1989) for proper balance at the high frequencies. It employs the total wave variance per square meter m_0 and the action density spectrum N (ECMWF 2013). The spectral wave model WAVEWATCH III, now used operationally at NOAA/NCEP (referred to as WWATCH), models S_{ds} with two contributions (Ardhuin et al. 2010), namely spontaneous dissipation $S_{sp}(k, \theta)$ that occurs when waves become steep and break, and cumulative dissipation $S_{cu}(k, \theta)$ that occurs when large-scale breakers overtake shorter waves and induce their breaking (Banner et al. 1989). The spontaneous breaking term $S_{sp}(k, \theta)$ is parameterized in terms of directional saturation spectrum $B(k, \theta)$ [i.e., related to $k^3F(k, \theta)$]. The cumulative term $S_{cu}(k, \theta)$ is parameterized in terms of Λ distribution, which, in turn, is represented with the breaking probability $P(k, \theta)$. Following Banner et al. (2002), the breaking probability is expressed via the saturation wave spectrum $B(k, \theta)$.

There are three approaches to obtain W from a spectral wave model using term S_{ds} or other functional representations.

Scanlon et al. (2016) approach relates the total energy dissipation ε_t (or Φ_{oc}) obtained with (11.10) directly to W. Following Kraan et al. (1996), Scanlon et al. (2016) assume a linear relationship between W and Φ_{oc}:

$$\langle S_{ds} \rangle \equiv \Phi_{\mathrm{oc}} = \gamma \rho_w g W \omega_p E \tag{11.14}$$

Here $E = (H_s/4)^2$ is the wave variance and factor γ represents the average fraction of total wave energy dissipated per whitecap event. Factor γ allows tuning of the results. From (11.14), W is obtained as:

$$W(\Phi_{\mathrm{oc}}) = \frac{\Phi_{\mathrm{oc}}}{\gamma \rho_w g W \omega_p E} \tag{11.15}$$

Leckler et al. (2013) approach uses Phillips (1985) concept for Λ distribution. Following Reul and Chapron (2003), the expression used is:

$$W(\Lambda) = \int_{c_{min}}^{c_p} a\lambda_c \Lambda(c) dc \tag{11.16}$$

where a is a constant and $\lambda_c = 2\pi c^2/g$ is the wavelength of the breaker. The $\Lambda(c)dc$ is converted to wavenumber form $\Lambda(k_b)dk_b$ and parameterized in terms the breaking probability $P(k)$. In addition to using it in (11.16), the $\Lambda(k_b)$ parameterization is also used to obtain the cumulative term $S_{cu}(k, \theta)$ in S_{ds}.

Anguelova and Hwang (2016) approach also uses the Phillips (1985) concept for Λ distribution. However, Anguelova and Hwang combine (11.11) and (11.12) to develop an expression for W in terms of $\varepsilon_t \equiv \langle S_{ds} \rangle$, not Λ:

$$W(\varepsilon_t) = \frac{gT}{4b\rho_w} \frac{\varepsilon_t}{c_{min}^4 \ln(c_{max}/c_{min})} \tag{11.17}$$

Here b is the breaking strength parameter (Drazen et al. 2008) and (c_{min}, c_{max}) define the range of breaking front speeds over which (11.11) is integrated. Expression (11.17) uses proper breaking statistics, but does not rely on $\Lambda(c)$ data, which are difficult to measure.

11.3.3 Modelled Whitecap Fraction

Scanlon et al. (2016) used the most recent version of ECWAM (model cycle 41R1) to obtain Φ_{oc} in (11.14) on 11-km resolution with 1-hourly output. To minimize the influence of swell-dominated sea on the W estimates, Scanlon et al. (2016) used the mean frequency $\overline{\omega}$ of the windsea part of the wave spectra instead of ω_p. The default setting of $\gamma = 0.01$ was used. The modelled W values were compared to photographically measure W values for both total (stages A + B) and active (stage A alone) whitecaps. A bias in the modeled W (positive intercept of the y axis), as compared to measured W, was minimized by introducing a threshold term in (11.15) depending on u_*:

$$W(\Phi_{oc}) = \begin{cases} \dfrac{\Phi_{oc}}{\gamma \rho_w g W \omega_p E} \left(\dfrac{u_* - u_{*T}}{u_*} \right)^3, & u_* > u_{*T} \\ 0, & u_* \le u_{*T} \end{cases} \tag{11.18}$$

where $u_{*T} = 0.065$ m s^{-1}. Tuning of the modeled W values with the γ factor also improved the comparison to measured W values. Setting $\gamma = 0.036$ and $\gamma = 0.0078$ provided the best comparisons to measured active and total W values, respectively. This γ tuning provided useful insights for the relative contributions of the active and

total whitecaps to the energy dissipation by breaking waves. The reduced γ values for the comparison to the total W data confirmed the expectation that the residual (decaying) whitecaps contribute much less to the energy transfer (from the wind to the wave to the underlying currents) than the active breaking crests.

Overall, Scanlon et al. (2016) results showed that the ECWAM dissipation term Φ_{oc} is more strongly related to the actively breaking crest (stage A whitecaps) than the mature whitecaps. Despite successful modifications as (11.18) and tuning with factor γ, the 1:1 comparison of modeled and measured W values still shows some scatter, especially at low W values. Scanlon et al. (2016) suggest that further refinement of the microscale breaking (without air entrainment) in Φ_{oc} and better account of additional metoc conditions on W may improve the modeled W values. Scanlon et al. (2016) see a great promise of providing global W data from ECWAM, which can help constrain satellite W data.

Leckler et al. (2013) used WWATCH (Sect. 11.3.2) to first compute the breaking probability $P(k)$, then $\Lambda(k_b)$, and finally obtaining $W(\Lambda)$ with (11.16). The choice of model settings (denoted TEST570 in their Table 11.1) makes the computations of the cumulative dissipation term (Sect. 11.3.2) more consistent with the spontaneous dissipation term compared to previous TEST settings. The wind speed dependence of the modeled W values compares reasonably well to that of W obtained with the W (U_{10}) expression of Monahan and Woolf (1989). Comparison of the WWATCH modeled W values to satellite W values obtained with the early (interim) version of the $W(T_B)$ algorithm (Sect. 11.2.3) gives larger spread. Leckler et al. (2013) attribute part of this spread to the use of ECMWF U_{10} data instead of the U_{10} data used to obtain the satellite W values. This is consistent with the analysis of Albert et al. (2016, their Sect. 3.1.2) who estimated about 5% differences in W values obtained from parametrizations using U_{10} from different sources. The 1:1 comparison of the WWATCH W data to satellite W data (Fig. 8 in Leckler et al. 2013) is better for satellite data at 10 GHz than at 37 GHz. Because satellite data at 10 GHz are more representative of active (stage A) whitecaps, this result corroborates the result of Scanlon et al. (2016) that wave models predict active W better. Leckler et al. (2013) see great advantage in modeling W for constraining the WWATCH dissipation term. Finally, Leckler et al. (2013) also see promise in the synergy between global WWATCH W data and satellite W data for further improvements of both methods.

Rogers et al. (2012) also modeled W with (11.16) using WWATCH but with TEST451 settings (Table 1 of Leckler et al. 2013). Figure 11.3 shows the calculated total dissipation term $\langle S_{ds} \rangle$ on a global scale. Rogers et al. (2012) investigated the sensitivity of S_{ds} and W calculations to the choice of the maximum prognostic frequency $f_{r\max}$ used for the S_{ds} integration. Using $f_{r\max} = 3.85$ Hz, the calculations include in the S_{ds} modeling waves as short as 10 cm; this is optimal for the S_{ds} prediction. Use of $f_{r\max} = 0.76$ Hz includes waves no shorter than 2.7 m; this may underestimate S_{ds}, especially at lower wind speeds. The results showed that the choice of $f_{r\max}$ has modest effect on $\langle S_{ds} \rangle$: the change from 0.76 Hz to 3.85 Hz increased $\langle S_{ds} \rangle$ value by 24%. However, the same change of $f_{r\max}$ increased the W values by a factor of 3.6. Modeled W values are also sensitive to the setting of constant a in (11.16). For a fixed $f_{r\max} = 0.76$ Hz, the change of a from 0.3 to 0.8

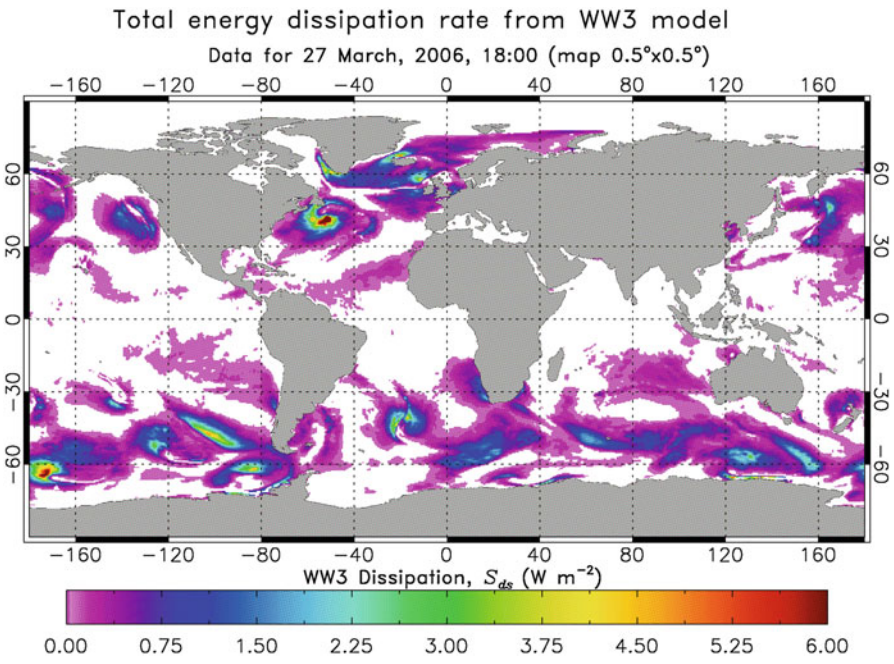

Fig. 11.3 Global map of the total energy dissipation rate from WAVEWATCH III model

increases W by a factor of 2.6. Comparison of the modeled W to satellite W (at 10 GHz) in Fig. 11.4 constrains the choice of this constant to $a = 0.3$, thus predicting W up to 5% over the globe.

Anguelova and Hwang (2016) used (11.17) to obtain W from buoy data with the parametric model of Hwang and Sletten (2008) for ε_t. However, the total dissipation in (11.17) can be obtained with other means, including the use of the wave model dissipation term $\langle S_{ds} \rangle$. Expression (11.17) is a viable alternative to both (11.15) and (11.16). On one hand, it relies solely on $\langle S_{ds} \rangle$, as in (11.15), but incorporates sound physics for the breaking statistics by virtue of its derivation from (11.11 and 11.12). On the other hand, it circumvent uncertainties in determining W caused by $\Lambda(c)$ that might be present in (11.16). Therefore, future work on using (11.17) with wave model S_{ds} is recommended.

11.4 Conclusions

The field of determining whitecap coverage W from sea state photographs, and the associated whitecap method of parameterizing air-sea fluxes of heat, gases, and sea spray, builds on the long-term, dedicate work of Dr. Edward C. Monahan. Photographic in situ measurements of W are invaluable for detail studies of air-sea

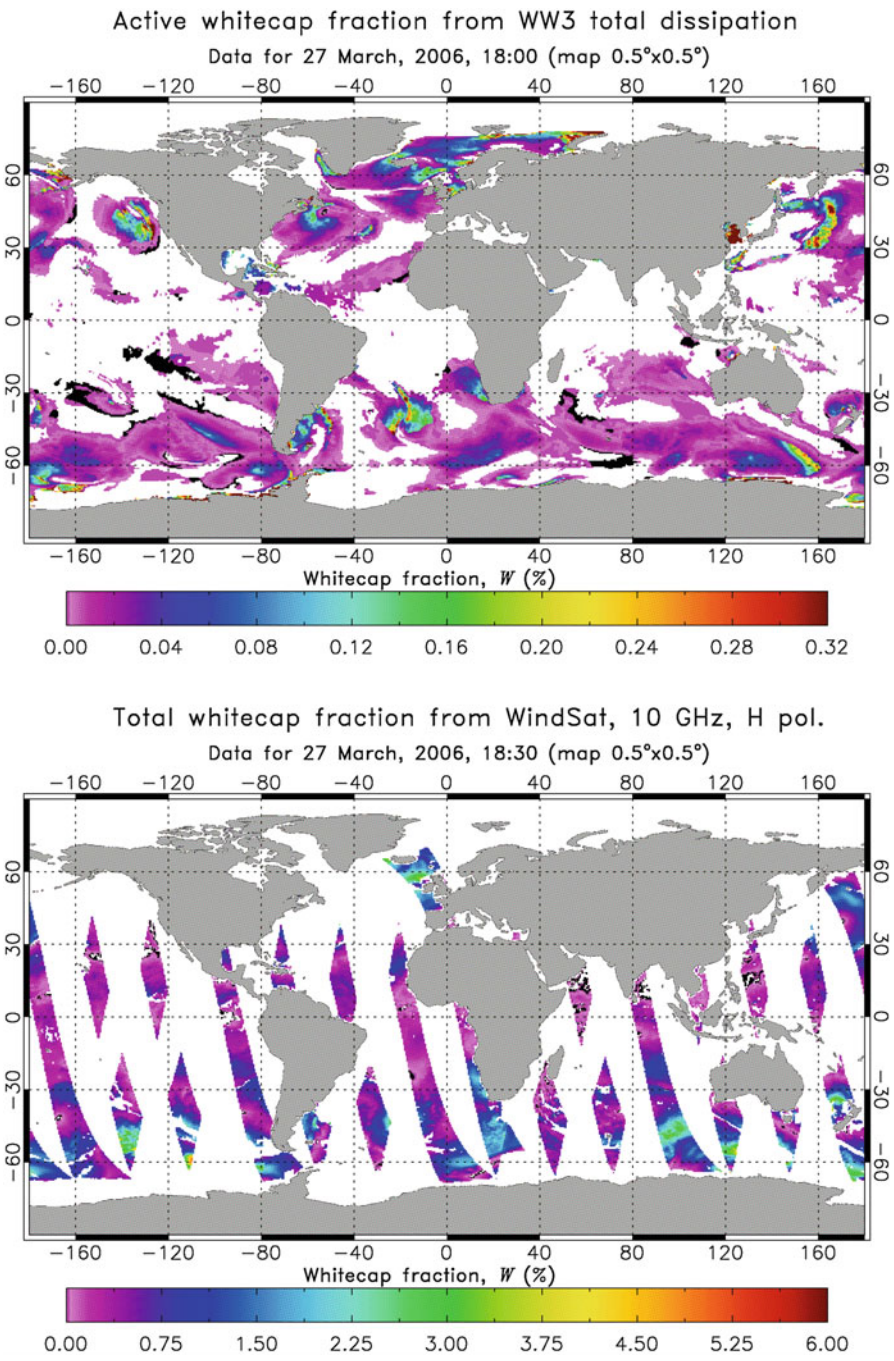

Fig. 11.4 Global maps of: (top panel) Active (stage A) whitecap fraction W from WAVEWATCH III model obtained with (11.16); (bottom panel) Predominantly active whitecap fraction W from satellite radiometric observations at 10 GHz (H polarization), obtained with early (interim) version of the $W(T_B)$ algorithm

processes. However, to improve the applicability of whitecap parametrizations to global scales, different methods need to complement the photographic W data.

Remote sensing methods at visible, infrared, and radio wavelengths and frequencies are now available to observe and measure whitecaps. Passive remote sensing of W uses brightness temperature T_B to determine W after atmospheric correction. Different versions of the $W(T_B)$ algorithm have been developed using physically sound models and various data sources as model inputs. Early versions using external data, while successful, showed wider spread of the estimated W data due to collocation mismatch. The latest version uses T_B data and model inputs from WindSat and shows improved W retrievals. Work on tuning and improving the W (T_B) algorithm is ongoing.

Inferring W from wave models shows great promise for inferring W on a global scale. The dissipation term from a wave model is used to determine W. Three different approaches of determining W are now demonstrated. Comparisons to in situ and satellite W data establish that wave models predict well the active whitecaps. The synergy between W data from satellite retreivals and wave modeling provide basis for mutual constrain and further improvements of these new methods.

Acknowledgments I am deeply grateful to Peter W. Gaiser and Richard M. Bevilacqua for unwavering support in pursuing passive remote sensing of whitecaps at Remote Sensing Division, NRL. The significant contributions of Michael H. Bettenhausen and William F. Johnston in developing the WindSat forward model and producing the WindSat data is acknowledged and highly appreciated. Credit is due to W. Erick Rogers for his work on the wave modeling. This work was sponsored by the Office of Naval Research (NRL program element 61153 N).

References

Albert, M. F. M. A., Anguelova, M. D., Manders, A. M. M., Schaap, M., & de Leeuw, G. (2016). Parameterization of oceanic whitecap fraction based on satellite observations. *Atmospheric Chemistry and Physics, 16*, 13725–13751. https://doi.org/10.5194/acp-16-13725-2016.

Anguelova, M. D. (2008). Complex dielectric constant of sea foam at microwave frequencies. *Journal of Geophysical Research, 113*, C08001. https://doi.org/10.1029/2007JC004212.

Anguelova, M. D., & Bettenhausen, M. H. (2019). Whitecap fraction from satellite measurements: Algorithm description. *Journal of Geophysical Research, 124*, 1827–1857. https://doi.org/10.1029/2018JC014630.

Anguelova, M. D., & Gaiser, P. W. (2011). Skin depth at microwave frequencies of sea foam layers with vertical profile of void fraction. *Journal of Geophysical Research, 116*, C11002. https://doi.org/10.1029/2011JC007372.

Anguelova, M. D., & Gaiser, P. W. (2012). Dielectric and radiative properties of sea foam at microwave frequencies: Conceptual understanding of foam emissivity. *Remote Sensing, 4*, 1162–1189. https://doi.org/10.3390/rs4051162.

Anguelova, M. D., & Gaiser, P. W. (2013). Microwave emissivity of sea foam layers with vertically inhomogeneous dielectric properties. *Remote Sensing of Environment, 139*, 81–96. https://doi.org/10.1016/j.rse.2013.07.017.

Anguelova, M. D., & Hwang, P. A. (2016). Using energy dissipation rate to obtain active whitecap fraction. *Journal of Physical Oceanography, 46*, 461–481. https://doi.org/10.1175/JPO-D-15-0069.1.

Anguelova, M. D., & Webster, F. (2006). Whitecap coverage from satellite measurements: A first step toward modeling the variability of oceanic whitecaps. *Journal of Geophysical Research, 111*, C03017. https://doi.org/10.1029/2005JC003158.

Ardhuin, F., Rogers, E., Babanin, A., Filipot, J.-F., Magne, R., Roland, A., van der Westhuysen, A., Queffeulou, P., Lefevre, J.-M., Aouf, L., & Collard, F. (2010). Semi-empirical dissipation source functions for ocean waves: Part I, definitions, calibration and validations. *Journal of Physical Oceanography, 40*, 1917–1941.

Asher, W. E., et al. (1995). Measurement of gas transfer, whitecap coverage, and brightness temperature in a surf pool: An overview of WABEX-93. In B. Jähne & E. Monahan (Eds.), *Air-water gas transfer* (pp. 205–216). Hanau: AEON Verlag.

Asher, W. E., Wang, Q., Monahan, E. C., & Smith, P. M. (1998). Estimation of air--sea gas transfer velocities from apparent microwave brightness temperature. *Marine Technology Society Journal, 32*, 32–40.

Banner, M. L., Jones, I. S. F., & Trinder, J. C. (1989). Wavenumber spectra of short gravity waves. *Journal of Fluid Mechanics, 198*, 321–344. https://doi.org/10.1017/S0022112089000157.

Banner, M. L., Gemmrich, J. R., & Farmer, D. M. (2002). Multiscale measurement of ocean wave breaking probability. *Journal of Physical Oceanography, 32*, 3364–3374.

Banner, M. L., & Peregrine, D. H. (1993). Wave breaking in deep water. *Annual Review of Fluid Mechanics, 25*(1), 373–397. https://doi.org/10.1146/annurev.fl.25.010193.002105.

Bettenhausen, M. H., Smith, C .K., Bevilacqua, R. M., Wang, N.–Y., Gaiser, P. W., and Cox, S. (2006). A nonlinear optimization algorithm for WindSat wind vector retrievals. Transactions on Geoscience and Remote Sensing, 44(3), 597–610. https://doi.org/10.1109/TGRS.2005.862504.

Bobak, J. P., Asher, W. E., Dowgiallo, D. J., & Anguelova, M. D. (2011). Aerial radiometric and video measurements of whitecap coverage. *Transactions on Geoscience and Remote Sensing, 49*(6), 2183–2193. https://doi.org/10.1109/TGRS.2010.2103565.

Bondur, V., & Sharkov, E. (1982). Statistical properties of whitecaps on a rough sea. *Oceanology, 22*, 274–279.

Bourassa, M. (2004). An improved sea state dependency for surface stress derived from in situ and remotely sensed winds. *Advances in Space Research, 33*, 1136–1142.

Brumer, S. E., Zappa, C. J., Brooks, I. M., Tamura, H., Brown, S. M., Blomquist, B. W., Fairall, C. W., & Cifuentes-Lorenzen, A. (2017). Whitecap coverage dependence on wind and wave statistics as observed during SO GasEx and HiWinGS. *Journal of Physical Oceanography, 47*, 2211–2235. https://doi.org/10.1175/JPO-D-17-0005.1.

Cardone, V. J. (1969). *Specification of the wind distribution in the marine boundary layer for wave forecasting* (Tech. Rep. 69–1, Geophys) (131 pp). Sci. Lab: New York University.

Chen, D., Tsang, L., Zhou, L., Reising, S. C., Asher, W. E., Rose, L. A., Ding, K. H., & Chen, C. T. (2003). Microwave emission and scattering of foam based on Monte Carlo simulations of dense media. *IEEE Transactions on Geoscience and Remote Sensing, 41*, 782–790.

de Leeuw, G., Andreas, E. L , Anguelova, M. D., Fairall, C. W., Lewis, E. R., O'Dowd, C. D., Schulz, M., and Schwartz, S. E. (2011). Production flux of sea-spray aerosol. Reviews of Geophysics, 49, RG2001. https://doi.org/10.1029/2010RG000349.

Donelan, M., Dobson, F., Smith, S., & Anderson, R. (1993). On the dependence of sea surface roughness on wave development. *Journal of Physical Oceanography, 23*, 2143–2149.

Drazen, D. A., Melville, W. K., & Lenain, L. (2008). Inertial scaling of dissipation in unsteady breaking waves. *Journal of Fluid Mechanics, 611*, 307332. https://doi.org/10.1017/S0022112008002826.

Droppleman, J. (1970). Apparent microwave emissivity of sea foam. *Journal of Geophysical Research, 75*, 696–698.

ECMWF. (2013). *IFS documentation CY40r1, Part VII: ECMWF Wave Model*. ECMWF Model Doc., 79 p., http://www.ecmwf.int/sites/default/files/IFS_CY40R1_Part7.pdf

Fairall, C., Hare, J., Edson, J., & McGillis, W. (2000). Parameterization and micrometeorological measurement of Air–Sea gas transfer. *Boundary-Layer Meteorology, 96*, 63–106.

Gaiser, P. W., St Germain, K. M., Twarog, E. M., Poe, G. A., Purdy, W., Richardson, D., et al. (2004). The WindSat spaceborne polarimetric microwave radiometer: Sensor description and early orbit performance. *Transactions on Geoscience and Remote Sensing, 42*, 2347–2361. https://doi.org/10.1109/TGRS.2004.836867.

Goddijn-Murphy, L., Woolf, D. K., & Callaghan, A. H. (2011). Parameterizations and algorithms for oceanic whitecap coverage. *Journal of Physical Oceanography, 41*, 742–756.

Hanson, J. L., & Phillips, O. M. (1999). Wind sea growth and dissipation in the open ocean. *Journal of Physical Oceanography, 29*, 1633–1648.

Hasselmann, K. (1974). On the spectral dissipation of ocean waves due to whitecapping. *Boundary-Layer Meteorology, 6*, 107–127.

Hwang, P. A., & Sletten, M. A. (2008). Energy dissipation of wind-generated waves and whitecap coverage. *Journal of Geophysical Research, 113*, C02012. https://doi.org/10.1029/2007JC004277. (Corrigendum 2009, 114, C02015. https://doi.org/10.1029/2008JC005244).

Janssen, P. A. E. M., Lionello, P., Reistad, M., & Hollingsworth, A. (1989). Hindcasts and data assimilation studies with the WAM model during the Seasat period. *Journal of Geophysical Research, C94*, 973–993.

Jessup, A. T., Zappa, C. J., Loewen, M. R., & Hesany, V. (1997). Infrared remote sensing of breaking waves. *Nature, 385*, 52–55.

Komen, G. J., Cavaleri, L., Donelan, M., Hasselmann, K., Hasselmann, S., & Janssen, P. A. E. M. (1994). *Dynamics and modeling of ocean waves* (532 pp). Cambridge: Cambridge University Press.

Kraan, C., Oost, W., & Janssen, P. (1996). Wave energy dissipation by whitecaps. *Journal of Atmospheric and Oceanic Technology, 13*, 262–267.

Leckler, F., Ardhuin, F., Filipot, J. F., & Mironov, A. (2013). Dissipation source terms and whitecap statistics. *Ocean Modelling, 70*(2013), 62–74. https://doi.org/10.1016/j.ocemod.2013.03.007.

Meissner, T., & Wentz, F. J. (2012). The emissivity of the ocean surface between 6 and 90 GHz over a large range of wind speeds and earth incidence angles. *Transactions on Geoscience and Remote Sensing, 50*(8), 3004–3026. https://doi.org/10.1109/TGRS.2011.2179662.

Melville, W., & Matusov, P. (2002). Distribution of breaking waves at the ocean surface. *Nature, 417*, 58–63.

Militskii, Y. A., Raizer, V. Y., Sharkov, E. A., & Etkin, V. S. (1978). Thermal radio emission from foam structures. *Soviet Physics – Technical Physics, 23*, 601–602.

Mironov, A. S., & Dulov, V. A. (2008). Detection of wave breaking using sea surface video records. *Measurement Science and Technology, 19*, 015405. https://doi.org/10.1088/0957-0233/19/1/015405.

Monahan, E. C. (1971). Oceanic whitecaps. *Journal of Physical Oceanography, 1*, 139–144.

Monahan, E. C., Hooker, G., Zappa, C. J. (2015). The latitudinal variation in the wind-speed parameterization of oceanic whitecap coverage; implications for global modelling of air-sea gas flux and sea surface aerosol generation. In: *19th Conference on Air-Sea Interaction, January 04–08, Phoenix, AZ.*

Monahan, E. C., & Lu, M. (1990). Acoustically relevant bubble assemblages and their dependence on meteorological parameters. *Journal of Oceanic Engineering, 15*(4), 340–349. https://doi.org/10.1109/48.103530.

Monahan, E. C., & O'Muircheartaigh, I. (1980). Optimal power-law description of oceanic whitecap coverage dependence on wind speed. *Journal of Physical Oceanography, 10*, 2094–2099. https://doi.org/10.1175/1520-0485(1980)010<2094:OPLDOO>2.0.CO;2.

Monahan, E. C., & O'Muircheartaigh, I. (1986). Whitecaps and the passive remote sensing of the ocean surface. *International Journal of Remote Sensing, 7*, 627–642. https://doi.org/10.1080/01431168608954716.

Monahan, E. C., & Woolf, D. K. (1989). Comments on variations of whitecap coverage with wind stress and water temperature. *Journal of Physical Oceanography, 19*, 706–709.

Nordberg, W., Conaway, J., Ross, D., & Wilheit, T. (1971). Measurements of microwave emission from a foam-covered, wind-driven sea. *Journal of the Atmospheric Sciences*, *28*, 429–435.

Padmanabhan, S., Reising, S. C., Asher, W. E., Rose, L. A., & Gaiser, P. W. (2006). Effects of foam on ocean surface microwave emission inferred from radiometric observations of reproducible breaking waves. *IEEE Transactions on Geoscience and Remote Sensing, 44*, 569–583.

Paget, A. C., Bourassa, M. A., & Anguelova, M. D. (2015). Comparing in situ and satellite-based observations of oceanic whitecaps. *Journal of Geophysical Research, 120*, 2826–2843. https://doi.org/10.1002/2014JC010328.

Pandey, P., & Kakar, R. (1982). An empirical microwave emissivity model for a foam-covered sea. *Journal of Oceanic Engineering, 7*(3), 135–140. https://doi.org/10.1109/JOE.1982.1145527.

Phillips, O. M. (1985). Spectral and statistical properties of the equilibrium range in wind-generated gravity-waves. *Journal of Fluid Mechanics, 156*, 505–531.

Potter, H., Smith, G. B., Snow, C. M., Dowgiallo, D. J., Bobak, J. P., & Anguelova, M. D. (2015). Whitecap lifetime stages from infrared imagery with implications for microwave radiometric measurements of whitecap fraction. *Journal of Geophysical Research, 120*, 7521–7537. https://doi.org/10.1002/2015JC011276.

Randolph, K., Dierssen, H. M., Cifuentes-Lorenzen, A., Balch, W., Monahan, E. C., Zappa, C., Drapeau, D., & Bowler, B. (2017). Novel methods for optically measuring whitecaps under natural wave breaking conditions in the Southern Ocean. *Journal of Atmospheric and Oceanic Technology, 34*, 533–554. https://doi.org/10.1175/JTECH-D-16-0086.1.

Reul, N., & Chapron, B. (2003). A model of sea-foam thickness distribution for passive microwave remote sensing applications. *Journal of Geophysical Research, 108*(C10), 3321. https://doi.org/10.1029/2003JC001887.

Rogers, W. E., Anguelova, M. D., Hwang, P. A. (2012). *Satellite radiometer (Windsat) estimates of whitecap coverage interpreted using a global numerical wave model hindcast*. Abstract OS13E-1780 presented at 2012 fall meeting, AGU, San Francisco, Calif., 3–7 Dec.

Rose, L. A., Asher, W. E., Reising, S. C., Gaiser, P. W., St Germain, K. M., Dowgiallo, D. J., Horgan, K. A., Farquharson, G., & Knapp, E. J. (2002). Radiometric measurements of the microwave emissivity of foam. *IEEE Transactions on Geoscience and Remote Sensing, 40*, 2619–2625.

Ross, D., & Cardone, V. (1974). Observations of oceanic whitecaps and their relation to remote measurements of surface wind speed. *Journal of Geophysical Research, 79*, 444–452.

Salisbury, D. J., Anguelova, M. D., & Brooks, I. M. (2013). On the variability of whitecap fraction using satellite-based observations. *Journal of Geophysical Research, 118*, 6201–6222. https://doi.org/10.1002/2013JC008797.

Scanlon, B., Breivik, Ø., Bidlot, J.-R., Janssen, P., Callaghan, A., & Ward, B. (2016). Modelling whitecap coverage with a wave model. *Journal of Physical Oceanography, 46*, 887–894. https://doi.org/10.1175/JPO-D-15-0158.1.

Smith, P. M. (1988). The emissivity of sea foam at 19 and 37 GHz. *IEEE Transactions on Geoscience and Remote Sensing, 26*, 541–547.

Snyder, R., & Kennedy, R. (1983). On the formation of whitecaps by a threshold mechanism. Part I: Basic formalism. *Journal of Physical Oceanography, 13*, 1482–1492.

Stogryn, A. P. (1967). The apparent temperature of the sea at microwave frequencies. *Transactions on Antennas and Propagation, 15*(2), 278–286. https://doi.org/10.1109/TAP.1967.1138900.

Stogryn, A. P. (1972). The emissivity of sea foam at microwave frequencies. *Journal of Geophysical Research, 77*(9), 1658–1666. https://doi.org/10.1029/JC077i009p01658.

Sugihara, Y., Tsumori, H., Ohga, T., Yoshioka, H., & Serizawa, S. (2007). Variation of whitecap coverage with wave-field conditions. *Journal of Marine Systems, 66*, 47–60. https://doi.org/10.1016/j.jmarsys.2006.01.014.

Taylor, P., & Yelland, M. (2001). The dependence of sea surface roughness on the height and steepness of the waves. *Journal of Physical Oceanography, 31*, 572–590.

Tolman, H. L., Balasubramaniyan, B., Burroughs, L. D., Chalikov, D. V., Chao, Y. Y., Chen, H. S., & Gerald, V. M. (2002). Development and implementation of wind-generated ocean surface wave models at NCEP. *Weather Forecasting, 17*, 311–333. https://doi.org/10.1175/1520-0434(2002)017,0311:DAIOWG.2.0.CO;2.

WAMDI Group. (1988). The WAM model—A third generation ocean wave prediction model. *Journal of Physical Oceanography, 18*, 1775–1810. https://doi.org/10.1175/1520-0485(1988)018,1775:TWMTGO.2.0.CO;2.

Wang, Q., Monahan, E., Asher, W., & Smith, P. (1995). Correlations of whitecap coverage and gas transfer velocity with microwave brightness temperature for plunging and spilling breaking waves. In B. Jähne & E. Monahan (Eds.), *Air-water gas transfer* (pp. 217–225). Hanau: AEON Verlag.

Wentz, F. J. (1975). A two-scale scattering model for foam-free sea microwave brightness temperatures. *Journal of Geophysical Research, 80*(24), 3441–3446. https://doi.org/10.1029/JC080i024p03441.

Wentz, F. J. (1983). A model function for ocean microwave brightness temperatures. *Journal of Geophysical Research, 88*(C3), 1892–1908. https://doi.org/10.1029/JC088iC03p01892.

Wentz, F. J. (1997). A well-calibrated ocean algorithm for special sensor microwave/imager. *Journal of Geophysical Research, 102*(C4), 8703–8718. https://doi.org/10.1029/96JC01751.

Williams, G., Jr. (1969). Microwave radiometry of the ocean and the possibility of marine wind velocity determination from satellite observations. *Journal of Geophysical Research, 18*, 4591–4594.

WISE Group. (2007). *Progress in Oceanography, 75*, 603–674. https://doi.org/10.1016/j.pocean.2007.05.005.

Woolf, D. K. (2005). Parametrization of gas transfer velocities and sea-state-dependent wave breaking. *Tellus, 57B*, 87–94.

Wu, J. (1979). Oceanic whitecaps and sea state. *Journal of Physical Oceanography, 9*, 1064–1068.

Wu, J. (1988). Variations of whitecap coverage with wind stress and water temperature. *Journal of Physical Oceanography, 18*, 1448–1453.

Wu, J. (1992). Individual characteristics of whitecaps and volumetric description of bubbles. *IEEE Transactions on Antennas and Propagation, 17*, 150–158.

Zhao, D., & Toba, Y. (2001). Dependence of whitecap coverage on wind and wind-wave properties. *Journal of Oceanography, 57*, 603–616.

Chapter 12
The Case for Measuring Whitecaps Using Ocean Color and Initial Linkages to Subsurface Physics

Alejandro Cifuentes-Lorenzen and Kaylan Randolph

Abstract Breaking waves enhance the transport of gas, momentum and heat between the atmosphere and ocean, facilitating climate-relevant physical and chemical processes. But years of effort have proven that breaking waves are difficult to measure, to describe analytically and parameterize using forcing. Because breaking waves have a marked impact on the color of the surface ocean, altering the magnitude and spectral shape of reflected light in unique ways for the submerged air cavity, fresh and decaying foam and entrained bubbles, measurements of ocean color could prove useful as a proxy for the processes associated with wave breaking. The earliest known measurements of whitecap coverage were collected in the late 1960s by Edward Monahan. Much of this work builds on the work of Monahan and his collaborators. The whitecap statistics presented here are compared directly to those presented by Monahan and the work that has followed as a demonstration of the potential use of ocean color as an accurate, practicable approach, given the high sensitivity and low detection limit of the radiometers. Here, an ocean color derived intensity metric is related to the surface and subsurface manifestation of wave breaking, including the enhancement in TKE dissipation rates and the penetration depth of bubble plumes. The radiometric dataset used here, collected as a part of the Southern Ocean Gas Exchange Experiment, serves as a preliminary dataset for this investigation; it was not collected with the dedicated purpose of measuring whitecaps. However, these data and planned measurements make the case for the use of ocean color to measure upper ocean physics.

12.1 Introduction

Breaking waves are a critical component of the earth climate system (Cavaleri et al. 2007, 2012); breaking facilitates physical and chemical processes in the ocean. The exchange of gas (*e.g.,* CO_2, CH_4, DMS; water-side controlled gases in particular), momentum and heat between the atmosphere and ocean and the production of sea

A. Cifuentes-Lorenzen (✉) · K. Randolph
California State University Maritime Academy, Vallejo, CA, USA
e-mail: ACifuentes@csum.edu; krandolph@csum.edu

P. Vlahos (ed.), *Recent Advances in the Study of Oceanic Whitecaps*,
https://doi.org/10.1007/978-3-030-36371-0_12

salt aerosols are all facilitated by wave breaking (e.g. (Blanchard 1963; De Leeuw et al. 2011; Melville 1996; EC Monahan et al. 1982; E.C. Monahan and Spillane 1984; Thorpe 1982; Vlahos and Monahan 2009; Woolf 1997; Woolf et al. 2007). Breaking waves are a key dissipative mechanism for wave energy and directly affect wave evolution (Cavaleri et al. 2007). Breaking contributes to wave-driven upper ocean turbulence dynamics and has the capacity to modify the ocean mixed layer (e.g. Kukulka and Brunner 2015 and Belcher et al. 2012). Because of the relevance to upper ocean dynamics and climate, measuring and parameterizing whitecapping (e.g. Monahan 1971; Bondur and Sharkov 1982; Monahan and Spillane 1984; Monahan and Muircheartaigh 1980; Toba and Koga 1986; Liss and Merlivat 1986; Asher et al. 2002; Fairall et al. 2011, 2003; Scanlon et al. 2016) has been of much interest to the community.

The ephemeral breaking wave evolves over a continuum, but breaking is typically parsed into two stages, A and B (Monahan and Woolf 1989). Stage A includes the spilling crest and a dense, broad bubble size spectrum. Stage B is the maturing Stage A whitecap, which covers a larger area and has a relatively narrow bubble size spectrum. During Stage A breaking, an air cavity is introduced into the surface layer of the ocean and undergoes fragmentation (*i.e.,* the α bubble plume) (Monahan and Lu 1990). Bubbles undergo stabilization, dissolution and buoyancy (bursting) during the quiescent Stage B phase (*i.e.,* β-plume), are largely responsible for the production of primary marine aerosols and can impact heat flux (Monahan et al. 1986; Andreas et al. 1995). Under moderate to high wind conditions, whitecaps can support bubble populations in uniform, persistent subsurface plumes (*i.e.,* γ-plumes in the usage of Monahan and Lu 1990), relevant to the supersaturation of dissolved gases in the surface ocean (Thorpe 1982; Monahan 1993). It is thought that air-sea gas transfer velocities, of CO_2 in particular, momentum transfer, and turbulent mixing should be based on the fractional coverage of Stage A whitecaps (e.g. Andreas et al. 2008; Andreas and Monahan 2000; Asher et al. 1995; William Asher et al. 2002; Medwin and Clay 1998; Melville 1996; E.C. Monahan 2002).

In particular, wave breaking has been identified as an important source of near surface turbulence. In a rigid wall, the shear production of total kinetic energy (TKE) is balanced by dissipation (i.e. law of the wall scaling). Nonetheless, in the presence of breaking surface gravity waves an enhancement in TKE dissipation near the surface beyond the rigid wall scaling has been shown and linked to wave breaking (*e.g.* Terray et al. 1996; Drennan et al. 1996; Gemmrich and Farmer 2004; Gemmrich 2010; Schwendeman et al. 2013; Scully et al. 2016). Directly at the surface, the wave energy dissipated by breaking (S_{ds}) has been related to whitecaps, specifically the total fractional coverage of whitecaps, W or the fractional coverage of active stage A whitecaps, W_A (e.g. Anguelova and Hwang 2016; Callaghan 2018; Hwang et al. 2008; Schwendeman and Thomson 2015). If the wave energy dissipated by wave breaking can be related to whitecaps and the subsurface signature of wave breaking can be linked to TKE dissipation rate enhancements, then whitecaps can be related to the subsurface TKE dissipation rates. The underlying assumption is a balance between wind-input (i.e. wave-growth) and dissipation of wave energy (i.e. wave breaking) (e.g. Callaghan 2018), assuming that most of the vertically

integrated TKE dissipation rate, ε is supported by wave breaking (e.g. Schwendeman et al. 2014) or that the different terms contributing to the subsurface TKE budget can be parsed and identified.

$$S_{ds} \approx \rho_w \int \varepsilon(z) dz \tag{12.1}$$

These relationships are largely built on or tested with various measurements of whitecap coverage.

The earliest known measurements of whitecap coverage were collected in the late 1960s by Monahan (1969). This was a manually intensive process, requiring the selection and removal of whitecaps from a triangulated scene; coverage was determined as the fractional weight of whitecap areas to the weight of the triangulated region (*e.g.,* Monahan 1971; Monahan 1981; Toba 1973). The work of Monahan and his collaborators informed the video and photographic techniques that that are now in wide use. With advancement in computing power, automated techniques have been devised to process hundreds of high-resolution digital images (*e.g.,* hundreds to thousands of square meters), obtained using camera systems positioned at an oblique angle 15–20 m above the sea surface, geo-rectified and interpolated onto a rectangular grid, for fractional coverage using a brightness threshold to identify whitecaps within each scene (e.g. Callaghan and White 2009; Schwendeman and Thomson 2015). These datasets usually quantify W, without partitioning W_a and W_b and do not capture entrained bubbles. Less efforts have been made to separate Stages A and B by increasing the intensity (i.e. brightness) threshold used (e.g. Monahan and Woolf 1989; Asher et al. 2002) and incorporating information on whitecap shape and motion (e.g. Kleiss and Melville 2011; Mironov and Dulov 2007; Scanlon and Ward 2013). Recently, IR imagery has been used for separating whitecap stages (Potter et al. 2015), an approach that has been effectively applied for measuring microbreaking (Jessup et al. 1997; Zappa 2006; Zappa et al. 2004)).

Measurements of ocean color could prove useful as a proxy for the processes associated with wave breaking. Breaking waves have a marked impact on the color of the surface ocean, altering the magnitude and spectral shape of reflected light in unique ways for the submerged air cavity, foam generation and decay and entrained bubbles (e.g. Koepke 1984; Frouin et al. 1996; Moore et al. 2000; Stramski and Tegowski 2001; Terrill et al. 2001; Zhang et al. 2002; Randolph et al. 2014; Randolph 2015). Unlike digital camera systems that exclusively measure the surface extent of whitecaps, the high sensitivity of ocean color radiometers allows for the capture of subtle differences in brightness and color, for example due to the presence of entrained bubbles. The color of fresh foam generally shows a spectrally flat response in the visible portion of the spectrum. Decaying foam or foam stabilized by surfactants will diverge in color from bright white fresh foam; a decrease in reflectance in the red portion of the spectrum due to the strong absorption properties of water molecules will occur (Frouin et al. 1996; Moore et al. 1998) and the spectral shape in the blue and green changes markedly with entrained bubbles, depending on

the water optical properties (Kokhanovsky 2004; Moore et al. 1998; Randolph 2015; Stramski and Tegowski 2001). These effects support the use of ocean color for estimating the near surface physical processes associated with whitecaps (e.g. Moore et al. 2000; Randolph et al. 2017). Furthermore, rapidly evolving remote sensing technology, higher resolution sensors, big data and computing power, support the need for quantifying the effects of breaking waves on ocean color.

The development of a radiometric method for measuring whitecap coverage from a single band (nominally 410 nm) was described in Randolph et al. 2015. When reduced to the brightest features only (i.e. fresh surface foam), the radiometrically derived fractional whitecap coverages were consistent with those measured using a digital imaging system (see Brumer et al. 2017). Radiometric measurements of whitecaps can be used to retrieve more metrics with a higher specificity, including duration, decay time, and albedo. A breaking intensity metric (i.e. more or less energetic), determined by the slope and scale of breaking waves, wave-wave interaction, and wind stress was also estimated.

The results presented here demonstrate the potential use of ocean color as an accurate, practicable approach for measuring whitecap statistics and, given the high sensitivity and low detection limit of the radiometers, a means for differentiating different whitecap features. We hypothesize that these metrics can be directly related to the surface and subsurface manifestation of wave breaking, including the enhancement in TKE dissipation rates (e.g. Anis and Moum 1994; J. Gemmrich 2010; J. R. Gemmrich and Farmer 2004; Schwendeman et al. 2013; Terray et al. 1996), the volume of air entrained, and the nature of bubble plumes. The radiometric dataset used here, collected as a part of the Southern Ocean Gas Exchange Experiment, serves as a preliminary dataset for this investigation; it was not collected with the dedicated purpose of measuring whitecaps. A forthcoming field campaign (2019) focused on retrieving measurements of whitecaps from measurements of ocean color with concurrently measured subsurface physics is described.

12.2 Methodology

12.2.1 Field data

The data used in this analysis was collected as a part of the Southern Ocean Gas Exchange Experiment (SO GasEx) conducted on the NOAA ship the *R.V. Ronald H. Brown* in the Atlantic sector of the Southern Ocean (50°S, 40°W and a single station 300 km north of South Georgia Island) from March 7 to April 4, 2008. The primary objective of SO GasEx was to measure gas transfer at high wind speeds and to identify predictors, in addition to wind, for estimating gas transfer. The experiment produced a comprehensive dataset, including a full suite of meteorological observations with turbulent fluxes for stress, heat and gas based on the direct covariance method (J. B. Edson et al. 2011). Wave statistics, included one-dimensional frequency spectrum where significant wave height and period

were provided by an X-band radar, a laser altimeter and a microwave sensor. Data collected using the X-band radar and the laser altimeter together produced wave spectra over a frequency range of 0.035 to 1.2 Hz with a high-frequency slope of f^{-4} and high signal-to-noise ratio (Cifuentes-Lorenzen et al. 2013). Bubbles generated by breaking waves were measured optically at a single depth (i.e. size distributions; Randolph et al. 2014) and acoustically to estimate plume penetration depths (A. Cifuentes-Lorenzen and C. J. Zappa, *in prep*). The full experiment is discussed in detail in Ho et al. (2011) and Edson et al. (2011).

12.2.2 Radiometric Quantities

The approach for retrieving measurements of whitecaps from above surface radiometry is described in detail in Randolph et al. (2017). Here, the path 2 approach is used. In short, changes in the magnitude and spectral distribution of radiance due to wave breaking are determined from the total upwelling radiance signal normalized by the downwelling irradiance signal, both measure a high sampling frequency above the sea surface. Upwelling radiance from the surface ocean, L_t (θ,ϕ,λ), is the spectral distribution of light, or radiant power per unit area, wavelength and solid angle (W m^{-2} nm^{-1} sr^{-1}), emerging from the ocean in polar and azimuthal directions θ and ϕ, respectively (Mobley 1999). L_t is dependent on the water optical properties, the geometric structure of the incident radiance distribution (*i.e.,* solar zenith angle), the geometry of the surface, and the illumination conditions (*e.g.,* cloud cover) and is the sum of the radiance signal of the undisturbed water column (L_w), the radiance signal from breaking waves L_b, and the surface reflected portion of the incident sky radiance (L_r) (see Fig. 1 in Randolph et al. 2017). Radiance reflectance, R (sr^{-1}), the ratio of $L_t(\theta,\phi,\lambda,t)$ to the downwelling spectral place irradiance incident on the sea surface $E_d(\lambda,t)$ (W m^{-2} nm^{-1}) at each time step, accounts for changes in the illumination conditions and produces a stable measurement of the water, surface reflected skylight (i.e. skylight reflected off of the wavy surface), and breaking waves. Assuming the measured L_t (θ, ϕ) is the same across all viewing directions (θ and ϕ), which is a gross approximation, a Lambertian Equivalent Reflectance (*LER*) can be estimated by multiplying by π and the measurement becomes similar to a dimensionless albedo, hereafter R.

12.2.3 Radiometric Data Collection and Processing for Whitecap Metrics

The data here was collected using a system of three-radiometers, each with seven channels between 412 and 680 nm (10 nm spectral bandwidth), measuring downwelling irradiance, upwelling radiance and sky radiance. Radiometric data

was processed to produce calibrated and dark current corrected data interpolated onto common time coordinates. The downward looking radiometer measuring upwelling radiance, L_t was positioned above the water surface to maintain a ~1 m^2 instantaneous field of view (i.e. 6° radiometer field of view deployed from the bow of the ship at 8 m above the water surface). In the open ocean, the spatial coverage condition is satisfied for record lengths of 20–40 min or more, depending on the drift velocity and number of events observed under those conditions (see Randolph et al. 2017). The system was configured to measure L_t over an azimuthal range of 270° across the heading of the ship while the solar zenith angle is above 20°. Sun glint and shadowing effects were minimized by maintaining a viewing direction 120° from the sun's azimuth. A viewing angle 40° from nadir was employed to minimize specular reflectance of the sun's direct beam into the detector (Mueller et al. 2003). These angles were maintained using a computer-based system that calculates the sun's azimuth angle relative to the ship and adjusts the position of the detector using a stepping motor (see Balch et al. 2011).

The upward-looking radiometer measuring downwelling irradiance was mounted at 18 m on the jackstaff of the ship to avoid ship shadow. Ship motion produced regular fluctuations in the E_d signal at approximately the period of the swell (*e.g.,* ~10 s). The peak period of motion-induced fluctuations, determined from the average power spectral density of E_d (~1 min segments), was used as the window length when applying a moving average filter to remove the fluctuations (See Randolph et al. 2017). Data were collected as a 0.5~2.5 h time series while on station and from 11:00 to 16:00 GMT, during which the ship maintained a constant heading into the wind. A third radiometer was used to measure sky radiance $[L_s(\theta,\phi,\lambda)]$ incident on the sea surface. L_s is used to estimate the skylight reflected by the wavy surface into the viewing angle of the downward-looking radiometer (see Lee et al. 2010; Mobley 1999; Mueller et al. 2003).

A non-stationary R signal can arise from changes in L_w (*e.g.,* the color of the water column without bubbles or foam). A stationary time series of reflectance, R', can be estimated from the measured, non-stationary R signal by applying a moving minimum-maximum (min-max) filter (*e.g.,* Briggs et al. 2011 following Lemire 2006). The baseline accounts for magnitude differences in R due to spectral changes in the water color itself (i.e. R_w). This is particularly important when collecting measurements of upwelling radiance while underway. The moving min-max filter simultaneously finds the minimum and maximum elements within a sliding time window of a specified length. The window length is optimized so as not to erode whitecap features. Because non-uniform skies are accounted for in R, short window lengths are not necessary for L_t to approach a stationary condition, avoiding errors in identifying the limits of the whitecap feature.

The baseline-removed radiance reflectance R' has a distribution that is positively skewed to a degree dependent on the presence of foam and bubbles. The frequency and magnitude of variance in the upwelling radiance signal is the result of skylight reflected of the wavy surface, including gravity waves on the order of meters in length to capillary waves on the order of millimeters in length, at each time step. The greater the surface reflected skylight, the larger the variance in the background

signal. Because the intensity of surface reflected skylight presents as low magnitude, high frequency variance distributed nearly equally across the length of the record, its spectral distribution is analyzed in frequency space (analogous to a noise floor in the frequency domain). The magnitude of the surface reflected skylight signal determines the lower detection limit of whitecaps, especially in the presence of spilling waves.

Whitecaps are identified (i.e. indexed) in the R' signal and radiometrically derived metrics to be related to near surface physics (e.g. enhancement in TKE dissipation rate) are calculated using R'. Data used here were reduced to whitecaps considered to be complete (i.e. whitecaps containing typical growth and decay phases). The color of the evolving whitecap, while indexed using the R' signal, is analyzed using $R(\lambda)$. The features of the whitecap, including fresh foam (Stage A), decaying foam and the bubble plume, can, in a simplified sense, be differentiated using measurements of $R'(t)$ and $R(\lambda, t)$. Here, both individual and assemblages of whitecap events are analyzed.

The optically derived visible manifestation of breaking waves, including the incorporation of the air cavity by the spilling crest, bubble and foam generation, should be related to the duration, decay time and intensity of the breaking. Duration, d includes the active and decay phases, whereas decay time, τ describes the whitecap decay phase only. Because whitecap areas are known to decay almost exponentially (see Monahan and Zietlow 1969) with time, a time constant τ is used to describe the e-folding time. Both d and τ for each whitecap are obtained from R' for discrete whitecap events considered to be complete (see Randolph et al. 2015). Following Monahan and Zietlow (1969), τ is calculated from the exponential fit to the decaying portion of R' for each whitecap event, following:

$$R'(t) = R'(t_o)e^{-t/\tau} \tag{12.2}$$

where t_0 is the peak brightness value.

A measure of breaking intensity from reflectance, I that describes the energy associated with the breaking wave (i.e. spilling crests are less energetic than plunging breakers), was estimated by integrating R' over the time length of the whitecap event, t where

$$I = \int_t R'(t)dt \tag{12.3}$$

I is normalized by duration of the breaking event (I_d) or the decay time (I_τ) to produce a dimensionless intensity value. Normalizing by duration produces an intensity that closely resembles the averaged enhancement in reflectance, whereas normalizing by τ produces an intensity most closely related to the brightest manifestation of the breaking event.

For comparison to wind and wave measurements and estimations of wind energy input, enhancement in TKE dissipation rate and bubble plume penetration depth, intensity values are derived from individual whitecap events over 10-min records.

12.2.4 Wind and Wave Measurements and Estimated Enhancement in TKE Dissipation Rates

The radiometrically-derived whitecap statistics were related to subsurface physics using wind, wave field and bubble measurements. Turbulent wind velocity fluctuations, wind speed and direction, relative humidity and air temperature measurements were collected at 18 m using a direct covariance flux package (Edson et al. 2011). Heat fluxes (sensible and latent), and long-wave (IR) radiative flux were estimated based on the COARE algorithm (Fairall et al. 2003). Neutral wind speeds at the reference height of 10 m (U_{10N}) were obtained by accounting for stability based on the Monin-Obukhov Similarity theory (Edson and Fairall 1998). The wave frequency spectrum from 0.03 to 1.2 Hz was determined by combining measurements from a X-band radar (Wave Monitoring System or WaMoS II), a laser altimeter (Riegl LD-90), and a microwave unit (TSKA SWHM) (Cifuentes-Lorenzen et al. 2013). Wave field statistics, including the significant wave height of the dominant waves (H_s) and the phase speed at the spectral peak (c_p) were determined from the measured wave frequency spectrum. Measured frequency spectra were extended to 2 Hz following a f^{-4} Hz tail roll off to resolve wave scales ~ 0.7 m in wavelength with phase speeds of 1 m s^{-1}. This frequency spectrum was used to determine the wind energy input (see Eq. 12.4).

Inverse wave age (c_p/u_*) was also derived from the measured wave number and frequency spectra to describe the state of the wind-wave field. For open ocean conditions, wave age values, $c_p/u_* \geq 32$ are considered mature or fully developed; lower values of c_p/u_* are considered young or developing seas (Kudryavtsev and Makin 2002).

Bubble clouds were identified in measurements of acoustic backscatter (120 kHz). The Acoustic Doppler Current Profiler (ADCP), deployed on a drifting, autonomous MAPCO$_2$ Buoy, collected data at high sampling frequency (2 Hz) in 75 bins, each measuring 25 cm. The portion of the signal attributable to bubbles, referred to as the acoustic backscatter anomaly, was determined by the removal of the mean signal of backscatter known to be bubble free. A bubble penetration depth scaling approach, that builds on the approach of Thorpe (1992), was developed using this dataset (see Randolph et al. 2014). Instead of scaling with the dominant wavelength at the spectral peak, the characteristic wave scale (i.e. the actively wind-coupled wave scale) was used in the dispersion relation for deep-water waves to retrieve a mean characteristic wavelength, λ_w (Cifuentes-Lorenzen et al. 2013).

Whitecap intensity metrics were compared to the wind energy going into the wave field, F_{aw}. F_{aw} is derived directly from the surface wave spectra and a given wave growth spectral parameterization (e.g. Cifuentes-Lorenzen et al. 2018; Donelan et al. 2006; Snyder et al. 1981; Terray et al. 1996)

$$F_{aw} = \rho_w \, g \int_{\omega} \omega \beta(\omega) S(\omega) d\omega, \tag{12.4}$$

where $S(\omega)$ is the one-dimensional wave spectrum, $\beta(\omega)$ is a wave-growth parameter, ω is the angular frequency ($\omega = 2\pi f$), and g is acceleration due to gravity. The TKE injection into the water column associated with breaking waves can be linked theoretically to the wind-driven energy flux (Eq. 12.4) assuming spectral-equilibrium between input and dissipation (e.g. Kukulka and Brunner 2015).

If the effect of wave breaking on the TKE dissipation rate near the surface of the ocean is proportional to the breaking intensity metric, as is postulated here, then the energy input (Eq. 12.3) associated with wave-growth relative to the predicted TKE dissipation rate, $\varepsilon_p(z)$ based on the classic rigid wall-layer scaling

$$\varepsilon_p(z) = \frac{\left(u_*^w\right)^3}{\kappa \, z}, \tag{12.5}$$

could be used to define the theoretical enhancement, Γ. Here, u_*^w is the water-side friction velocity and κ is the von Karman constant of proportionality. The enhancement, Γ the ratio of wind-driven energy input to the depth integrated ε_p

$$\Gamma = F_{aw} / \int_Z \varepsilon_p dz, \tag{12.6}$$

could be used to track the subsurface manifestation of wave breaking, serving as a breaking intensity metric. Here, the assumption is that more energetic wave breaking events injecting larger kinetic energy into the water column and enhancing the TKE dissipation rate will have a brighter surface manifestation, all intimately linked to bubble dynamics. Following this rationale, the optically derived breaking intensity I (Eq. 12.2) should be proportional to the wave breaking-driven subsurface turbulence enhancement (Eq. 12.6).

12.3 Results

Over 35 hours of radiometric data were collected while on station between the Subantarctic and Polar fronts in ~5 °C water and at a station 40 km northeast of South Georgia Island (SGI, 54°S 37°W) in 3 °C water. High wind speeds (3–15 m s^{-1} on average), large significant wave heights (3 m), and near neutral

atmospheric stability were measured during SO GasEx (Edson et al. 2011; Cifuentes-Lorenzen et al. 2013). Whitecap coverage, measured using digital imagery, ranged from 0 to 6% (see Brumer et al. 2017). Overall mature seas were observed, with the exception of young seas near South Georgia Island. While 95% of c_p/u_* measured between 18 and 150, radiometric data presented here were largely collected with $25 \leq c_p/u_* \leq 34$ (Fig. 12.1). Spectrally, the energetic swell-component of the wave field had the tendency to overshadow the less energetic wind-driven waves, resulting in a dominant wave-scale in the $0.08 < f < 0.12$ Hz range.

Bubble penetration depths, d_0 estimated using the acoustic backscatter anomaly measured during three separate deployments of the $MAPCO_2$ buoy (indicated using gray brackets along the top panel of Fig. 12.1) were 3.88 m, 4.86 m and 5.20 on average (Table 12.1). These data, used to devise a bubble penetration depth parameterization based on forcing, produced mean wave-scaled penetration depths d_0/λ_w of 0.78, 0.86 and 0.98, where mean penetration depths of 3.88 m, 4.86 m and 5.50 m were observed (Table 12.1).

The measurements of whitecaps presented here are of full events, including clear growth and decay phases (e.g. Fig. 12.2). The statistics used to describe individual

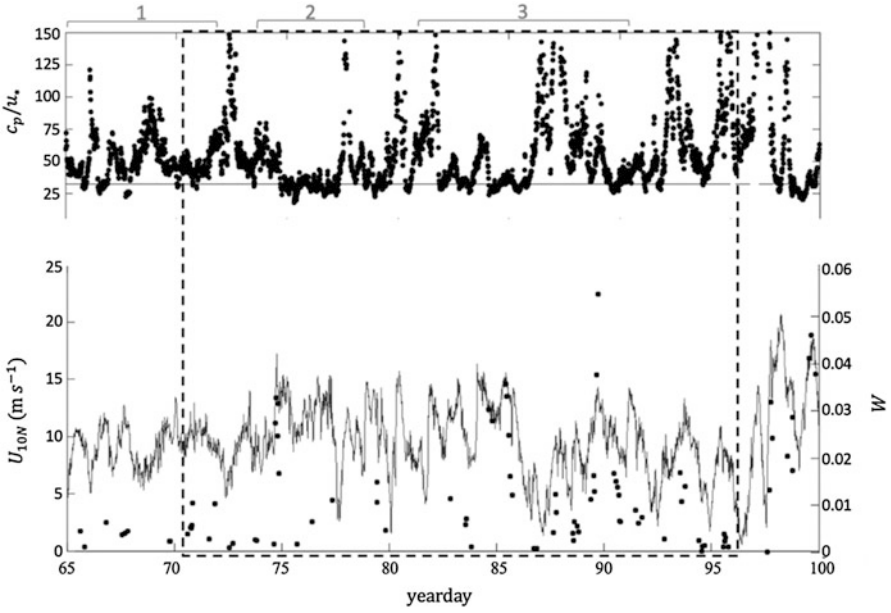

Fig. 12.1 During SO GasEx, 10 m neutral wind speeds ranged from 4 to 20 m s^{-1} (bottom panel, black line). Measurements of wave age (top panel) suggest that seas were mostly developed (c_p/u_*> 32, 32 denoted using the gray line; 95% of the c_p/u_* measured between 18 and 150). Whitecap coverage, measured using the digital imaging technique and processed following Callaghan and White 2009 ranged from 0 to 6% (bottom panel, black circles). Deployments 1, 2, and 3, distinctive time periods during which data, including acoustic backscatter anomaly, were collected from the MAPCO2 buoy

Table 12.1 A description of the three deployment periods from which bubble penetration depths $\langle d_0 \rangle$ were estimated from thee measured acoustic backscatter anomaly and scaled using the characteristic wavelength of the actively wind-coupled waves, $\langle d_0/\lambda_w \rangle$. Included are the forcing conditions, described using wind speed (U_{10}; mean, max), mean wave age $\langle c_p/u_* \rangle$ and significant wave height $\langle H_s \rangle$ for each period

Deployment	1	2	3
Yeardays	69–72	74–78	81–92
$\boldsymbol{U_{10}}$ (m s^{-1})	12.4, 16	12.9, 17	13.1, 16
$\langle \boldsymbol{c_p/u_*} \rangle$	31.73 ± 1.83	29.23 ± 3.38	30.90 ± 2.65
$\langle \boldsymbol{H_s} \rangle$ (m)	3.00 ± 0.48	2.86 ± 0.36	3.14 ± 0.63
$\langle \boldsymbol{d_0} \rangle$ (m)	3.88 ± 1.28	4.86 ± 2.15	5.20 ± 2.00
$\langle \boldsymbol{p_d/\lambda_w} \rangle$	0.78 ± 0.29	0.98 ± 0.49	0.86 ± 0.30

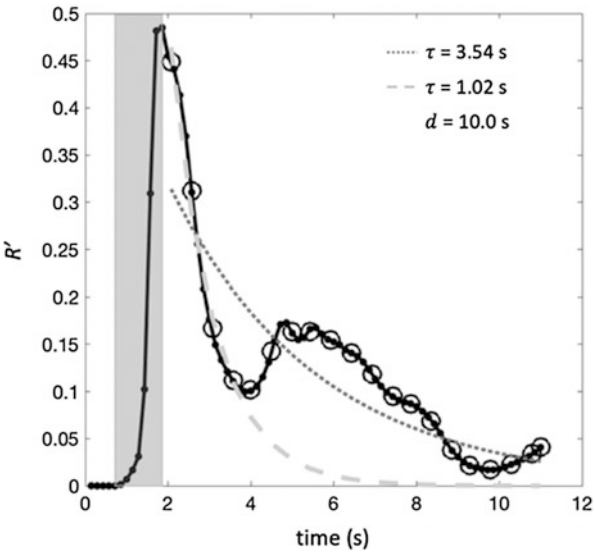

Fig. 12.2 The features of the whitecap on which the metrics are based, including (**a**) growth (shaded region) and (**b**) decay (unshaded region) phases, delineated by the maximum R'

whitecaps are conventional. In reality, wave breaking is a complicated, variable process (e.g. Bondur and Sharkov 1982; Callaghan 2018; Callaghan et al. 2012; Sharkov 2007). While the statistics serve as a necessary simplification, the way in which they are calculated markedly changes how the whitecap is being described and therefore interpreted. Here, both common and novel statistics are presented for 126 individual whitecaps from large scale breaking waves in the Southern Ocean (Fig. 12.3). The determination of each is described in detail. Because the full assemble of d, τ and I are positively skewed, results are described using the median, interquartile range (IQR, 25th and 75th percentiles), and ~1.5IQR (roughly equivalent to $\pm 2.7\sigma$ or 99.3% for normally distributed data).

Duration, while reliably retrieved from the R' record and seemingly straightforward in its determination, may not be directly comparable with those presented in past studies. Here, duration includes what could be considered the full growth and

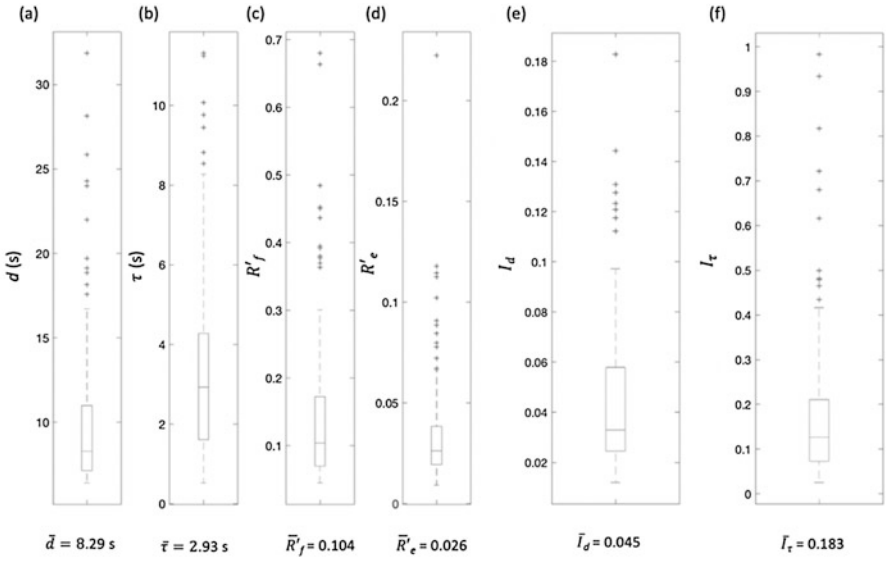

Fig. 12.3 Radiometrically derived whitecap metrics for 126 large-scale breaking events measured in the Atlantic sector of the Southern Ocean during mostly mature seas, including (**a**) duration, t (**b**) e-folding time, τ (**c**) brightness of whitecap foam, R'_f and (**d**) the average brightness, accounting for the foam and bubbles, R'_e. Intensity metrics, (**e**) I_d, where $T = d$ and (**f**) I_τ, where $T = \tau$ are also included. Box plots indicate the median (midline), interquartile range (IQR, box), spread ($2{*}IQR$) and outliers (+). Median values for each metric are included beneath the boxplots

decay phase, where the termination of the event is defined as the point in time when no bubbles are detected in the R' signal. Duration, calculated in such a way, also includes the portion of the whitecap that is governed by processes affecting bubble buoyancy and dissolution, which is not necessarily intrinsic to the breaking, but to the local biogeochemistry. These processes though, are inextricably tied or at least very difficult to separate. Here, median whitecap duration was 8.3 s; half of the values were between 7.1 s and 11.0 s. Whitecap duration generally ranged from 6.5 s to 16.7 s (99.3% of the data), with several outliers ($n = 9$) between 17.6 s and 31.9 s (Figure 12.3a).

Similarly, there are various ways to fit an exponential model to a time resolved whitecap event (Monahan and Zietlow 1969; Monahan et al. 1982; Nolan 1988; Sharkov 2007) and depending on how the model is fitted, markedly different decay times are produced. For example, the e-folding time, τ calculated as the exponential fit from the peak brightness value, t_0 through the detectable portion of the bubble plume, binned to ~3.5 Hz, produced an e-folding time of 3.54 s (Fig. 12.2, grey dotted line). When fit in this way, the exponential model accounted for 79% of the variability in the R' data. Fitting between t_0 and a transition point between what could be considered fresh foam and the quiescent bubble plume and/or foam and bubbles stabilized by surfactants, through the use of a weighting function, produced an e-folding time of 1.02 s (Fig. 12.2, grey dashed line). Depending on the process

that is being predicted from the data, for example the production of primary marine aerosols (e.g. Monahan et al. 1982, 1986, Callaghan 2013), a piecewise fit separating the stages (e.g. Monahan year) might be preferable. The decay time statistics presented here are the result of fitting an exponential model to the full event. The median decay time for the full ensemble was ~2.9 s. Half of the τ values fell between 1.6 s and 4.3 s and the e-folding time generally ranged from 0.5 s and 8.3 s (99.3% of the data; Figure 12.3b).

Three measures of whitecap brightness are also included here: fresh foam R'_f, the average brightness (i.e. accounting for the foam and bubbles, R'_e), and intensity I, which includes a dimensionless, normalized intensity I_d and I_τ (Fig. 12.3c–f). The reflectance of fresh foam generally ranged from 7% to 17% above the background water reflectance. Foam brightness values as high as 68% above background were measured at 412 nm. When accounting for the full event, until submerged bubbles are no longer detected in R' signal, a median reflectance of ~3% above the background water reflectance was measured. Median intensity statistics I_d and I_τ, used to indirectly estimate the intensity of breaking (i.e. energy being dissipated by breaking), were 0.03 ($0.01 \leq I_d \leq 0.18$) and 0.13 ($0.03 \leq I_\tau \leq 0.98$) respectively. Both time-scaling parameters could offer insight to different breaking dynamics.

Estimates of the radiometrically estimated intensity, I (Eq. 12.1) were compared to energy input, F_{aw} (Eq. 12.4; Fig. 12.4a) and to bubble penetration depths from a parameterization based on observations of the acoustic backscattering anomaly during SO GasEx (Randolph et al. 2014; Cifuentes-Lorenzen et al. *in prep*; Fig. 12.4b). For I, 90% of the data is represented by values of 0.31 s^{-1} or less, within the 0.05–0.42 s^{-1} range. The energy input ranged from 0.35 to 1.35 W m^{-2}, with 90% of the estimates explained by 1.07 W m^{-2} or lower (corresponding to wind speeds in the range 9.7–15.3 m s^{-1}). These preliminary results suggest that estimates of the subsurface manifestation of breaking based on penetration depths

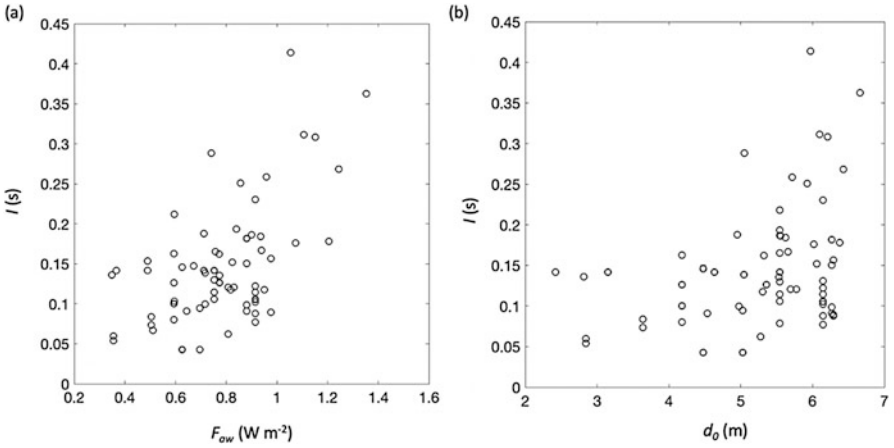

Fig. 12.4 Measurements of whitecap intensity I (s) and (**a**) wind driven energy flux (F_{aw}) and (**b**) bubble penetration depths (d_0; m). The range of wave ages for the data presented is $25 \leq c_p/u_* \leq 34$

and energy-inputted are proportional to the radiometrically derived breaking intensity, the optically detectable manifestation of breaking.

The ratio of the wind-driven input to the predicted TKE dissipation rate Γ (Eq. 12.6) that describes the expected enhancement of energy attributed to wave-breaking was 40 on average, suggesting a 40-fold enhancement relative to the rigid-wall scaling under the assumption that F_{aw} is balanced by dissipation in the wave-field (i.e. wave breaking). Maximum values suggest a 10^2 enhancement (i.e. $\Gamma \sim 130$).

12.4 Discussion

The statistics measured suggest that the life and decay time of the whitecaps are highly variable under the full set of wind and wave conditions during which large scale wave breaking was measured. During the SO GasEx field campaign, moderate to high winds ($5 \leq U_{10} \leq 18$ m s^{-1}; with a mean wind stress of 0.26 N m^{-2} $\pm$ 0.23 N m^{-2}) and significant wave heights (~3.2 m on average, 7 m under severe conditions) were measured. Spectrally, the wind-wave peaks were generally overwhelmed by the swell component. In sum, the energetic swell-component of the wave field had the tendency to overshadow the less energetic wind-driven waves. These conditions are somewhat narrow in their range (i.e. mostly mature seas), limiting the dynamic range over which relationships between radiometrically derived whitecap statistics and subsurface physics were analyzed. Furthermore, under mature seas the dynamics of the energy exchange and the breaking scales are expected to change limiting the validity of the assumptions used to derive F_{aw} (Cifuentes-Lorenzen et al. 2018). Nonetheless, an exploration of the relationship between optically retrieved intensity and Γ is warranted, beginning with measures of subsurface physics based on intuitive manifestations of breaking waves (Fig. 12.4).

Intensity, I was expected to be directly proportional to or increase linearly with F_{aw}. Here, the wind-driven energy (F_{aw}; Eq. 12.4) provided a direct estimate of the kinetic energy input into the wave field. Under a spectral balance assumption (i.e. spectral equilibrium), F_{aw} can serve as a proxy for the loss of energy associated with wave energy being dissipated by breaking (e.g. Callaghan 2018). Here, under open ocean conditions, F_{aw} might be an overestimation of the energy available for breaking, as other dissipative mechanisms might be at play (e.g. Sutherland and Melville 2015). Some sensitivity to the wave-growth parameterization chosen is expected. The results here indicate that the radiometrically retrieved intensity exhibits a direct proportionality to the wind-driven energy, further affirming linkages made between wave-energy loss (breaking) to the optically active manifestation of the phenomenon (i.e. whitecap measurements) (e.g. Schwendeman and Thomson 2015).

Bubble plume penetration depths were also expected to show a strong correlation with I; bubbles efficiently backscatter light, especially when coated with organic

material (see Kingsbury and Marston 1981; Stramski et al. 2004; Terrill et al. 2001). Thus, brighter water due to foam and bubbles is theoretically accompanied by larger penetration depths. Though the forcing conditions measured are limited, here $I \propto {d_0}^n$ (Figure 12.4b). The penetration depth is thought to address the effect of breaking waves of different geometries (i.e. steepness) and the proposed parameterization captures the scale of the breaking waves.

Because I is expected to effectively capture the wind energy input and be highly sensitive to the bubble plume, it should also scale with the observed TKE enhancement in the water column. Such an investigation requires a dimensionless I. Normalizing by e-folding time, I_τ, while including the full bubble plume, gives greater weight to the stage A, fresh foam portion of the whitecap. Intuitively, there is an expectation of larger e-folding times associated with larger breaking and therefore, higher energy dissipation (e.g. Schwendeman and Thomson 2015). The dynamic range of Γ for the conditions presented here suggests a mean wave-breaking enhancement of roughly 44 times the predicted TKE dissipation rate. While I increases with wind-driven energy input (F_{aw}) (Figure 12.4a), Γ failed to explain the observed variance in I_τ; no relationship exists between F_{aw} and τ. Nor does e-folding time show a correlation with penetration depth. Here, penetration depths shallower than 6.3 m with an average e-folding time of approximately 3.0 s explain 90% of the data.

Data from the SO GasEx serves as a preliminary dataset for this investigation; it was not collected with the dedicated purpose of measuring whitecaps and so does not provide a full picture of the phenomenon. The lack of a strong relationship between normalized intensity and TKE enhancement in the water column is likely in part, a direct consequence of a narrow range of conditions measured, but also linking the optically active manifestation of breaking (foam and bubbles) to the subsurface enhancement of TKE (i.e. subsurface physics) may be difficult to achieve, particularly under open ocean conditions. Because the observations in-hand are limited in number, the methods of collection are not optimized for this investigation, future field campaigns are planned to address this relationship in particular.

12.5 Planned work

In order to accurately quantify the effect of wave breaking on reflectance and its utility for generating estimates of upper ocean physics, a statistically robust dataset of reflectance measurements of breaking waves collected during a wide range of well-characterized physical forcing conditions, especially under strong forcing, statistically undersampled to date, is necessary. A field campaign, at the Air-Sea Interaction Tower (ASIT) at Martha's Vineyard Coastal Observatory (MVCO), designed to measured reflectance of naturally breaking waves under a wide range of forcing conditions, TKE dissipation rates near the surface, bubble size distributions and void fraction, is underway in spring and fall 2019 to adequately assess the relationship between the ocean color signal and upper ocean physics.

While data collected at the ASIT is representative of the coastal zone (shallow water waves) 3 km off of the northeast coast of the US (south of Martha's Vineyard, MA) in the Atlantic Ocean; this location experiences amplified conditions (e.g., fetch, tidal currents) contributing to wave breaking. According to a five-year record collected during fall and winter at ASIT, approximately 44% of the wave age measurements represent actively growing, young seas, ideal for wind-wave generation and wave breaking.

During these conditions, hyperspectral reflectance measurements of breaking waves and estimates of the TKE dissipation rate profiles will be collected to elucidate the potential for expanding the role of ocean color into assessments of the air-sea flux and the role of wave breaking in turbulent kinetic energy exchange. The outcomes of this work will include quantification of the dependence of hyperspectral reflectance on entrained air using optical measurements of bubble size distributions and void fraction, exploration of the relevant scales in the relationship between hyperspectral reflectance (i.e. ocean color-derived breaking intensity) and the enhancement in the subsurface TKE dissipation rates (3) quantification of the effects of wind-roughened sea surfaces on hyperspectral reflectance for a wide range of wind and wave conditions.

Acknowledgements We thank Bruce Bowler, Dave Drapeau and Barney Balch from Bigelow Laboratory for Ocean Sciences for collection of the radiometric data. We thank Christopher Zappa for the collection of wave and acoustic backscatter data and James Edson for the collection and processing of meteorological data. Finally, we thank Edward Monahan for years of insight from decades of wisdom on all things whitecaps.

References

Andreas, E. L., & Monahan, E. C. (2000). The role of whitecap bubbles in air–sea heat and moisture exchange. *Journal of Physical Oceanography, 30*(2), 433–442.

Andreas, E. L., Edson, J. B., Monahan, E. C., Rouault, M. P., & Smith, S. D. (1995). The spray contribution to net evaporation from the sea: A review of recent progress. *Boundary-Layer Meteorology, 72*(1–2), 3–52.

Andreas, E. L., Persson, P. O. G., & Hare, J. E. (2008). A bulk turbulent air–sea flux algorithm for high-wind, spray conditions. *Journal of Physical Oceanography, 38*(7), 1581–1596.

Anguelova, M. D., & Hwang, P. A. (2016). Using energy dissipation rate to obtain active whitecap fraction. *Journal of Physical Oceanography, 46*(2), 461–481.

Anis, A., & Moum, J. (1994). Prescriptions for heat flux and entrainment rates in the upper ocean during convection. *Journal of Physical Oceanography, 24*(10), 2142–2155.

Asher, W. E., Karle, L., Higgins, B., Farley, P., Leifer, I., & Monahan, E. (1995). The effect of bubble plume size on the parameterization of air/seawater gas transfer velocities. *Air-Water Gas Transfer*, 227–238.

Asher, William, Edson, J., Mcgillis, W., Wanninkhof, R., Ho, D. T., & Litchendor, T. (2002). Fractional area whitecap coverage and air-sea gas transfer velocities measured during GasEx-98. *Gas Transfer at Water Surfaces*, 199–203. American Geophysical Union. Retrieved from https://doi.org/10.1029/GM127p0199.

Balch, W. M., Drapeau, D. T., Bowler, B. C., Lyczskowski, E., Booth, E. S., & Alley, D. (2011). The contribution of coccolithophores to the optical and inorganic carbon budgets during the

Southern Ocean gas exchange experiment: New evidence in support of the "Great Calcite Belt" hypothesis. *Journal of Geophysical Research, 116*, C00F06. https://doi.org/10.1029/2011JC006941.

Belcher, S. E., Grant, A. L., Hanley, K. E., Fox-Kemper, B., Van Roekel, L., Sullivan, P. P., et al. (2012). A global perspective on Langmuir turbulence in the ocean surface boundary layer. *Geophysical Research Letters, 39*(18), L18605.

Blanchard, D. C. (1963). The electrification of the atmosphere by particles from bubbles in the sea. *Progress in Oceanography, 1*, 73–202.

Bondur, V. G., & Sharkov, E. A. (1982). Statistical properties of whitecaps on a rough sea. *Oceanology, 22*(3), 274–279.

Briggs, N., Perry, M. J., Cetinić, I., Lee, C., D'Asaro, E., Gray, A. M., & Rehm, E. (2011). High-resolution observations of aggregate flux during a sub-polar North Atlantic spring bloom. *Deep Sea Research Part I: Oceanographic Research Papers, 58*(10), 1031–1039.

Brumer, S. E., Zappa, C. J., Brooks, I. M., Tamura, H., Brown, S. M., Blomquist, B. W., et al. (2017). Whitecap coverage dependence on wind and wave statistics as observed during SO GasEx and HiWinGS. *Journal of Physical Oceanography, 47*(9), 2211–2235.

Callaghan, A. H. (2013). An improved whitecap timescale for sea spray aerosol production flux modeling using the discrete whitecap method. *Journal of Geophysical Research: Atmospheres, 118*(17), 9997–10010. https://doi.org/10.1002/jgrd.50768.

Callaghan, A. H. (2018). On the relationship between the energy dissipation rate of surface-breaking waves and oceanic whitecap coverage. *Journal of Physical Oceanography, 48*(11), 2609–2626.

Callaghan, A. H., & White, M. (2009). Automated Processing of Sea Surface Images for the Determination of Whitecap Coverage. *Journal of Atmospheric and Oceanic Technology, 26*(2), 383–394. https://doi.org/10.1175/2008JTECHO634.1.

Callaghan, A. H., Deane, G. B., Stokes, M. D., & Ward, B. (2012). Observed variation in the decay time of oceanic whitecap foam. *Journal of Geophysical Research, Oceans, 117*(C9), C09015.

Cavaleri, L., Alves, J.-H., Ardhuin, F., Babanin, A., Banner, M., Belibassakis, K., et al. (2007). Wave modelling–the state of the art. *Progress in Oceanography, 75*(4), 603–674.

Cavaleri, L., Fox-Kemper, B., & Hemer, M. (2012). Wind waves in the coupled climate system. *Bulletin of the American Meteorological Society, 93*(11), 1651–1661.

Cifuentes-Lorenzen, A., Edson, J. B., Zappa, C. J., & Bariteau, L. (2013). A Multisensor Comparison of Ocean Wave Frequency Spectra from a Research Vessel during the Southern Ocean Gas Exchange Experiment. *Journal of Atmospheric and Oceanic Technology, 30*(12), 2907–2925. https://doi.org/10.1175/JTECH-D-12-00181.1.

Cifuentes-Lorenzen, A., Edson, J. B., & Zappa, C. J. (2018). Air–Sea interaction in the Southern Ocean: Exploring the height of the wave boundary layer at the air–sea interface. *Boundary-Layer Meteorology*, 1, 461–22, 482.

De Leeuw, G., Andreas, E. L., Anguelova, M. D., Fairall, C., Lewis, E. R., O'Dowd, C., et al. (2011). Production flux of sea spray aerosol. *Reviews of Geophysics, 49*(2), RG2001.

Donelan, M. A., Babanin, A. V., Young, I. R., & Banner, M. L. (2006). Wave-follower field measurements of the wind-input spectral function. Part II: Parameterization of the wind input. *Journal of Physical Oceanography, 36*(8), 1672–1689.

Drennan, W. M., Donelan, M. A., Terray, E. A., & Katsaros, K. B. (1996). Oceanic Turbulence Dissipation Measurements in SWADE. *Journal of Physical Oceanography, 26*(5), 808 15.

Edson, J., & Fairall, C. (1998). Similarity relationships in the marine atmospheric surface layer for terms in the TKE and scalar variance budgets. *Journal of the Atmospheric Sciences, 55*(13), 2311–2328.

Edson, J. B., Fairall, C. W., Bariteau, L., Zappa, C. J., Cifuentes-Lorenzen, A., McGillis, W. R., et al. (2011). Direct covariance measurement of CO2 gas transfer velocity during the 2008 Southern Ocean gas exchange experiment: Wind speed dependency. *Journal of Geophysical Research, 116*, C00F10. https://doi.org/10.1029/2011JC007022.

Fairall, C. W., Bradley, E. F., Hare, J. E., Grachev, A. A., & Edson, J. B. (2003). Bulk parameterization of air–sea fluxes: Updates and verification for the COARE algorithm. *Journal of Climate, 16*(4), 571–591. https://doi.org/10.1175/1520-0442(2003)016<0571:BPOASF>2.0.CO;2.

Fairall, C., Yang, M., Bariteau, L., Edson, J., Helmig, D., McGillis, W., et al. (2011). Implementation of the coupled ocean-atmosphere response experiment flux algorithm with CO2, dimethyl sulfide, and O3. Journal of Geophysical Research. *Oceans, 116*(C4).

Frouin, R., Schwindling, M., & Deschamps, P.-Y. (1996). Spectral reflectance of sea foam in the visible and near-infrared: In situ measurements and remote sensing implications. *Journal of Geophysical Research, 101*(C6), 14361–14371. https://doi.org/10.1029/96JC00629.

Gemmrich, J. (2010). Strong turbulence in the wave crest region. *Journal of Physical Oceanography, 40*(3), 583–595. https://doi.org/10.1175/2009JPO4179.1.

Gemmrich, J. R., & Farmer, D. M. (2004). Near-surface turbulence in the presence of breaking waves. *Journal of Physical Oceanography, 34*(5), 1067–1086. https://doi.org/10.1175/1520-0485(2004)034<1067:NTITPO>2.0.CO;2.

Ho, D. T., Sabine, C. L., Hebert, D., Ullman, D. S., Wanninkhof, R., Hamme, R. C., et al. (2011). Southern Ocean gas exchange experiment: Setting the stage. *Journal of Geophysical Research, 116*, C00F08. https://doi.org/10.1029/2010JC006852.

Hwang, P. A., Sletten, M. A., & Toporkov, J. V. (2008). Analysis of radar sea return for breaking wave investigation. *Journal of Geophysical Research, 113*, C02003. https://doi.org/10.1029/2007JC004319.

Jessup, A., Zappa, C. J., & Yeh, H. (1997). Defining and quantifying microscale wave breaking with infrared imagery. *Journal of Geophysical Research, Oceans, 102*(C10), 23145–23153.

Kingsbury, D. L., & Marston, P. L. (1981). Mie scattering near the critical angle of bubbles in water. *Journal of the Optical Society of America, 71*(3), 358–361.

Kleiss, J. M., & Melville, W. K. (2011). The analysis of sea surface imagery for whitecap kinematics. *Journal of Atmospheric and Oceanic Technology, 28*(2), 219–243.

Koepke, P. (1984). Effective reflectance of oceanic whitecaps. *Applied Optics, 23*(11), 1816–1824.

Kokhanovsky, A. A. (2004). Spectral reflectance of whitecaps. *Journal of Geophysical Research, Oceans, 109*(C5), C05021. https://doi.org/10.1029/2003JC002177.

Kudryavtsev, V., & Makin, V. (2002). Coupled dynamics of short waves and the airflow over long surface waves. *Journal of Geophysical Research, Oceans, 107*(C12).

Kukulka, T., & Brunner, K. (2015). Passive Buoyant Tracers in the Ocean Surface Boundary Layer: 1. Influence of Equilibrium Wind-Waves on Vertical Distributions. *Journal of Geophysical Research: Oceans, 120*(5), 3837–3858. https://doi.org/10.1002/2014JC010487.

Lee, Z., Ahn, Y.-H., Mobley, C., & Arnone, R. (2010). Removal of surface-reflected light for the measurement of remote-sensing reflectance from an above-surface platform. *Optics Express, 18*(25), 26313–26324.

Lemire, D. (2006). Streaming maximum-minimum filter using no more than three comparisons per element. *ArXiv Preprint Cs/0610046*.

Liss, P. S., & Merlivat, L. (1986). Air-sea gas exchange rates: Introduction and synthesis. In P. Buat-Menard (Ed.), *The role of air-sea exchange in geochemical cycling* (pp. 113–129). Washington: Reidel.

Medwin, H., & Clay, C. (1998). Fundamentals of acoustical oceanography academic. *New York, 24*.

Melville, W. K. (1996). The role of surface-wave breaking in air-sea interaction. *Annual Review of Fluid Mechanics, 28*(1), 279–321.

Mironov, A. S., & Dulov, V. A. (2007). Detection of wave breaking using sea surface video records. *Measurement Science and Technology, 19*(1), 015405.

Mobley, C. D. (1999). Estimation of the remote-sensing reflectance from above-surface measurements. *Applied Optics, 38*(36), 7442–7455.

Monahan, E. C. (1969). Fresh water whitecaps. *Journal of the Atmospheric Sciences, 26*(5), 1026–1029.

Monahan, E. C. (1971). *Oceanic Whitecaps, 1*(2), 139–144.

Monahan, E. C. (1981). Determination of surface wind speed from remotely measured whitecap coverage, a feasibility assessment. *European Space Agency, 167*, 103–109.

Monahan, E. C. (1993). Occurrence and evolution of acoustically relevant sub-surface bubble plumes and their associated, remotely monitorable, surface whitecaps. In B. R. Kerman (Ed.), *Natural physical sources of underwater sound* (pp. 503–517). Dordrecht: Springer. Retrieved from https://doi.org/10.1007/978-94-011-1626-8_37

Monahan, E. C. (2002). Oceanic whitecaps: Sea surface features detectable via satellite that are indicators of the magnitude of the air-sea gas transfer coefficient. *Journal of Earth System Science, 111*(3), 315–319. https://doi.org/10.1007/BF02701977.

Monahan, E. C., & Lu, M. (1990). Acoustically relevant bubble assemblages and their dependence on meteorological parameters. *IEEE Journal of Oceanic Engineering, 15*(4), 340–349. https://doi.org/10.1109/48.103530.

Monahan, E. C., & Muircheartaigh, I. (1980). Optimal power-law description of oceanic whitecap coverage dependence on wind speed. *Journal of Physical Oceanography, 10*(12), 2094–2099. https://doi.org/10.1175/1520-0485(1980)010<2094:OPLDOO>2.0.CO;2.

Monahan, E. C., & Spillane, M. C. (1984). The role of oceanic whitecaps in air sea gas exchange. In W. Brutsaert & G. H. Jirka (Eds.), *Gas transfer at water surfaces* (pp. 495–504). Norwell: D. Reidel.

Monahan, E. C., & Woolf, D. K. (1989). Comments on variations of whitecap coverage with wind stress and water temperature. *Journal of Physical Oceanography, 19*(5), 706–709. https://doi.org/10.1175/1520-0485(1989)019<0706:COOWCW>2.0.CO;2.

Monahan, E. C., & Zietlow, C. R. (1969). Laboratory comparisons of fresh-water and salt-water whitecaps. *Journal of Geophysical Research, 74*(28), 6961–6966. https://doi.org/10.1029/JC074i028p06961.

Monahan, E. C., Davidson, K., & Spiel, D. (1982). Whitecap aerosol productivity deduced from simulation tank measurements. *Journal of Geophysical Research, Oceans, 87*(C11), 8898–8904.

Monahan, E. C., Spiel, D. E., & Davidson, K. L. (1986). A model of marine aerosol generation via whitecaps and wave disruption. In *Oceanic whitecaps* (pp. 167–174). Dordrecht: Springer.

Moore, K. D., Voss, K. J., & Gordon, H. R. (1998). Spectral reflectance of whitecaps: Instrumentation, calibration, and performance in coastal waters. *Journal of Atmospheric and Oceanic Technology, 15*(2), 496–509. https://doi.org/10.1175/1520-0426(1998)015<0496:SROWIC>2.0.CO;2.

Moore, K. D., Voss, K. J., & Gordon, H. R. (2000). Spectral reflectance of whitecaps: Their contribution to water-leaving radiance. *Journal of Geophysical Research, 105*(C3), 6493–6499. https://doi.org/10.1029/1999JC900334.

Mueller, J. L., Morel, A., Frouin, R., Davis, C. O., Arnone, R. A., Carder, K. L., et al. (2003). Ocean optics protocols for satellite ocean color sensor validation, revision 4, volume III: Radiometric measurements and data analysis protocols. *NASA Tech. Memo*, 01674–0.

Nolan, P. (1988). *Oceanic whitecaps and the fluxes of droplets from, bubbles to, and gases through the sea surface*. Groton: Marine Sciences Institute, University of Connecticut.

Potter, H., Smith, G. B., Snow, C. M., Dowgiallo, D. J., Bobak, J. P., & Anguelova, M. D. (2015). Whitecap lifetime stages from infrared imagery with implications for microwave radiometric measurements of whitecap fraction. *Journal of Geophysical Research, Oceans, 120*(11), 7521–7537.

Randolph, K. L. (2015). *Optical measurements of whitecaps and bubbles during large scale wave breaking in the Southern Ocean*. Ph.D. dissertation, University of Connecticut, 146 pp.

Randolph, K., Dierssen, H. M., Twardowski, M., Cifuentes-Lorenzen, A., & Zappa, C. J. (2014). Optical measurements of small deeply penetrating bubble populations generated by breaking waves in the Southern Ocean. *Journal of Geophysical Research: Oceans*. https://doi.org/10.1002/2013JC009227.

Randolph, K., Dierssen, H. M., Cifuentes-Lorenzen, A., Balch, W. M., Monahan, E. C., Zappa, C. J., et al. (2017). Novel methods for optically measuring whitecaps under natural wave-

breaking conditions in the Southern Ocean. *Journal of Atmospheric and Oceanic Technology, 34*(3), 533–554.

Scanlon, B., & Ward, B. (2013). Oceanic wave breaking coverage separation techniques for active and maturing whitecaps. *Methods in Oceanography, 8*(0), 1–12. https://doi.org/10.1016/j.mio.2014.03.001.

Schwendeman, M., & Thomson, J. (2015). Observations of whitecapcoverage and the relation to windstress, wave slope, and turbulentdissipation. *Journal of Geophysical Research, Oceans, 120*, 8346–8363. https://doi.org/10.1002/2015JC011196.

Schwendeman, M., Thomson, J., & Gemmrich, J. R. (2013). Wave breaking dissipation in a Young Wind Sea. *Journal of Physical Oceanography, 44*(1), 104–127. https://doi.org/10.1175/JPO-D-12-0237.1.

Schwendeman, M., Thomson, J., & Gemmrich, J. R. (2014). Wave breaking dissipation in a young wind sea. *Journal of Physical Oceanography, 44*(1), 104–127.

Scully, M. E., Trowbridge, J. H., & Fisher, A. W. (2016). Observations of the Transfer of Energy and Momentum to the Oceanic Surface Boundary Layer beneath Breaking Waves. *Journal of Physical Oceanography, 46*(6), 1823–1837.

Sharkov, E. A. (2007). *Breaking ocean waves: Geometry, structure and remote sensing*. Berlin: Springer Science & Business Media.

Snyder, R., Dobson, F., Elliott, J., & Long, R. (1981). Array measurements of atmospheric pressure fluctuations above surface gravity waves. *Journal of Fluid Mechanics, 102*, 1–59.

Stramski, D., & Tegowski, J. (2001). Effects of intermittent entrainment of air bubbles by breaking wind waves on ocean reflectance and underwater light field. *Journal of Geophysical Research, 106*(C12), 31345–31360. https://doi.org/10.1029/2000JC000461.

Stramski, D., Boss, E., Bogucki, D., & Voss, K. J. (2004). The role of seawater constituents in light backscattering in the ocean. *Progress in Oceanography, 61*(1), 27–56.

Sutherland, P., & Kendall Melville, W. (2015). Field Measurements of Surface and near-Surface Turbulence in the Presence of Breaking Waves. *Journal of Physical Oceanography, January*. https://doi.org/10.1175/JPO-D-14-0133.1.

Terray, E., Donelan, M., Agrawal, Y., Drennan, W., Kahma, K., Williams, A., et al. (1996). Estimates of kinetic energy dissipation under breaking waves. *Journal of Physical Oceanography, 26*(5), 792–807. https://doi.org/10.1175/1520-0485(1996)026<0792:EOKEDU>2.0.CO;2.

Terrill, E. J., Melville, W. K., & Stramski, D. (2001). Bubble entrainment by breaking waves and their influence on optical scattering in the upper ocean. *Journal of Geophysical Research, 106*(C8), 16815–16823. https://doi.org/10.1029/2000JC000496.

Thorpe, S. A. (1982). On the clouds of bubbles formed by breaking wind-waves in deep water, and their role in air – Sea gas transfer. *Philosophical Transactions of the Royal Society of London. Series A, Mathematical and Physical Sciences, 304*(1483), 155–210.

Thorpe, S. A. (1992). Bubble clouds and the dynamics of the upper ocean. *Quarterly Journal of the Royal Meteorological Society, 118*, 1–22.

Toba, Y. (1973). Quantitative expression of the breaking of wind waves on the sea surface. *Recreation: Oceanography Works Japan, 12*, 1.

Toba, Y., & Koga, M. (1986). A parameter describing overall conditions of wave breaking, whitecapping, sea-spray production and wind stress. In *Oceanic whitecaps* (pp. 37–47). Dordrecht: Springer.

Vlahos, P., & Monahan, E. C. (2009). A generalized model for the air-sea transfer of dimethyl sulfide at high wind speeds. *Geophysical Research Letters, 36*(21), L21605.

Woolf, D. K. (1997). Bubbles and their role in air-sea gas exchange. In P. S. Liss & R. A. Duce (Eds.), *The sea surface and global change* (pp. 173–205). New York: Cambridge University Press.

Woolf, D. K., Leifer, I. S., Nightingale, P. D., Rhee, T. S., Bowyer, P., Caulliez, G., et al. (2007). Modelling of bubble-mediated gas transfer: Fundamental principles and a laboratory test. *Journal of Marine Systems, 66*(1–4), 71–91. https://doi.org/10.1016/j.jmarsys.2006.02.011.

Zappa, C. J. (2006). *Investigating wave processes important to air-sea fluxes using infrared techniques*. Fort Belvoir: COLUMBIA UNIV PALISADES NY LAMONT-DOHERTY EARTH OBSERVATORY.

Zappa, C. J., Asher, W. E., Jessup, A. T., Klinke, J., & Long, S. R. (2004). Microbreaking and the enhancement of air-watertransfer velocity. *Journal of Geophysical Research, 109*, C08S16. https://doi.org/10.1029/2003JC001897.

Zhang, X., Lewis, M., Lee, M., Johnson, B., & Korotaev, G. (2002). The volume scattering function of natural bubble populations. *Limnology and Oceanography, 47*(5), 1273–1282.

Chapter 13
Bright Oceans: Spectral Differentiation of Whitecaps, Sea Ice, Plastics, and Other Flotsam

Heidi M. Dierssen and Shungudzemwoyo P. Garaba

Abstract Whitecaps are evident in ocean color imagery, but are currently removed as part of the atmospheric correction techniques. Whitecaps enhance the backscattering of light from the ocean surface and appear "white" or having spectrally flat reflectance in the visible wavelengths (400–700 nm). However, measurements shows that the whitecap spectral reflectance is not flat in the near infrared and short wave infrared and contains dips and peaks related to liquid water absorption that are related to the intensity of the whitecap signal. This signal can be potentially used to assess whitecaps from satellites. However, the first step in such an algorithm will be to differentiate whitecaps from other constituents that also serve to elevate spectral reflectance. Here, we describe the spectral properties of constituents found at or above the sea surface including whitecaps, ocean plastics, sea ice and clouds which may appear white to the human eye, but have unique spectral signatures that can be used to quantitatively differentiate them using optimized sensors with the appropriate wavebands. The aim is to develop sensors and approaches that can be used to accurately identify whitecaps and these other constituents, improve the atmospheric correction process, and develop new products from ocean color imagery.

13.1 Introduction

Viewed from space, the ocean is a dark surface underlying a thick atmosphere which reflects sunlight back to the sensor. More than 90% of the signal measured from an ocean color satellite occurs from molecular scattering within the atmosphere and only a few percent of the signal represents photons that have penetrated into the ocean. The ocean is generally dark because light is predominantly scattered in a

H. M. Dierssen (✉)
Department of Marine Sciences, University of Connecticut, Groton, CT, USA
e-mail: heidi.dierssen@uconn.edu

S. P. Garaba
Marine Sensor Systems Group, Institute for Chemistry and Biology of the Marine Environment, Carl von Ossietzky University of Oldenburg, Wilhelmshaven, Germany

P. Vlahos (ed.), *Recent Advances in the Study of Oceanic Whitecaps*,
https://doi.org/10.1007/978-3-030-36371-0_13

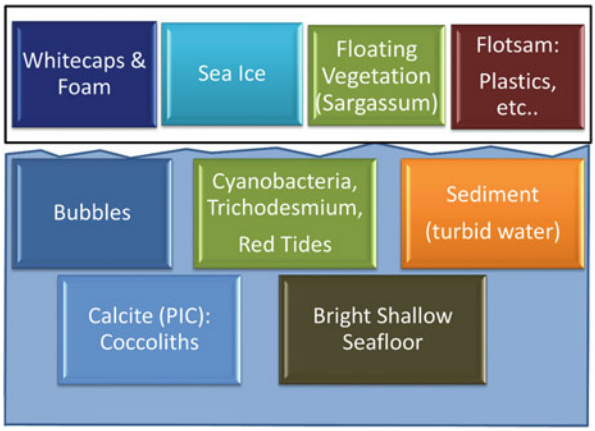

Fig. 13.1 Conceptual schematic of constituents that can enhance the reflectance (upwelling irradiance normalized to downwelling incident irradiance) of the sea surface. The constituents outlined in the black box are surface features that are much more reflective than typical ocean color signals. Constituents within the water such as intense phytoplankton blooms, calcite, bubbles, sediment, and scattering off the shallow seabed also serve to enhance water-leaving reflectance but are not considered in this study

forward direction and penetrates downward into the ocean fueling photosynthesis. Ocean surfaces, however, are not *always* dark. Various optically active constituents both in the water and on the sea surface can enhance the surface albedo and make the oceans appear much "brighter" than normal (Fig. 13.1). These bright waters serve to enhance water reflectance and can include the presence of whitecaps and foam, sea ice, plastics, and other flotsam at the sea surface. Differentiating between these sea surface constituents, many of which appear "white" or spectrally flat in the visible spectrum (400–700 nm), is the objective of this study with the intent to understand how the unique reflectance features of different floating materials can be used to develop new parameters from ocean color imagery.

A user of ocean color imagery might presume that bright water features would appear as enhancements in the ocean color reflectance signal. However, standard National Aeronautics and Space Administration (NASA) ocean color processing aims to mask or quantitatively remove these bright features as part of the "atmospheric correction" techniques (Gao et al. 2007; Bailey et al. 2010; Ibrahim et al. 2018). Current atmospheric correction aims to partition the top-of-atmosphere reflectance into the contributions by air molecules and aerosols $\rho_a(\lambda)$, sea surface specular reflectance of sunlight $\rho_g(\lambda)$, and by whitecaps and foam $\rho_{wc}(\lambda)$ to derive an estimate of water- leaving reflectance $\rho_w(\lambda)$. As part of that effort, thresholds are also introduced to mask pixels that may obscure the ocean color due to the presence of clouds. Between the thresholds and the partitioning of the retrieved signal, as further described below, any pixels that are significantly brighter than average are either masked out completely or the enhanced reflectance is removed and erroneously attributed to another scattering constituent such as aerosols.

The influence of brightly scattering constituents within the water column (e.g., suspended sediment, bright sand sea beds, etc.) on the sea surface spectral albedo and heat flux was considered in a recent manuscript (Fogarty et al. 2018). Here, we describe the spectral properties of constituents found at or above the sea surface including whitecaps, ocean plastics, sea ice and clouds which may appear white to the human eye, but have unique spectral signatures that can be used to quantitatively differentiate them using optimized sensors with the appropriate wavebands. The aim is to develop sensors and approaches that can be used to accurately identify these constituents and thereby improve the atmospheric correction process and the ultimate utility of ocean color imagery. Instead of removing or flagging pixels with surface enhanced reflectance, methods can be developed to quantify these constituents from space globally.

13.2 Whitecaps

Although technically not a constituent of the atmosphere, corrections for whitecaps, foam, and bubbles are included in the current atmospheric correction routines. Whitecap reflectance is often modeled using an empirical cubic relationship to wind speed and an approximate reflectance value for an individual whitecap. While useful for understanding long-term processes such as air-sea gas exchange (Monahan and Mac Niocaill 2012), climatological relationships for whitecaps can never quantify the instantaneous whitecap distribution required to process an individual image. At the same wind speed, whitecap coverage can vary by several orders of magnitude (Anguelova and Webster 2006). The fraction of whitecaps can be influenced by the fetch and duration and the wind, water temperature, water salinity, air temperature and stability of the lower atmosphere, current shear and long wave interaction, wave age, and the presence of surfactants such as organic films (reviewed in Scanlon and Ward 2016) . Recent studies at high winds have shown that individual measurements of whitecap coverage is highly variable across a large range in wind speed (Brumer et al. 2017).

Uncertainties from using wind speed parameterizations to characterize instantaneous whitecap reflectance are so large that the standard NASA atmospheric correction techniques apply a threshold in the operational code when wind speeds exceed 12 m s^{-1}. Hence, the highest fraction whitecap fraction allowable in the models is 1.6%, even though the fractional whitecap coverage can approach 10% in very active seas (Brumer et al. 2017). This technique may retrieve reasonably accurate water-leaving reflectance but results in large omissions and commission errors in the other terms of the atmospheric correction. Namely, the whitecap reflectance is underestimated and the aerosol reflectance is overestimated. The spectral shape of marine aerosols are often considered similar to whitecaps, but they are not equivalent and this has implications for wind-prone regions like the Southern Ocean and North Atlantic where whitecaps occur frequently.

Bubbles also elevate the ocean color reflectance, but their concentrations and penetration depths cannot be described as a simple function of wind speed. In a recent study conducted with natural breaking waves in the Southern Ocean (Randolph et al. 2014), bubbles penetrated to depths of 9–10 m and differences in bubble concentrations were dependent on the environmental conditions. Relatively young seas, with an inverse wave age of approximately 0.88 and shorter characteristic wave scales, produced lower bubble concentrations, shallower bubble penetration depths, and steep bubble size distribution slopes. Conversely, older seas, with an inverse wave age of 0.70 and longer characteristic wave scales, produced relatively higher bubble concentrations penetrating to 15 m depth, larger bubble sizes, and shallower bubble size distribution slopes. Bubbles, particularly small bubbles, can also be persistent due to coating by organic matter and lead to elevated backscattering.

When considering spectral enhancements due to whitecaps, traditional image processing methods to determine whitecap coverage have been shown to underestimate the contribution of bubbles to the water-leaving reflectance (Randolph et al. 2017). When using the lowest thresholds, Randolph et al. (2017) found that radiometric fractional whitecap coverage retrievals were consistently higher than fractional coverage from high-resolution digital images. Radiometry was able to capture more of the decaying bubble plume area that is difficult to detect with the human eye and even with photography. Using a ship-mounted radiometer is an effective method for determining the fractional coverage of both Stage A and Stage B whitecaps and can provide more information on the intensity, and decay time of whitecaps. Radiometers can be purchased off-of-the-shelf and are easy to mount on moorings or ships for field investigations. Given appropriate deployment strategies, the time-averaged measurement corresponds to a spatially-averaged measurement (Moore et al. 2000; Randolph et al. 2017)

An additional problem with the current approach to treat whitecaps and bubbles in ocean color imagery is that they presume the pixel size is large enough to capture a spatially-averaged whitecap fraction. This assumption may apply to 1-km scale pixels common to traditional ocean color imagery. However, higher spatial resolution sensors from both aircraft and satellites have become common in recent years. The recently launched satellites Sentinel-2 and Landsat-8 have 10–15 m resolution that can also incorporate individual whitecap features over the ocean rather than areal averages (Fig. 13.2a, b). Higher resolution imagery <10 m pixel sizes from aircrafts or aerial unmanned systems, for example, can resolve *individual* wave features. High spatial resolution image obtained with the PRISM sensor in Monterey Bay (Fig. 13.2c) shows the sun glint reflected over individual wave fronts (Dierssen 2013, p. 201; Mouroulis et al. 2013).

For the above reasons, the concept of whitecap fraction may require reanalysis. In a practical sense, the "limit" to the extent of a whitecap and bubbles on the sea surface can only be rigorously quantified using optics that measured directly how whitecaps, foam and bubbles enhance the reflectance beyond the background reflectance. Optical measurements can provide both a measure of the intensity of the breaking event and a quantifiable limit to the impacted area. Dierssen (2019) proposed that enhanced reflectance from whitecaps and bubbles could be related to

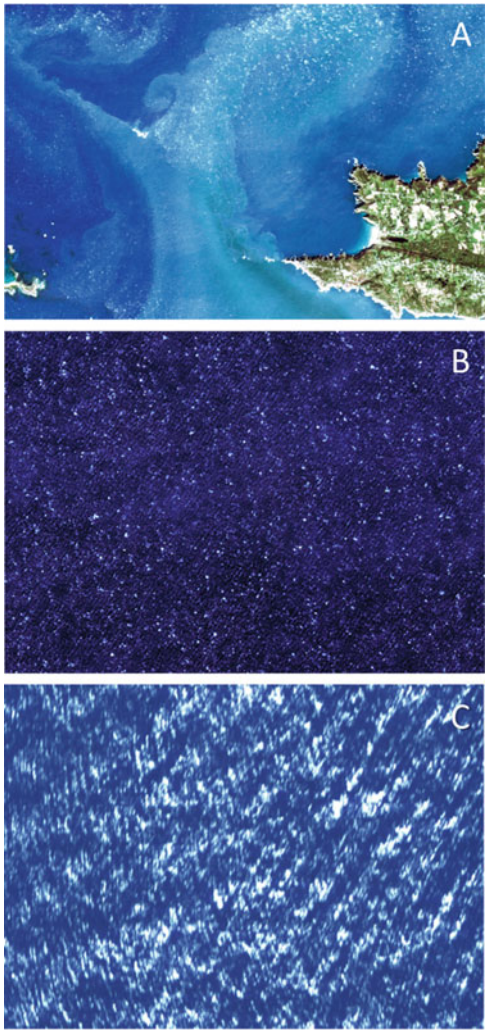

Fig. 13.2 Pseudo-true color image from a 15-m pan sharpened Landsat-8 OLI image from the coast of Normandy with winds estimated at 12.5 m s^{-1} illustrating whitecap features in the midst of (**a**) colorful coastal waters and (**b**) darker offshore waters. (**c**) Individual wave features resolved with the PRISM instrument in Monterey Bay show the impact of sun glint on ocean color measurements at <1 m resolution

an optical measurement called the "whitecap factor", A. This is the enhancement of reflectance due to whitecaps and bubbles above a background reflectance. Numerically, a simple equation can be used to relate the total reflectance, R_t as:

$$R_t = AR_f + (1 - A)R_w \tag{13.1}$$

Where R_f represents the reflectance of a standard whitecap and R_w represents the background reflectance. However, multi-layer models could be incorporated to consider the potentially different spectral reflectance profiles for bubbles and whitecaps.

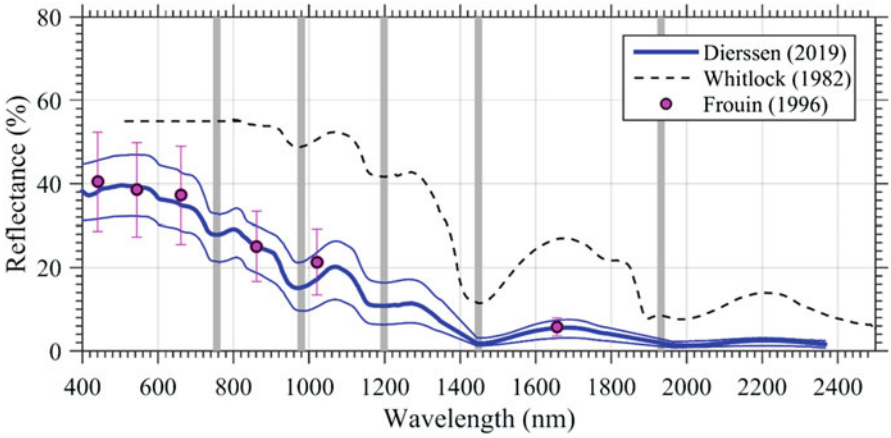

Fig. 13.3 The mean hyperspectral whitecap spectrum measured recently in Long Island Sound, USA shown as the blue line with one standard deviation (Dierssen 2019) and modeled using Eq. 13.2. Historic whitecap reflectance measured over the last 25 years from an indoor tank (Whitlock et al. 1982) and natural breaking in the surf zone (Frouin et al. 1996). The Whitlock et al. (1982) spectrum was modeled using the published relationship to absorption by waters spectrum for wavelengths >800 nm and corrected for the reflectivity of the barium sulfate standard (dashed black line)

Dierssen (2019) presents a standardized whitecap spectrum across the visible, near infrared (NIR) and into short wave infrared (SWIR) (400–2500 nm) taken from measurements in Long Island Sound, USA. Whitecap reflectance was on average ~40% in visible wavelengths with a general "gray" color, even though whitecaps often appear "white" to your eye or a photograph compared to the dark background waters (Fig. 13.3). The spectrum decreased significantly into the near infrared and shortwave infrared following published multi-spectral trends determined from actively breaking waves in the surf zone of San Diego (Frouin et al. 1996). A simple third order polynomial on the log-transformed water absorption is a near match to the average whitecap reflectance spectrum across the visible to SWIR wavelengths (Dierssen 2019):

$$R_f = 0.47x^3 - 1.62x^2 + 8.66x + 31.81 \tag{13.2}$$

where: $x = \log(a_{w.})$

Practically, water absorption across these wavelengths can be retrieved online from "The Water Optical Properties Processor (WOPP)" (Rottgers et al. 2011). As shown in Fig. 13.3, this spectrum is significantly different in the NIR and SWIR from the previous measurements of breaking waves (Whitlock et al. 1982). As detailed in Dierssen (2019), Whitlock et al. (1982) measurements are too high due to the standard used in the measurement, potential sensor and tank artifacts, and incorrect water absorption values in visible wavelengths making their parameterization inaccurate.

The localized troughs in R_f correspond to peaks in liquid water absorption and depths of the troughs are correlated to the amount and intensity of the breaking waves. Reflectance dips are prominent particularly at 750, 980, and 1200 nm resulting from enhanced multiple scattering of light in and around the bubbles and foam and enhanced absorption by water. If hyperspectral measurements are available across these wavebands, then the depths of these spectral features can be used as a method to estimate the whitecap factor A. Including these wavebands into future measurements from ships, aircraft, UAVs and satellites could potentially provide new tools to estimate whitecap contributions to reflectance more accurately than with wind speed.

13.3 Ocean Plastics

The rising amounts of ocean plastics of varying sizes is considered a threat to ocean health (Bergmann et al. 2015) and an emerging challenge for ocean color remote sensing (Maximenko et al. 2017; Garaba and Dierssen 2018). Ocean plastics have an enhanced spectral reflectance and distinct shapes in the NIR to SWIR spectrum whilst also exhibiting apparent color features in visible wavelengths (Cloutis 1989; Huth-Fehre et al. 1995; Garaba and Dierssen 2018). Because manufactured plastics are very diverse in color, floating ocean plastics can be easily mistaken for typical color producing agents of natural waters in the visible spectrum (Garaba and Dierssen 2018; Garaba et al. 2018). Green ocean plastics could appear as floating vegetation or algae, yellowish to brownish plastics might appear as enhanced sediments, and blue ocean plastics could enhance scattering in blue wavelengths similar to reflections of skylight (Fig. 13.4a). However, specific peaks in the NIR at 931, 1215, 1417 and 1732 nm appear to be distinct and related to hydrocarbons.

Microplastics (diameter < 5 mm) harvested from the marine surface layer, however, have a much more consistent spectral shape. As shown in Garaba and Dierssen (2018), these microplastics have presumably been subject to environmental weathering, such as bleaching from the sun, and have had a whiter spectrum in the visible spectrum. A microplastic spectral "endmember" was identified that could represent a pixel covered completely by weathered surface plastic (Fig. 13.4b). Plastics would likely be wet at the sea surface and some of the enhancements in NIR signal would be diminished by overlying water. As shown in Fig. 13.4b, the overall magnitude of the spectrum is lower and the peaks are less pronounced for wet plastics. Moreover, it is not expected that microplastics would cover a complete pixel, but such endmembers could be used in theory to assess the abundance of this endmember in a mixed pixel of dark water and are used in linear mixing models to estimate the contribution by dry and wet plastics.

Analyses of the NIR and SWIR signal of ocean plastic also suggest despite the strong absorption of light by the ocean in these wavelength ranges, aggregated floating plastics can inflate the reflectance of the target ocean pixels (Garaba et al. 2018). In light of this, there is a need to account for the spectral contribution of ocean

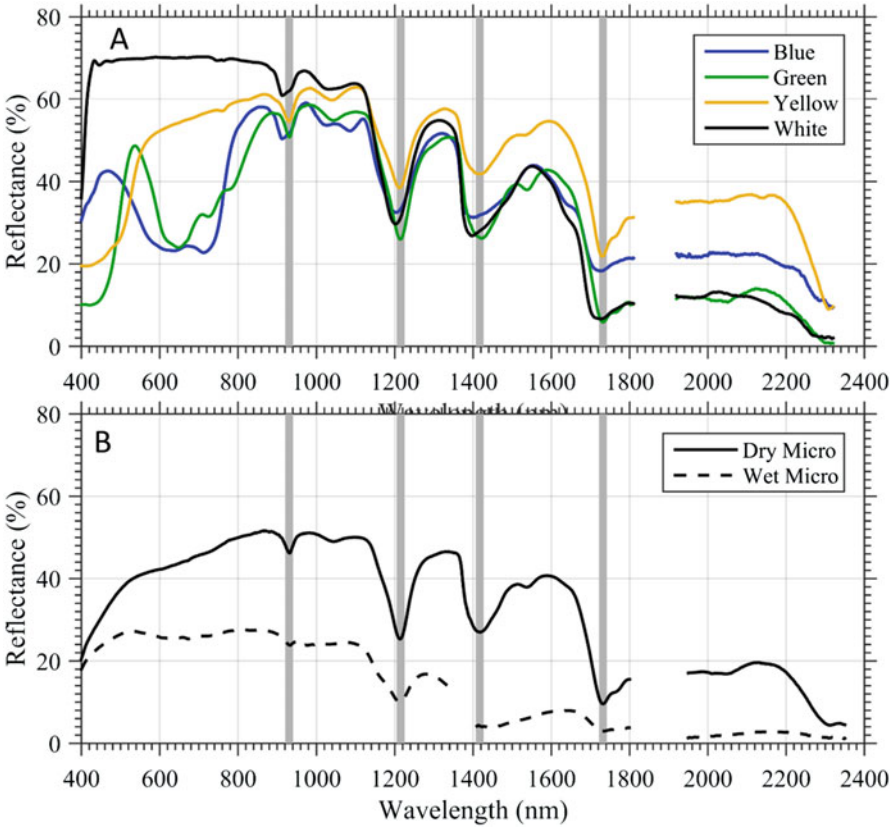

Fig. 13.4 (**a**) Spectra of marine macroplastics from Garaba and Dierssen (2018) showing the variability corresponding to color in visible wavelengths (400–700 nm) and the consistency in the spectra at near infrared and short wave infrared wavelengths. (**b**) Dry microplastics harvested from the North Atlantic show more consistent spectral features in visible wavelengths likely due to bleaching. When the pieces are wetted, the magnitude of the signal decreases across the spectrum. The gray lines represent the spectral features identified as unique to hydrocarbons and potentially useful for identifying these flotsam

plastics to the bulk signal reaching a satellite. If plastics are concentrated, then the contribution of signal in the NIR could be significant. Some of the features unique to plastics may be absorbed by gases in the atmosphere, but some of the absorption features may be observable at the top of the atmosphere. If sensors are designed with the appropriate wavelengths and appropriate spatial resolutions, the unique spectral features of hydrocarbons may allow for detection of surface floating plastics.

13.4 Differentiation from Other White Constituents

The differentiation of whitecaps from plastics, sea ice, and potentially even from the presence of clouds is a remaining problem in ocean color remotes sensing. The basic approach at present is to apply the whitecap, glint and Rayleigh corrections to the imagery in the first step to remove some of the signal due to these contributions (Fig. 13.5). The second step involves a cloud mask that removes pixels from the retrieval that may be cloud contaminated and the signal from water-leaving reflectance is presumed to be too low for accurate retrieval. The cloud masking algorithms tend to be simple thresholds that can remove brightly scattering pixels that may include sun glint, sea ice, other flotsam like plastics and other highly reflective waters. This mask, however, can also remove pixels that contain high amounts of sediment or scattering particles like coccoliths (Balch et al. 2005). The aerosol retrievals are conducted at the last stage and application of the aerosol model which presumes that any residual signal in the NIR from any source is attributable to aerosols. Hence, the aerosol signal will include signals from whitecaps, plastics, sea ice and any other signal that is not removed in the prior steps.

Future measurements in the NIR and SWIR wavelengths using advanced sensor technology is anticipated to further improve the portioning the bulk signal reaching a satellite sensor into the different bright target components. As shown in Fig. 13.6,

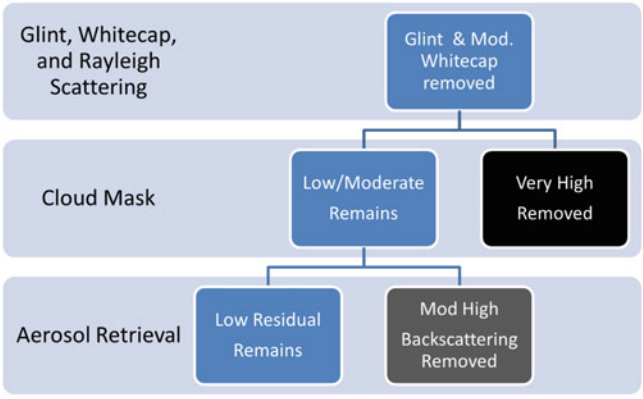

Fig. 13.5 Typical ocean color atmospheric correction techniques are designed to remove bright reflective signals from ocean color imagery. This diagram outlines the atmospheric correction steps and how pixels with high reflectance are either removed from the data stream or the enhanced signal is removed during the correction routines. *Mod* Moderate

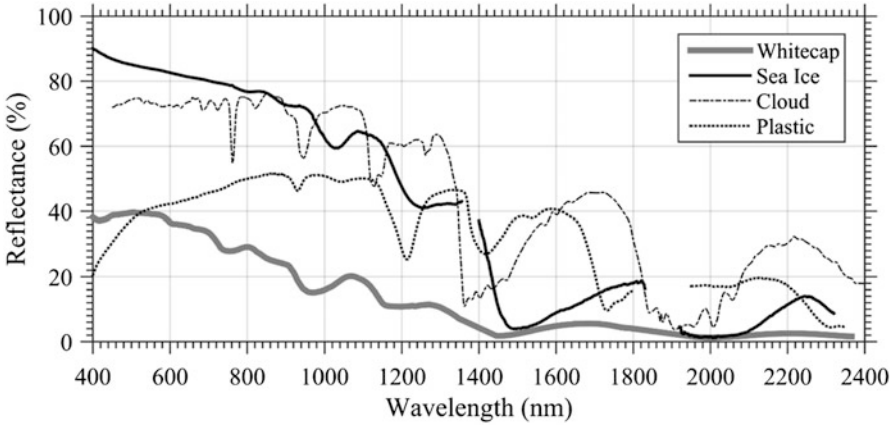

Fig. 13.6 Different targets that may appear white to the human eye have similar spectrally flat reflectance in the visible wavelengths (400–700 nm). The signal in the near infrared and short wave infrared, however, is quite unique to each of these constituents and could be used to identify their presence in ocean color imagery

constituents that may appear spectrally indistinct in visible wavelengths because of their flat "gray-like" reflectance, may have unique spectral responses in the NIR and SWIR that will allow us to differentiate them. Water in different phases absorbs differently and will result in shifts in the reflectance spectra based on whether water is in the gas phase (clouds), liquid phase (whitecaps), or solid phase (sea ice) (Green et al. 2002). For example, the absorption band at 940 nm occurs for clouds, but is shifted longer to 980 nm for whitecaps, and 1030 nm for sea ice (Fig. 13.6). Snow or ice with different amounts of black carbon can also be spectrally differentiated (Khan et al. 2017). These spectral "fingerprints" also differ from those in flotsam like floating wet and dry marine plastics. Future research will allow us to include more bright pixels in our analyses and potentially provide new products based on the spectral signature in the NIR and SWIR. This will also improve estimates of aerosol concentrations and presumably result in more accurate retrievals of water-leaving reflectance.

Acknowledgments We acknowledge the intellectual contributions of Dr. Edward Monahan broadly to the field of whitecaps and the many fruitful discussions and interactions with him over the years. Funding was provided by NASA Ocean Biology and Biogeochemistry through the PACE project (NNX15AC32G) and Forschungsgemeinschaft (DFG, German Research Foundation) – Projektnummer 417276871.

References

Anguelova, M. D., & Webster, F. (2006). Whitecap coverage from satellite measurements: A first step toward modeling the variability of oceanic whitecaps. *Journal of Geophysical Research: Oceans, 1978–2012*, 111.

Bailey, S. W., Franz, B. A., & Werdell, P. J. (2010). Estimation of near-infrared water-leaving reflectance for satellite ocean color data processing. *Optics Express, 18*, 7521–7527.

Balch, W. M., Gordon, H. R., Bowler, B. C., Drapeau, D. T., & Booth, E. S. (2005). Calcium carbonate measurements in the surface global ocean based on Moderate-Resolution Imaging Spectroradiometer data. *Journal of Geophysical Research, 110*, C07001.

Bergmann, M., Gutow, L., & Klages, M. (2015). *Marine anthropogenic litter*. Springer.

Brumer, S. E., Zappa, C. J., Brooks, I. M., Tamura, H., Brown, S. M., Blomquist, B. W., Fairall, C. W., & Cifuentes-Lorenzen, A. (2017). Whitecap coverage dependence on wind and wave statistics as observed during SO GasEx and HiWinGS. *Journal of Physical Oceanography, 47*, 2211–2235.

Cloutis, E. A. (1989). Spectral reflectance properties of hydrocarbons: Remote-sensing implications. *Science, 245*, 165–168.

Dierssen, H. M. (2013). Overview of hyperspectral remote sensing for mapping marine benthic habitats from airborne and underwater sensors. In *Imaging spectrometry XVIII. Proceedings of the SPIE* (pp. 1–7).

Dierssen, H. M. (2019). Hyperspectral measurements, parameterizations, and atmospheric correction of whitecaps and foam from visible to shortwave infrared for ocean color remote sensing. *Frontiers in Earth Science, 7*, 14.

Fogarty, M. C., Fewings, M. R., Paget, A. C., & Dierssen, H. M. (2018). The influence of a sandy substrate, seagrass, or highly turbid water on Albedo and surface heat flux. *Journal of Geophysical Research: Oceans, 123*, 53–73.

Frouin, R., Schwindling, M., & Deschamps, P.-Y. (1996). Spectral reflectance of sea foam in the visible and near-infrared: In situ measurements and remote sensing implications. *Journal of Geophysical Research: Oceans (1978–2012), 101*, 14361–14371.

Gao, B. C., Montes, M. J., Li, R. R., Dierssen, H. M., & Davis, C. O. (2007). An atmospheric correction algorithm for remote sensing of bright coastal waters using MODIS land and ocean channels in the solar spectral region. *IEEE Transactions on Geoscience and Remote Sensing, 45*, 1835–1843.

Garaba, S., Aitken, J., Slat, B., Dierssen, H. M., Lebreton, L., Zielinski, O., & Reisser, J. (2018). Sensing ocean plastics with an airborne hyperspectral shortwave IR imager. *Environmental Science & Technology, 52*, 11699–11707. https://doi.org/10.1021/acs.est.8b02855.

Garaba, S. P., & Dierssen, H. M. (2018). An airborne remote sensing case study of synthetic hydrocarbon detection using short wave infrared absorption features identified from marine-harvested macro-and microplastics. *Remote Sensing of Environment, 205*, 224–235.

Green, R. O., Dozier, J., Roberts, D., & Painter, T. (2002). Spectral snow-reflectance models for grain-size and liquid-water fraction in melting snow for the solar-reflected spectrum. *Annals of Glaciology, 34*, 71–73.

Huth-Fehre, T., Feldhoff, R., Kantimm, T., & others. (1995). NIR-remote sensing and artificial neural networks for rapid identification of post consumer plastics. *Journal of Molecular Structure, 348*, 143–146.

Ibrahim, A., Franz, B., Ahmad, Z., Healy, R., Knobelspiesse, K., Gao, B.-C., Proctor, C., & Zhai, P.-W. (2018). Atmospheric correction for hyperspectral ocean color retrieval with application to the Hyperspectral Imager for the Coastal Ocean (HICO). *Remote Sensing of Environment, 204*, 60–75.

Khan, A. L., Dierssen, H., Schwarz, J. P., Schmitt, C., Chlus, A., Hermanson, M., Painter, T. H., & McKnight, D. M. (2017). Impacts of coal dust from an active mine on the spectral reflectance of Arctic surface snow in Svalbard, Norway. *Journal of Geophysical Research: Atmospheres, 122*, 1767–1778.

Maximenko, N., J. Arvesen, G. Asner, and others. 2017. Remote sensing of marine debris to study dynamics, balances and trends. In *Community white paper produced at the workshop on mission concepts for marine debris sensing* (p. 22).

Monahan, E. C., & Mac Niocaill, G. (2012). *Oceanic whitecaps: And their role in air-sea exchange processes*. Springer Science & Business Media.

Moore, K. D., Voss, K. J., & Gordon, H. R. (2000). Spectral reflectance of whitecaps: Their contribution to water-leaving radiance. *Journal of Geophysical Research: Oceans (1978–2012), 105*, 6493–6499.

Mouroulis, P., Gorp, B. V., Green, R., Dierssen, H. M., Wilson, D. W., Eastwood, M., Boardman, J., Gao, B., Cohen, D., Franklin, B., Loya, F., Lundeen, S., Mazer, A., McCubbin, I., Randall, D., Richardson, B., Rodriguez, J. I., Sarture, C., Urquiza, E., Vargas, R., White, V., & Yee, K. (2013). The Portable Remote Imaging Spectrometer (PRISM) coastal ocean sensor: Design, characteristics and first flight results. *Applied Optics, 53*(7), 1363–1380.

Randolph, K., Dierssen, H. M., Cifuentes-Lorenzen, A., Balch, W. M., Monahan, E. C., Zappa, C. J., Drapeau, D. T., & Bowler, B. (2017). Novel methods for optically measuring whitecaps under natural wave-breaking conditions in the Southern Ocean. *Journal of Atmospheric and Oceanic Technology, 34*, 533–554.

Randolph, K., Dierssen, H. M., Twardowski, M., Cifuentes-Lorenzen, A., & Zappa, C. J. (2014). Optical measurements of small deeply penetrating bubble populations generated by breaking waves in the Southern Ocean. *Journal of Geophysical Research: Oceans., 119*, 757–776.

Rottgers, R., Doerffer, R., McKee, D., & Schonfeld, W. (2011). *Algorithm theoretical basis document: The water optical properties processor (WOPP).* Tech. rep., Helmholtz-Zentrum Geesthacht, University of Strathclyde, Geesthacht.

Scanlon, B., & Ward, B. (2016). The influence of environmental parameters on active and maturing oceanic whitecaps. *Journal of Geophysical Research: Oceans, 121*, 3325–3336.

Whitlock, C. H., Bartlett, D. S., & Gurganus, E. A. (1982). Sea foam reflectance and influence on optimum wavelength for remote sensing of ocean aerosols. *Geophysical Research Letters, 9*, 719–722.

Part IV
A Historical Perspective by E.C. Monahan

Chapter 14
Twixt Wind and Waves: A First-Person Account of the Early Years of the Study of Oceanic Whitecaps

Edward C. Monahan

Abstract While describing my own field and laboratory research on oceanic, and fresh-water, whitecaps, I have tried to provide in this chapter a global over-view touching on the work that many of the other researchers on this topic conducted in the last third of the twentieth century and in the early years of the current century. In approaching this task, I have chosen to describe my personal introduction to air-sea interaction research for those who will be interested in how one embarked on such a career in the early 1960 s.

14.1 Introduction

Let us begin these recollections back on the second day of October 1966, when I found myself out on Lake Superior, heading west from Marquette, Michigan, aboard the bulk carrier *S.S. Cadillac*, an "ore boat" of the Cleveland Cliffs Iron Company, steaming west of the Keweenaw peninsula toward Superior, Wisconsin, bound to pick up a cargo of iron ore. I was not just along for the ride, rather I had a modest program of observations that I intended to carry out on this cruise. My main mission was to make a photographic record of the water surface, a record that could be analyzed to yield an estimate of the fraction of the lake surface that was covered at any instant by whitecaps, the coherent, if somewhat tenuous, patches of bubbles, that were produced each time a surface wave broke, and in doing so entrained air. If someone else had happened to come out on deck, they would have seen me carrying out of the "owner's cabin" a tripod-mounted 35 mm Beattie Varitron (Model VDT) automatic electric sequence camera, equipped with a 50 mm lens and a data recording back with provision for a card, a counter and a clock. I set this camera up looking over the windward rail, and pointing slightly down from the horizontal, so that the images recorded encompassed the lake surface from the horizon down to a few tens of meters off this rail, and once I had plugged in the requisite extension cord, I began taking the first 100 "Ektachrome" images for a "gallery" that would

E. C. Monahan (✉)
Department of Marine Sciences, University of Connecticut, Groton, CT, USA
e-mail: ed.monahan@comcast.net

P. Vlahos (ed.), *Recent Advances in the Study of Oceanic Whitecaps*,
https://doi.org/10.1007/978-3-030-36371-0_14

Fig. 14.1 The author taking some of his early (fresh water) whitecap photographs using a tripod-mounted Beattie Varitron automatic sequence camera aboard the S.S. Detroit Edison in the Spring of 1968. (From author's photo archive)

ultimately include many thousands of such photographs. Figure 14.1 shows me taking such photographs in 1968.

Before describing how we initially went about analyzing these photos, we should perhaps take a step back and explain why we were making our first measurements on a lake, albeit one of the largest lakes in the world, and why we were so interested in cataloguing the fraction of the water surface covered by whitecaps for various wind speeds and wave states.

Why the interest in whitecaps? Well, I had just recently defended my dissertation (Monahan 1966) at MIT, which focused on the production of sea spray droplets, and I had concluded that my at-sea observations were "consistent with the hypothesis that the observed droplets are thrown aloft by the bursting of bubbles and [furthermore] that the droplet-producing bubbles occur in patches on the sea surface, i.e. whitecaps". I had accepted the idea of Duncan Blanchard, one of the many insights I gained from studying his *magnum opus* (Blanchard 1963), that the rate of production of spray droplets at the sea surface at any instant was more or less proportional to the fraction of the sea surface covered by whitecaps at that moment. And I was hoping to parameterize whitecap fraction in terms of routinely measured meteorological parameters such as 10-meter elevation wind speed, the stability of the lower marine atmospheric boundary layer (as reflected in the temperature difference between the surface sea water and the air at 10 meters elevation), wind duration, and fetch, based on my whitecap photographs and associated meteorological

Fig. 14.2 The author reading the surface water temperature using a "thermometer bucket" lowered from the deck of a Great Lakes "ore boat" in the Spring of 1967. (From author's photo archive)

measurements. (A measurement of surface water temperature being taken from an "ore boat" in 1968 is depicted in Fig. 14.2.)

It would be years yet before my colleagues and I would come up with an explicit model for the "sea surface aerosol generation function" (Monahan et al. 1982a, 1986a), but already I was looking for an approach that would make it possible to estimate the rate of sea spray production locally, and with access to the world meteorological data bases, the global sea spray production rate as well. Only later would it come to my attention that some of the passive microwave satellite remote sensing techniques that were used to infer surface wind speed over the oceans relied on the effect that whitecaps have on the emissivity of the ocean surface (e.g, Gordon and Jacobs 1977; Monahan and O'Muircheartaigh 1986), as reflected in an enhancement in the apparent microwave brightness temperature of this surface, to "back out" this wind speed (Ross and Cardone 1974; Webster et al. 1976), and thus these measurements of enhanced microwave brightness temperatures could be used directly to infer fractional whitecap coverage.

But this just opens up another question, why did I find the whole subject of sea salt aerosols so interesting? And to answer that question I need your indulgence as I drop back further and touch briefly on my early introduction to oceanography which occurred upon my arrival in Massachusetts in 1963. This topic will be the subject of the next section.

14.2 Settling, Belatedly, on a Career Research Focus

By the time I graduated from High School I had pretty well decided that I wanted to pursue a career as a scientist, but that was about as far as my career planning had gotten.[1] And by the time I finished the then-five-year undergraduate program in Engineering Physics at Cornell, I was pretty sure I wanted to eventually teach, and conduct research in, Physics when I had completed my graduate education. Thanks to the encouragement of my undergraduate advisor, Dale Corson,[2] I spent the summers before and after my fifth year at Cornell[3] in the Physics Department at the University of California, Berkeley, and as I look back on those summers, I recall with particular pleasure the time I spent helping a graduate student launch primary cosmic ray detectors, suspended from a cluster of helium-filled balloons,[4] which may reflect a budding enthusiasm for the application of physics in pursuit of an understanding of our macroscopic world, i.e. of our environment writ large.

I spent my first two graduate years at the University of Texas, Austin, studying Physics and conducting an experiment to characterize a resonance in the elastic scattering of neutrons by Carbon-12 (Monahan 1961). But the summer between my 2 years in Austin was spent at the National Radio Astronomy Observatory in Green Bank, WV, where I spent my days working with radio telescopes (and many an early evening spelunking in the nearby limestone caves). Among the many people who happily shared stimulating ideas with me and the other summer NRAO graduate assistants were Frank Drake,[5] John Findley, and Otto Struve, the Director. When I returned to Austin that fall, I was determined to shift the focus of my graduate education to some field of physics, broadly defined, where I would not find myself confined to the laboratory.

I then explored options ranging from Astrophysics to Physical Oceanography, and was fortunate to be offered a three-year graduate Ford Fellowship at MIT, that would enable me to study Oceanography in the Department of Meteorology. When I and my family arrived in Cambridge, MA, in September 1961, Oceanography was a growing discipline at MIT, but the establishment of an all-encompassing Department

[1] I imagine that my bent toward science would have manifested itself anyway, but this decision "benefited" from a misdiagnosis that had me bedridden for several months, and sedentary for several years, while in grade school. By the time I reached my last year in high school I was on the soccer team, and had left these well-intended but misplaced constraints behind me, but in the meantime my love of books and nature had fully taken hold.

[2] Dale R. Corson, who went on to serve as the 8th president of Cornell, had earned his Ph.D. at Berkeley.

[3] By contrast, I had spent the summers before each of my first 4 years at Cornell working as a yard clerk for the New York Central Railroad in Weehawken, NJ.

[4] These detectors were launched from the 50 yard-line in the UC, Berkeley, memorial stadium, to allow them to gain significant vertical velocity before they were subject to crosswinds.

[5] Frank D. Drake, who received his B. Engin. Phys. from Cornell in the early 1950s, was in the summer of 1960 actively developing the "Drake Equation" as a means of estimating the number of advanced extra-terrestrial civilizations in our galaxy.

of Earth, Atmospheric, and Planetary Sciences was still several decades away,[6] with at this time Oceanography courses being offered by the Department of Meteorology headed by Professor Henry G. Houghton[7] and by the Department of Geology and Geophysics under the leadership of Professor Robert Rakes Schrock.[8] There was in these early years a fairly flexible curriculum, and in my 2 years in residence in Cambridge I ended up taking courses in both of these departments, and in several other MIT units, and at Harvard as well, via a cross-registration arrangement. My first introduction to cloud condensation nuclei and marine aerosols in particular was in a course taught by Henry Houghton. His careful, lucid, presentation of the role of sea salt and other aerosols in marine cloud formation attracted me to this topic. I spent a portion of the summer between my 2 years in residence at MIT at the Institute of Naval Studies, Center of Naval Analyses, in Cambridge, where Dr. Hans Wetzstein encouraged me to investigate sea surface phenomena, of which sea salt aerosol production was one. At this point I tentatively decided to investigate the role of sea spray in air sea exchange for my dissertation research. But it was apparent, at least to me, that I would need to develop equipment to sample sea spray, and I would need to gain routine access to the ocean to make the measurements I was beginning to envision. And at about this point, Henry Stommel,[9] with whom I was taking a reading course at Harvard, asked me if I had yet visited the Woods Hole Oceanographic Institution. (The formal MIT/WHOI Joint Program was not to be initiated until 1968.) When I allowed as how I had not yet made that pilgrimage some 75 miles to the south, Stommel invited me along on his next trip to Woods Hole. That one visit convinced me that Woods Hole was the ideal location for me to conduct my dissertation research on sea spray. On that, or a later visit to Woods Hole, I got to meet Eric B. Kraus (see, e.g., Kraus 1972), in WHOI's Department of Theoretical Oceanography and Meteorology, who at some point invited me to spend the final year of my MIT Ford Fellowship in residence at WHOI.

By the time I started my second year in Cambridge I had gotten the agreement of Professor Houghton that he would serve as the advisor on my dissertation, but I was

[6]EAPS was formally established at MIT in 1983 via the amalgamation of the Department of Earth and Planetary Sciences and the Department of Meteorology and Physical Oceanography.

[7]Henry Houghton's initial work on fog suppression, during the early days of Meteorology at MIT, and in particular his interaction with the sponsor of this work, Colonel "Ned" Green, the beneficiary of the "Hetty" Green fortune, is delightfully described in Lewis (1963), a book that Duncan Blanchard called to my attention. The results of some of Houghton's early research on fog can be found in Houghton and Radford (1938).

[8]This Professor R.R. Schrock, a distinguished geologist and author of a two volume history of Geology at MIT (Schrock 1977, 1982), is not to be confused with Richard Royce Schrock, another Indiana native and MIT professor, who is a chemist and a Nobel laureate.

[9]Henry Stommel, who was in 1982 to share the first Crafoord Prize in Geosciences administered by the Royal Swedish Academy of Sciences with Edward Lorenz of the Meteorology Department of MIT, was perceived by many of us to be the foremost Physical Oceanographer of his generation, for reasons that are apparent from a reading of the brief contributions of Arnold Aarons, George Veronis, Fritz Fuglister, and others that appear on pp. xiv–xxvii, and the associated material on pp. xxviii–xxxiv, in Warren and Wunsch (1981).

still searching for help as regards the design and construction of my sea spray sampling system. One of my fellow grad students, having heard about my need for help, suggested I contact Professor Harold E. Edgerton[10] in MIT's Electrical and Electronic Engineering Department, in whose lab he was spending time. I duly visited "Doc" Edgerton,[11] who heard me out as I described my plans, but did not, as I understood his brief responses, offer any immediate assistance. And then a week or two later, my grad student friend passed on to me the news that Doc Edgerton was asking why I had not showed up in his lab again.[12] By the end of our second conversation, it dawned on me that Doc had kindly offered me the run of his MIT shop, and his, and Bill Roberts',[13] assistance if I wanted to go forward with the construction of a camera-flash system to photographically record spray droplets in the lower marine boundary layer. I accepted this offer "in a flash" and spending several afternoons a week in Doc's lab during the 1962–1963 academic year, I was able, with ample help, to assemble an underwater camera modified with a shutter mechanism, and an appropriate stroboscopic flash unit. Many of the components were available, to some degree assembled, right in the lab, and others appeared magically from EG & G[14] (although I was told that an old coil that I co-opted in the construction of the flash unit came from a Renault of Jacque Cousteau (see, e.g., Cousteau 1954, 1985), with whom Doc - "Papa Flash" to Cousteau's team - often collaborated when it came to underwater photographic equipment and sonar systems). So in early May of 1963, having just successfully completed my General Exams, I was able to depart for Woods Hole, with my small family and my sea spray photography system (with each element housed in a windowed sheet metal cylinder), to begin my dissertation research in earnest.

Upon our arrival in Woods Hole, I was able to devote full time, and then some, to preparing my dissertation equipment, and helping prepare the instruments and equipment of Eric Kraus' small group for an expedition to Aruba that was scheduled for early in 1964. I soon headed off to some local beaches, to try my luck at

[10]Harold Edgerton was responsible for the practical development of the "stroboscope", and for much of the early stobe lighting used in industry as well as photography, see, e.g. Jussim (1987) and Bruce (1994).

[11]Doc Edgerton was not only held in justly high esteem by his fellow engineers and scientists – he was awarded the National Medal of Science in 1973 – but he was one of the most widely recognized MIT faculty members when it came to the community at large. I would be very surprised if anyone reading this has not seen one or more of Doc's iconic photographs – be it his milk drop corona, or his bullet passing through an apple, or another one of his stroboscopic photographs that graced the pages of National Geographic and other national magazine.

[12]I had misconstrued Doc Edgerton's Nebraska manner of speaking, or had been led astray by his brusque façade, and it was surely just a façade. Doc was the first in the Cambridge community to invite my wife and me over for an evening, during part of which he sat on the floor playing his guitar, surrounded by some fascinating marine archeological artifacts.

[13]W.M. Roberts was the senior technician in H. Edgerton's MIT strobe lab (and an employee of Edgerton, Germeshausen, and Grier).

[14]Harold Edgerton founded the precursor to EG&G in the early 1930s with two of his former students, Kenneth Germeshausen and Herbert Grier.

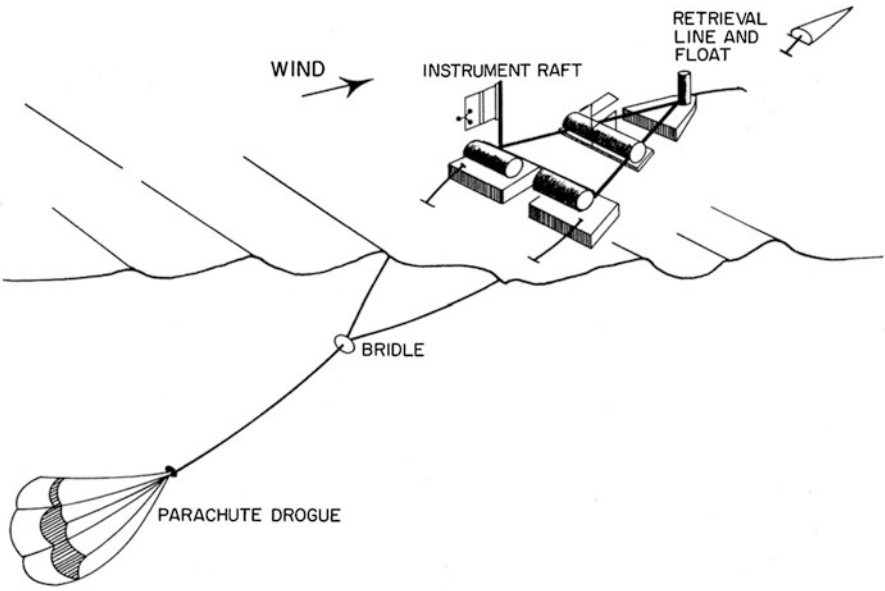

Fig. 14.3 Sea spray instrument raft deployed down wind of a drogue. (From author's Ph.D. dissertation, Monahan 1966)

photographing the spray originating in the surf zone. I quickly became aware of the shortcomings of the system, and took about designing some much-needed modifications. Thanks to the ever-helpful group in the WHOI machine shop, I soon had three thick-walled PVC cylindrical housings, two with plexiglass windows – for the camera and the stobe unit – and a third to contain the batteries that powered the camera motor and shutter mechanism. And now I needed a suitable system that would allow me to take spray photographs just above the open sea surface, free of the interference that might be caused by a ship or other large platform. Having made and tested a few 1/8 scale models, I quickly hit upon a suitable "raft" design. The raft that we built consisted of three fairly small, rectangular, fibre-glass-clad, blocks of foam, or "pontoons", held together by a horizontal triangular frame of angle-iron (see Fig. 1, in Monahan 1968a). When deployed behind a sea anchor (see Monahan and Monahan 1973, for illustrations of various sea anchor, i.e. drogue, designs, including that of the small pilot parachute used with this raft), as shown in Fig. 14.3, the optical axis was held pretty much perpendicular to the wind direction, and was at an average elevation of 13 cm above the open water between the two forward, i.e., up-wind, pontoons.

Before I mention the actual at-sea deployments of this gear I want to acknowledge the support, intellectual, moral, and practical, that I received from the many scientists, technicians, and support staff at WHOI with whom I interacted during my time there. Eric Kraus saw to it that I had an office and the supplies that I needed, and made the suggestion that I undertake to evaluate the contributions that spray droplets might make to the downward transport of horizontal momentum, i.e. to sea surface

stress, that was ultimately a focus of my dissertation. (The earliest expression of this hypothesis that subsequently came to my attention was that of Munk (1955). I also had the opportunity to discuss this conjecture with Hans Roll (see Roll 1965) when he visited Eric Kraus' group while I was in Woods Hole.) Dr. Kraus also supported me for a further year of residence in Woods Hole after my MIT Ford Fellowship had run its course. And Duncan Blanchard was a font of insights and advice, and provided me ready access to his laboratory and his equipment during my 2 years at WHOI.[15]

When in late January of 1964 I, Eric Kraus, and the other members of his research group, joined Earlston Doe and his group from the Bedford Institute of Oceanography aboard the Canadian Scientific Ship Baffin in Bourne, MA, for a research cruise to the British Virgin Islands and Aruba in the Netherland Antilles. My raft and the spray photographic system having been safely stowed in the hold of the Baffin, but not before this gear was repeatedly tested in local Massachusetts waters.[16] During the month of February I was able, using my raft mounted photographic system, to take photographs of sea spray immediately above the sea surface on a number of occasions off the west coast of Aruba. Once the Baffin had visited Woods Hole on its way back to Halifax, I again had access to my photographic equipment, and during the ensuing year I was able on a number of occasions to take sea spray photographs in Buzzards Bay and Vineyard Sound, again making good use of the R/V Asterias This gear aboard the R/V Asterias at the WHOI pier is shown in Fig. 14.4.

Sailing aboard WHOI's R/V Gosnold[17] to "Site D" in the western North Atlantic in April 1965, and aboard the U.S. Coast Guard Cutter Campbell to Ocean Station "Charlie", well offshore of Cape Farewell (Uummannarsuaq in Greenlandic), Greenland, in August of that same year provided me with additional occasions when I was able to launch my raft-mounted spray photography system and thus collect the additional spray photographs, the analysis of which I hoped would enable me to complete my dissertation.[18] But this, my first of many periods of residence in Woods

[15]Duncan Blanchard had also been a Graduate Student of H.G. Houghton. Very early in his career, just after receiving his B.S. degree from Tufts in 1947, Duncan went to work at the General Electric Company in Schenectady, NY, where he was a member of a research group headed by Irving Langmuir, the 1931 Nobel laureate in Chemistry. A delightful description of much of Duncan Blanchard's research can be found in Blanchard (1967).

[16]Most, if not all, of these local deployments were made from WHOI's 40 foot R/V Asterias (the first of two vessels of that name).

[17]I shared one of the below decks cabins on the Gosnold with Bob Heinmiller and a very noisy gyroscope. Bob had been one of the WHOI group on the Baffin cruise to Aruba in early 1964, having joined Eric Kraus' lab after receiving his B.S. in Physics at MIT in 1962. He went on to head WHOI's buoy operations group, and later, having left WHOI, developed an email system that markedly changed how oceanographers interacted, for which in 1995 he received the American Geophysical Union's Ocean Science Award.

[18]I retained the various elements of my raft mounted sea spray photographic system for another decade, but while again resident in Woods Hole in 1975–1976 I was contacted by Doc Edgerton, who, having ascertained that I had no immediate plans for using this equipment, asked that I send to him at MIT the camera, flash unit, and power supply, in their water-tight cases, so that he might

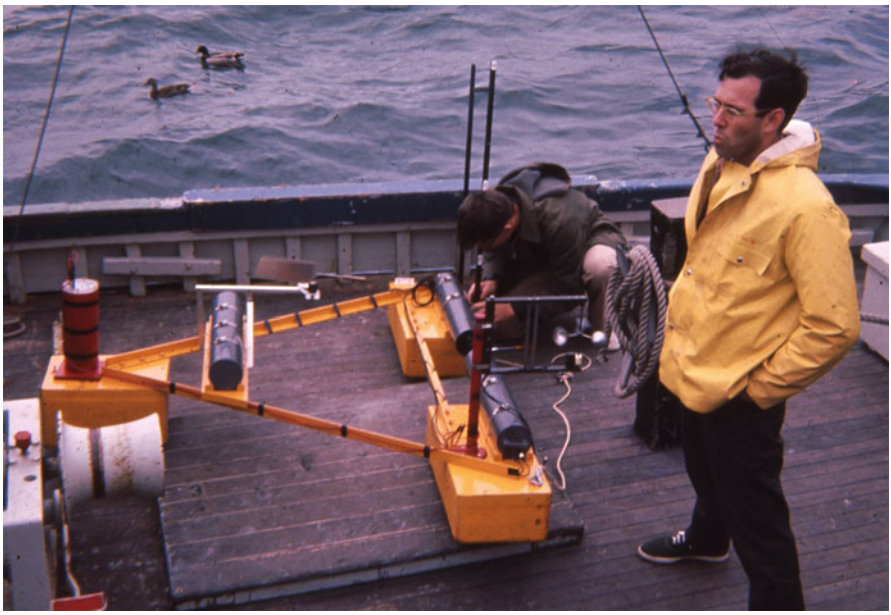

Fig. 14.4 The author and Duncan Blanchard (standing) aboard the R/V Asterias about to leave the pier at the Woods Hole Oceanographic Institution. (From author's photo archive, 1965)

Hole was up, my one-year appointment was over, and I needed to take up one of the several academic positions that had been offered to me. I chose Northern Michigan University in Marquette, MI, which was right on the south shore of Lake Superior, where I was appointed as Assistant Professor of Physics. (And this explains why I undertook in the first instance to study fresh water whitecaps. I was quite literally following Booker T. Washington's 1895 admonition, "Cast down your bucket where you are".) As I and my family left Woods Hole for Marquette it was with the hope that I would be able to return to WHOI the following summer.

I did indeed return to the Woods Hole Oceanographic Institution for the summer of 1966, this time as a Guest Investigator in the laboratory of Duncan Blanchard and Claes Rooth.[19] And this time my working visit was supported by a contract from the

include these items with the other gear he was about to ship to Scotland, where he was participating in an acoustic and photographic search for the Lough Ness monster. I was happy to do so. This was not my only "brush" with Nessie, P.H. LaBlond and M.J. Collins (1987), had occasion to cite one of my whitecap papers (Monahan 1971) in their discussion of the possible size of a Nessie-like object whose head appeared above the waves in a photograph.

[19]Claes G.H. Rooth, who had previously been a member of Carl-Gustaf Rossby's research group in Stockholm, would, after a protracted period at WHOI, move to Miami, where he joined Eric Kraus in what would evolve into the Division of Meteorology and Physical Oceanography of the Rosenstiel School of Marine and Atmospheric Science of the University of Miami, FL.

Office of Naval Research awarded to Northern Michigan University.[20] The main thrust of my efforts that summer were the design and construction of an automatic "whitecap photo-system", that could be used aboard "ships of opportunity" as well as on research vessels, an instrument that will be described in the next section of this paper. But this summer also saw me defend my dissertation, and fulfill the remaining requirements for my Ph.D.

14.3 Photographing Fresh Water Whitecaps, and Making the Required Field Measurements of Wind Speed and Other Variables

For reasons that will be alluded to later in this section, all of the fresh water whitecap photographs, the analysis of which contributed to the data base for our publication on fresh water whitecapping, were taken with one of our several Beattie Varitron automatic sequence cameras mounted on a tripod as described in the first section of this paper. We did proceed with the design and construction of our automatic "port-and-starboard whitecap photo-system", whose construction was begun during my 1966 summer at WHOI. A technical drawing of this "photo-system" is shown in Fig. 14.5, while a photograph of the actual system, in the author's laboratory at Northern Michigan University, is reproduced as Fig. 14.6.

To some, at first glance this system, deployed, appeared to be not all that unlike a shop (or pub) sign of the 1700s, suspended from a bracket, or crane, out over the walkway. Both the old pub signs, and our port-and-starboard whitecap photo-system, were intended to be free to swing back and forth beneath the horizontal cranes from which they were suspended. But unlike the land-based signs which were intended to swing in response to the wind, our photo-system, which was mounted with its rotational axis aligned fore-and-aft, was expected to swing in response to the roll of the ship it was mounted upon. Indeed, depending on the natural roll periods of the photo-system as suspended, and of the ship on which it was mounted, the roll of the photo-system was projected to be either less or more than the roll of the ship. But the relevant key design feature of the photo-system was that, regardless of what the ship did, the photo system would frequently pass through the vertical plane. And the optical axis of the camera, which was parallel to the sides of the housing (the two sides of the "sign") would be precisely pointing to the nadir at each of those instances when the swinging photo-system passed through the vertical and the pitch of the ship was momentarily zero. Now even if the bottom of the photo-system was transparent, we did not want to take pictures of the underlying deck, so

[20]The first of a sequence of ONR contracts via NMU, Hobart and William Smith Colleges, the University of Michigan, University College, Galway, the Naval Postgraduate School, the University of Maine, and the University of Connecticut, without which I would not have been able to pursue my research on whitecapping.

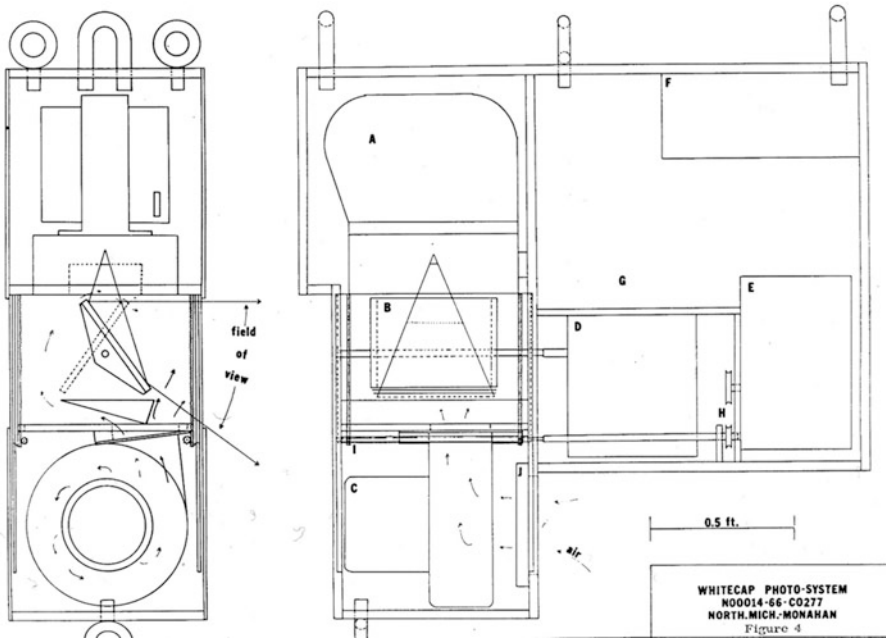

Fig. 14.5 Technical Drawing of the Whitecap Camera System as constructed at WHOI and NMU. (From uncopyrighted report, Monahan 1967)

we included, directly in line with the camera's optical axis, an 11.4 cm by 13.3 cm first surface mirror, which was caused to "flip" between photographs from an orientation that would cause the camera to "see" the ocean surface off the port rail from the horizon (actually from a few degrees above it) downward 44°, when the camera's optical axis was vertical, to an orientation that would yield a photograph with the complementary field of view off the starboard rail.

Now how could we be sure that the camera only took pictures when the camera axis was pointing to the nadir? One of the senior technicians[21] at WHOI suggested we incorporate in our whitecap photo-system the gyroscopic level sensor portion of a World War II era Norden bombsight (see, e.g., Pardini 1999). By mounting a collimated light source and a collimated photo-detector both "looking down" at the gyroscopically stabilized small mirror from the bombsight in such a fashion that the Law of Reflection criterion was only met when the camera's optical axis was pointing in the nadir direction, we had a way to trigger the camera, using the pulse from the photo-detector, at just the right moment to give us the desired field of view. When, by means of a horizontal axel, the first surface mirror was rotated from the port-look to the starboard-look position, the system was then allotted 1 min to wait

[21]If memory serves, this suggestion was made by A.T. (Ted) Spenser, who assisted with the design and construction of the whitecap photo-system during the 1966 summer.

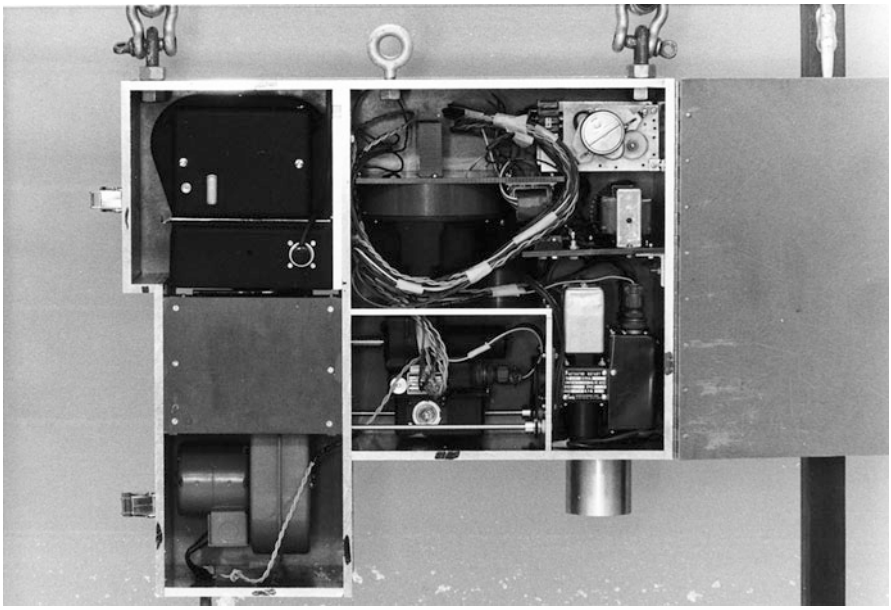

Fig. 14.6 Whitecap Camera System with view of interior components in laboratory at Northern Michigan University. (From uncopyrighted report, Monahan 1967)

for a pulse from the photo-detector to trigger the camera, and at the end of 5 min the horizontal axel was rotated in the opposite direction so that the first-surface mirror was back in the port-look position. This switch back and forth between port and starboard continued every 5 min throughout the deployment. The clock in the data recording back on the Beattie Varitron camera provided a record of the actual time each photograph was taken.

But in a multi-hour deployment it was necessary to protect the camera lens, not to mention the first-surface mirror, from sea spray droplets when the system was used at sea, from fresh water droplets when used on lakes, and from rain droplets and dust in either environment. Our port-and-starboard photo-system was therefore entirely enclosed within a metal and plastic housing, with port- and starboard-doors that were only opened, by means of racks and pinions, when the camera was posed to take a photograph out of that side of the housing. But, since one door was open for 1 min out of every 5, it was vitally important that the interior of the system housing was over-pressured by means of a centrifugal blower, which drew air into the housing through a suitable filter, whenever one of these doors was open.

This whitecap camera system was designed and built before the availability of microprocessors and integrated circuits, so the reader should not be surprised to learn that the automatic operation of this system was overseen by a program controller, which, by means of six cams and six micro-switches, controlled three rotary actuators and the centrifugal blower, and activated pulleys, racks, and pinions.

Fig. 14.7 Whitecap Camera System suspended so that it could move about a fore and aft axis in the rigging of the USCGC Naugatuck. (From uncopyrighted report, Monahan and Zietlow 1968)

Most of the mechanical elements of the whitecap camera system, including the housing itself and the first-surface mirror mounting, had been completed by the time I left Woods Hole at the end of the 1966 summer, and we continued to work on its construction and testing after I had returned to NMU.[22] This system was deployed at least twice, once on the USCGC Nagatuck in Lake Superior in September 1967, as shown in Fig. 14.7, and subsequently from the Buzzards Bay Entrance Light Station, as documented in Fig. 14.8, but it was never made fully operational. The gyroscope from the Norden bombsight, intended for installation on aircraft, was a 115v, 400 Hz device, and we never were able to locate a 60 Hz, or DC, unit that would have proved more compatible with the other electrical components of the whitecap camera system. When used on a fixed structure, such as the BBELS, we simply bypassed this element in our camera system. And experience demonstrated that on the large

[22]M. Grimes, a Physics student at NMU and a former Naval Electronics Technician, proved to be an invaluable assistant in these efforts.

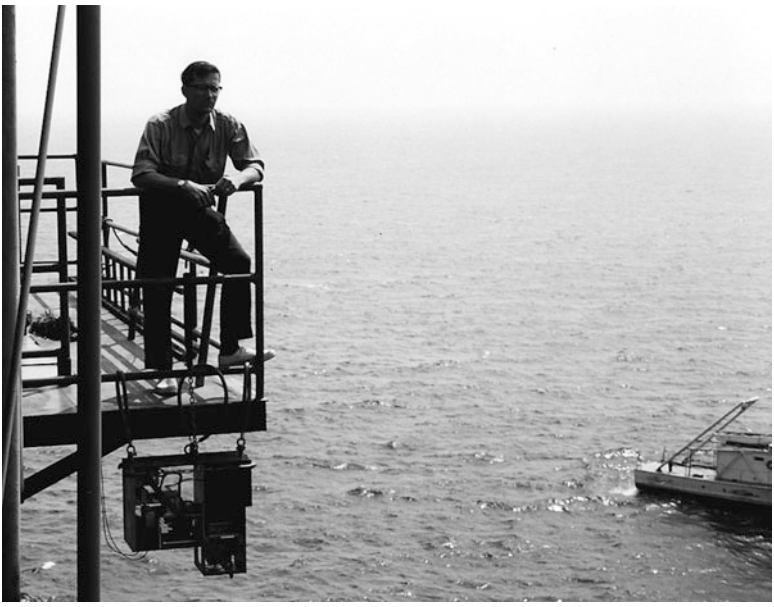

Fig. 14.8 The NMU Whitecap Camera System suspended beneath the deck of the Buzzards Bay Entrance Light Station. (From author's photo archive, circa 1968)

bulk carriers, and on the bigger research vessels such as the F/S Polarstern,[23] ship roll and pitch was not the problem it was on smaller "ships of opportunity". But I think the main reason for the relegation of this whitecap camera system from its originally intended central role in our whitecap photography endeavor was a dawning realization that this system would not, without a complete re-design, accommodate our need to rapidly record relatively large numbers of images of the sea (or lake) surface, a need that will be discussed further in this paper.

Before we could begin our whitecap observation program in earnest, we had to assemble and test the suite of instruments we needed to make the measurements of those meteorological and oceanographic/limnological variables to which we intended to relate our whitecap measurements. First and foremost was the need for accurate anemometers to measure the relative (to the moving ship) wind speed. For this purpose we purchased first one, and then a second, Casella three-cup anemometer. (We had as back-ups four Geodyne Sensitive anemometers.[24]) To record the number of rotations of these cup-anemometers in a given time interval, i.e. the "run

[23]This 387 foot long Arctic and Antarctic research vessel of the Alfred Wegener Institute of Bremerhaven was built in 1982.

[24]These Geodyne anemometers, which I had calibrated initially on a novel "whirling machine" at WHOI (see Monahan 1966) for use in the Aruba wind profile experiment, had been subsequently used by me on the sea spray photography raft to provide a record of the low-elevation wind speed, and on a low elevation wind profiling spar buoy.

of the wind", we used a unit comprised of a D.C. electro-mechanical counter, an isolating circuit, and a battery power supply. (If a host vessel was equipped with an anemometer, readings were taken with this instrument as well.) On our earlier whitecap observation cruises we took along a hand held wind vane, but since all that ships we sailed aboard had either a mounted wind vane, or wind sock, on our later cruises we chose to use these permanently mounted elements to determine the relative wind direction.

To determine the deck-height air temperature, and relative humidity, we used a Central Scientific sling psychrometer, and always took a spare psychrometer and wick with us. Sea surface temperature was measured using a Anscheutz total immersion thermometer mounted within an "A.B.C. sea-surface temperature bucket"[25] built in the shops at NMU.

14.4 The Manual Analysis of Our Whitecap Photographs

The Beattie Varitron cameras as configured for our use yielded "double frame" images of the sea surface, i.e. the resulting transparencies had the same dimensions as the old "2 × 2 (inch)" slides. Our original intention was to project each image of the lake, or sea, surface on a screen on which we had drawn the appropriate Canadian prospective grid, and then to measure the area of each whitecap, and the area of the grid element in which each such whitecap appeared, using a polar planimeter. From these measures we had hoped to determine the actual area of each whitecap that appeared in the image under analysis, and from these same measurements determine the apparent fraction of the water surface covered by whitecaps as a function of the vertical angle between the horizontal and the line from the camera to the element of interest on the sea surface (see example of a Canadian perspective grid in Fig. 14.9 in Monahan 1967). But we quickly discovered that our mechanical planimeters were not suitable for the measurement of the area of the very small images of the typical whitecap as it appeared on the screen.[26]

We soon adopted the technique of using as a screen a large sheet of high quality, i.e. uniform areal density, paper, on which we outlined each whitecap that appeared in the projected image of the water surface. The persons conducting these analyses - and our goal was to have three independent analysts, and never fewer than two, analyze each frame – were instructed to outline those portions of the water surface that appeared to be covered by bubbles, or that appeared "discolored" or lighter than the surrounding water due to the presence of significant numbers of bubbles submerged just beneath the water surface. Before the analysis of a particular image of the water surface, each analyst was instructed to draw the horizon as it appeared in

[25]This thermometer bucket is described in Crawford (1966).

[26]The linear dimension of a whitecap image on the screen was magnified approximately 25 fold over the dimension of the image of that whitecap as it appeared on the transparency frame.

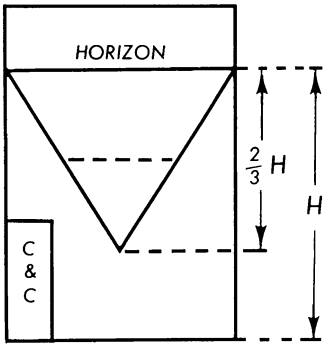

Fig. 14.9 The area of each image subject to analysis for whitecap coverage, see text for details. © American Meteorological Society, used with permission. (From Monahan 1969.)

the image, and then to draw an inverted isosceles triangle on the sheet of paper, one whose base was the horizon and whose apex was located two-thirds of the way down from the horizon toward the bottom of the projected image, as depicted in Fig. 14.9.

Only those whitecaps within the inverted triangle where to be included in the analysis. The other aqueous portions of the image were excluded from the analysis to avoid corrupting the result with any breaking elements of the bow wave (as many of the images were taken from ships underway), or breaking caused by the interaction of waves reflecting off the hull with waves progressing toward the ship (Monahan 1969). Since a view of the camera's clock and counter appeared in the lower left corner image, it did not fall within the area analyzed.

Once an analyst had drawn the horizon and the inverted triangle, and outlined all of the whitecaps within the triangle, the sheet of drafting paper was taken down and placed on a cutting board. The analyst then recorded the width of the base of the triangle, i.e. the width of the horizon, and the height of the triangle, and proceeded to cut out from within the triangle all the whitecaps they had outlined, and from elsewhere on the sheet of paper, a square 5 cm on a side. This square, and all of the excised whitecaps, were then placed in the same covered Petri dish. When all of the photographic frames that represented one "whitecap observation" had been subject to this process, then for each frame the collection of whitecap cutouts[27] were weighed, as was, separately, the reference square for that frame, on a chemist's precision micro-balance, and logged. From the weight of the 25 cm^2 reference square, and the aggregate weight of all of the whitecap cutouts from that same frame, the area of all of the whitecaps in the triangle could be computed. (By keeping the whitecap cutouts and the reference square from the same photograph in the same Petri dish until they were weighed meant that they were all subject to the same relative humidity, and thus had the same areal density.) And now that aggregate whitecap area, divided by the area of the inverted triangle, yielded the fractional whitecap cover within the triangle for that photographic frame. Ultimately, the standard was to analyze 10–20 frames from one whitecap interval, but never less

[27] An idea as to the appearance of such whitecap cutouts ("confetti") can be gleaned from the last figure in Monahan (1968b).

than five, to provide the average whitecap coverage associated with that whitecap interval. Often several sets of 10–20 water surface images were taken at each of several camera aperture settings during one whitecap observation interval, and then the set on which the whitecaps appeared in greatest contrast to the background water were selected to be analyzed in the manner described above. Analysts were instructed to select photographs for analysis based on these criteria, not to select particular images because they appeared to contain more (or less) whitecaps than others taken during the same whitecap observation interval. It was deemed appropriate to undertake the analysis of a larger set of photographic images, when, as often was the case for a whitecap observation interval that corresponded to low wind conditions, few whitecaps were detected in the first set of images analyzed.

Now it is apparent that if we wished to have at least 20 water surface images, and were to use our port-and-starboard whitecap photographic system, it would take a whitecap observation interval of more than one and a half hours to collect this set of photographs.[28] Recognizing that the wave state, and the wind speed, etc., could change markedly in this long an interval, it was concluded that we would be better in most instances using the camera alone to collect the needed photographs. Now the appropriate maximum frequency of photography of the water surface is not constrained by the maximum repetition rate of the camera, but, if we want each photograph to be the basis for an independent measure of whitecap coverage, by the characteristic lifetime of an individual whitecap, the e-folding decay time for such a whitecap. Our early laboratory whitecap simulations (Monahan and Zietlow 1969) indicated that the e-folding time for a decaying fresh water whitecap was about 2.5 s, while the e-folding time for an oceanic whitecap was longer, about 3.8 s. Recent studies of decay time scales of oceanic whitecaps (See, e.g., Callaghan et al. 2012; Callaghan 2013) indicate the complexity of such scales, but leave intact our original conclusion that if sequential photographs of the water surface are to be the basis of independent estimates of whitecap coverage they should be spaced at least 10 s apart. Even so, 10 such photographs can be recorded in less than 2 min, and a 20 photograph whitecap observation interval can be completed in less than three and one-half minutes.

This analysis protocol has been described here in some detail as this analysis technique, was, with few exceptions (and certainly in the case of images taken from ship-borne cameras) used on all of the photographically recorded whitecap images analyzed by my assistants and me.

The relative wind velocity (constructed from our log of relative wind speed and relative direction) was added vectorally to the ship's velocity (based on speed and course as recorded on the bridge[29]) to obtain the absolute, or true, wind velocity.

[28]Even if we had undertaken to modify this automatic photographic system so that it would shift every minute between port and starboard "looks", it would still have taken more than 20 min to complete a "whitecap observation interval".

[29]Hard to believe as it may be in these days of universal global positioning systems, I was left with the impression that these great lakes bulk carriers navigated in the 1960s primarily by using a direction-finding radio with loop antenna to determine when they were abeam of an aircraft radio

And by extending a line upwind, in the direction from which the true wind came, from the position on a nautical chart which showed where each whitecap observation was taken, until it intersected a coastline, we obtained an estimate for each observation interval of fetch, which was pertinent even on a lake as large as Lake Superior.

14.5 Fresh Water Whitecap Results

By the time we had acquired the relevant instruments to take the necessary ancillary environmental measurements and had "fine tuned" our whitecap photography protocols, it was late spring of 1967. But we then began our whitecap observations in earnest, logging more than 2500 on the Great Lakes, mostly aboard bulk carriers, between June and September of that year (Monahan 1968c). We took further whitecap observations on Lakes Superior and Huron in the Spring of 1968, and then, having relocated to Hobart and William Smith Colleges[30] in Geneva, NY, took further whitecap photographs on Lake Seneca[31] and Lake Erie in the autumn of that same year. With the analyses of these results to hand, we duly published our findings in September 1969 (Monahan 1969). (We are still unaware of any other published systematic field observations of fresh water whitecaps, nor do we know of any such observations in the "grey literature".) I would encourage the readers of the current paper to peruse for themselves our September 1969 paper, as I would likewise encourage them to access the other primary sources cited herein.[32] But I will nonetheless highlight here a few of the conclusions contained in that paper.

---

beacon. Of course they also took visual bearings on lighthouses, other traditional navigational aids such as buoys, and landmarks if we were in sight of shore. It seemed to me that when, and only when, they had one of the radio beacons on their beam, did they change course, and then they stayed on this new course until they had the next radio beacon on their beam. Since they were thus sailing rhumb-lines between these radio beacons, it was not difficult to keep track of the ship's course. (The only verbal communication device they the captains seemed to regularly avail themselves of was the telephone. When we arrived at one of our infrequent ports of call, the captain would walk to the foot of the pier and call Ohio on the land-line phone in the phone-booth which seemed to be a feature of every "ore dock".)

[30]Where, as the colleges' first Assistant Professor of Oceanography, I had the opportunity to teach not only Oceanography but also Meteorology.

[31]Lake Seneca, with a length of 38 miles shares with Lake Cayuga the distinction of being one of the two longest of the Finger Lakes in upstate New York, and it is also the by far the deepest (with a maximum depth of 188 m).

[32]We wish our readers to avoid the confusion and inaccuracies as regards the findings of the original author that often occur if one uses secondary sources for these findings and conclusions. In this same vein, it is insightful to see how investigators' interpretations of their own earlier findings mature with the passage of time and this can only be gleaned from a reading of their earlier papers as well as their more recent ones.

Given that the Great Lakes are in the middle of a continental land mass, it was not unduly surprising that exceptionally large ΔTs[33] were found in association with many of the whitecap observations taken on these lakes. From our admittedly limited set of finite fresh water whitecap coverage values we concluded that, for about the same wind speed, "greater whitecap coverage is observed when the atmosphere is thermally unstable than when it is stable". This is in accord with many oceanic observations (See Roll 1965, pp. 140–150), and with the observations of the ship's cook on one of the ore boats, who came along the deck while I was tending one of our Beattie cameras and said, and here I paraphrase, "You know, there are a lot more breaking waves for about the same wind in October, as you'll find in May". And he was right, in October the air is usually markedly colder than the lake surface, i.e. the lower MABL is markedly unstable, and in May the air can be quite warm, the lake surface is often still cold, and as a consequence the lower atmosphere is typically quite stable. Figure 1.4a on pg. 14 of Monahan (1968c) shows that even on the 4th of July, 1967, the surface water temperature out toward the middle of Lake Huron was only 5.1 °C shortly before 3:00 PM.

One of the conclusions in this fresh water whitecap paper, which we arrived out from a consideration of the results from only 20 whitecap observation intervals, was that there appeared to be "an abrupt, increase [in fractional whitecap coverage] as the wind speed increases from ~7 to ~8 m sec^{-1}". We went on to conclude that this abrupt increase was "in qualitative agreement" with the findings described in Walter Munk's 1947 paper. I hasten to point out that our subsequent extensive field studies of oceanic whitecaps have led us to set aside this concept of a "critical wind speed" for the onset of whitecapping. In this fresh water whitecap paper, and previously in the main paper arising from our dissertation (Monahan 1968a), we drew inferences regarding the wind speed dependence of oceanic whitecap coverage from both this early paper by Munk, and from Blanchard's 1963 paper. These two papers, along with the paper by Gathman and Trent (1968), are the only three previously published[34] journal articles that included information on the wind dependence of whitecap coverage. We will briefly in the next section describe what whitecap data are available in these three papers. But first it is appropriate that we mention the 1969 work of Vincent Cardone.[35] Cardone contacted us when our fresh water whitecap paper came out, if not while it was in manuscript, and sought assurances as regards the fetch, duration, etc., associated with our whitecap observations. Cardone,

[33]When ΔT, the sea (or lake) surface water temperature minus the 10 m-elevation air temperature, was less than -0.4 C° the marine atmospheric boundary layer was taken to be stable; when ΔT was greater than +0.6 C° the MABL was deemed to be unstable, and when -0.4 C° < ΔT < +0.6 C° the MABL was described a being "near neutral".

[34]We are as of this date still unaware of any other pre-1969 journal articles that contain field data on the wind dependence of whitecap coverage.

[35]See Cardone (1969). It is our recollection that this NYU technical report is essentially all or part of Cardone's 1970 dissertation work, which he did under the guidance of Willard J. ("Bill") Pierson. Vincent Cardone went on to co-found Oceanweather, Inc. in 1977. Bill Pierson was one of the best know wave modelers of his era, See, e.g., Donelan and Cardone (2003).

assuming that the fraction of the water "surface covered by whitecaps. . .is directly related to the rate of energy transfer from the air flow to the fully developed spectral components [of the waves] through a combined Miles-Phillips type instability mechanism", was then able to calculate in his 1969 report the wind speed dependence of whitecap coverage that should pertain to a fully developed (fresh water) sea, under conditions of neutral MABL stability. We will discuss this further when we review the findings of our initial ocean whitecaps paper (Monahan 1971), but we will state here that his results led us to adopt power-law expressions in U, the 10-m elevation wind speed, to describe the fraction of the sea surface to be covered by oceanic whitecaps.[36]

14.6 The First Published Descriptions of the Wind Dependence of Whitecap Coverage

The first journal article that described field observations on the variation of whitecapping with wind speed was the 1947 paper of Walter Munk cited above. Among the photographic plates included in this article are photographs taken by the U.S. Navy, some are oblique views of the sea surface taken from an elevation of 200 feet (61 m), and others are nadir views taken from an elevation 1000 feet (300 m). The eight[37] photographs used for the estimation of the frequency of whitecapping were those taken from 300 m, each of which captured some 10^4 m^2 of the sea surface. Munk summarized their these images as showing "no foam patches at wind speeds of less than 5 m/sec, but there are 10 to 15 foam patches for winds exceeding 7 m/sec". This finding is depicted on his Fig. 47, where he described the wind dependence of whitecapping with a step function, (i.e. no whitecaps for winds below 7 m/s and ~13 whitecaps per 10^4 m^2 of sea surface when the winds were above 7 m/s).

In this same article Munk had recourse to the Beaufort Scale,[38] as it appeared in a 1938 U.S. Dept. of Agriculture publication (U.S.D.A., Weather Bureau 1938). This

[36]Cardone (1969) was not the only investigator to take interest in these findings regarding fresh water whitecap coverage and its variation with wind speed. Williams Jr. (1970) put forth an explanation for "the discrepancy between Monahan's results and Blanchard's (1963)" to which we responded (Monahan 1970), and then Blanchard (1971) contributed to this discussion. In his note Blanchard pointed out that Williams own whitecap coverage values were approximately 30% below his, even though "Williams obtained his data (Murphy 1968) from duplicates of the same photographs used in my [Blanchard's] analysis".

[37]This number is inferred from the number of n(U) points, 8, that appear on Fig. 47.

[38]The Beaufort Wind Scale, as pointed out by Kinsman (1969a, b), was originally developed by Sir Francis Beaufort to categorize, for each of 12 Wind Forces, the sailing characteristics of an eighteenth century man-of-war, i.e. the amount of sail such a ship could safely carry for each Force, i.e. not the physical appearance of the sea surface for each wind category. Blair Kinsman was a dedicated teacher, a true "wave man", and the author of a standard book on wind waves (Kinsman 1965). Some idea of his career can be gleaned from Phillips (1991).

version of the Beaufort Scale, in its description of Beaufort 3 (3.6–5.1 m/s), mentions "scattering incipient whitecaps making their appearance". And its description of Beaufort 4 (5.7–8.2 m/s) calls for "numerous well developed whitecaps, which give the ocean a spotted appearance". Munk concluded that these descriptions were consistent with his step function, as "the lowest instantaneous wind speed sufficient to bring about whitecaps appears to lie in the range 11 to 16 knots [5.7–8.2 m/sec]". Among the published data he referenced in support of his thesis as regards the existence of a discrete discontinuity, perhaps reflecting the onset of a Kelvin-Helmholtz instability, at about 7 m/s, were Alfred Woodcock's[39] observations of changes with wind speed (and atmospheric stability) of the soaring patterns of seagulls (Woodcock 1940).

The second article that presented some data on the wind dependence of whitecapping was the extensive 1963 paper of Blanchard[40] mentioned above. In the section on "the world ocean charge production" he estimated the rate of charge production at the surface of the world ocean contributed by various mechanisms. In a subsection on "charge transfer by intense bubbling" he calculated the rate of global charge production from Aliverti and Lovera's laboratory results on the net positive charge transfer across a unit area of saltwater surface subjected to intense bubbling (Aliverti and Lovera 1939), and his own estimate of the area of the global ocean's surface covered by whitecaps, per degree of latitude, and by season. He had obtained this estimate of the seasonal area of whitecaps per degree of latitude by combining data on the areas of the world ocean subjected to specific mean wind speeds with a description of oceanic whitecap coverage as a function of wind speed which in turn he generated from his analysis of five nadir photographs taken of the Caribbean Sea from elevations of 120–180 m by the U.S. Navy (1952) for "the express purpose of illustrating the state of the sea surface as a function of the wind speed". While later in this same paper Blanchard decided to set aside this particular charging mechanism when he listed the various world ocean charge production mechanisms, his Figure 31, showing oceanic whitecap coverage as a function of wind speed, has proved useful to many subsequent investigators.

A brief description of how these five Weather Squadron aerial photographs were analyzed for fractional whitecap coverage appears in this 1963 paper of Blanchard. These photographs were in such format that it was possible to place them on a light table, and all the "whitecaps, large and small were" then carefully "traced onto

[39] An introduction of the work of Al Woodcock, who is better known for his careful observational work on sea salt aerosols than for his insightful investigations on gull soaring (Woodcock 1940) and the sailing of the Portuguese Man-of-War jellyfish (Woodcock 1944), can be found in Blanchard (1986).

[40] We would suggest to any serious students of marine aerosols that it would be well worth their time to read this 170 page-long paper (Blanchard 1963). Readability has been a hallmark distinguishing all of Duncan Blanchard's technical papers, and of his books (e.g., Blanchard 1967) and articles (e.g., Blanchard 1970) intended for a more general readership.

1millimeter-square graph paper".[41] By summing up the total number of such "millimeter squares covered by whitecaps" in each photograph, and divided the aggregate whitecap area by the area of the respective photograph he was able to obtain the fractional whitecap area to identify with the wind speed listed with that photograph. When the results of this analysis were plotted (Figure 31 in Blanchard 1963), the five points could be described by a simple curve, that intersected the abscissa at a wind speed "of about 6 knots" (i.e., ~ 3 m/s),[42] and for winds higher than 10 knots (~5 m/s) could be fitted by a quadratic expression,[43] i.e. the whitecap coverage, W, was found to vary with the square of the wind speed, U.

When one compares the area of sea surface captured in one of these Weather Squadron nadir photographs taken from 120–180 m elevation with the effective sea surface area included in one of our deck-height oblique photographs, it is reasonable to conclude that each aerial image included significantly more sea surface area than one of our oblique images, but far less than the aggregate sea surface area included in the 10 oblique images that represented one of our standard "observation intervals". Yet when we compare, as we will in a later section, the fractional whitecap coverage of a group of our whitecap observation intervals all taken at a roughly common wind speed, we find a very wide spread in the W-values. Thus if we were to arbitrarily select the W-value from only one of our whitecap observation intervals to represent each wind speed "bin", we would certainly not be able to fit a simple smooth curve through these few points. (Such a "curve" might not even show a monatonic increase in W with U.) Why then were the five points obtained by Blanchard from the analysis of those Weather Squadron photographs amenable to description by a smooth (quadratic) curve? We will never at this stage know for certain, but since it apparently was the purpose of that Navy manual to provide aviators with a tool for estimating the "on the deck", i.e., very low elevation, wind speed, by the expedient of comparing these photographs with what they saw looking down from their aircraft, it is not unreasonable to suggest that individual photographs were carefully selected so that they represented what the assemblers of this manual believed were typical images of the sea surface for each of the selected wind speeds.[44]

[41] I can only imagine that Duncan Blanchard or Ted Spenser mentioned this "tracing each whitecap" approach to us. But we then opted for the "cutting and weighing", rather than the "counting the squares", approach to get the actual aggregate whitecap areas.

[42] It is interesting to note that Blanchard contended that this intercept was "in excellent agreement with the. . .Beaufort scale. . . which states that whitecaps begin to appear at a wind force of 3,. . .", and then juxtapose this statement with Munk's appeal to the Beaufort scale as support for his finding of a force 4, ~7 m/s, onset of whitecapping.

[43] Blanchard, in a footnote, suggested that "this [quadratic dependence] implies that the [wind] stress is directly proportional to the areal coverage of whitecaps".

[44] When we were approached a number of years ago by a publisher of a book and CD on waves with the request that we provide short video "clips", each about a minute in duration if I remember correctly, to illustrate the appearance of the sea surface for each Beaufort force, we were faced with a challenge. We could easily identify one or more video tapes (this was after we have taken up digital imaging of the sea surface) which contained footage collected at each Beaufort stage, but we realized that such a brief "clip" from that subset of tapes might be very unrepresentative of the

In the third precursor article, the one by Gathman and Trent also cited above, it was suggested that whitecaps were totally absent from the sea surface for winds less than or equal to 6 kt (3.1 m/s), "but they did occur 80% of the time when the wind speed was > 6 kt". This inference was based on the analysis of 44 photographs taken during a cruise of the USNS Eltainin from San Francisco to Pago Pago. These authors concluded "that a wind speed between 6 and 20 kt is not a precise indicator of whitecap activity". This short article unfortunately does not contain a tabulation, or graph, showing the whitecap numbers, or whitecap coverage, and wind speed, associated with each image in this set of sea surface photographs.

It is of interest to note that while there are surprisingly few early written descriptions of whitecapping, there are certainly many early graphic representations of whitecaps, i.e. many old seascapes depicting the wind-blown, whitecap strewn, ocean surface. Since many of these same paintings also include images of warships under sail, and since the original Beaufort Scale defined the various wind forces in terms of the sail-carrying capacity of just such men of war (see Kinsman 1969a, b), if we were to take copies of a large group of such paintings and determine the fractional whitecap coverage by the "confetti weighing technique" described elsewhere in this paper, we could then plot whitecap coverage versus Beaufort Force, or equivalents, wind speed, and then see how the resulting plot compares with present day W (U) expressions.[45]

14.7 Our Initial Oceanic Whitecap Observations

We were able to make our initial systematic observations of oceanic whitecaps during the summer of 1968 when we were again back at the Woods Hole Oceanographic Institution, some from the USCGC White Sage in Buzzards Bay, and were then able to extend our oceanic whitecap data base in the summer of 1969, which we again spent as a Visiting Investigator at WHOI. Over that summer of 1969 I was transitioning from Hobart and William Smith Colleges to the University of Michigan in Ann Arbor, and was able to arrange for a graduate student, Mike Walters, of my soon-to-be U-M colleague, Donald Portman, using one of our Beattie Varitron

average whitecap coverage to be expected for that force on the Beaufort scale. But by this time we had a well-established curve that represented our best understanding of how the fraction of the sea surface covered by those whitecaps amenable to video resolution varied with 10-meter elevation wind speed (or Beaufort force). And so we set about finding, for each subset of tapes taken when the wind corresponded to a particular Beaufort force, a 1 min "clip" for which the average whitecap coverage corresponded closely to the value of W for that U as defined by our published curve (Monahan and Wang 1996). We think it reasonable to suggest that the anonymous preparers of this 1952 Weather Squadron manual did something comparable in identifying photographs to represent each wind speed range.

[45]We would be curious to see if many of the painters of these seascapes had taken "artistic license" and incorporated in their images a few too many whitecaps for the conditions consistent with the range of sails shown unfurled on the ships in their paintings.

cameras, to take extensive sets of whitecap photographs to windward of Barbados in May of that year from the R/V Flip[46] and its tender the U.S.S. Salish, as part of BOMEX, Barbados Oceanographic and Meteorological Experiment. That summer I made some whitecap observations in nearby Buzzards Bay and in late July and August managed to augment our growing collection of whitecap observation intervals while sailing from Hoboken, NJ, via Guantanamo Bay, Cuba, to Puerto Cortez, Honduras, and then back to Hoboken, aboard the S.S. Fra Berlanga, a refrigerated "banana boat" of the United Fruit Company. Further observations were recorded for me later that same August on a cruise from Woods Hole to Bermuda. Before discussing the results of our analysis of these oceanic whitecap observations, we will digress briefly to describe a new whitecap observation system that we built and tested during that Woods Hole summer.

Aware of the challenges of using photographs taken with the camera's optical axis pointing other than perpendicularly downward at the sea surface, i.e. "nadir look", for the assessment of fractional whitecap coverage, and particularly for the determination of the size distribution of whitecaps, we decided to develop a balloon-borne nadir look system that would allow us to continue to make use of our Beattie Varitron cameras. This system consisted of a fibre-glass-clad, polyurethane, clam-shell-shaped, "capsule" to accommodate the camera, and a pair of ~ 3 m-diameter "fixed altitude" helium-filled balloons to sustain the capsule some 15–45 m above the sea surface. The capsule was pierced top-to-bottom by a trunk, or shaft, which was sealed by a water-tight plexi-glass window and gasket at the bottom and by another plexi-glass plate at the top. The camera was mounted toward the bottom of the trunk, pointing downward. The size of the capsule was such that it would provide sufficient buoyancy to keep itself, the camera, and the associated rigging, afloat in case it came down on the sea surface having lost the lift of both of the balloons. The aggregate lift of the two balloons was such that the angle of the tether that secured the balloon-camera-system to the tending ship would not exceed ~60° from the vertical for the maximum design wind.[47] Two smaller balloons were chosen rather

[46]The R/V Flip (FLoating Instrument Platform), operated by SIO for ONR, is a 355 foot long vessel which is towed while horizontal to the field site, in this case by the US. Navy tugboat U.S.S. Salish, and then by ballasting one end, it is caused to "flip" to a vertical orientation, where it extends 55 feet above the water, and 300 feet below the sea surface, making it an excellent, stable, platform, essentially a spar buoy, for oceanographic, meteorological, and acoustic measurements.

[47]Since what we are reporting on here occurred more than 45 years ago, we trust that we are not putting our engineering credentials at risk by describing a momentary lapse in logic that occurred when we were first testing this balloon-camera system. If the net lift of the balloons is represented by L, and the weight of the capsule and camera is W, then the system will lift off when the wind is calm if L gt; W, indeed the tension in the tether line, T, is simply T = L−W in this instance. In a flurry of spur of the moment design adjustments, the camera capsule, rather than being suspended directly from the two balloons, was suspended from a line which in turn was run over a pulley attached beneath the two balloons, and then fed down to the tender. The balloons were still attached to the tender by the tether line. (The not-so-great idea was that this arrangement would allow the observer to easily move the camera up and down, without needing to change the elevation of the balloons.) When this arrangement was put into effect on a day of still airs, and the balloons were

Fig. 14.10 Test of balloon-borne camera system over Vineyard Sound, MA. Note camera "capsule", or gondola, suspended from two helium-filled fixed altitude balloons. If one balloon failed, then the camera bearing gondola would make a soft landing on the sea surface. (From author's photo archive, circa 1969)

than one larger one so that, in the instance where one balloon burst, the camera system would make a relatively "soft landing" on the water surface. An electrical cable, and a shutter control cable, ran with the tether line from the capsule down to the tender, which contained the battery supply for the camera, and an observer who would trigger the camera shutter at suitable intervals. The camera capsule, or gondola, suspended from two balloons, with the whole system tethered to a small tender is shown in Fig. 14.10.

released by their handlers on the pier at WHOI, the balloons rose only a few feet until the line over the pulley became taught, and that is as high as they would go. A hastily sketched free-body-diagram for the pulley quickly showed us the error of our ways. The upward force on the pulley remained L, the net lift of the two balloons, but the downward forces on the pulley were three in number, the downward force of the line that led to the camera capsule, W, the downward force exerted on the pulley by this same line after it went over the pulley, which is of course also W, and finally the tension in the tether line, T. The static equilibrium calls for the sum of the downward forces to equal the magnitude of the upward force, i.e. T + 2 W = L. For the balloon and camera system to lift off, T gt; 0, i.e. L gt; 2 W! We quickly did away with the pulley system, and then the two balloons handily lifted the camera gondola off the pier and we were duly required to tug on the tether to cause the system to stop rising.

Fig. 14.11 View of bottom surface of fibre-glassed polyurethane gondola, showing camera window at bottom of vertical trunk. (From author's photo archive, circa 1969)

Figure 14.11 provides a close-up view of the bottom of the capsule, showing the Plexiglas window through which the nadir-look photographs of the sea surface were taken. This system worked under the light winds under which it was tested in Woods Hole harbor. And we learned that we could keep the tether angle as desired by running down wind with the tender. But it became apparent that if we wished to take such nadir-look photographs at the higher wind speeds where much of our interest focused, we would need to substitute a parafoil kite, or some other lift system that had a similar lift-to-drag ratio, in place of the balloons.[48] (Since the lift obtained from a balloon goes as its volume, which is proportional to R^3, and the drag goes roughly as its cross-sectional area, which is proportional to R^2, it would have been possible to get a higher lift-to-drag ratio using substantially larger balloons, but at the price of having to handle a much more unwieldy apparatus and of needing to install a hefty winch to deal with the greater tension in the tether line.) We did manage to quickly obtain a small parafoil kite, and were pleased with its flying behavior, but the summer came to an end before we were able to get such a kite large enough to lift our camera capsule system with enough lift to spare to assure us that even under high wind conditions it would still be flying not too far from overhead.

Let us now return to a discussion of what was found when we analyzed the oceanic whitecap photographs that were taken in 1968 and 1969. All told, some 432 photographs, taken during 70 whitecap observation intervals, were each analyzed as

[48]Nowadays we would undoubtedly be considering a small UAV, i.e. unmanned aerial vehicle, to carry our whitecap camera aloft.

described in our fresh water whitecaps paper. What follows represents a brief summary of the findings we reported in our 1971 oceanic whitecaps paper cited previously.

It was determined that for wind speeds greater than 4 m/s Eq. 14.1 defines a curve

$$W\% = 0.00135\ U^{3.4} \tag{14.1}$$

that "coincides with the highest whitecap coverage observations at the various wind speeds, thus forming an envelope over all the data points." The equivalent expression for this "envelope", in terms of fractional whitecap coverage, is given by Eq. 14.2.

$$W = 1.35 \times 10^{-5} U^{3.4} \tag{14.2}$$

Wishing to compare this with Cardone's semi-empirical calculations (see Cardone 1969, and Ross and Cardone 1970), which were for fresh water whitecap coverage in terms of a wind measured at 19.5 m above the sea surface, we first had to make adjustments to the coefficient to take into account the disparate lifetimes of salt water and fresh water whitecaps as found in the laboratory studies of Monahan and Zietlow (1969). Assuming that for the same wind speed, atmospheric stability, fetch, and duration, one can expect to have about the same number of breaking waves occurring per second per unit surface area in fresh water as in salt water, but noting that individual salt water whitecaps were found to have an e-folding lifetime some 1.51 times longer than the lifetime of fresh water whitecaps, it is reasonable to conclude that for the same meteorological conditions the instantaneous whitecap coverage of an ocean will be 1.51 greater than the coverage of a large fresh water body. We therefore multiplied Cardone's expression by this factor.[49] We now have Cardone's equation for oceanic whitecap coverage, but for winds, U, measured at 19.9 m elevation, and what we want is this expression in terms of the 10 m-elevation winds. We obtained the desired equation, Eq. 14.3, "by adjusting the abscissa values of the points forming this curve in accord with the family of logarithmic wind profiles" found in Roll's 1965 book. A comparison of this equation with Eq. 14.1 shows similarities in both the

$$W\% = 0.0012\ U^{3.3} \tag{14.3}$$

coefficients and in the exponents of U. It is noted in this paper, and is apparent for Fig. 2 of this article, that these oceanic whitecap observations, often referred to collectively as "BOMEX Plus", are in accord with Gathman and Trent's suggestion that the onset of whitecapping occurs at a wind speed of about 3 m/s, and conversely,

[49]This same adjustment for "salt water effects" was subsequently adopted by Ross and Cardone (1974).

these observations do not support Munk's "contention that there is an abrupt onset of whitecapping as the wind speed exceeds 6m/sec".

As the reader will note, there is a gap of some eight or nine years between our 1971 oceanic whitecaps paper discussed in this section and our next papers on this topic which are referenced in the following section of this paper. While ONR continued to support our work on whitecaps after our move to the University of Michigan, we soon found ourselves heavily involved in the Michigan Sea Grant enterprise. Our Sea Grant sponsored work focused almost exclusively on current measurements, both Eularian and Lagrangian, and their interpretation (see Monahan and Monahan 1973, and Monahan et al. 1975). After I left Michigan in early 1975, by then an Associate Professor in what had become the Department of Atmospheric and Oceanic Sciences, I took up an administrative post with a small undergraduate program, the Sea Education Association, which had just relocated to Woods Hole (see, Helfrich 1994). It was not until 1978, two years after we had moved to Ireland to what was then University College, Galway (and now is the National University of Ireland, Galway), that, again with the support of ONR, I was in a position to refocus my research efforts on whitecapping and sea spray production.

14.8 In Search of Capaill Bhána,[50] the White Horses of Ireland

When I arrived in Galway I found myself the only physical oceanographer in Ireland, or certainly the only one with the freedom of choice as regards research agenda that we associate with a university post. I was encouraged to take a fresh look at the physical oceanography of the coastal waters of Ireland and as a consequence I found myself spending a fair amount of time aboard a 70 foot-long stern trawler, the R/V Lough Beltra, particularly on the waters west of Ireland (see, e.g., Monahan 1978, and Monahan and Pybus 1978). But just about a year after we took up residence in Galway, colleagues in the Department of Physics of UCG hosted the 9th International Conference on Atmospheric Aerosols, Condensation and Ice Nuclei (Roddy and O'Conner 1981), and while attending this meeting I encountered several representatives of the U.S. Office of Naval Research. They asked me if I was the Monahan who had published on whitecapping, and when I acknowledged that I was, they encouraged me to submit a proposal to ONR outlining further research on this topic. I took them up on their suggestion, and my proposal to study "whitecap influence on [the] marine atmosphere" was funded with a start date of 1 July 1978.

[50]A Gaelic expression for whitecaps, whose literal translation is "white horses" (an alternative, more poetic term is "Capaill Mhananáinn" which is an allusion to Manannán mac Lir, a sea deity that features in Irish mythology). Many cultures and languages have their own representations, animate and inanimate, for oceanic whitecaps. Many of these are featured in a quilted wall hanging, a reproduction of which appears as the frontispiece in a book on oceanic whitecaps (Monahan and MacNiocaill 1986).

I, and the several graduate students who had applied to work with me, were able to immediately "kick-start" our new investigations on whitecaps without any delay, thanks in part to the fact that the Oceanography Department at UCG was a solely post-graduate department, i.e. was only engaged with students working on their M. Sc. and Ph.D. degrees, and in that department in those days these students were strictly research students, with no formal classes to attend. (I do enjoy teaching, and for a number of years I did teach a module, "Introduction to Physical Oceanography", in the Physics Department of UCG.) Specifically, we were able to participate in the Joint Air Sea Interaction field experiment, which was carried out northwest of Ireland and west of Scotland in the general vicinity of tiny isle of Rockall. One of my students, Evelyn M. Murphy (Murphy 1978), took whitecap observations in early August of 1978 aboard RRS Challenger[51] during JASIN Cruise 1978-11B, and then in September I took whitecap photographs during Challenger JASIN Cruise 1978-11D. The results of the initial analyses of the whitecap photographs taken on Leg 11D of that Challenger Cruise first appeared in Table 2, Section 4A of the first "UCG Whitecap Report", issued in July 1979 (Monahan 1979), and the results of the analyses of the photographs taken during both Legs 11B and 11D can be found in Table 1.2, UCG Whitecap Report No.3 (Monahan et al. 1981a),[52] and in the proceedings of a 1981 European Space Agency symposium volume (Monahan et al. 1981c). We had constructed that autumn the UCG "whitecap simulation tank" in space provided by the UCG Physics Department. This tank, and it successors, were expressly intended for use in experiments aimed at determining the number of sea spray droplets, in each size band, produced as a consequence of the complete decay of a whitecap of known initial area,[53] and thus by the bursting of all the bubbles that were produced when this whitecap was formed by a breaking wave. And, having kept an eye on the relevant literature, we were anxious to contribute again to the journal literature on this topic.

Toba and Chaen published a paper in 1973 which included a well-documented set of whitecap observations based on a number of photographs that were taken from aboard the R/V Hakuhō Maru during a July 1970 cruise in the East China Sea and at locations near the coast of Japan. During each whitecap observation interval color photographs were taken from a "height of 14m, in the four directions relative to the direction of the wind waves". The analysis of these photographs involved projecting each enlarged color image on a sheet of paper so that the width of the image was

[51]This Challenger was a 180 foot-long research vessel operated by the Natural Environmental Research Council of the UK, and was named after the HMS Challenger that made the 1873–1876, 126,000 km, research cruise under the leadership of C. Wyville Thomson.

[52]Table 1.2 in this annual report lists the whitecap fraction for each of 57 whitecap observation intervals, and is based on 1161 analyses of some 599 different JASIN images of the sea surface. This UCG Whitecap Report No.3, and most, but not all, of the reports in this UCG report series, are readily accessible via the website, arran.library.nuigalway.ie, which is "NUI, Galway's open access repository of research publications maintained by the James Hardiman library".

[53]See Monahan (1986a) for a complementary treatment where sea spray production is related to the decay of a bubble plume of unit initial volume.

180 mm, and then outlining each "white area". The image on the paper was divided up into six zones, from the horizon downward, with the two zones nearest the horizon being 5 mm in vertical extent, and each subsequent zone further from the horizon being of greater vertical extent (i.e., 10 mm, 20 mm, 40 mm, and 80 mm). The illustration that accompanied this paper shows a seventh, unanalyzed, zone which appears to be about 80 mm in vertical extent, thus, as with the Monahan analysis protocol (Monahan 1969), the portion of the sea surface that occupies the lowest third of the image, as measured from the horizon to the bottom of the photograph, was excluded from the analysis. The precise manner in which the area of each traced whitecap was measured on the paper is not described, but it does state that "the unit of the reading of the breaking area is 1 mm^2 in the above described projection". Toba and Chaen, whose primary aim was to investigate the dependence of whitecap coverage on the dimensionless variable, $u*L\nu$ (where $u*$ is the friction velocity, L is the significant wavelength, and ν is the kinematic viscosity of air), do not provide an explicit expression for whitecap coverage, W, as a function of wind speed, U. They do state that "in Fig. 2 are plotted the [W]-values against U. Blanchard (1963) and Monahan (1971) expressed the value as a function of U, and our result is of the same order with Monahan's". Toba and Chaen, concerned that the reduced resolution of more distant whitecaps, the preferential location of whitecaps near wave crests, and other factors might influence the apparent whitecap fraction as one moves from the horizon to the near field, determined, for all the Hakuhō Maru photographs, the apparent whitecap coverage in each of their six zones, and documented the average W value for each zone in their Table 1. They concluded that "it does not seem that the average [W] value has any systematic change with distance". We do note that the average W for the upper sixth of their images of the sea surface, i.e. zones 1–4 combined, was 0.774%, while the average W for the middle half of these images, i.e., zones 5 and 6 combined, was 0.660%. They also divided all of their whitecap photographs up into three categories, defined by the orientation of the camera with respect to the wind-wave direction, and presented these results in their Table 2. They again concluded that "[i]n this case also, a significant systematic difference is not seen". We would mention that only in the case of the "Front" photographs, which we interpret to mean those taken into the wind, was the W value obtained for zones 1 and 2 combined, larger (by some 33%) than the W value found for zones 3–5 combined. (In neither the case of the "Side" nor the "Rear" photographs was the W value for zones 1 and 2 as large as the value for zones 3–5.) Motivated by some of these same concerns, we had, in our 1969 Fresh Water whitecap paper, compared, for 55 photographs from one Whitecap Observation Interval, the apparent whitecap coverage for our entire region of analysis, i.e. the inverted triangle, to the apparent coverage we obtained when we limited our analysis to the truncated inverted triangle that stretched from the horizon down one-third of the way to the bottom of the image, i.e., to the "far field". For the far field alone we found W a value of 0.698%, while for the entire triangle, i.e. the far field and mid-field combined, we found a W value of 0.565%. Since the area of the mid-field is only one-third of the area of the far field, and since its inclusion in the analysis area reduced the apparent whitecap coverage by some 19%, the conclusion that "some positive bias was resulting from the use of oblique photography" seemed

at the time warranted. Recognizing that the aggregate sea surface area imaged in the mid-field analysis area of all 55 photographs was quite small, and that any random whitecap that might appear, or not appear, in this mid-field area, would appear on the image typically an order of magnitude larger than a similar whitecap that appeared in the far field of this image, it is reasonable to conclude in retrospect that certainly our 55 photographs represented an under-sampling of the mid-field region, and that as a consequence "the jury is still out" on the extent, if any, of a positive far field whitecap coverage bias associated with oblique photographs. It should be noted that Aaron Paget, in a recent, as yet unpublished, study, applied a sophisticated automatic extraction technique developed by Callaghan and White (2009) to a digitized set of oblique whitecap photographs collected during the MIZEX83 field experiment (Monahan et al. 1984). The results show essentially no far field bias, but significant near field bias, the latter associated with the portion of each image which was systematically excluded from analysis in the Monahan analysis protocol.

A 1971 paper by Nordberg and colleagues (1971) includes a description of the results regarding foam cover obtained from the analysis of a limited number of nadir-look photographs taken in March 1969 over the eastern North Atlantic and North Sea from a NASA aircraft. For four of their six cases, we might designate them observation intervals, they list in their Table 1, among other measurements, the nominal deck height wind speed, air and sea surface temperatures, and the fraction of the sea surface covered by foam and by "streaks" as determined from the analysis of "several consecutive photographs". For a fifth case they list everything except foam (and streak) coverage, but elsewhere state that "no whitecaps were observed for [this] case". We do not know of any group which has determined a W(U) expression, or a Streak(U) expression, from this small data set.

In early 1974 Ross and Cardone, in their paper previously cited, presented their results on whitecap and "streak" coverage based on the analysis of some 427 nadir-look photographs taken during 13 whitecap observation intervals as part of an aircraft observational program that involved flights over the North Sea, the North Atlantic Ocean, the Gulf of Mexico, and the Caribbean Sea. Their Table 2 lists, among other quantities, the 19.5 m-elevation wind speed, air-sea temperature difference, fetch, percentage whitecap coverage, percentage streak coverage, total foam coverage, and the number of photographs analyzed, for each of these 13 observation intervals. Figure 2 in this paper shows, for eight observation intervals for which the winds ranged from 10 to almost 25 m/s, the whitecap, and total foam (whitecap plus streak), coverages plotted against the 19.5 m-elevation wind speed. Also plotted on this figure is the sea water W(U) curve, essentially the one we derived in our 1971 paper from Cardone's 1969 semi-empirical expression (based on our 1969 fresh water whitecap results), modified to take into account the greater persistence of salt water whitecaps compared to fresh water whitecaps as determined in our 1969 laboratory studies mentioned earlier. (This is the C-M-Z 19.5 m curve on Fig. 2 of our 1971 paper, not the C-M-Z 10m curve on our figure.) For the five observations between 10 and 17 m/s shown on this figure, the whitecap coverage values agree well with this modified semi-empirical curve, and these are the observations that Ross and Cardone identify with "nearly fully developed seas". The three other whitecap values plotted on this figure, which presumably do not correspond to

fully developed seas, fall well below the semi-empirical curve. For the intervals identified with wind speeds from 13 to 20 m/s, the total foam percentages, i.e. the sum of the respective whitecap and streak coverages, fall well above this curve. These authors proceed to develop another expression, Eq. 14.4, where F is the total foam cover, W is the fractional whitecap coverage, and R_{SW} is the

$$F = (1 + R_{SW})W \tag{14.4}$$

empirically derived ratio of streak-to-whitecap area (given by $R_{SW} = -1.99 + 0.25\,U$, where U is the 20 m-elevation wind speed). The streaks found in Ross and Cardone's high wind speed photographs are what in our nomenclature are called "spume lines". It is our belief that these spume lines are lines of bubbles that have become stabilized by accreting to their surfaces organics and other surfactant materials. The presence and areal extent of spume lines is thus dependent on the organic richness of the local surface waters as well on the wind speed. These bubbles persist long enough to be winnowed into long, down-wind, lines. These lines can form at high winds in the absence of any Langmuir cells or other organized surface circulations, but certainly the presence of such cells will enhance the growth and persistence of such windrows. Ross and Cardone's W does correspond closely to our W, and our W, as will be described in due course in this paper, is, as is Ross and Cardone's W, comprised of both "actively forming whitecaps and large new foam patches".

Tang (1974) cites an unpublished 1972 report of Stogryn to NASA, for Eq. 14.5,

$$W = 7.75 \times 10^{-6} U^{3.231} \tag{14.5}$$

which we have rendered here in our notation, i.e. W is the fractional whitecap coverage, and U is the 10-m elevation wind speed. It is to be noted that Tang states that Stogryn obtained this expression "by a least-squares fit to several groups of experimental data (Murphy 1968; Williams Jr. 1970; Rooth and Williams 1970; Monahan 1969, 1971)". We should mention here, as we have commented elsewhere (Monahan and O'Muircheartaigh 1980a), that from a remark in Williams' 1970 note, and a comment in Blanchard's 1971 paper, it seems that the 1968 unpublished results of Murphy, and Williams' own conclusions, were based on a consideration of the same U.S. Navy Weather Squadron photographs as were analyzed by Blanchard in his 1963 paper. We have previously in this paper outlined our thoughts as to the utility of these Weather Squadron photographs.

Another landmark paper regarding the wind speed parameterization of whitecap coverage was the one published in 1979 by Jin Wu. He began with the reasonable assumption that the fraction of the sea surface covered by whitecaps, W, should be proportional to the rate at which energy was being transferred from the wind to the sea surface, $\dot{E}$. We would wish to "fine tune" this assumption with the proviso that this simple proportionality only pertains when the 10 m-elevation wind speed is well above the threshold velocity for macroscopic wave breaking, i.e. for the onset of whitecapping. Now energy is the ability to do work, and that work, $\mathcal{W}$, is given by Eq. 14.6, where F is the force applied to an object, like a parcel of sea water, and

$$\mathcal{W} = \mathrm{F\,D} \tag{14.6}$$

D is the distance that parcel of sea water moves in the direction of the applied force, and as a specific response to the application of that force. It follows that $\dot{E}$, the rate of energy transfer to the sea surface, or power, is given by Eq. 14.7, where V_{SD} is the wind-

$$W \sim \dot{E} = F\,V_{SD} \tag{14.7}$$

induced surface drift current. Now if we focus on a parcel of sea water that occupies a unit area of sea surface, then we can substitute T, the surface stress for F. And Wu, following the approach in Wu (1975), took the wind-induced surface drift current, V_{SD}, to be proportional to $u*$, the (wind) friction velocity. In this fashion he arrived at Eq. 14.8. Now the wind stress on the sea surface, T, can be expressed in terms of the

$$W \sim Tu* \tag{14.8}$$

10 m-elevation wind speed, U_{10}, and the drag coefficient, C_{10}, as shown in Eq. 14.9, where

$$T = \rho\, C_{10} U_{10}{}^2 \tag{14.9}$$

ρ is the density of air (see, e.g., Roll 1965). Likewise, $u*$ can be expressed in terms of U_{10}, in the manner shown in Eq. 14.10 (see, e.g., Eq. 4.51 in Roll 1965).

$$u* = C_{10}{}^{0.5} U_{10} \tag{14.10}$$

Substituting the essence of Eqs. 14.9 and 14.10 in Eq. 14.8 yields Eq. 14.11.

$$W \sim C_{10}{}^{1.5} U_{10}{}^3 \tag{14.11}$$

Finally Wu went one step further, and citing his 1969 paper, where he concluded that $C_{10} \sim U_{10}{}^{0.5}$, he arrived at Eq. 14.12, which he then undertook to test against the

$$W \sim U_{10}{}^{3.75} \tag{14.12}$$

"BOMEX+" (Monahan 1971) and "East China Sea" (Toba and Chaen 1973) whitecap data sets. In carrying out this test of his U-to-the-3.75 power law against the "BOMEX+" data set, he first omitted "some data points with nearly zero whitecap coverage at rather high wind velocities", because "Monahan's photographic technique is believed unlikely to provide a resolution of the coverage of less than 0.01%." He then stated "Moreover, a fairly well displayed trend in the data shown with the frame of [Wu's] Fig. 1a further substantiates our omission of

those data outside the frame (W < 100 PPM)." Wu then concludes that "A straight line with a slope of 3.75:1, as suggested by [his Eq.] (2), is seen in [the log-log plot] Fig. 1a to fit reasonably well to each data set. . .". Having fitted both the "BOXEX +" and "East China Sea" data sets, sets that he acknowledged "show remarkable agreement", to $W = \alpha U_{10}^{3.75}$ power-laws, he concluded from the "BOMEX +" data set that the coefficient, α, showed a monatonic decrease as one went from only data collected under stable MABL conditions, to only data collected under neutral conditions, to only data collected when the MABL was unstable. In the case of the "East China Sea" data set, he found that α decreased as one went from data collected when the MABL was stable to data collected with the lower atmosphere manifested near neutral stability. Wu acknowledged that it was reported (Monahan 1969) for the fresh water data set that there was greater whitecap coverage when the MABL was unstable.

Aware that to date only in an unpublished contract report by Stogryn (1972) was there a statistically fitted (by the method of least squares) power-law description of the dependence of W upon U, and acknowledging the concerns we harbored about the majority of the data sets used by Stogryn,[54] we felt that it was "high time" that objective statistical analyses be applied to several well documented whitecap data sets. I was fortunate to find a statistician colleague right within University College, Galway, and am forever grateful that I was able to interest him in the statistical analysis of the various whitecap data sets. The first fruits of what was to turn out to be a decades long collaboration were the Monahan and O'Muircheartaigh papers that appeared in 1980 (Monahan and O'Muircheartaigh 1980a, b). In the *Journal of Physical Oceanography* paper of that year, after reviewing the various W (U) power-law expressions in the literature, we presented power-law expressions where both λ, the exponent of U, and α, the coefficient before the exponential term, were obtained using both the ordinary least squares (OLS) and robust biweight fitting (RBF) statistical approaches to the "BOMEX+" and "East China Sea" whitecap data sets, treated individually and as one combined data set. Using the mean square error as a measure of the goodness of fit of the six resulting expressions, it was demonstrated that in each instance our W(U) expressions, better fit the data sets, taken separately or in combination, than did Wu's expressions (where, as you will recall, the power-law exponent, λ, was constrained on theoretical grounds to in all instances have a value of 3.75). Below, as Eqs. 14.13 and 14.14,[55] are our

[54]Note that several of the data sets used by Stogryn in his statistical analysis appear to have arisen from independent analyses of the photographs in the 1952 unpublished Navy Weather Squadron manual, and we have previously expressed our concern as to how these photographs were selected for inclusion in that manual. Having demonstrated in the laboratory (Monahan and Zietlow 1969) why fresh-water, and salt-water, whitecap coverage should be different for the same meteorological conditions, we think it was inappropriate for Stogryn to include the Monahan (1969) fresh water whitecap set in his data base that otherwise consisted only of sea water whitecap data sets.

[55]This RBF W(U) expression was incorporated in the Monahan et al. (1986) sea surface aerosol generation function, which has in turn been incorporated in a number of global climate models.

two power-law expressions for the combined "BOMEX+" and "East China Sea" data set. As can be seen from Fig. 2 in

$$W_{OLS} = 2.95 \times 10^{-6} U^{3.52} \tag{14.13}$$

$$W_{RBF} = 3.84 \times 10^{-6} U^{3.41} \tag{14.14}$$

this paper, the incorporation of the early JASIN data set into the omnibus whitecap data set results in a reduction of λ, the power-law exponent. That Fig. 2 is reproduced here as Fig. 14.12.

We will return later to a discussion of the apparent Latitude-dependence of λ, of which this was the first manifestation, and explain why this might be so. In the JASIN News article of that same year (Monahan and O'Muircheartaigh 1980b), these authors, by applying the OLS statistical analysis to the first 21 JASIN whitecap observation W,U-couplets, obtained Eq. 14.15. It is apparent, that the λ for this

$$W = 3.8 \times 10^{-5} U^{2.81} \tag{14.15}$$

JASIN data, when taken alone, is clearly smaller than the OLS (and RBF) derived λ-values from the "BOMEX+" and "East China Sea" data sets, taken alone or in combination, as can be seen from the λ-values listed in Tables 2 and 3 of the *Journal of Physical Oceanography paper.* This preliminary JASIN result can be taken as the first hint of a latitudinal variation of λ, the power-law exponent. Specifically, when considered in light of the lower latitude BOMEX+ and East China Sea λs, the JASIN quite high latitude λ was the first suggestion that λ typically decreases as the latitude of the region where the observations were taken increases. This topic will be discussed in detail in a later section of this paper.

The Wu 1979, 1982 *Journal of Physical Oceanography* papers, and the Monahan and O'Muircheartaigh 1980a, 1982a articles in this same journal, represented the first formal exchange that laid out two divergent views as regards how one might use observational data on whitecaps. Wu diligently used the various whitecap data sets as they appeared in an attempt to confirm his theoretically derived whitecap dependence on wind speed (as presented in Eq. 14.12), while Monahan, O'Muircheartiagh, and our co-workers were willing to follow the data, and the objective statistical analyses of these data sets, where they led us.

While in the papers already discussed, and in those still to be introduced, we have primarily focused on the dependence of whitecapping on wind speed, U, on ΔT (SST- T_A), on SST (often as a surrogate for latitude, or for the duration of high wind speed events), and on u∗, the friction velocity, it was recognized that there are other independent variables that might influence whitecap coverage. In particular, sea state and the various parameters defining the wave field have often been pointed out as being important, in themselves, in controlling the extend of whitecapping. It was hoped that the 1978 JASIN experiment would provide at least some of the wave data that could be correlated with the results of our routine whitecap observations. The logistics did not eventuate as we had hoped, but we were able to obtain the hourly

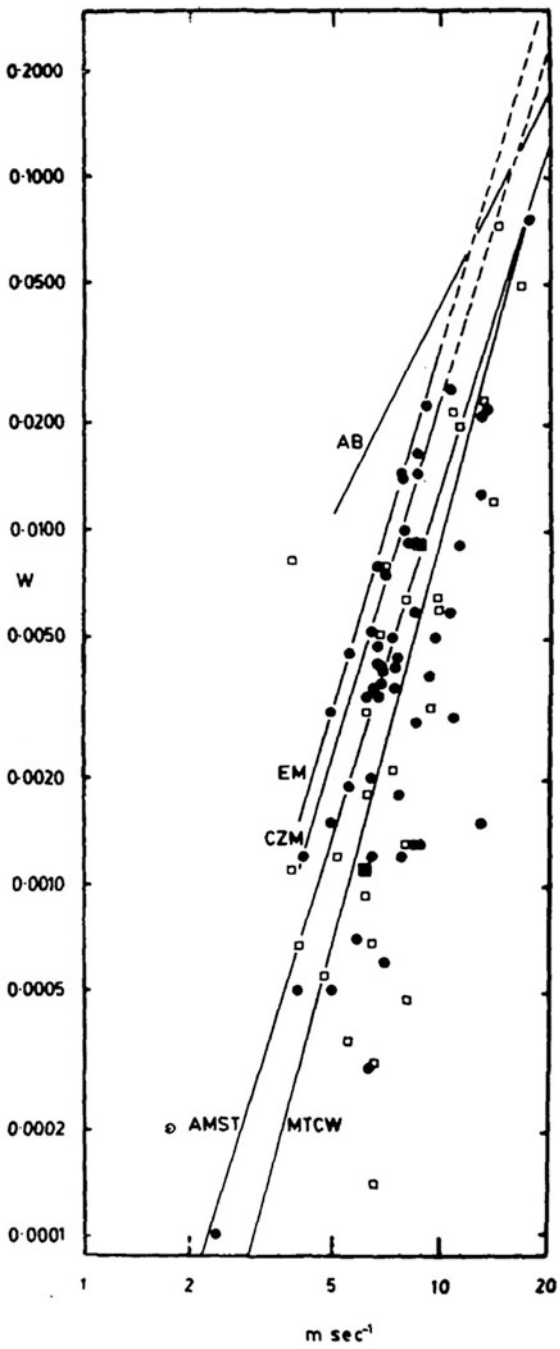

Fig. 14.12 The fraction, W, of the ocean covered by whitecaps versus the 10 m-elevation wind speed, U. Open circles, preliminary whitecap coverage values from the JASIN experiment. The line MTCW is the one Wu fitted to the combined BOMEX+ (Monahan 1971) and East China Sea (Toba and Chaen 1973) data sets. Line OLS is the optimal power-law expression for W (U) based on ordinary least-squares fitting applied to this same combined data set. Line Σ + J is OLS fit power-law describing this same combined data set augmented with initial JASIN data. © American Meteorological Society, used with permission. (From Monahan and O'Muircheartaigh 1980a)

W.M.O. visual wave observations taken from the H.N.L.M.S. Tydeman[56] during the period while we were photographing the sea surface according to our whitecap observation protocol aboard the R.R.S Challenger. Given the nature of the available wave data, and the fact that the wave observations and the whitecap recordings were taken on two different ships often quite separated within the Rockall region, we soon recognized that our findings would be preliminary at best (Monahan et al. 1981b). We chose in the first instance to use as our independent variables U, the wind, and N, the significant wave height, both as recorded on the Tydeman to correlate with W, the whitecap coverage deduced from the photographs taken aboard the Challenger, so that in comparing the resulting W(U) and W(N) correlations we would not have to address the question of proximity bias as we would if we had used the wind measurements taken aboard the Challenger. We fitted the data to the generic power law expression shown in Eq. 14.16,

$$W = \gamma X^{\delta} \tag{14.16}$$

where X represents alternately the wind speed, U, and the significant wave height, N, using ordinary least squares fitting. We also undertook to optimize the correlation of U, or of N, with W by selecting winds and wave heights taken at various time steps prior to the whitecap recordings. (For this purpose we generated continuous U and N files from the typical hourly observations by the expedient of linear interpolation.) The highest correlation coefficient of U with W, which occurred in the case of the wind measured 1.08 h prior to the whitecap observation, was 0.731. By contrast the highest correlation coefficient of N with W, which occurred for the waves recorded 0.5 h before the whitecap observations, was 0.593. (An essentially identical correlation coefficient, 0.592, was found for N with W, in the case of simultaneous observations.) Thus, the preliminary findings were that whitecap coverage is clearly positively correlated with both wind speed and wave height, and suggest that whitecap coverage is more closely correlated with wind speed than it is with wave height.

14.9 Whitecap Coverage and Satellite Remote Sensing

We had long been aware that the apparent elevated microwave brightness temperature detected via various satellite-borne passive microwave sensors was being used to infer surface wind speeds, and that it was the presence of whitecaps that was causing the enhanced microwave emissivity of the sea surface at the higher wind speeds. We now decided to derive, in our contribution to the Oceanography from Space volume (Monahan and O'Muircheartaigh 1981), initially from the BOMEX+

[56]The HNLMS Tydeman was a 296 foot-long research vessel of the Royal Netherlands Navy launched in 1975.

and East China Sea whitecap data sets, a power-law expression for U in terms of W, as shown in Eq. 14.17, starting with the

$$U = \beta\, W^{\mu} \tag{14.17}$$

observational data and taking W to be the independent variable and U the dependent variable, and using both the ordinary least squares and robust biweight fitting approaches. Wu, in his previously cited 1979 *Journal of Physical Oceanography* paper, also attempted to evaluate Eq. 14.17, but he did so by simply "solving" his W (U) equation (essentially Eq. 14.12, or specifically his Eq. 4), for U. This gave him, for the same BOMEX+ and East China Sea whitecap data sets, Eq. 14.18. (Note that the exponent, μ,

$$U = 0.87\, W^{0.267} \tag{14.18}$$

in Eq. 14.18[57] is just the reciprocal of 3.75, the λ that Wu adhered to on theoretical grounds.) In our Oceanography from Space paper, we stress "that the optimal U (W) expression is not the inverse of the optimal W(U) expression". And we go on to demonstrate, for the same combined whitecap data set, that the U(W) expression we obtain using the ordinary least squares approach (Eq. 14.19), has a smaller M.S.E. (3.90 $m^2\ s^{-2}$)

$$U = 22.64\, W^{0.19} \tag{14.19}$$

than we get by taking the inverse of the W(U) expression we had obtained for this same combined data set in our 1980 *Journal of Physical Oceanography* paper (M.S.E. of 4.91 $m^2\ s^{-2}$). Likewise the M.S.E. for the robust biweight fit U (W) expression for this combined data set (Eq. 14.20) was smaller than the M.S.E. for the inverse of the

$$U = 24.63\, W^{0.23} \tag{14.20}$$

W(U) expression we had obtained in 1980 for this same combined data set.

In order to improve our ability to infer near-surface, over-water, wind speeds, U, from whitecap coverage retrieved from satellite-borne passive microwave sensors, W, and assuming that sea-surface water temperature, T_W, and "deck height" air temperature, T_A, could be assessed from satellite- or other measurements, it was decided to develop (Monahan et al. 1981c), via multiple regression applied to the aforementioned BOMEX+, East China Sea, and JASIN data sets, an expression of the form shown in Eq. 14.21.

[57]This expression, where, as per Wu's notation, W is expressed in parts per million, appears to contain an error. The simple inverse of his Eq. 4 would be $U = 1.15\, W^{0.267}$.

$$\ln U = C_0 + C_1 \ln W + C_2 \ln T_A + C_3 \ln T_W \tag{14.21}$$

The result of this multiple regression analysis is presented in Eq. 14.22. It is apparent from the relative magnitudes and the algebraic signs of the exponents of T_A and T_W that

$$U = 23.81\, W^{0.19} T_A{}^{0.84} T_W{}^{-0.88} \tag{14.22}$$

what is seen here is primarily the effect of the stability of the marine atmosphere boundary layer on the U(W) relationship. For the same W and the same T_W but an increase in T_A, i.e. for an increase in the atmospheric stability, a larger U is required to sustain this same W. Likewise, to sustain the same W, in the case where T_A has remained constant but that T_W has increased, i.e. where the stability of the MABL has decreased, a smaller U is required, or associated with this same W. Noting that the magnitude of the exponents of T_A and T_W are not the same, provides a hint that a secondary temperature-associated influence may be affecting the U(W) relationship. We will discuss in a later section the possible influence of sea-surface water temperature, T_W, or of viscosity, which varies significantly over the observed range of oceanic surface temperatures, may have on W. In another paper published that same year (1981) these same authors (Monahan et al. 1981a), in addition to discussing in detail Eq. 14.22 and other U(W) expressions, evaluated Eq. 14.17, U upon W, for the BOMEX+, East China Sea, and JASON data sets individually, for the BOMEX+ and East China Sea data sets combined, and for all three of the data sets combined, and compared these results with those obtained by determining the W (U) expressions, W upon U, and then inverting these expressions. The resulting expressions, and the mean square error "goodness of fit" for each of these expressions, are listed in Table 14.1. As these authors stated, "It is apparent from the listed mean squared errors (MSE) of Table [1] that the inverse of an optimal W (U) expression is not as good a description of U(W) as the U(W) function directly calculated". Likewise "Wu's U(W) expression, which he obtained by taking the inverse of his W(U) fit is clearly not a preferred expression for the estimation of wind speed from whitecap coverage".

The opportunity to collect additional high latitude W,U-observations arose with the announcement of the Storm Transfer Response Experiment. This experiment was duly carried out in the Gulf of Alaska in late 1980, and we were fortunate that David M. Doyle, a Graduate Student in the Department of Oceanography of University College, Galway, was able to sail on two legs of the NOAA R/V Oceanographer STREX cruise in November and December of that year. An initial description of Doyle's participation in this cruise is to be found in UCG Whitecap Report #3.[58]

[58]Chapter 4, "U.C.G. Participation in the 1980 STREX Experiment in the Gulf of Alaska", by D.M. Doyle, in Monahan et al. (1981b).

Table 14.1 Terms β and μ as in Eq. 14.17

Data set	Method	Coeff. β	Exponent μ	M.S.E. ($m^2\ s^{-2}$)
BOMEX+ (B)	Ols	25.59	0.22	3.48
	Rbf	18.62	0.18	4.31
	Olsi	35.97	0.27	4.32
	Rbfi	42.80	0.32	4.40
East China Sea	Ols	26.83	0.22	3.61
(C)	Rbf	24.06	0.20	3.66
	Olsi	40.31	0.31	4.74
	Rbfi	44.80	0.34	5.55
JASIN (J)	Ols	22.71	0.21	2.52
	Rbf	22.76	0.21	2.52
	Olsi	43.79	0.37	5.70
	Rbfi	36.47	0.30	3.78
B + C	Ols	26.03	0.22	3.56
	Rbf	24.00	0.22	3.96
	Olsi	37.83	0.29	4.25
	Rbfi	40.38	0.30	4.47
	Wu,i	34.80	0.267	4.71
B + C + J	Ols	25.27	0.22	3.27
	Rbf	23.98	0.22	3.42
	Olsi	40.96	0.33	4a.80
	Rbfi	38.21	0.30	4.21

Source: Table 4 from Monahan et al. (1981a)
Abbreviations: *ols* ordinary least squares, *rbf* robust biweight fit, *olsi* inverse of ordinary least squares fit W(U), *rbfi* inverse of robust biweight fit W(U), *Wu,i* inverse of Wu's W(U) equation (Wu 1979), *M.S.E.* Mean Square Error

The preliminary whitecap and related observational results from this cruise can be found in UCG Whitecap Report #4 of 1982 (Chapt. 2 in Monahan et al. 1982b). The final version of the STREX whitecap, wind, T_A, and SST data set can be found in either Doyle (1984a) or Doyle (1984b).[59]

14.10 Further Thoughts on the Analysis of Whitecap Photographs

While all of the whitecap images recorded on photographic film by the UCG, Galway, group where analyzed using the "manual" technique described in detail earlier in this paper, this group was not unaware of the potential benefits that might accrue if an automated digital technique for the analysis of such photographs could

[59]Doyle (1984b) is accessible via the website, arran.library.nuigalway.ie

be implemented. We were therefore delighted when we were invited by Roland Doerffer[60] to visit GKSS[61] Forschungszentrum, Geesthacht, for an interval in January and February 1981, to work collaboratively with his group in a feasibility study of such techniques as applied to photographic images of the sea surface. The first approach used to gray scale "slicing" of the image to separate the whitecaps in a photograph (the lighter gray portions of the image) from the background sea surface (the darker gray portions), and to record the area of the whitecaps in each such image to the total area selected for analysis in each image. This approach proved unsatisfactory as the contrast levels, and general brightness, varied markedly from image to image as one progressed through the images taken during one of our Whitecap Observation Intervals. Ultimately a semi-automated approach was tested and proved satisfactory. This approach involved a human operator who for each photographic frame verified the gray level that differentiated the whitecaps from the background sea water. A fuller description of this approach, and of the other analytic techniques tested, can be found in Michael C. Spillane's report that appears in UCG Whitecap Report No.3 (See Spillane 1981).

Another approach which we thought, and still think, has great potential involved the digitizing, with a pixel resolution of 50 μm, of a set of color images of the sea surface, for their transmissivity at red, green, and blue wavelengths. The eight photographs used in this analysis were large format (70 mm) transparent color images taken from aircraft during the FLEX Experiment. These particular FLEX images were selected as they each showed a well-defined whitecap, a spume line, sun glitter on a whitecap-free sea surface, diffuse sky reflection (glitter) on a whitecap-free sea surface, or a combination of two or three of these features. The initial results appeared to suggest sufficient spectral differences between these several features such that, if one had available images that were not over exposed for this purpose, one could not only distinguish between glitter and "white water"(i.-e. whitecaps and spume lines), but might possibly be able to distinguish spectrally between new whitecaps and spume lines.

[60]R. Doerffer and E. Monahan first worked together during the EURASEP Ocean Color Scanner 1977 pre-launch experiment conducted in the North Sea. They and their assistants were aboard the Belgian naval mine-sweeper ZM-FN Mechelen which sailed out of Zeebrugge on 4 days over a several week period.

[61]The Gesellschaft fur Kernenergieverwertung in Schiffbau and Schiffahrt, Geesthacht, as its name suggests, was established as the research support base for a nuclear-powered merchant vessel (the Otto Hahn), but like many such laboratories in Europe and the U.S., they branched out into such fields of remote sensing and environmental studies.

14.11 In the Shade of the Butterfly Grove

It is only appropriate that we make mention here of the 1981–1982 sabbatical year spent at the Naval Postgraduate School in Monterey,[62] California, where during the fall 1981 term I was the occupant of the George J. Haltner Research Chair in Meteorology. This sabbatical visit was a follow up to three working visits paid to our "whitecap laboratory" in University College, Galway by Professor Kenneth L. Davidson[63] of the NPS in the spring of 1979 (see Monahan 1979), and again in the summers of 1980 and 1981 (see Monahan et al. 1980, 1981a, b, c, d, 1982b) when on both occasions he was accompanied by Donald E. Spiel of BDM. We mention these working visits only in passing, as they focused primarily on aerosol measurements in the field and in our whitecap simulation tank #2, not on observations of oceanic whitecaps. But whitecap measurements were made of the whitecaps formed by the wave-wave interactions produced in this tank. We wish to note with thanks the contributions of Dr. Brigid D. O'Regan to these tank experiments.

During this sabbatical visit the first journal article detailing what has come to be known as the "discrete whitecap method" (see, e.g., Callaghan 2013) for parameterizing the sea surface spray generation function was revised and prepared for submission (Monahan et al. 1982a). This visit to the NPS, which made possible many discussions with colleagues not only at NPS but also at the nearby Naval Environmental Prediction Facility, put me in a position where I was able to write up, toward the end of my sabbatical year, when I spent several summer months as a Visiting Professor of Oceanography in the Department of Geological Sciences of the University of Maine, Orono, a detailed description of a further revised "sea surface aerosol generation model No. 4" (Monahan 1982a). This revised model subsequently was presented at the 1983 Galway "Whitecap Workshop", and published in "Oceanic Whitecaps, and Their Role in Air Sea Exchange Processes"(Monahan et al. 1986a). This version of our sea surface spray flux model was cited in the Intergovernmental Panel on Climate Change's Climate Change 2001: The Scientific Basis (Houghton et al. 2001), and was described by Grythe et al. (2014) as still "the most widely used source function".

Another paper that arose from my stay at the NPS, and written with NPS colleagues (Monahan et al. 1983c), dealt with the inter-relationship between 10 m-elevation wind speed, oceanic whitecap coverage, and marine aerosol concentrations, as deduced from the JASIN data sets, and those collected in the East China Sea (Toba and Chaen 1973; Chaen 1973). Using the aerosol and whitecap data from both of these data sets, and applying the robust bi-weight fitting technique, it was

[62] While at the NPS in Monterey, we rented a house in nearby Pacific Grove, which is known for the butterfly grove up on the hill, where Monarch butterflies appear in great numbers during their annual migration.

[63] I had known Ken Davidson since 1969, when I arrived at the University of Michigan as an Assistant Professor in the Department of Meteorology and Oceanography and Ken was writing his Ph.D. dissertation under the guidance of Professor Don Portman.

determined that the concentration of the large aerosol fraction, i.e., the number of those particles whose radius was greater than 7.9 μm (at a relative humidity of 80%) per cubic meter of air, $N_{8+,}$ varied with fractional whitecap coverage, W, as shown in Eq. 14.23. A companion expression, describing how the concentration of this large aerosol

$$N_{8+} = 3.59 \times 10^5 W^{0.707} \tag{14.23}$$

fraction, N_{8+}, varied with the 19 m-elevation wind speed, U, measured in m/s, was likewise determined using the RBF technique, and is included here as Eq. 14.24. Given

$$N_{8+} = 6.50 \times U^{3.23} \tag{14.24}$$

Equation 14.23, it is not at all surprising that the concentration of the large aerosol fraction just above the sea surface was found to vary with wind speed in a similar manner ($W \sim U^{3.31}$) when again the RBF technique was applied to the combined JASIN and East China Sea data sets. When one recalls that the larger aerosol fraction has a short effective residence time in the marine atmospheric boundary layer, it is apparent that the above equations are consistent with the "discrete whitecap method" assumption that the flux of large sea spray droplets up from the sea surface is a function of the rate of decay of whitecap coverage, which in turn is proportional to the instantaneous whitecap coverage. Additional analyses presented in this paper show that the logarithm of the fraction of the marine air volume filled with aerosol particles per unit increment in particle radius, dV/dr, shows a positive, near linear dependence on the logarithm of the fractional whitecap coverage, W, and that this dependence increases with aerosol particle size until for spray particles/droplets with radii 15–17 μm dV/dr is approximately proportion to W (see Eqs. 14.25a and 14.25b). This is likewise consistent with the assumptions of the

$$\text{(a) RBW}: \quad dV/dr = 6.85 \times 10^{-10} W^{1.043} \tag{14.25a}$$

$$\text{(b) OLS}: \quad dV/dr = 2.76 \times 10^{-10} W^{0.860} \tag{14.25b}$$

"discrete whitecap" model of marine aerosol generation. In this same *Quarterly Journal of the Royal Meteorological Society* paper we considered the marine aerosol size spectrum, and how it changed with wind speed. Here we considered not only the various marine aerosol spectra obtained during the JASIN experiment, but also aerosol spectra published by Woodcock (1953), by Metnieks (1958),[64] and by Patterson et al. (1980).[65] As can be seen in Fig. 5 of that paper, reproduced here as Fig. 14.13, most of these aerosol spectra, which have all been adjusted to 80%

[64]Metnieks aerosol spectra measured on Inishmore, at the mouth of Galway Way.

[65]Whose aerosol spectra were obtained during the GAMETAG experiment.

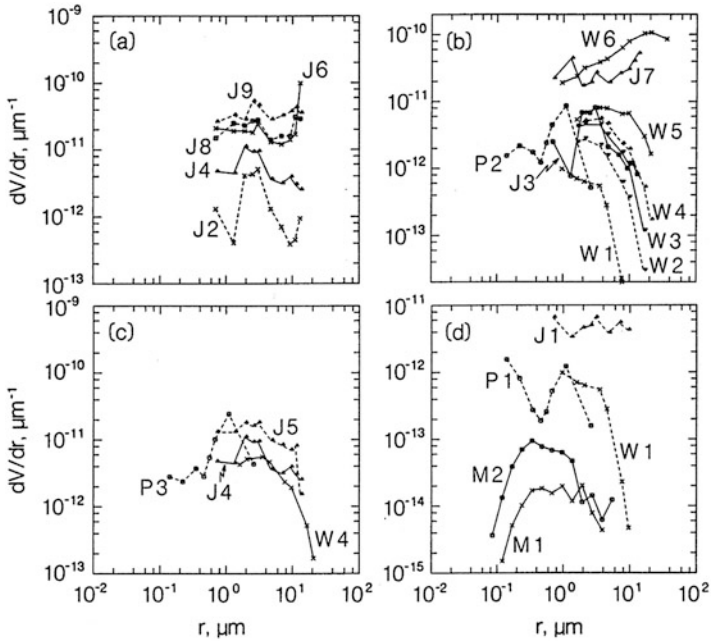

Fig. 14.13 Marine aerosol spectra normalized to a relative humidity of 80%. On logarithmic axes the fraction of the low-elevation marine air volume occupied by sea-water droplets which fall within a unit increment in droplet radius is plotted here versus droplet radius. The spectral curves labeled J are results for various wind speeds measured during the JASIN experiment. The spectra labeled W were derived from Woodcock (1953), and the spectra labeled P are based on the GAMETAG results found in Patterson et al. 1980). The spectra labeled M were determined from the Inishmore measurements of Metnieks (1958). © Royal Meteorological Society. Used with permission. (From Monahan et al. 1983c)

relative humidity, are quite similar in shape, with their amplitude tending to increase with wind speed. This is consistent with the "bubble mediated" production term, dF_0/dr, of the "discrete whitecap" aerosol generation model discussed in the previous paragraph. But the spectra associated with higher wind speeds, specifically those measured when the wind speed ranged from 13 m/s to 35 m/s, differ from the others in that their dV/dr values turn upward at the larger radii, typically for radii greater than 10 μm. This in turn is consistent with the "spume drop" direct production term, dF_1/dr, of the same aerosol generation model, which, as originally formulated, was only expected to became significant, when compared to the dF_0/dr production term at high winds for spray droplets of radii 10 μm and larger. (The "bubble mediated" spray production term covers the generation of jet-droplets and film-droplets, while spume droplets are produced directly from the wave crests.[66])

[66]Sketches of jet- and film-droplet, and spume drop, production are included as Fig. 1 in Monahan et al. (1983, 1986a) and as inserts in Fig. 1 of Andreas et al. (1995).

Least the above several paragraphs appear to be a digression from our topic of whitecap observations, we should emphasize that the basic "bubble mediated", dF_0/dr, term described above, and first presented in Monahan et al. (1979), can, in its most basic form, be written as Eq. 14.26, where W is the instantaneous fraction of the sea surface covered by

$$dF_0/dr = W T^{-1} dE/dr \tag{14.26}$$

whitecaps, T is the time constant, in seconds, describing the exponential decay of an individual whitecap, and dE/dr is the simulation tank derived "incremental whitecap aerosol productivity" (the number of spray droplets, per unit droplet radius increment, produced as the result of the decay of a unit area of whitecap, expressed in $m^{-2}\ \mu m^{-1}$). Thus the successful application of Eq. 14.26 depends upon having an estimate of whitecap coverage, either from contemporaneously recorded images, or from a parameterization of whitecap coverage. We have been motivated to assimilate more and more whitecap data sets, and with them to hand, develop improved whitecap parameterizations, for just such applications as this.

A further discussion of the JASIN whitecap data set in the 1982 Processes in Marine Remote Sensing volume (Monahan 1982b) includes the "tentative suggestion that $u*$, or the surface stress, might be more appropriate than U for scaling W". (For a number of the JASIN whitecap observation intervals $u*$ values were obtained from stability dependent bulk aerodynamic formulae.)

Our sabbatical stay at the Naval Postgraduate school also led indirectly to other significant advances in our understanding of the dependence of oceanic whitecapping on environmental parameters such as wind speed. These other advances were a consequence of a short working visit paid by my Galway colleague, Dr. Iognaid O'Muircheartaigh to the NPS while I was in residence there. In particular, this visit resulted in a variety of collaborative efforts between Dr. O'Muircheartaigh and Dr. Donald Gaver, a statistician on the faculty of the "PG School", that extended over a number of years. This collaboration resulted in a number of publications that dealt with arriving at optimal W(U) and U(W) expressions from our expanding whitecap data sets.[67]

At the end of the 1982 spring semester we drove east from Monterey to Lewes, Delaware, where we spent 3 weeks in June as the guest of Professor Jin Wu, at the University of Delaware's wind-wave flume laboratory at Cape Henlopen. We then drove north to Orono, Maine, where E.C. Monahan, as mentioned earlier, spent July and August as a Visiting Professor at the University of Maine, and finished up his report on "sea surface aerosol generation model No. 4". By late September the Monahans were back in Galway.

[67] Among the relevant publications that resulted from this collaboration were O'Muircheartaigh and Gaver (1985, 1986), and O'Muircheartaigh et al. (1987).

14.12 1983: An Active Year on Several Whitecap Fronts

In late April of 1983 I traveled to Bremerhaven, Germany, and participated in several planning meetings held at the Alfred-Wegener-Institut für Polarforschung[68] for the summer 1983 and summer 1984 Marginal Ice Zone Experiment (MIZEX), and visited the F/S Polarstern.[69]

On 5 May, aboard the R/V Lough Beltra out on Galway Bay, we made video recordings of whitecaps with the intention of subsequently analyzing these video tapes to determine the e-folding time constant, T, characterizing the decay of whitecaps in the field. We wanted to compare these results with those that we had obtained from observations in the UCG whitecap simulation tank. This was our first field deployment of our video whitecap data acquisition system, which was comprised of a SONY SMF Trinicon colour video camera, model DXC-1800P and a SONY U-matic portable color video recorder, model VO-4800P, which accommodated 0.5 inch U-matic tape cassettes. This short cruise enabled us to test this portable video data acquisition system, which we intended to take to sea on the first Arctic cruise of the F/S Polarstern in the coming months. This cruise, which began in Bremerhaven in late June, and the MIZEX83 leg of which ended in Longyearbyen, Svalbard, in late July, will be described in more detail in the next section of this paper.

In the Whitecap Report issued in late May of this year (Monahan et al. 1983b), Dr. M.C. Spillane and David Doyle presented the definitive versions of both the STREX (Storm Transfer Response Experiment), both Leg 1 and Leg 2, and the JASIN (Joint Air-Sea Interaction experiment), whitecap data sets. In the previous report issued in 1982 (Monahan et al. 1982b) they looked at the effect that SST (sea surface water temperature) and atmospheric stability, as inferred from ΔT ($SST\text{-}T_A$) where T_A is the air temperature at 10 m-elevation, had on the coefficient, α, and the power-law exponent, λ, in Eq. 14.27, using for their data base the

$$W = \alpha\, U^{\lambda} \tag{14.27}$$

whitecap data sets we have designated BOMEX+, East China Sea, JASIN, and the whitecap data derived from the analysis of only Leg 1 of the STREX experiment. In their contribution to the 1983 report they repeated this analysis, but using the STREX data from both Leg 1 and Leg 2, the definitive JASIN data set, and again, the BOMEX+ and East China Sea data sets. We will focus here on the apparent relationship found between λ, the power law exponent, and SST and ΔT. They found in their analyses reported in 1983 that λ appeared to increase significantly as SST

[68]Now the Alfred-Wegener-Institut, Helmoltz-Zentrum für Polar und Meeresforschung.

[69]This research icebreaker was completed in late 1982, and is operated by the Alfred-Wegener-Institut. It is 387 foot-long, displaces 17,300 metric tons, and can break ice 1.5 meters thick. In 1991, accompanied by the Swedish icebreaker Oden, Polarstern reached the North Pole, making them the first two conventionally powered vessels to do so.

increased. They also found, and reported in 1983, that as ΔT went from negative values, indicative of atmospheric stability, to near zero values (specifically within the range $-0.4 < \Delta T < 0.6$ C°) corresponding to near neutral stability, and then on to positive values of ΔT indicative of atmospheric instability, the exponent λ decreased, with a particularly marked decrease as ΔT went from values associated with neutral stability to values denoting an unstably stratified atmosphere. In arriving at these conclusions they thereby confirmed their preliminary conclusions which had been reported in 1982.

In the month following that in which this 1983 Whitecap Report was issued, i.e. in June, we attended two meetings in the United States, the first was the American Meteorological Society's Ninth Conference on Aerospace and Aeronautical Meteorology held in Omaha, Nebraska. At that meeting we presented a paper (Monahan et al. 1983a), on the role of whitecaps and wave disruption in generating marine aerosol particles. The second of these two meetings was the first of what eventually has become a long-running series of symposia[70] on Gas Transfer at Water Surfaces and was held in Ithaca, N.Y., where we presented a paper which we co-authored with M.C. Spillane on "The role of oceanic whitecaps in air-sea gas exchange". This paper, which duly appeared in the resulting proceedings volume in 1984 (Monahan and Spillane 1984), laid out a specific model for air-sea gas transfer that posited a major role for whitecaps in this process, and which had therefor as its corollary that at all but the lowest wind speeds the gas transfer coefficient, or "piston velocity", should have a near-cubic dependence on wind speed. And in late August we spent a week in Hamburg, Germany, attending the XVIII General Assembly of the International Union of Geodesy and Geophysics. At this meeting we presented a paper, which we co-authored with M.C. Spillane, on the role of whitecaps in mass exchange across the sea surface (Monahan and Spillane 1983).

In early September of 1983 I had the privilege of convening a whitecap workshop at University College, Galway. It drew some 56 participants from three continents, including many of the investigators cited in the current paper; D.C. Blanchard, Y. Toba, and J. Wu, to mention just a few. The proceedings volume arising from this workshop, Oceanic Whitecaps, and Their Role in Air-Sea Exchange Processes, was duly published in 1986 (Monahan and MacNiocaill 1986), and is dedicated to A.H. Woodcock. We cannot adequately summarize the 23 full papers and 18 abstracts that appear in this volume within the page constraints of the present paper, but hope that our readers will be able to access this volume through their libraries or bookstores.

Towards the end of September 1983 I accompanied my U.C.G. colleague I.G. O'Muircheartaigh on a trip to Lisbon, Portugal, where he presented our paper, "Aspects of oceanic whitecap coverage dependence on wind speed: Heteroscedasticity in the data and the estimation of the Beaufort velocity"

[70]We had the privilege of co-chairing the third of the symposia in this series in Heidelberg in 1995, which resulted in a volume that contained a number of papers that demonstrated the role of breaking waves and whitecaps in air-sea gas exchange. See Jähne and Monahan (1995).

(O'Muricheartaigh and Monahan 1983a), at the Second International Meeting on Statistical Climatology. And in November of that same year I.G. O'Muircheartaigh attended the Eight Conference on Probability and Statistics in the Atmospheric Sciences in Hot Springs, Arkansas, and presented a paper on the potential use of the Box-Cox transformation in our work (O'Muricheartaigh and Monahan 1983b).

We rounded out our scientific travels for 1983 by again traveling in late November to Bremerhaven, where we took part in the Second Alfred-Wegener-Conference on Air-Sea-Ice Interactions and attended the MIZEX84 Science Group and General Planning Meeting.

14.13 Leaving the Arctic Circle far to the South

I was in Bremerhaven by June 26th of 1983, in time to see my crates of equipment loaded aboard the P/F Polarstern. We departed on the first Arctic cruise, and the third cruise overall, of this new research icebreaker on June 29th, and the first MIZEX83 film whitecap observations were made on this date. The first MIZEX video whitecap recording was made on the following day. Figure 14.14 shows the video recording of the sea surface from an upper deck of the P/F Polarstern.

By the time we arrived at the end of the MIZEX83 and Fram Strait cross-section leg of this cruise in Longyearbyen, Svalbard, on July 19th, we had recorded 44 film

Fig. 14.14 The author with shoulder-mounted Beattie Veritron Video-camera on an upper deck of the F/S Polarstern during MIZEX83. (From author's photo archive, 1983)

Fig. 14.15 A view of the F/S Polarstern moored to an the pack-ice east of Greenland during MIZEX83. The deck from which the film and video images of whitecaps were taken was the one outside the top, white, portion of the superstructure. (From author's photo archive, 1983)

whitecap observation intervals, and 53 video whitecap observation intervals. We also recorded 11 film ice coverage observation intervals and 6 video observation intervals devoted to recording the decay of a sequence of individual whitecaps. All told we took 1042 film images of the sea surface, and recorded 250 minutes of video observations of this same surface. Given that the laboratory in which we kept our video recorder and other gear was some 13 m above the sea surface (see Fig. 14.15 for an elevation view of this ship's superstructure), and that except when the ship was moving through heavy ice it remained "on an even keel", we carried out our filming and videography at the port and starboard rails of this same deck, with the Beattie Varitron automatic sequence camera simply mounted on a tripod, and the, by today's standards, somewhat bulky SONY SMF Trinicon video camera supported by me on a shoulder mount. In order to take advantage of the audio channel on the U-Matic tapes we wore, when we were at the rail recording, a full rigid helmet that was equipped with a microphone.[71] The detailed cruise report on Arktis I was duly

[71]This Italian helmet was designed for those who raced high performance motorcycles. For our application, it was worn without the clear plastic visor. The built-in microphone was located just beneath the visor opening, and just above the wearer's chin. When one listened to the resulting audio channel on this whitecap tapes the information as to time, date, and the "verbal footnotes" were all clearly audible, but so was the wearer's breathing. When we subsequently encountered Darth Vader in the Starwars motion pictures, we were immediately reminded of these whitecap audio recordings.

published by the Afred-Wegener-Institut für Polarforschung in 1984 (Augstein et al. 1984). On July 7th we reached our furthest north on this cruise, 81°31.5′.

The MIZEX83 Whitecap Observation Log for this cruise, with the date, time, Latitude, Longitude, wind data, T_A, SST, and ship's speed and direction, is to be found in the whitecap report issued in October 1984 (Monahan et al. 1984), as are the results of the analyses of the MIZEX83 whitecap segments, and the preliminary analyses of the MIZEX83 video cassettes.

An inter-comparison of the MIZEX83 film and video results[72] will show that the whitecap coverage as deduced from the analysis of the video recordings is typically markedly lower than the whitecap coverage obtained from the film records for the same wind speeds. This is very apparent when one compares the results of, in order, a film observation, a video observation, and then another film observation, all taken within an hour's time. This discrepancy, and the insights we have gained from this apparent inconsistency, will be discussed once we have described the second summer's MIZEX whitecap observations.

In early January 1984 we traveled to Enfield, England, to visit Hakudo, Ltd., and inspected the Hamamatsu Area Analyser, Model C1143-00, which we then purchased so that our laboratory at University College, Galway, would be in a position of being able to routinely analyze the whitecap video tape records obtained during the MIZEX83 and subsequent field experiments. The plans called for us to sail on the University of Bergen's R/V Haakon Mossby[73] during the 1984 MIZEX field season, and given that the Haakon Mossby was a sturdy, but considerably smaller, ship than the Polarstern, we purchased a stainless steel, windowed, instrument shelter from Logstrup Ireland, Ltd. This rectangular box-like shelter, which was to house both a Beattie Varitron film camera and a SONY Trinicon video camera, was outfitted in our Galway laboratory with a heating system and appropriate installation so that our cameras would operate efficiently, and the window of the shelter would remain unfrosted, in the Arctic weather that would be encountered during MIZEX84. Figure 14.16 shows a rear view of the Logstrup shelter aboard Haakon Mosby, while Fig. 14.17 shows the window on the front of this shelter.

We flew to Florida in February 1984 to attend the MIZEX84 Final Operational Planning Meeting, which was held at the University of Miami's Environmental Field Station on Pigeon Key.

In early May 1984 we flew to Bergen, Norway, where we made to arrangements for the mounting of this Logstrup Instrument Shelter aboard the R/V Haakon Mosby. It was determined that the shelter would be mounted above the starboard wing of the bridge aboard the Haakon Mosby during the MIZEX84 cruise, and that the equipment to control and monitor the video camera in this shelter would be mounted in an

[72]This involves the inter-comparison of the MIZEX83 film results as they appear on pg. 22 or Monahan et al. (1984), with the MIZEX83 preliminary video results as listed on pg. 24 of this same report.

[73]The R/V Haakon Mosby (or Håkon Mosby) was launched in 1980. It is 47.2 m long, and has a gross tonnage of 699. It is now operated by the Institute of Marine Research of the University of Bergen.

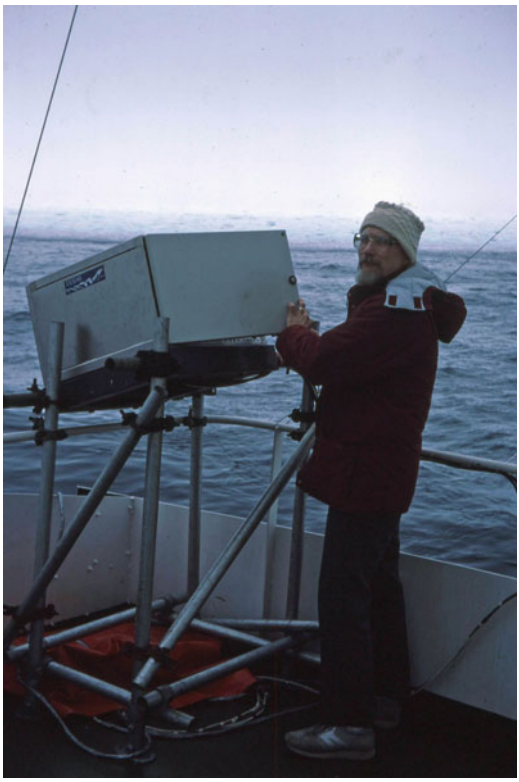

Fig. 14.16 The author checking the film and video cameras inside the Logstrup Instrument Shelter mounted above the bridge on the R/V Haakon Mosby. Note the edge of the ice sheet in the mid-distance. (From author's photo archive, 1984)

interior laboratory on the main deck of this ship. We purchased a SONY Camera Control Unit, Model CCU-1800P, a small monitor, Model DFX-4OCE, and the required power supplies, which were all needed to complete this setup. We also obtained a second SONY model DXC-1800P camera which could be used in the shoulder-mounted mode on this cruise.

We, accompanied by Peter Bowyer, arrived back in Bergen by June 9th, to complete our preparations for our MIZEX84 cruise aboard the Haakon Mosby. We duly sailed from Bergen on June 12th, and took our first film and video recordings of whitecaps on June 13th. We put in briefly at Tromsø in far northern Norway, and then sailed to Ny-Ålesund on the northwest coast of Svalbard.[74] The Haakon Mosby on this cruise on a number of occasions reached latitudes higher than 80° N. On June 27th, we flew in a small helicopter at low elevation over extensive fields of pancake ice from a large ice floe to which the Haakon Mosby was temporarily moored to a larger, distant, floe next to the leased sealer Kvitbjorn. A day to two later the Kvitbjorn broke out of the ice and proceeded to Longyearbyen,

[74]When we went ashore at Ny-Ålesund I immediately recognized the old lattice-structure dirigible mast used in the 1920s by R. Amundsen's expedition over the North Pole aboard the Norge, and by U. Nobile aboard the Italia on a subsequent, less successful, dirigible flight.

Fig. 14.17 The Logstrup Instrument Shelter above the bridge on the Norwegian R/V Haakon Mosby during MIZEX84. Note that the shelter is tilted so that enclosed cameras are pointed obliquely at sea surface. (From author's photo archive, 1984)

from which we flew south on our way back to Ireland. Peter Bowyer remained aboard the Haakon Mosby, and continued to record film whitecap observations until July 14th. All told, on this MIZEX84 cruise on the Haakon Mosby a total of 73 film whitecap observation intervals were recorded, as were 88 video whitecap observation intervals. During this cruise another 7 tape segments were recorded with a shoulder-mounted video camera to document the bubble production around rocking ice floes, windrow features, or the decay of individual whitecaps.

The MIZEX84 (preliminary) Whitecap Observation Log, containing the same information for the Haakon Mosby cruise as did the MIZEX83 Whitecap Observation Log for the Polarstern cruise, appears on pp. 28–35 of the October 1984 Whitecap Report (Monahan et al. 1984).

The tabulated MIZEX83 whitecap film data,[75] in preliminary form appeared in MIZEX Bulletin IV (Monahan and Bowyer 1984), and in final form on pg. 22 in the October 1984 UCG Whitecap Report cited above. The whitecap video data from MIZEX83 are found tabulated in preliminary form on pg. 24 of this same report, and

[75]These extensive film recordings of whitecaps were analysed by M.R. Higgins, T. Luibheid, S. MacGearain, and C. Maloney, and the mean values and standard deviations for each observation interval were computed by M.R. Higgins and D.M. Doyle. The assistance of these students and assistants in our Galway laboratory were, and are, greatly appreciated.

in final form on pg. 124 in the October 1985 UCG Whitecap Report (Monahan et al. 1985). The data tabulations arising from the analysis of the MIZEX84 whitecap films appear in Table 3.2 on pp. 58–59, and the results of the analysis of the whitecap video cassettes from this field experiment appear in Table 3.1 on pp. 56–57 of this same October 1985 report. These same MIZEX84 whitecap film and video data tabulations appear in the February 1986 UCG Whitecap Report,[76] but with each tabulation now including a column containing the relevant friction velocity, u^*.

And it is time now to return to the apparent discrepancies in the whitecap coverage values obtained via the analysis of 35 mm film compared to the values obtained by the digital analysis of video records collected at roughly the same wind speeds. The cause for this discrepancy is easily explained. In analyzing manually the film images of the sea surface, the individual analysts were able, after a little practice, to outline on the projected image of each such frame the entire whitecap in that view of the sea surface. In other words they were able to follow the procedures described in the earlier section of this paper devoted to "The Manual Analysis of Our Whitecap Photographs". But when it came to using the Hamamatsu digital device to determine the whitecap coverage on a video clip taken during a whitecap observation interval, it readily became apparent that the operator could not select, based on the analysis of one "frame" at the beginning of a video tape segment, a particular gray scale value as the discriminant between whitecap covered sea surface and non-whitecap areas, and then run the entire tape segment to ascertain the average whitecap coverage during the whitecap observation interval corresponding to this tape segment. The challenge was much greater than that. Often on an individual "frame" of a video record of the sea surface, other, non-whitecap-covered portions of the sea surface were brighter, i.e. had a higher gray scale value, than all, or at least major portions, of what were clearly whitecap-covered areas. The practical solution to this last challenge was to select only the brightest portions of the whitecaps that appeared on a particular video "frame", and define this as the video-resolvable whitecap, which we later defined as W_A. Having selected the discriminant level at such a high gray scale value had the additional practical benefit of allowing the operator to analyze significant portions of the typical video cassette tape, often corresponding to a complete whitecap observation interval, without having to re-set the discriminant level to a new gray scale value. In this fashion, with constant monitoring of the semi-automatic video analysis, and re-setting the gray scale discriminant when needed during the running of such a video cassette tape, the operators were able to generate reliable W_A values for our various video whitecap observation intervals.

[76]See Monahan et al. (1986b), which appears as Appendix A of Monahan and Woolf (1986).

14.14 Striving for a Consistent Nomenclature to Describe Whitecaps and Bubble Plumes

So now we were generating W_A values that clearly did not correspond to the total whitecap areas, i.e. the W values, we had obtained, and were continuing to obtain, from the manual analysis of film segments. But what, if anything, did W_A correspond to?

The answer to this question, or a good lead to the answer, lay before us when we opened an envelope that arrived 1 day in our mail at UCG. We need admit that, a third of a century later, we don't actually recall the specifics of how a "reprint"[77] of the Bondur and Sharkov (1982) article in *Oceanologiya* found its way to us. We eventually retained the services of a translator who provided us with a rough English version of this important Russian paper. What immediately caught our attention was that they distinguished between two kinds of "whitecap", the white-water associated with a spilling wave crest, which is referred to by some as the active whitecap, and the decaying foam patch (see, e.g., Bortkovskii 1987). In particular, their results indicated that the individual decaying foam patch was typically more than an order of magnitude larger in area than the active spilling wave crest for the same wind speed. And while they had observations at only a few wind speeds, their results showed that the typical areas of individual whitecaps, of both categories, increased significantly with increasing wind speeds. Specifically, they found that spilling wave crests increased in average area from approximately 0.4 m^2 at a wind speed of 5 m/s to 1.2 m^2 for winds of 10.5 m/s, while their results indicated that the average area of decaying foam patches increased from about 18 m^2 to 28 m^2 as the wind increased from 5 to 10.5 m/s. This last finding was at least qualitatively consistent with the earlier observation, contained in a footnote to a paper by Walter Munk (1947), that whitecap "diameters do increase from 3 feet for a [wind] speed of about 7 m/sec to 25 feet for speeds exceeding 13 m/sec".

We would shortly thereafter come up with several graphic depictions of the evolution of not only a whitecap, but also of its associated sub-surface bubble plume, that suggested how not only the size, but the surface brightness, i.e. visible albedo, of a whitecap might evolve with time from the first breaking of the parent wave. In a volume on "Sea Surface Sound" (Monahan 1988a) we published a figure, reproduced here as Fig. 14.18, that showed an idealized columnar bubble cloud, whose cross-section diminished exponentially with depth, representing "an idealized plume immediately after formation by a breaking wave", and included sketches meant to represent later decay stages of this plume. The focus of this figure was the

[77]This harkens back to the period when an author routinely obtained a number of copies (typically 50 or 100) of their paper (often, as in this case, with a cover/wrapper) from the publisher of the journal that contained this article. The author could them mail one of these "separates" to each of those who requested such a copy. (Since our 1971 *Journal of Physical Oceanography* paper on whitecaps is cited in this Bondur and Sharkov paper, it is quite possible that they kindly sent it to me.)

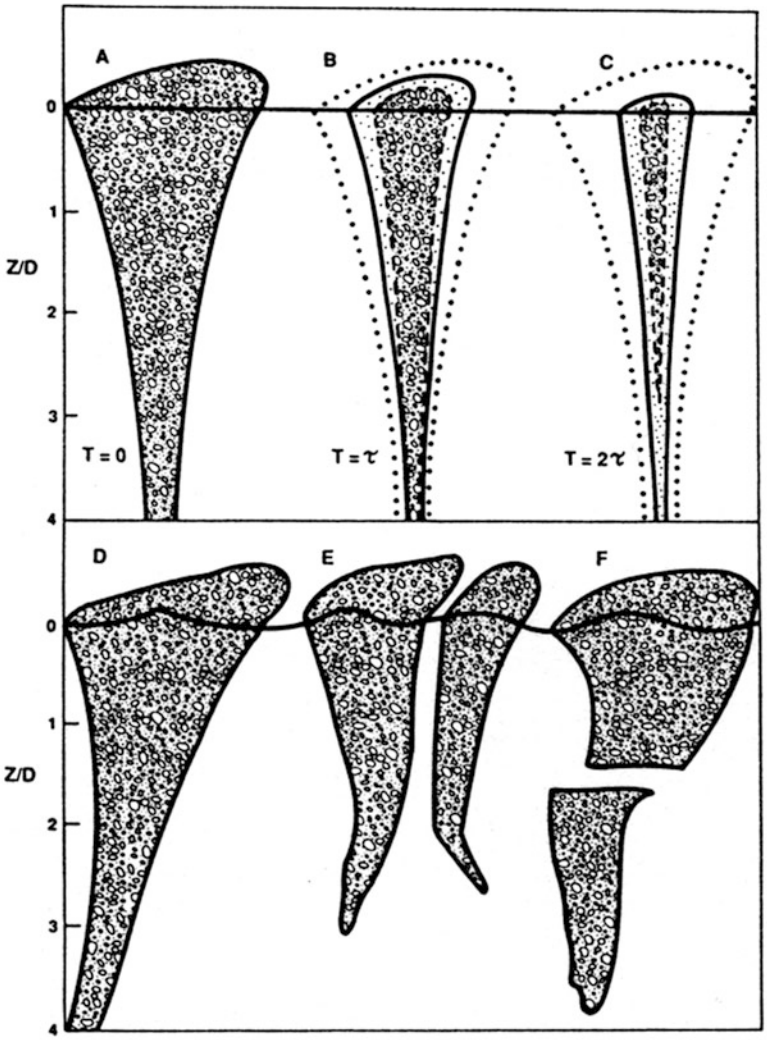

Fig. 14.18 Vertical sections through an idealized bubble plume produced by a breaking wave, increasing in age from left to right. (**a**, **b**, **c**): in absence of current shears in the oceanic surface layer. (**d**, **e**, **f**): in the presence of current shear. © Springer International Publishing AG. (From Monahan 1988a)

proposed influence of the rise velocity of the larger bubbles on the lifetime of the surface whitecap. In early 1988 we presented a paper (Monahan 1988b) entitled "near-surface bubble concentration and oceanic whitecap coverage" which included a figure, reproduced here as Fig. 14.19, hypothesizing how a bubble plume immediately beneath the sea surface might evolve with time from its formation, and how its surface manifestation, the whitecap, would hence decay with time. This same

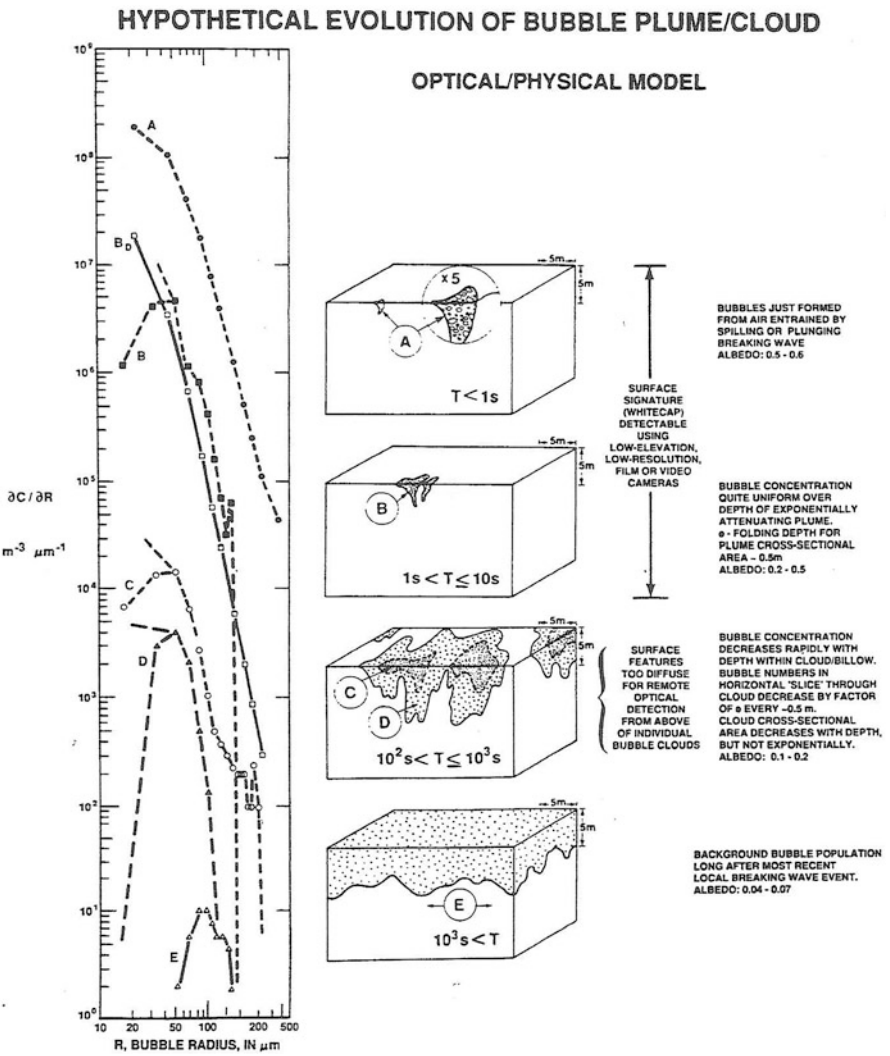

Fig. 14.19 Whitecap decay and bubble cloud evolution. Concentration spectrum A in left-hand panel has been assigned shape of sea-surface bubble flux spectrum, while spectra B, C, D, and E are based on population spectra measured by Johnson and Cook (1979) and Kolovayev (1976), but with, in most instances, amplitudes modified in accord with assumed plume geometries. © American Meteorological Society, used with permission. (From Monahan 1988b, where spectrum B_D is described)

figure included a panel with candidate spectra identified with each stage of plume decay. The penultimate figure in this series of representations of the various stages in the life of an oceanic whitecap and its associated bubble plume is to be found in a

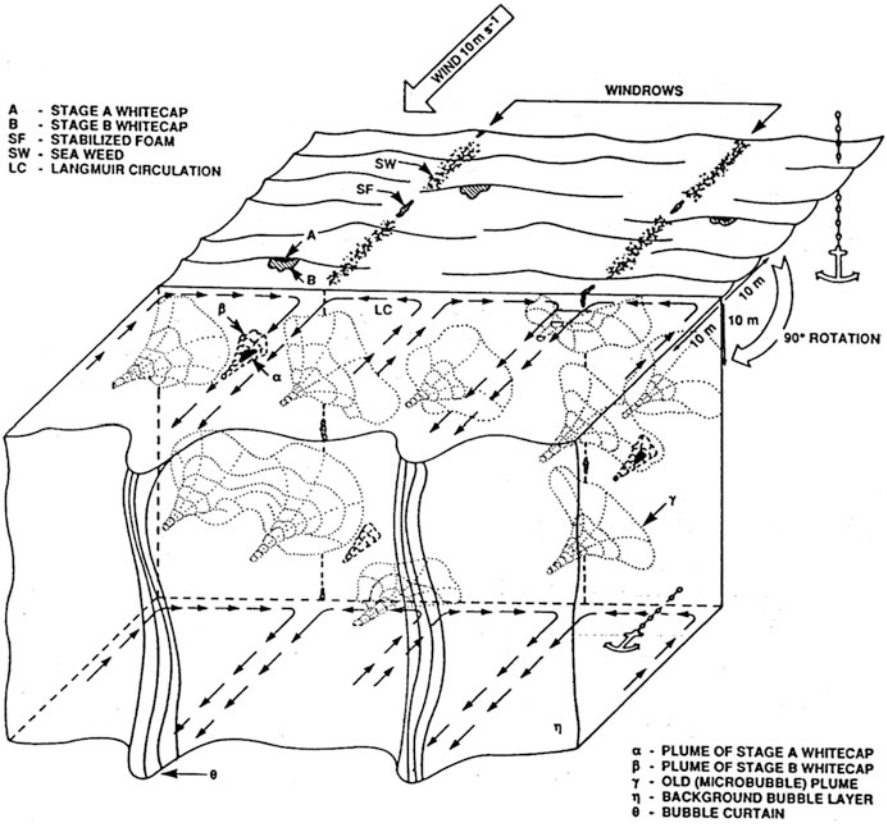

Fig. 14.20 Stages in the evolution of a whitecap and its associated bubble plume produced when air is entrained by a spilling wave crest. The influence of Langmuir circulation on the bubble plumes and the background bubble population is also shown in this figure. Note the arrows at the right end of the "hinge" in this "gate-leg table" figure marking off 10 m along the axes of this scale drawing. ©1990 IEEE. (Reprinted with permission from Monahan and Lu 1990. See References section for complete citation to this IEEE J. Oceanic Engin. article)

paper published by Monahan and Lu (1990)[78] in which, within one "gate-leg table" figure, can be see the several stages in the evolution of discernible whitecaps, and the various stages on the bubble plumes formed by breaking waves, including those late stages that are no longer associated with optically resolvable surface whitecaps. This figure also depicts the complexity expected in the distribution of stabilized surface foam, and of the late stage sub-surface bubble plumes, which can be attributed to the influence of Langmuir circulation in the surface mixed layer of the ocean. This figure appears here as Fig. 14.20. The notation found on this figure is the one now adopted by many in discussing oceanic whitecaps, i.e. the spilling wave crest of Bondur and

[78]This same figure can be found in Monahan (2001).

Sharkov, or the active whitecaps of Bortkovskii, are referred to as Stage A whitecaps, while the decaying foam patches of these authors are designated as Stage B whitecaps. (And as a consequence, the fraction of the sea surface covered by spilling wave crests is denoted W_A, and the fraction of this surface covered by decaying foam patches is labeled W_B.) The bubble plumes beneath Stage A whitecaps are referred to as α-plumes, the plumes dependent from Stage B whitecaps are marked as β-plumes, and the yet older, still acoustically distinguishable, bubble plumes that no longer have optically discernible whitecaps associated with them are designated γ-plumes. The ultimate version of this illustration, which includes, in addition to the image just described, a second "gate-leg table" showing the distribution of surface whitecaps and sub-surface bubble plumes in the absence of any Langmuir circulation or strong vertical shear in the ocean mixed layer, can be found in a proceedings volume dealing with the "natural sources of underwater sound"(Monahan 1993). The portion of this figure showing the distributions of whitecaps and plumes in the absence of Langmuir cells is reproduced here as Fig. 14.21.

The contention that a Stage A whitecap is optically distinct from the successor Stage B whitecap, with this stage having a reflectance, or visible albedo, of 0.55, and then, as the whitecap ages, spreads, and the number of layers of bubbles in intimate contact with the sea surface decreases markedly, this reflectance rapidly diminishes, is supported by several early experimental and theoretical studies (see. e.g., Whitelock et al. 1982; Stabeno and Monahan 1986; Koepke 1986).

14.15 On to the North Sea

In mid-October 1984 several of us visited the Koninklijk Nederlands Meteorologisch Institut in de Bilt, to prepare our UCG film and video whitecap recording systems for installation on the Meetpost Noordwijk[79] off the Dutch coast in the North Sea as part of the Humidity Exchange Over the Sea (HEXOS) experiment. During the period 6–22 November of that year, KNMI personnel made 28 video, and only 11 film, whitecap observations aboard the Meetpost Noordwijk using this equipment. Photographs of this platform and other relevant material can be found in a report issued by the Bedford Institute of Oceanography (Oost et al. 1984). The whitecap observation log for this experiment appears in UCG Whitecap Report # 8 (Monahan et al. 1985), as does the resulting W_A (video) data which was designated the HEXOS84, or HEXPILOT, set. These same HEXOS84 W_A data appear tabulated in a HEXOS85 workshop volume (Monahan 1986b) issued by KNMI. The UCG whitecap recording systems arrived back in Galway from KNMI in April 1985.

[79]This "Texas tower"-like structure had originally served as a "pirate" radio station, but upon it seizure by the Dutch government and the removal of the tall radio mast, it become a research platform.

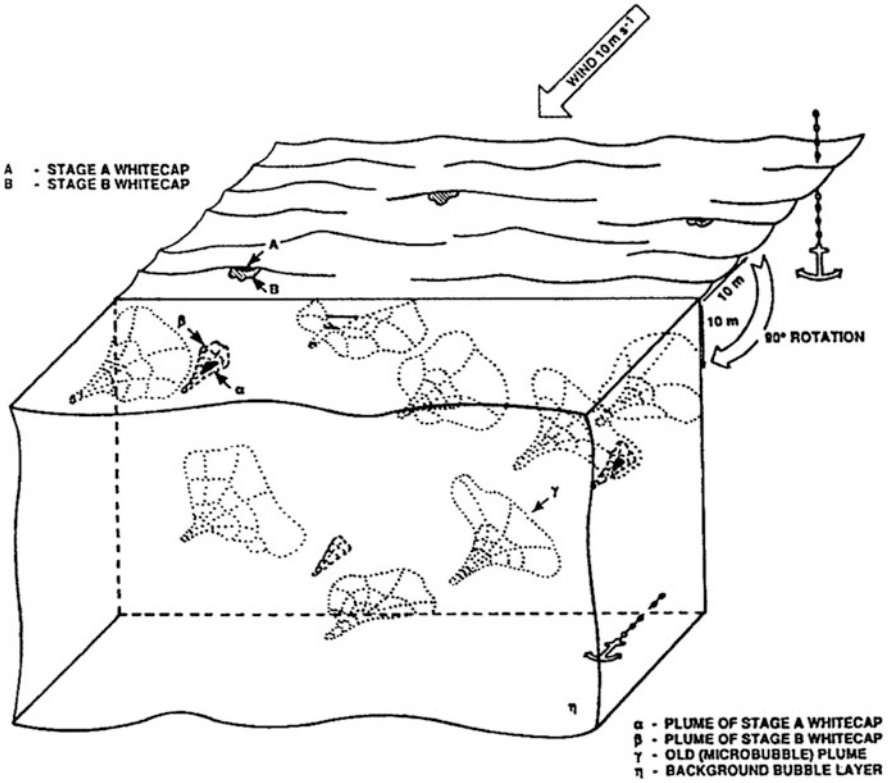

Fig. 14.21 The various stages in the evolution of whitecaps, and their associated bubble plumes, in the absence of surface-layer shear, Langmuir circulation, and other complicating flow features. Note the anchors which provide a vertical reference in each portion of this "hinged" illustration. © Springer International Publishing AG. (From Monahan 1993)

Our "whitecap project" equipment was shipped in a freight container from Galway on February 18th 1986, bound for the University of Connecticut's marine campus in Groton, where I was soon to take up a new appointment that contained a provision that would enable me to continue with my research on marine aerosols and oceanic whitecaps. We have decided that this migration back across the Atlantic would mark the end of the "early years" I have undertaken to chronicle in this paper. But it seemed appropriate to include within this paper some mention of our participation in HEXOS86, or HEXMAX. The steel container with all of our whitecap and marine aerosol equipment having arrived in Connecticut on March 27th, on August 4th we duly shipped three wooden boxes of whitecap recording equipment back across the Atlantic to KNMI, de Bilt. And in early October I visited KNMI, bringing some additional equipment, and spending time checking on the performance of the whitecap recording gear before it was deployed again to the Meetpost Noordwijk. This time only video whitecap observations were recorded. The resulting HEXOS86

W_A values, some 159 of them, are tabulated in a 1988 University of Washington technical report (Monahan et al. 1988), along with the 10 m-elevation wind speed, and air and surface water temperatures for each whitecap observation interval. October 1986 proved to be a busy month, as I was pleased to be able to accept an invitation from the Polish Academy of Sciences to spend a week in Poland during that month, and gave several lectures during a multi-day "Seminar on Climate and Air-Sea Interaction" held at the Instytut Oceanologii of the Polska Akademia Nauk, located at Sopot on the Baltic coast.

This then will conclude our description of new whitecap field campaigns in which we participated, but for a mention that we did continue to send our suite of video gear to sea to record whitecaps, and to analyse the results video records (see, e.g., Monahan and Wilson 1990a, b; Monahan et al. 1991).

We would be remiss if we did not acknowledge the burgeoning number of investigators who have contributed to the research community's whitecap data base in the past quarter century, with observations taken from platforms, ships, aircraft, and satellites.

14.16 Nomenclature Revisited

We previously discussed how, at a particular wind speed, the typical area of a spilling wave crest, or Stage A whitecap was, according to the findings of Bondur and Sharkov (1982), more than an order of magnitude smaller than the typical size of a decaying foam patch, or Stage B whitecap, at the same wind speed. They also found, at a wind speed such as 5 m/s, that the fraction of the sea surface covered by Stage A whitecaps, W_A, was more than 40 times smaller than the fraction of that surface covered by Stage B whitecaps, W_B. This can be seen from the accompanying Fig. 14.22 (from Monahan 1989), where the line designated A2 is a curve through their W_A points, and the curve B3 is fitted to their W_B, i.e. foam streak, points. The amplitude of their W_B curve is more than 40 times greater than the amplitude of their W_A curve at a wind speed of 5 m/s, and this disparity appears to only diminish slightly with increasing wind speed.

Now as to nomenclature: Given these findings of Bondur and Sharkov, we felt that our previously reported W values, the fraction of the sea surface covered by all stages of whitecaps, could be taken as essentially equivalent to W_B values. We did just this in our contribution to proceedings stemming from the April 1988 NATO workshop held in Epe, the Netherlands (Monahan et al. 1988). In this proceedings volume we presented a table showing that, for wind speeds of 15 m/s or less, and using a preliminary $W_A(U)$ expression (Eq. 14.28) derived from our analyses of the MIZEX83, MIZEX84, HEXOS84, and HEXOS86

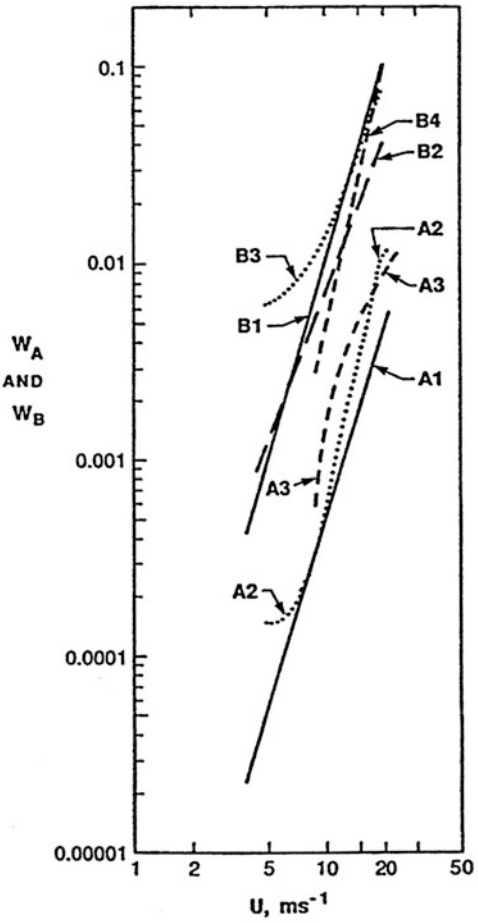

Fig. 14.22 The wind dependence of Stage A and Stage B whitecap coverage. See text for description of relevant A and B curves. (Note that both axes bear logarithmic scales. © Connecticut Sea Grant College Program, reprinted with permission from Monahan 1989)

$$W_A(U) = 4.58 \times 10^{-7} U^{3.094} \tag{14.28}$$

whitecap video tapes, our estimate of the W_A/W_B ratio was at most 10%.[80] Essentially this same conclusion can be drawn from a comparison of line A1 (based on a $W_A(U,\Delta T)$ expression derived for these same four W_A data sets, here taking $\Delta T = 0$) and line B1 (Eq. 14.14, but taking W_{RBF} to represent W_B) as shown on Fig. 14.22. When in 1986 we had the opportunity to become familiar with Roman Bortkovskii's

[80]This factor of roughly 10:1, W_B:W_A, was confirmed in a later, more detailed analysis by Monahan and Lu (1990), using the W_A values from the same four video data sets used to derive Eq. 28, and the W_B data sets from the BOMEX+, East China Sea, JASIN, STREX, MIZEX83, and MIZEX84 field experiments. (See text at the bottom of the right-hand column on pg. 345 of this paper.)

book on air-sea exchange,[81] we were belatedly introduced to his extensive study of whitecaps, and the rich set of whitecap observations which he had amassed.[82] His results for active whitecaps, i.e. spilling wave crests, are summarized by curve A3 on Fig. 14.22, while his description of whitecap and foam cover is described by curve B4 on this same figure. All of these observations were taken when the SST was between 3° and 15°C. It is apparent that for winds speeds just above 10 m/s these two curves are separated by considerably less than a decade (perhaps only a factor of slightly above 3) on this log-log representation, i.e. clearly less than the order of magnitude, or greater, reported in the other studies summarized on this figure. Further insights into the potential range of W_A/W_B ratios can be found in the recent work of Callaghan and colleagues (see, e.g., Callaghan et al. 2008, 2012; and Callaghan 2013). An update on the analysis of digital whitecap data can be found in Scanlon and Ward (2013, 2016).

In summary, W, as measured in the early studies conducted by our group, was the sum of W_A and W_B. The Russian literature cited above provided two quantities, W_A and W_B. The reader should be aware of the confusion that has arisen in some instances by our group, for the reasons cited above, taking $W_B \approx W$.

14.17 Some Final Thoughts on the "Great λ Controversy"

I would be remiss, as we approach the conclusion of these personal impressions of the early years of research on whitecapping, if I did not return to the controversy, as regards the magnitude of the power-law exponent, λ, in the W(U) expression (Eq. 14.27), "kicked off" by the previously mentioned series of papers, comments, and replies authored by Wu and by Monahan and O'Muircheartaigh, that began appearing in 1979–1982.[83] Wu continued to advocate for a λ value for 3.75 based on the rationale summarized in Eq. 6–12 (see, e.g., Wu 1988, 1992, 2000), while my group continued to follow the field data wherever it lead us. It should be stressed that Jin Wu was always collegial in his contributions to this protracted dialogue, as can be seen from his "Reply" (Wu 1989) to a "Comments" paper published by Monahan and Woolf (1989). We should also mention Wu's early paper on wind stress and surface roughness (Wu 1969).

We agreed with Wu's contention that whitecap coverage should be proportional, at least nominally, to $C_{10}{}^{1.5}U_{10}{}^{3}$, i.e. with the rationale embodied in Eqs. 14.6, 14.7,

[81] I was pleased to serve as the editor of the revised English edition (Bortkovskii 1987) of his earlier Russian language volume (Bortkovskii 1983).

[82] Roman Bortkovskii kindly shared with me tabulations of the W_A and W_B (our usage) data sets obtained from the analysis of photographs taken during no less than six Russian expeditions, and the Bortkovskii and Kuznetsov (1982) paper that appeared in the *Taifun75* reports.

[83] Participation in this protracted academic exchange-in-print did not deter the academic careers of several of those involved. Iggy O'Muircheartaigh capped his career as President of the National University of Ireland, Galway, and Jin Wu went on to serve as the first President of the National Cheng Kung University in Tainan and then spent several years as Taiwan's Minister for Education.

14.8, 14.9, 14.10, and 14.11. But we were not convinced that C_{10} varied as the $\sqrt{U_{10}}$, and became more and more convinced with the passage of time that the argument behind Eq. 14.11 was only valid in the case of an equilibrium sea. We went so far in Monahan and O'Muircheartaigh (1982b), based on our consideration of an augmented whitecap data base, to infer "that the wind dependence of the drag coefficient is considerably less than the square-root-of-the-wind dependence previously suggested by Wu". If we can jump forward a third of a century to a paper in the *Journal of Physical Oceanography* by Edson et al. (2013) which details refinements (COARE 3.5) in the analysis of the results of the Coupled Ocean-Atmosphere Response Experiment as it relates to the wind-dependence of the drag coefficient, we note from Fig. 10 in this paper that $C_{D10}(U_{10})$ does not vary simply as $\sqrt{U_{10}}$, and that the magnitude of this coefficient only increases by a factor of about 1.8 as the wind speed increases from 3 m/s, the wind speed that corresponds to both the minimum amplitude of the drag coefficient and to the onset of whitecapping, to 15 m/s, while over this same wind speed range, we would expect the drag coefficient, if it varied as $\sqrt{U_{10}}$, to increase by a factor of 2.24.[84]

As our group began to amass whitecap observation data sets such as those from the JASIN and STREX experiments, which were recorded in colder, more northern, seas and oceans, we noted that the λs associated with these data sets had magnitudes often less than 3 (see, e.g., Spillane and Doyle 1983, and Doyle 1984a, b), and certainly considerably smaller than the λs we had previously found for data sets collected in warmer, more southern, oceans and gulfs (see, e.g., Monahan and O'Muircheartaigh 1980a). We did at this time also devote some thought as to why, even if for most wind speeds the W-values for such a cold water whitecap observation set as MIZEX83 would be less than for the warm water whitecap observation sets, yet none-the-less at low wind speeds the cold water W-values were often higher than the warm water W-values. These theories focused on why α, the coefficient in the W(U) power-law expression (Eq. 14.27) would change in magnitude with changes in T_W. Before we headed to the Arctic for this first MIZEX field period, we had hypothesized that α would decrease as T_W increased (Monahan and Bowyer 1984). The specific idea that we entertained was that since the kinematic viscosity of sea water, ν, decreased with increasing T_W, the bubble plumes sustaining the surface whitecaps would take less time to "out gas", i.e. it would take bubbles less time to rise to the surface, in warmer waters than in cooler waters. Thus even if the same new whitecap area was produced per unit time for the same wind speed in both the Arctic and the Trade Wind regions, since the Arctic whitecaps would, according to this argument, take longer to decay, the instantaneous whitecap coverage in the Arctic would be greater than in the Trade Wind regions. There are several rationales that subsequently came to mind, as to why, for the same wind speed, U, and atmospheric stability, ΔT, there could be a smaller portion of the sea surface covered by whitecaps in cooler oceans than in warmer ones, as is the case

[84]This wind speed range of 3–15 m/sec encompasses the vast majority of the whitecap observations reported in the literature by ourselves and others.

at higher wind speeds. Consider another effect of kinematic viscosity, ν: this time its influence on the size of the bubbles that form when a wave breaks. It is reasonable to conclude that in warmer, less viscous water, there will be more, but characteristically smaller, bubbles produced for the same wave breaking than in cooler water. Now we know that in salt water, there are, due to the influence of salinity, more, and smaller, bubbles, produced by the same wave breaking than in fresh water. And as we demonstrated back in Monahan and Zietlow (1969), the whitecaps formed in fresh water have shorter e-folding decay times than those formed in salt water, as the bigger fresh water bubbles will rise faster than the smaller salt water ones. By analogy it could be hypothesized that the whitecaps formed on the surface of cooler water bodies might have shorter characteristic life times than the whitecaps formed on warmer waters, and hence for the same wind speed, and the same number of breaking waves per unit area per unit time, the instantaneous fraction of the cooler water surface covered by whitecaps might be less than the fraction of the warmer water surface covered by such features. Another argument that could be made in support of the hypothesis that for the same wind speed and atmospheric stability there should be less whitecap area on the surface on a cool ocean than on a warm ocean follows from a consideration of an implicit assumption underlying the development of Eqs. 14.6, 14.7, 14.8, 14.9, 14.10, and 14.11. And that assumption is as follows: for the same wind speed and atmospheric stability, a fixed fraction of the work done on the sea surface by the wind per unit time is dissipated via small scale turbulence within the liquid, and another fixed fraction is expended in macroscopic wave breaking with the associated entrainment of air, regardless to the water temperature, T_W, i.e. regardless of the kinematic viscosity, ν, of the liquid. Now in cool, more viscous, water is it not reasonable to expect that more of the energy from the wind per unit time can be effectively dissipated via small scale turbulence within the liquid, than in warmer, less viscous, water? If this were to be the case, then it could be argued that in cooler, more viscous, ocean waters a smaller fraction of the work per unit time done on the sea surface by the wind is dissipated via wave breaking and whitecap formation, and a larger fraction is expended on small scale turbulence within this ocean surface layer, than in the case of a warmer, less viscous, ocean surface layer. Only with careful laboratory studies of the effect of T_W on the spectrum of bubbles found in the new α-bubble plume that results for a breaking wave, and of the effect that temperature-associated changes in kinematic viscosity would have on the terminal rise velocities of these bubbles, would we be able to fully sort out these competing considerations.

But above all we need remember that the dependence of W(U) on T_W will be a consequence of the T_W-dependence of both α and λ. We have over the years devoted considerable effort to determine the magnitude of the T_W-dependence of λ, and to explain why there appears to be such a dependence. The T_W-dependence of λ will be addressed in the following section of this paper, where we will discuss the various findings we obtained from analyzing the omnibus whitecap data comprised of the relevant data from the BOMEX+, East China Sea, JASIN, STREX, and MIZEX83 field campaigns. And we will "sneak in" some recent findings on the T_W-dependence of α as well as some recent findings on the T_W-dependence of λ.

14.18 A "Review" to Close out the "Early Years" of Research on Whitecapping

We have reached the point where we think it appropriate to summarize the early years of whitecap research, and to that end we would like to summarize some of the findings in our review article in *The International Journal of Remote Sensing* (Monahan and O'Muircheartaigh 1986). The first topic we tackled in this paper was the wind speed associated with the onset of whitecapping, which we refer to as the Beaufort velocity,[85] U_B. Specifically we defined U_B as the 10 m-elevation wind speed associated with a 50% probability of detecting one or more whitecap in the set of images comprising a whitecap observation interval. Our findings, based on the analysis of the BOMEX+, East China Sea, JASIN, STREX, and MIZEX83 photographic data sets, suggested that whitecaps first appeared at a wind speed of some 3–3.5 m/s, with this onset velocity varying with atmospheric stability, ΔT, and to a degree with sea surface temperature, $T_{W,}$ as reflected in Eqs. 14.29 and 14.30.

$$U_B = 3.27 \times 10^{-0.0458\Delta T}\ (\mathrm{m/s}) \tag{14.29}$$

$$U_B = 3.36 \times 10^{-0.00309T}{}_{w}(\mathrm{m/s}) \tag{14.30}$$

These findings were in marked contrast to the 7 m/s cited by Munk (1947) for the first appearance of whitecaps, a wind speed repeated down through the years by many authors, particularly those in the field of marine remote sensing (see, e.g., Ross et al. 1970; Gloersen and Barath 1977; Zheng et al. 1983). By way of contrast we should recall that Gathman and Trent (1968) stated "that the 'threshold wind velocity' is a value which may depend on other factors" beyond wind speed, and reported, based on shipboard photographs of the sea surface, that there was no whitecaps when the wind speed was equal or below 6 knots (3.1 m/s), but that whitecaps "did occur 80% of the time when the wind speed was" greater than this value. For an up-to-date discussion of the Beaufort Velocity the reader is referred to a paper by Scanlon and Ward (2016).

Using the same set of whitecap data sets, we investigated the effect of the stability of the lower atmospheric boundary layer on whitecap coverage and arrived at Eq. 14.31.

$$W_B = 1.95 \times 10^{-5} U^{2.55} \times e^{0.0861\Delta T} \tag{14.31}$$

The three-dimensional surface shown here in Fig. 14.23, illustrates how W_B varies with the 10 m-elevation wind speed, and with ΔT. As one should expect, for the same 10 m-elevation wind speed, the more positive the value of ΔT, i.e. the more

[85] See Kinsman (1969a, b) for a discussion of Sir Francis Beaufort and his Wind Force Scale. Many current versions of the Beaufort Wind Scale refer to the degree of whitecapping and the extent of foam coverage in defining most of the Forces.

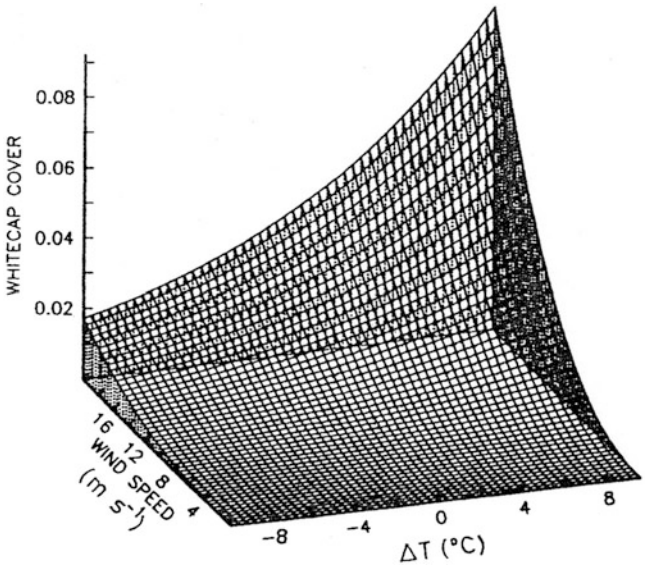

Fig. 14.23 Oceanic whitecap coverage, expressed as a fraction, plotted against ΔT, i.e. $T_W - T_A$, and U, the 10 m-elevation wind speed. Surface determined from a consideration of the 5 data sets referenced in the text. © Taylor and Francis Ltd. (http://www.tandfonline.com), reprinted with permission from Monahan and O'Muircheartaigh 1986. (See References section for complete citation to this International J. of Remote Sensing article)

unstable the marine atmospheric boundary layer, the greater the magnitude of W_B, and likewise, the more negative the value of ΔT, i.e. the more stable the MABL, the smaller the magnitude of W_B, for this same wind speed.

Using the various values of λ, the power law exponent in Eq. 14.27, determined by the application of various power-law statistical fits to these same five whitecap data sets (at least three statistical models were used in fitting each of these data sets), it was apparent, as can be seen from Fig. 10 from this *International Journal of Remote Sensing* paper, that λ increased markedly as one went from the cold water whitecap data sets such, as those collected during the STREX and MIZEX field experiments, to the warm water data sets that were obtained during the East China Sea and BOMEX+ field studies. If we jump to a paper we presented at the 18th Conference on Air-Sea Interaction (Monahan and O'Muircheartaigh 2012), and adopt the notations of the current paper, we have the results we obtained by using as our input meta-data 47 $W_B(U)$ power law expressions from the literature. In this recent paper we found that $\lambda(T_W)$ could be described as shown in Eq. 14.32, and the $\alpha(T_W)$ could be expressed as shown in Eq. 14.33. Before we

$$\lambda(T_W) = 2.272 + 0.0365\, T_W \tag{14.32}$$

$$\alpha(T_W) = 4.81 \times 10^{-5} \times 10^{-0.0303T_W} \tag{14.33}$$

comment on these results, we need mention that the 47 expressions used as the meta-data for these analyses were originally 54 in number, but 7 expressions had to be set aside as we could not identify sea water temperatures to associate with them. The original 54 equations were derived in turn from no more than 19 whitecap data sets, taken individually or in combination, by the various authors. And it should be further noted as a caveat that the BOMEX+ data set, taken alone or in combination, was used in deriving no less than 23 (i.e. 42.6%) of these 54 equations, and the East China Sea data set was likewise used, alone or in combination, in the derivation of 22 (i.e. 40.7%) of these equations. All 19 data sets are listed in the 18ASI AMS Confex paper.

We note from Eq. 14.32 that $\lambda(T_W)$ increases markedly with sea water temperature, increasing from a value of 2.45 at a SST of 5°C to a value of 3.29 at 28°C, and that $\alpha(T_W)$ does decease with increasing T_W. (Thus our initial hypothesis as to the variation of α with T_W appears to be correct, but this does not mean that our reasoning for the nature of this variation is valid.)

The 1986 paper is, we think, worthy of quoting here; "An explanation for this variation of λ with T_W rests on the observation that both the typical wind duration and the mean sea-water temperature vary latitudinally. Many of the warm-water observations were made in trade-wind regions, where even the fairly high winds persist long enough to produce a fully developed sea, one commensurate with those winds. On the other hand, the whitecap observations made over colder waters were taken in regions such as the Atlantic north-west of Ireland, the Gulf of Alaska, and Fram Strait, where the typical duration associated with high wind events was often quite short, and thus the wave spectrum had usually not become fully saturated. . . . It follows that in the colder regions such as where the JASIN, STREX, and MIZEX83 observations were made, the rate of whitecap formation and the whitecap coverage would frequently be less than they would have been in the case of a fully developed sea, and it would be expected that this reduction in whitecap coverage associated with the lack of spectral saturation, would become more pronounced, the higher the windspeed category, and the shorter the wind duration" (this quote appears on pp. 637–638 of Monahan and O'Muircheartaigh 1986).

If we can now take one last jump into the present, we will summarize some of the recent results presented by us at the 19th Conference on Air-Sea Interaction (Monahan et al. 2015). We at this stage had available to us the characteristic latitudes for no less than eight whitecap data sets: the "+" of BOMEX +; the BOMEX observations, i.e., including only those taken aboard the R/P FLIP and the U.S.S. Salish; East China Sea; JASIN; MIZEX83; MIZEX84; STREX; and the Southern Ocean set of Zappa.[86] When a statistical analysis was carried out[87] using

[86] A description of the Southern Ocean Experiment can be found in Randolph et al. (2014), the whitecap data can be found in Appendix A of Monahan et al. (2015).

[87] Succinctly, this analysis was carried out using the RGL-package in R-programing language.

the $\ln W_B$, lnU, and absolute latitude values from these eight data sets, the resulting values for λ and α in Eq. 14.27, in terms of the absolute latitude (abLat), were as shown in Eq. 14.34 and 14.35. It is clear from these

$$\lambda(\text{abLat}) = 3.75 - 0.0144\ (\text{abLat}) \tag{14.34}$$

$$\alpha(\text{abLat}) = 2.94 \times 10^{-6} \times e^{+0.0142(\text{abLat})} \tag{14.35}$$

expressions that λ does decrease with increasing absolute latitude, as was suggested in the quotation above from our 1986 *International Journal of Remote Sensing* paper. And likewise, α is seen to increase with increasing absolute latitude, which is consistent with our 'initial hypothesis' that α decreases with increasing surface sea water temperature.

In this same 2015 conference paper, a statistical analysis was carried out using no less than 14 whitecap data sets, that all included W_B, U values, and for each of which we had data on the surface sea water temperatures. These data sets included the eight mentioned above, plus the sets from the TYPHOON75, TYPHOON77, and MONSOON77 campaigns, and sets from a 1979–1980 cruise of the R/V V. Bugaev in the North Atlantic Ocean (BUGAEV), from a 1981–1982 cruise of the R/V Professor Zubov in the Southern Ocean (ZUBOV), and from a 1983 cruise of the R/V Priliv in the Pacific Ocean (PRILIV).[88] Each of the individual data points in these 14 data sets was assigned to one of two composite data sets, one comprised of all such data points for which the surface sea water temperature was less than 15 °C, the cool water set, and a second made up of all such points for which the water temperature was greater than 15 °C, the warm water set. As can be seen from Fig. 14.24, the linear fit to W_B vs Ln U for the cool water data set is less steep than the line representing the linear fit to ln W_B vs Ln U for the warm water data set. The cool water line corresponds to a λ of 2.89 while the λ for the warm water data set is 3.53. The slopes of these two lines are significantly different, with a P of 0.01625. Note that for wind speeds less than about 4.5 m/s the warm water W_B values tend to be less than the cool water W_B values for the same wind speed, but at wind speeds of 7.5 m/s and higher the warm water W_B values tend to be significantly higher than the cool water values at the same wind speed.

14.19 Some Closing Thoughts

At this juncture, we have discussed our early efforts aimed at determining the dependence of whitecap coverage not only on the 10 m elevation wind speed, U, but also on the stability of the lower marine atmospheric boundary layer, as signaled

[88]We are very grateful to our colleague Roman S. Bortkovskii of the Voeikov Main Geophysical Observatory, St. Petersburg, Russia, for providing us with tabulations of the whitecap data from the latter six field campaigns.

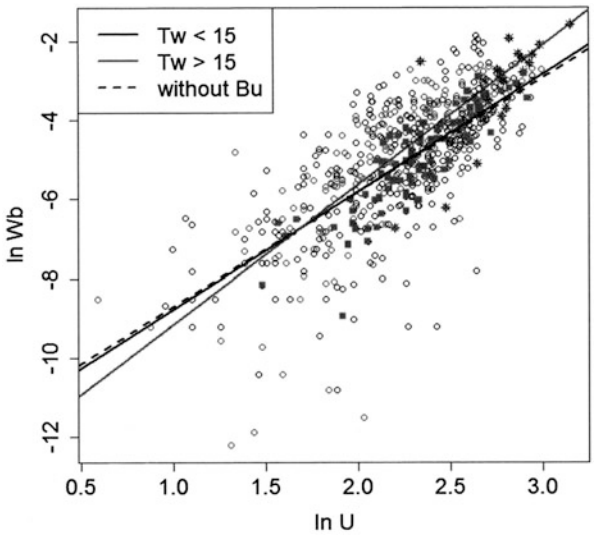

Fig. 14.24 Ln W_B vs ln U. $W_B(U)$ power-law expression for all data where sea surface temperature greater than 15 °C represented by steeper, solid grey, line, and for all data where SST less than 15 °C represented by shallower, solid black, line. Dashed black line was obtained by omitting the BUGAEV data from the cooler water data set. Warmer water data points shown as paler open circles, cooler water data points shown as darker open circles. Data points shown as solid circles come from recent Southern Ocean experiment and were derived from high resolution digital imagery. See text for description of 14 whitecap data sets used in preparing this figure. (Uncopyrighted figure from abstract of Monahan et al. 2015)

by ΔT, and, in an admittedly convoluted fashion, on wind duration (as we inferred from the apparent U-dependence on sea surface water temperature, T_W, which we took as a surrogate for latitude). We did not discuss our initial attempts, using visual estimates of the fraction of waves with whitecaps, the average width of these whitecaps, and other quantities estimated by the practiced observers who served on the Alte Weser Lightstation in the German Bight off the mouth of the Weser river.[89] Suffice it to say that we concluded that the W(U) expression we obtained for the case of extreme limited fetch was quite different for the expressions we derived for longer fetches (see Monahan and Monahan 1984, 1986). (For a recent discussion of the influence of fetch on whitecapping see Callaghan et al. 2008).

Attempts at parameterizing whitecap coverage have advanced apace. Stramska and Petelski (2003) provided several such parameterizations, and Anguelova and Webster (2006), in a paper directed at application of satellite remote sensing in the study of whitecaps, tabulated some 30 such parameterizations. More recently we had

[89]We wish to express our gratitude to our colleague Dr. Hans Gienapp, then at the Deutsches Hydrographisches Institut, for providing us with copies of the Alte Weser Lightstation Observers' Logs which contained some 1500 entries detailing their whitecap observations, and recording the associated wind speeds and directions from which we were able to determine fetch.

occasion to compile a list of such parameterizations (Monahan and O'Muircheartaigh 2012), from published articles and from the gray literature, and we enumerated no less than 262 such equations. These expressions ran the gamut from Munk's (1947) simple step function to a paper by Yuan et al. (2009) where they parameterized whitecap coverage in terms of more than 10 independent variables and fitted coefficients. (See the Appendix for a list of those papers, not cited elsewhere in this chapter, where some of these 262 equations can be found.) Additional recent work on parameterizing oceanic whitecap coverage has been carried out by Goddijn-Murphy et al. (2011).

It is perhaps appropriate here to remind the reader what we have not undertaken to do in this review. There is a rich literature within the field of theoretical fluid mechanics dealing with oceanic waves. We have not attempted to discuss the field of surface gravity waves here, not even to the extent of discussing those papers, such as those by Melville and co-workers (see, e.g., Melville 1982; Melville and Matusov 2002), that specifically deal with wave breaking, the proximate cause of whitecap formation. We will only note here that papers, such as that by Longuet-Higgins and Turner (1974), that relate specifically to whitecap formation, do exist in this literature. Further, we have focused in this review on macroscopic optical measurements of whitecaps, features of the immediate sea surface, i.e. features of the interface between "wind and waves". Thus we should stress that there is an extensive literature, beyond the few papers dealing with microwave remote sensing which we have cited, on the satellite remote sensing and measurement of oceanic whitecap coverage. We wish to acknowledge again the great potential of such remote sensing techniques for providing global, routine, measurements of whitecap coverage, and will mention in passing our own modest contributions to the microwave measurement of whitecap coverage (Asher et al. 1995, 1998; Wang et al. 1995), made subsequent to the decades covered in this review.

While we have mentioned sub-surface bubble plumes, and the sizes of the bubbles that comprise such plumes, we have not undertaken herein to provide a comprehensive review of the extensive literature on bubbles and bubble plumes. Needless to say, many workers were studying these specific topics, beginning in the several decades that have been our focus, and in the years since. Thorpe et al. (1992) extended Thorpe's early numerical modeling of the evolution of bubble spectra in the ocean. Some of these workers, such as Medwin (1977), Farmer and co-workers (see, e.g., Farmer and Lemon 1984; Farmer and Vagle 1988; Farmer and Li 1995) and Thorpe (1982, 1986), used acoustic techniques to measure bubbles and bubble plumes in the field. Others, such as Prosperetti and Lu (1984), Prosperetti et al. (1993) and Leighton (1994), focused on the physical mechanisms whereby bubbles, and bubble aggregates, produced or modified sound in the ocean. Carey et al. (1993) used a video "microscope" system to characterize the fresh and salt water bubble spectra that resulted from "breaking waves" produced by a tipping bucket and then hydrophones to detect the spectrum of the transient sound produced in these "breaking wave" events. A group that has used digital image recording and acoustic measurements to good effect in their investigations of breaking waves and bubble production is that of Deane and Stokes (1999, 2002, 2010).

The foregoing should give the reader some indication of the ever broadening scope of the work on whitecaps and related topics that has been carried out in the past several decades, and continues apace today. We are confident that whitecap research, in the hands of a new generation of scientists and engineers, has a bright and productive future.

References

Aliverti, G., & Lovera, G. (1939). I fenomeni meteorologica sull oceano e il campo el ettrico terrestre. *Atti Reale Accademica, Scienze di Torino, 74*, 573–590.

Andreas, E. L., Edson, J. B., Monahan, E. C., Rouault, M. P., & Smith, S. D. (1995). The spray contribution to net evaporation from the sea: A review of recent progress. *Boundary-Layer Meteorology, 72*, 3–52. https://doi.org/10.1007/BF00712389.

Anguelova, M. D., & Webster, F. (2006). Whitecap coverage from satellite measurements: A first step toward modeling the variability of oceanic whitecaps. *Journal of Geophysical Research, 111*, CO3017. https://doi.org/10.1029/2005JC003158.

Asher, W. E., Smith, P. M., Monahan, E. C., & Wang, Q. (1995). Estimation of air-sea gas transfer velocities from apparent microwave brightness temperature. In *Proceedings of the third thematic conference: Remote sensing of marine and coastal environments* (Vol. 1, pp. 104–115). Ann Arbor: Environmental Research Institute of Michigan.

Asher, W. E., Wang, Q., Monahan, E. C., & Smith, P. M. (1998). Estimation of air-sea gas transfer velocities from apparent microwave brightness temperature. *Marine Technology Society Journal, 32*(2), 32–40.

Augstein, E., Hempel, G., & Thiede, J. (1984). Farbericht (Cruise Report) der"Polarstern" Reise "Arltis I", 1983, *Berichte zur Polarforschung, 17/84*. Alfred-Wegener-Institut für Polarforschung, 78 pp.

Blanchard, D. C. (1963). The electrification of the atmosphere by particles from bubbles in the sea. *Progress in Oceanography, 1*, 71–202. https://doi.org/10.1016/0079-6611(63)90004-1.

Blanchard, D. C. (1967). *From raindrops to volcanoes*. Doubleday, 180pp. (Now available from Dover (paperback, 2004; NOOK Book, 2013).)

Blanchard, D. C. (1970). Wilson Bentley, the snowflake man. *Weatherwise, 23*, 260–269. https://doi.org/10.1080/00431672.1970.9932907.

Blanchard, D. C. (1971). Whitecaps at sea. *Journal of the Atmospheric Sciences, 28*, 645. https://doi.org/10.1175/1520-0469(1971)028<0645:WAS>2.0.CO;2.

Blanchard, D. C. (1986). The life and science of Alfred H. Woodcock. In E. C. Monahan & G. MacNiocaill (Eds.), *Oceanic whitecaps and their role in air-sea exchange processes* (pp. 1–10). Springer International Publishing AG. https://doi.org/10.1007/978-94-009-4668-2_1.

Bondur, V. G., & Sharkov, E. A. (1982). The statistical characteristics of foam formations on a wavy sea surface (in Russian). *Oceanologiya, 22*, 372–379.

Bortkovskii, R. S. (1983). *Teplo-i vlagoobmen atmosferei i okeana pri shtorme (in Russian)*. Petrograd: Gidrometeoizdat.

Bortkovskii, R. S. (1987). *Air-sea exchange of heat and moisture during storms*. D. Reidel (now Springer), 194 pp, https://doi.org/10.1007/978-94-017-0687-2.

Bortkovskii, R. S., & Kuznetsov, M. A. (1982). Some results of a study of the sea state. *Taifun-75, 1*, 90–105.

Bruce, R. R. (1994). *Seeing the unseen: Dr. Harold E. Edgerton and the Wonders of Strobe Alley*. MIT Press, 108pp.

Callaghan, A. H. (2013). An improved whitecap timescale for sea spray aerosol production flux modeling using the discrete whitecap method. *Journal of Geophysical Research, 118*, 1–14. https://doi.org/10.1002/jgrd.50768.

Callaghan, A. H., & White, M. (2009). Automated processing of sea surface images for the determination of whitecap coverage. *Journal of Atmospheric and Oceanic Technology, 26*, 383–394. https://doi.org/10.1175/2008JTECHO634.1.

Callaghan, A. H., Deane, G. B., & Stokes, M. D. (2008). Observed physical and environmental causes of scatter in whitecap coverage values in a fetch limited coastal zone. *Journal of Geophysical Research, 113*, C05022. https://doi.org/10.1029/2007JC004453.

Callaghan, A. H., Deane, G. B., Stokes, M. D., & Ward, B. (2012). Observed variation in the decay time of oceanic whitecap foam. *Journal of Geophysical Research, 117*, CO9015. https://doi.org/10.1029/2012JC008147.

Cardone, V. J. (1969). *Specification of the wind distribution in the marine boundary layer for wave forecasting* (Technical Report #GSL-69-1). New York University, 131pp.

Carey, W. M., Fitzgerald, J. W., Monahan, E. C., & Wang, Q. (1993). Measurement of the sound produced by a tipping trough with fresh and salt water. *Journal of the Acoustical Society of America, 93*, 3178–3192. https://doi.org/10.1121/1.405702.

Chaen, M. (1973). Studies on the production of sea-salt particles on the sea surface. *Memoirs of the Faculty of Fisheries, Kagoshima University, 22*, 49–107.

Cousteau, J. (1954). *The silent world*. National Geographic, 192pp.

Cousteau, J. -Y. (1985). *Jacque Cousteau: The ocean world*. H.N. Abrams Publication, 446pp.

Crawford, A. B. (1966). A replacement at last for "The Old Oaken Bucket". *Geo-Marine Technology, 2*, 25–27.

Deane, G. B., & Stokes, M. D. (1999). Air entrainment and bubble size distributions in the surf zone. *Journal of Physical Oceanography, 29*, 1393–1403. https://doi.org/10.1175/1520-0485(1999)029<1393:AEPABS>2.0.CO;2.

Deane, G. B., & Stokes, M. D. (2002). Scale dependence of bubble creation mechanisms in breaking waves. *Nature, 418*, 839–844. https://doi.org/10.1038/nature00967.

Deane, G. B., & Stokes, M. D. (2010). Model calculations of the underwater noise of breaking waves and comparison with experiment. *Journal of the Acoustical Society of America, 127*, 3394–3409. https://doi.org/10.1121/1.3419774.

Donelan, M. A., & Cardone, V. J. (2003). Willard J. Pierson (1922–2003), obituary. *EOS, Transactions of the American Geophysical Union, 84*(42), 443.

Doyle, D. M. (1984a). *Marine aerosol research in the Gulf of Alaska and on the Irish West Coast (Inishmore)* (M.Sc. Thesis). University College, Galway, 140 pp.

Doyle, D. M. (1984b). *Marine aerosol research in the Gulf of Alaska and on the Irish west coast (Inishmore)* (Whitecaps and the Marine Atmosphere, Report No. 6). University College, Galway, 140 pp.

Edson, J. B., Jampana, V., Weller, R. A., Bigorre, S. P., Plueddemann, A. J., Fairall, C. W., Miller, S. D., Mahrt, L., Vickers, D., & Hersbach, H. (2013). On the exchange of momentum over the open ocean. *Journal of Physical Oceanography, 43*, 1589–1610. https://doi.org/10.1175/JPO-D-12-0173.1.

Farmer, D. M., & Lemon, D. D. (1984). The influence of bubbles on ambient noise in the ocean at high wind speeds. *Journal of Physical Oceanography, 14*, 1762–1778. https://doi.org/10.1175/1520-0485(1984)014<1762:TIOBOA>2.0.CO;2.

Farmer, D., & Li, M. (1995). Patterns of bubble clouds organized by Langmuir circulation. *Journal of Physical Oceanography, 25*, 1426–1440. https://doi.org/10.1175/1520-0485(1995)025<1426:POBCOB>2.0.CO;2.

Farmer, D. M., & Vagle, S. (1988). On the determination of breaking surface wave distributions using ambient sound. *Journal of Geophysical Research, 93*, 3591–3600. https://doi.org/10.1029/JC093iC04p03591.

Gathman, S., & Trent, E. M. (1968). Space charge over the open ocean. *Journal of the Atmospheric Sciences, 25*, 1075–1079. https://doi.org/10.1175/1520-0469(1968)025<1075:SCOTOO>2.0.CO;2.

Gloersen, P., & Barath, F. T. (1977). A scanning multichannel microwave radiometer for Nimbus-G and SeaSat-A. *IEEE Journal of Oceanic Engineering, 2*, 172–178. https://doi.org/10.1109/JOE.1977.1145331.

Goddijn-Murphy, L., Woolf, D. K., & Callaghan, A. H. (2011). Parameterizations and algorithms for oceanic whitecap coverage. *Journal of Physical Oceanography, 41*, 742–756. https://doi.org/10.1175/2010JPO4533.1.

Gordon, H. R., & Jacobs, M. M. (1977). Albedo of the ocean-atmosphere system: Influence of sea foam. *Applied Optics, 16*, 2257–2260. https://doi.org/10.1364/AO.16.002257.

Grythe, H., Ström, J., Krejci, R., Quinn, P., & Stohl, A. (2014). A review of sea-spray aerosol source functions using a large global set of sea salt aerosol concentration measurements. *Atmospheric Chemistry and Physics, 14*, 1277–1297. https://doi.org/10.5194/acp-14-1277-2014.

Helfrich, L. C. (1994). Sailing ships, science, and stonework: The stuff one dream was made of. *Spritsail, A Journal of the History of Falmouth and Vicinity, 8*(2), 2–21.

Houghton, H. G., & Radford, W. H. (1938). On the measurement of drop size and liquid water content in fogs and clouds, *Papers in Physical Oceanography and Meteorology, 6*(4), 38pp, MIT/WHOI.

Houghton, J. T., Ding, Y., Griggs, D. J., Noguer, M., van der Linden, P. J., Dai, X., Maskell, K., & Johnson, C. A. (Eds.). (2001). *Climate change 2001: The scientific basis*. Published for the Intergovernmental Panel on Climate Change by Cambridge University Press.

Jähne, B., & Monahan, E. C. (Eds.). (1995). *Air-water gas transfer: Selected papers from the Third International Symposium on Air-Water Gas Transfer*. AEON Verlag and Studio, Hanau, 900 pp, plus 23 color plates.

Johnson, B. D., & Cook, R. C. (1979). Bubble populations and spectra in coastal waters: A photographic approach. *Journal of Geophysical Research, 84*, 3761–3766. https://doi.org/10.1029/JC084iC07p03761.

Jussim, E. (1987). *Stopping time: The photographs of Harold Edgerton*. H.N. Abrams publication, 167pp.

Kinsman, B. (1965). *Wind waves: Their generation and propogation on the ocean surface*. Prentice-Hall, Inc., 676pp.

Kinsman, B. (1969a). Historical notes on the original Beaufort scale. *The Marine Observer, 39*, 116–124.

Kinsman, B. (1969b). Who put the wind speeds in Admiral Beaufort's force scale? *Oceans, 2*(2), 18–25.

Koepke, P. (1986). Oceanic whitecaps and their effective reflectance. In E. C. Monahan & G. MacNiocaill (Eds.), *Oceanic whitecaps, and their role in air-sea exchange processes* (pp. 272–274). Springer International Publishing AG. https://doi.org/10.1007/978-94-009-4668-2_36.

Kolovayev, P. A. (1976). Investigation of the concentration and statistical size distribution of wind-produced bubbles in the near-surface ocean layer. *Oceanology, 15*, 659–661.

Kraus, E. B. (1972). *Atmosphere-Ocean interaction*. Oxford: Clarendon Press.

LeBlond, P. H., & Collins, M. J. (1987). The Wilson Nessie photo: A size determination based on physical principles. *Cryptozoology, 6*, 55–64.

Leighton, T. G. (1994). *The acoustic bubble*. London: Academic. https://doi.org/10.1016/B978-0-12-441920-9.X5001-9.

Lewis, A. H. (1963). *The day they shook the plum tree*. Harcourt, Brace, and World, 314pp.

Longuet-Higgins, M. S., & Turner, J. S. (1974). An 'entrained plume' model of a spilling breaker. *Journal of Fluid Mechanics, 63*, 1–20. https://doi.org/10.1017/S002211207400098X.

Medwin, H. (1977). *In situ* acoustic measurements of microbubbles at sea. *Journal of Geophysical Research, 82*, 971–976. https://doi.org/10.1029/JC082i006p00971.

Melville, W. K. (1982). The instability and breaking of deep-water waves. *Journal of Fluid Mechanics, 115*, 165–185. https://doi.org/10.1017/S0022112082000706.

Melville, W. K., & Matusov, P. (2002). Distribution of breaking waves at the ocean surface. *Nature, 417*, 58–63. https://doi.org/10.1038/417058a.

Metnieks, A. L. (1958). *The size spectrum of large and giant sea-salt nuclei under maritime conditions* (Geophysical bulletin) (Vol. 15). Dublin: Dublin Institute for Advanced Studies.

Monahan, E. C. (1961). *Search for a resonance in the elastic scattering of neutrons by C^{12}, over neutron energies between 16.5 and 19.8 MEV* (M.A. thesis). University of Texas, Austin, 56pp.

Monahan, E. C. (1966). *Sea spray and its relationship to low elevation wind speed* (Ph.D. dissertation), Department of Meteorology, Massachusetts Institute of Technology, Cambridge, 175pp.

Monahan, E. C. (1967). A study of the onset of whitecapping with increased surface wind speeds. In *Lake superior studies, report #1* (pp. 5–23). Marquette: Northern Michigan University.

Monahan, E. C. (1968a). Sea spray as a function of low elevation wind speed. *Journal of Geophysical Research, 73*, 1127–1137. https://doi.org/10.1029/JB073i004p01127.

Monahan, E. C. (1968b). Sea spray and whitecaps. *Oceanus, 14*, 21–24.

Monahan, E. C. (1968c). A study of the onset of whitecapping with increased surface wind speeds. In *Lake superior studies, report #2* (pp. 3–30). Marquette: Northern Michigan University.

Monahan, E. C. (1969). Fresh water whitecaps. *Journal of the Atmospheric Sciences, 26*, 1026–1029. https://doi.org/10.1175/1520-0469(1969)026<1026:FWW>2.0.CO;2.

Monahan, E. C. (1970). Reply. *Journal of the Atmospheric Sciences, 27*, 1220–1221. https://doi.org/10.1175/1520-0469(1970)027<1220:R>2.0.CO;2.

Monahan, E. C. (1971). Oceanic whitecaps. *Journal of Physical Oceanography, 1*, 139–144. https://doi.org/10.1175/1520-0485(1971)001<0139:OW>2.0.CO;2.

Monahan, E. C. (1978). The oceanography of Galway Bay and adjacent waters. In W. K. Downey & G. N. Uid (Eds.), *Coastal pollution assessment* (pp. 57–71). Dublin: National Board for Science and Technology.

Monahan, E. C. (1979). *The influence of whitecaps on the marine atmosphere, report No. 1*. Galway: University College. un-paginated.

Monahan, E. C. (1982a). *Sea surface aerosol generation model no. 4, prepared for the naval environmental research facility*. Department of Geological Sciences, University of Maine at Orono, 54 pp.

Monahan, E. C. (1982b). Whitecapping, a manifestation of air-sea interaction with implications for remote sensing. In F. J. Vernberg & F. P. Diemer (Eds.), *Processes in marine remote sensing* (Belle W. Baruch Library of marine science No. 12) (pp. 113–131). Columbia: University of South Carolina Press.

Monahan, E. C. (1986a). The ocean as a source of atmospheric particles. In P. Buat-Menard (Ed.), *The role of air-sea exchange in geochemical cycling* (pp. 129–163). Springer International Publishing AG, 10.1007/978-94-009-4738-2_6.

Monahan, E. C. (1986b). Whitecap observations during HEXPILOT. In W. A. Oost, K. B. Katsaros, & S. D. Smith (Eds.), *HEXOS workshop '85* (pp. 14–16). de Bilt: Koninklijk Nederlands Meteorologisch Institut.

Monahan, E. C. (1988a). Whitecap coverage as a remotely monitorable indication of the rate of bubble injection into the oceanic mixed layer. In B. R. Kerman (Ed.), *Sea surface sound* (pp. 85–96). Springer International Publishing AG. https://doi.org/10.1007/978-94-009-3017-9_7.

Monahan, E. C. (1988b). Near-surface bubble concentration and oceanic whitecap coverage. In *Preprint volume, 7th conference on ocean-atmosphere interaction, 31 January-5 February 1988, Anaheim, CA* (pp. 178–181). Boston: American Meteorological Society.

Monahan, E. C. (1989). From the laboratory tank to the global ocean. In E. C. Monahan & M. A. Van Patten (Eds.), *Climate and health implications of bubble-mediated sea-air exchange* (pp. 43–63). Groton: Connecticut Sea Grant College Program.

Monahan, E. C. (1993). Occurrence and evolution of acoustically relevant sub-surface bubble plumes and their associated, remotely monitorable, surface whitecaps. In B. R. Kerman (Ed.), *Natural physical sources of underwater sound* (pp. 503–517). Springer International Publishing AG. https://doi.org/10.1007/978-94-011-1626-8_37.

Monahan, E. C. (2001). Whitecaps and foam. In J. Steele, S. Thorpe, & K. Turekian (Eds.), *Encyclopedia of ocean sciences* (pp. 3213–3219). London: Academic Press.

Monahan, E. C., & Bowyer, P. A. (1984). Arctic whitecapping: Preliminary results. In *MIZEX bulletin, IV: Initial results and analysis from MIZEX 83* (pp. 53–56). Hanover: U.S. Army Cold Regions Research and Engineering Laboratory.

Monahan, E. C., & Lu, M. (1990). Acoustically relevant bubble assemblages and their dependence on meteorological parameters. *IEEE Journal of Oceanic Engineering, 15*, 340–349. https://doi.org/10.1109/48.103530.

Monahan, E. C., & MacNiocaill, G. (Eds.). (1986). *Oceanic whitecaps, and their role in air-sea exchange processes*. Springer International Publishing AG, 294 pp.

Monahan, E. C., & Monahan, E. A. (1973). Trends in drogue design. *Limnology and Oceanography, 18*, 981–985. https://doi.org/10.4319/lo.1973.18.6.0981.

Monahan, E. C., & Monahan, C. F. (1984). In E. C. Monahan, M. C. Spillane, P. A. Bowyer, M. R. Higgins, & P. J. Stabeno (Eds.), *The influence of fetch on whitecap coverage as deduced from the Alte Weser Light-station Observers' Log, Appendix A* (Whitecaps and the marine atmosphere, report No. 7) (pp. 61–73). Galway: University College.

Monahan, E. C., & Monahan, C. F. (1986). The influence of fetch on whitecap coverage as deduced from the Alte Weser Light-station Observers' Log. In E. C. Monahan & G. MacNiocaill (Eds.), *Oceanic whitecaps, and their role in air-sea exchange processes* (pp. 275–277). Springer International Publishing AG. https://doi.org/10.1007/978-94-009-4668-2_38.

Monahan, E. C., & O'Muircheartaigh, I. G. (1980a). Optimal power-law description of oceanic whitecap coverage dependence on wind speed. *Journal of Physical Oceanography, 10*, 2094–2099. https://doi.org/10.1175/1520-0485(1980)010<2094:OPLDOO>2.0.CO;2.

Monahan, E. C., & O'Muircheartaigh, I. G. (1980b). Status of JASIN whitecap analysis 21 months after data acquisition. *JASIN News, No. 20, I.O.S., Wormley, 5–7*, 17–18.

Monahan, E. C., & O'Muircheartaigh, I. G. (1981). Improved statement of the relationship between surface wind speed and oceanic whitecap coverage as required for the interpretation of satellite data. In J. F. R. Gower (Ed.), *Oceanography from space* (pp. 751–755). New York: Plenum.

Monahan, E. C., & O'Muircheartaigh, I. G. (1982a). Reply. *Journal of Physical Oceanography, 12*, 751–752.

Monahan, E. C., & O'Muircheartaigh, I. G. (1982b). The JASIN whitecap coverage observations and the resulting inferred wind dependence of the drag coefficient. *JASIN News No. 25, I.O.S. Wormley, 9*, 3–5.

Monahan, E. C., & O'Muircheartaigh, I. G. (1986). Whitecaps and the passive remote sensing of the ocean surface. *International Journal of Remote Sensing, 7*, 627–642. https://doi.org/10.1080/01431168608954716.

Monahan, E. C., & O'Muircheartaigh, I. G. (2012). *Oceanic whitecaps and the 10m-elevation wind speed: Toward improved power-law descriptions for use in climate modeling*. In Paper 6.1, 18th Conference on Air-Sea Interaction, American Meteorological Society, e-posted to AMS confex website, 3pp.

Monahan, E. C., & Pybus, M. J. (1978). Colour, ultraviolet absorbance and salinity of the surface waters off the west coast of Ireland. *Nature, 274*, 782–784. https://doi.org/10.1038/274782a0.

Monahan, E. C., & Spillane, M. C. (1983). The role of oceanic whitecaps in the exchange of mass across the air-sea interface. In *Paper 20/23, IUGG Inter-Disciplinary Symposia, Programme and Abstracts* (Vol. 2, p. 884). Hamburg: International Union of Geodesy and Geophysics, XVII General Assembly.

Monahan, E. C., & Spillane, M. C. (1984). The role of oceanic whitecaps in air-sea gas exchange. In W. Brutsaert & G. J. Jirka (Eds.), *Gas transfer at water surfaces* (pp. 495–503). Springer International Publishing AG. https://doi.org/10.1007/978-94-017-1660-4_45.

Monahan, E. C., & Wang, Q. (1996). The Beaufort wind force scale as manifest by the appearance of the sea surface, series of video clips. In I. R. Young & G. J. Holland (Eds.), *Atlas of the oceans: Wind and wave climate*. New York: Pergamon, Elsevier Science. 241pp. plus CD-ROM.

Monahan, E. C., & Wilson, M. B. (1990a). *Characterization of oceanic whitecap coverage observed during CST IV cruise, UConn whitecap report no. 8, to APL*. Baltimore: Johns Hopkins University. 117 pp.

Monahan, E. C., & Wilson, M. B. (1990b). *Foam (whitecap) coverage recorded on Georges Bank from R/V Cape Hatteras during Battelle-LDGO-UConn study of air-sea gas exchange* (UConn Whitecap Report No. 9, to Battelle PML), 154 pp.

Monahan, E. C., & Woolf, D. K. (1986). *Oceanic whitecaps, their contribution to air-sea exchange, and their influence on the MABL, whitecap report no. 1*. Groton: Marine Sciences Institute, University of Connecticut. 130 pp.

Monahan, E. C., & Woolf, D. K. (1989). Comments on "Variations of whitecap coverage with wind stress and water temperature". *Journal of Physical Oceanography, 19*, 706–709.

Monahan, E. C., & Zietlow, C. R. (1968). *Lake superior studies, report no. 2*. Marquette: Northern Michigan University. 74pp.

Monahan, E. C., & Zietlow, C. R. (1969). Laboratory comparisons of fresh-water and salt-water whitecaps. *Journal of Geophysical Research, 74*, 6961–6966. https://doi.org/10.1029/JC074i028p06961.

Monahan, E. C., Higgins, B. J., & Kaye, G. T. (1975). A comparison of vertical drift-envelopes to conventional drift-bottles. *Limnology and Oceanography, 20*, 141–147. https://doi.org/10.4319/lo.1975.20.1.0141.

Monahan, E. C., O'Regan, B. D., & Davidson, K. L. (1979). Marine aerosol production from whitecaps. In *Interdisciplinary symposium, abstracts and timetable* (p. 423). Canberra: International Union of Geodesy and Geophysics, XVII General Assembly.

Monahan, E. C., O'Regan, B. D., & Doyle, D. M. (1980). *The influence of whitecaps on the marine amosphere, report No. 2*. Galway: University College. 123 pp.

Monahan, E. C., O'Muircheartaigh, I. G., & FitzGerald, M. P. (1981a). Oceanic whitecap coverage as a function of wind speed and air-water temperature difference; a physical basis for wind retrieval algorithm development. In *A collection of extended abstracts presented at the symposium on the radiation transfer in the oceans and remote sensing of ocean properties, IAMAP 3rd scientific assembly, Hamburg* (pp. 33–34). Boulder, CO, publisher: IAMAP Radiation Commission.

Monahan, E. C., Bowyer, P. A., Doyle, D. M., FitzGerald, M. P., O'Muircheartaigh, I. G., Spillane, M. C., & Taper, J. J. (1981b). *Whitecaps and the marine atmosphere, report No. 3*. Galway: University College. un-paginated.

Monahan, E. C., O'Muircheartaiagh, I. G., & FitzGerald, M. P. (1981c). Determination of surface wind speed from remotely measured whitecap coverage, a feasibility assessment. In *Proceedings of an EARSeL-ESA Symposium, Applications of Remote Sensing Data on the Continental Shelf* (pp. 103–109). Voss: European Space Agency SP-167.

Monahan, E. C., O'Muircheartaiagh, I. G., & FitzGerald, M. P. (1981d). Whitecaps, telltales of waves or winds? *JASIN News No. 24, I.O.S., Wormley, 16*, 6–8.

Monahan, E. C., Davidson, K. L., & Spiel, D. E. (1982a). Whitecap aerosol productivity deduced from simulation tank measurements. *Journal of Geophysical Research, 87*, 8898–8904. https://doi.org/10.1029/JC087iC11p08898.

Monahan, E. C., Spillane, M. C., Bowyer, P. A., Doyle, D. M., & Taper, J. J. (1982b). *Whitecaps and the marine atmosphere, report no. 4*. Galway: University College. 75 pp.

Monahan, E. C., Spiel, D. E., & Davidson, K. L. (1983a). Model of marine aerosol generation via whitecaps and wave disruption, Preprint Volume. In *Ninth Conference on Aerospace and Aeronautical Meteorology* (pp. 147–158). Omaha: American Meteorological Society.

Monahan, E. C., Spillane, M. C., Bowyer, P. A., Doyle, D. M., & Stabeno, P. J. (1983b). *Whitecaps and the marine atmosphere, report no. 5*. Galway: University College. 93 pp.

Monahan, E. C., Fairall, C. W., Davidson, K. L., & Jones Boyle, P. (1983c). Observed inter-relationships between 10m winds, ocean whitecaps, and marine aerosols. *Quarterly Journal of the Royal Meteorological Society, 109*, 379–392. https://doi.org/10.1002/qj.49710946010.

Monahan, E. C., Spillane, M. C., Bowyer, P. A., Higgins, M. R., & Stabeno, P. J. (1984). *Whitecaps and the marine atmosphere, report no. 7*. Galway: University College. 103 pp.

Monahan, E. C., Bowyer, P. A., Doyle, D. M., Higgins, M. R., & Woolf, D. K. (1985). *Whitecaps and the marine atmosphere, report No. 8*. Galway: University College. 124 pp.

Monahan, E. C., Spiel, D. E., & Davidson, K. L. (1986a). A model of marine aerosol generation via whitecaps and wave disruption. In E. C. Monahan & G. MacNiocaill (Eds.), *Oceanic whitecaps, and their role in air-sea exchange processes* (pp. 167–174). Springer International Publishing AG. https://doi.org/10.1007/978-94-009-4668-2_16.

Monahan, E. C., Doyle, D. M., Higgins, M. R., & Woolf, D. K. (1986b). *Whitecaps and the marine atmosphere, report No. 9, Appendix A* (pp. 97–108 in Monahan and Woolf (1986)).

Monahan, E. C., Wilson, M. B., & Woolf, D. K. (1988). HEXMAX whitecap climatology: Foam crest coverage in the North Sea, 16 October-23 November 1986. In W. A. Oost, S. D. Smith, & K. B. Katsaros (Eds.), *Proceedings of the NATO advanced workshop, humidity over the sea experiment (HEXMAX), analysis and interpretation, University of Washington Technical Report AK-40* (pp. 105–115). Washington, DC: University of Washington.

Monahan, E. C., Wang, Q., Wang, W., & Wilson, M. B. (1991). The role of oceanic whitecaps and the associated sub-surface bubble plumes in various air-sea interface phenomena. In P. A. Beetham (Ed.), *UConn whitecap report. No. 11, to the Office of Naval Research*. 123 pp.

Monahan, E. C., Hooker, G., & Zappa, C. J. (2015). *The latitudinal variation in the wind-speed parameterization of oceanic whitecap coverage: Implications for global modeling of air-sea gas flux and sea surface aerosol generation*. In Paper 14.5, 19th Conference on Air-Sea Interaction, American Meteorological Society, e-posted to AMS confex website, 7pp.

Munk, W. H. (1947). A critical wind speed for air-sea boundary processes. *Journal of Marine Research, 6*, 203–218.

Munk, W. H. (1955). Wind stress over water: An hypothesis. *Quarterly Journal of the Royal Meteorological Society, 81*, 320–332. https://doi.org/10.1002/qj.49708134903.

Murphy, H. (1968). *Percentage foam vs wind velocity, internal report*. Coral Gables: University of Miami. 27 pp.

Murphy, E. M. (1978). *Circulation features and north-south water transports in the Rockall trough region of the north-East Atlantic Ocean* (M.Sc. thesis). University College, Galway, 134 pp.

Nordberg, W., Conaway, J., Ross, D. R., & Wilheit, T. (1971). Measurements of microwave emission from a foam-covered, wind-driven sea. *Journal of the Atmospheric Sciences, 28*, 429–435. https://doi.org/10.1175/1520-0469(1971)028<0429:MOMEFA>2.0.CO;2.

O'Muircheartaigh, I. G., & Gaver, D. P. (1985). *Estimation of sea-surface Windspeed from whitecap cover: Statistical approaches compared empirically and by simulation, report NPS55-85-021*. Monterey: Naval Postgraduate School. 63pp.

O'Muircheartaigh, I. G., & Gaver, D. P. (1986). Estimation of sea-surface wind speed from whitecap cover: Statistical approaches compared empirically and by simulation. *International Journal of Remote Sensing, 7*, 985–999. https://doi.org/10.1080/01431168608948904.

O'Muricheartaigh, I. G., & Monahan, E. C. (1983a). Aspects of oceanic whitecap coverage dependnece on wind speed: Heteroscedasticity in the data, and the estimation of the Beaufort velocity, Preprint Volume. In Second International Meeting on Statistical Climatology, 26–-30 September 1983, Lisboa, Portugal, pp. 2.7.1–2.7.4.

O'Muricheartaigh, I. G., & Monahan, E. C. (1983b). Use of the Box-Cox transformation in determining the functional form of the dependence of oceanic whitecap coverage on several environmental factors. In Paper 3.5, preprint volume, eighth conference on probability and statistics in Atmospheric Sciences, pp. 55–58.

O'Muircheartaigh, I. G., Monahan, E. C., & Gaver, D. P. (1987). *Whitecaps: An overview of remote sensing and statistical aspects* (Remote sensing yearbook 1987) (pp. 101–116). London: Taylor and Francis. https://doi.org/10.1080/10106048709354096.

Oost, W. A., Katsaros, K. B., & Smith, S. D. (Eds.). (1984). *Hexos pilot experiment, Meetpost Noordwijk, November 1984: Field project report*. Dartmouth: Bedford Institute of Oceanography. 49 pp.

Paget, A. C., Callaghan, A. H., Monahan, E. C., & Bourassa, M. (2019). MIZEX whitecap film revisited. *Journal of Geophysical Research* (MS in preparation).

Pardini, A. L. (1999). *The legendary Norden bombsight*. Atglen: Schiffer Publishing. 352 pp.

Patterson, E. M., Kiang, C. S., Delany, A. C., Wartburg, A. F., Leslie, A. C. D., & Huebert, B. J. (1980). Global measurements of aerosols in remote continental and marine regions: Concentrations, size distributions and optical properties. *Journal of Geophysical Research, 85*, 7361–7376. https://doi.org/10.1029/JC085iC12p07361.

Phillips, O. M. (1991). To Blair Kinsman. In R. C. Beal (Ed.), *Directional ocean wave spectra: Measuring, modeling, predicting, and applying* (p. ix). New York: The Johns Hopkins University Press.

Prosperetti, A., & Lu, N. Q. (1984). Cavitation and bubble bursting as sources of oceanic ambient noise. *Journal of the Acoustical Society of America, 84*, 1037–1041. https://doi.org/10.1121/1.396739.

Prosperetti, A., Lu, N. Q., & Kim, H. S. (1993). Active and passive acoustic behavior of bubble clouds at the ocean's surface. *Journal of the Acoustical Society of America, 93*, 3117–3127. https://doi.org/10.1121/1.405696.

Randolph, K., Dierssen, H. M., Twardowski, M., Cifuentes-Lorenzen, A., & Zappa, C. J. (2014). Optical measurements of small deeply penetrating bubble populations generated by breaking waves in the Southern Ocean. *Journal of Geophysical Research, 119*, 757–776. https://doi.org/10.1002/2013JC009227.

Roddy, A. F., & O'Conner, T. C. (Eds.). (1981). *Atmospheric aerosols and nuclei, proceedings of the ninth international conference on atmospheric aerosols, condensation and ice nuclei*. Galway: Galway University Press. 532 pp.

Roll, H. U. (1965). *Physics of the marine atmosphere*. New York: Academic. 426 pp.

Rooth, C., & Williams, G. (1970). *Microwave radiometry of the ocean, quarterly report*. Coral Gables: University of Miami. 69 pp.

Ross, D. B., & Cardone, V. J. (1970). *Laser observations of wave growth and foam density for fetch-limited 25/sec winds* (NASA Report MCS-03742) (pp. 85.1–85.20).

Ross, D. B., & Cardone, V. (1974). Observations of oceanic whitecaps and their relation to remote measurements of surface wind speed. *Journal of Geophysical Research, 79*, 444–452. https://doi.org/10.1029/JC079i003p00444.

Ross, D. B., Cardone, V. J., & Conaway, J. W., Jr. (1970). Laser and microwave observations of sea-surface condition for fetch-limited 17- to 25-m/s winds. *IEEE Transactions on Geoscience Electronics, GE-8*, 326–336. https://doi.org/10.1109/TGE.1970.271431.

Scanlon, B., & Ward, B. (2013). Ocean wave breaking coverage separation techniques for active and maturing whitecaps. *Methods in Oceanography, 8*, 1–12. https://doi.org/10.1016/j.mio.2014.03.001.

Scanlon, B., & Ward, B. (2016). The influence of environmental parameters on active and maturing oceanic whitecaps. *Journal of Geophysical Research, 121*, 3325–3326. https://doi.org/10.1002/2015JC011230.

Schrock, R. R. (1977). *Geology at MIT 1865–1965: A history of the first hundred years of geology at Massachusetts Institute of Technology* (Vol. 1). Cambridge: The Faculty and Supporting Staff, MIT Press. 1032pp.

Schrock, R. R. (1982). *Geology at MIT 1865–1965: A history of the first hundred years of geology at Massachusetts Institute of Technology* (Vol. 2). Cambridge: Department Operations and Projects, MIT Press. 762pp.

Spillane, M. C. (1981). *G.K.S.S./U.C.G. co-operative study on the feasibility of automated analysis of whitecap photographs*, Chapter 3 in, Monahan, Bowyer, Doyle, FitzGerald, O'Muircheartaigh, Spillane, and Taper, 1981.

Spillane, M. C., & Doyle, D. M. (1983). Final results from STREX and JASIN photo-analyses with preliminary search for whitecap algorithm. In E. C. Monahan, P. A. Bowyer, M. C. Spillane, D. M. Doyle, & P. J. Stabeno (Eds.), *Whitecaps and the marine atmosphere, report no. 5* (pp. 8–27). Galway: University College Galway.

Stabeno, P. J., & Monahan, E. C. (1986). The influence of whitecaps on the albedo of the sea surface. In E. C. Monahan & G. MacNiocaill (Eds.), *Oceanic whitecaps, and their role in air-sea exchange processes* (pp. 261–266). Springer International Publishing AG. https://doi.org/10.1007/978-94-009-4668-2_24.

Stogryn, A. (1972). *A study of radiometric emission from a rough sea surface, NASA Contract Report CR-2088*, 278 pp.

Stramska, M., & Petelski, T. (2003). Observations of oceanic whitecaps in the north polar waters of the Atlantic. *Journal of Geophysical Research, 108*, 31.1–31.10. https://doi.org/10.1029/2002JC001321.

Tang, C. C. H. (1974). The effect of droplets in the air-sea transition zone on the sea brightness temperature. *Journal of Physical Oceanography, 4*, 579–593. https://doi.org/10.1175/1520-0485(1974)004<0579:TEODIT>2.0.CO;2.

Thorpe, S. A. (1982). On the clouds of bubbles formed by breaking wind-waves in deep water and their role in air-sea gas transfer. *Philosophical Transactions of the Royal Society, London, Series A, 304*, 155–210. https://doi.org/10.1098/rsta.1982.0011.

Thorpe, S. A. (1986). Bubble clouds: A review of their detection by sonar, of related models, and of how K_v may be determined. In E. C. Monahan & G. MacNiocaill (Eds.), *Oceanic whitecaps, and their role in air-sea exchange processes* (pp. 57–68). Springer International Publishing AG. https://doi.org/10.1007/978-94-009-4668-2_6.

Thorpe, S. A., Bowyer, P., & Woolf, D. K. (1992). Some factors affecting the size distributions of oceanic bubbles. *Journal of Physical Oceanogrphy, 22*, 382–389. https://doi.org/10.1175/1520-0485(1992)022<0382:SFATSD>2.0.CO;2.

Toba, Y., & Chaen, M. (1973). Quantitative expression of the breaking of wind waves on the sea surface. *Records of Oceanographic Works in Japan, 12*, 1–11.

U.S. Department of Agriculture, Weather Bureau. (1938). *Instructions to marine meteorological observers* (6th ed.). Washington, DC: U.S. Government Printing Office. 120pp.

U.S. Navy. (1952). *Wind estimations from aerial photographs of sea conditions, weather squadron two (VJ-2)*. Naval Air Station Jacksonville, 28pp. (unpublished manual).

Wang, Q., Monahan, E. C., Asher, W. E., & Smith, P. M. (1995). Correlations of whitecap coverage and gas transfer velocity with microwave brightness temperature for plunging and spilling breaking waves. In B. Jähne & E. C. Monahan (Eds.), *Air-water gas transfer: Selected papers from the third international symposium on air-water gas transfer* (pp. 217–225). Hanau: AEON Verlag and Studio.

Warren, B. A., & Wunsch, C. (Eds.). (1981). *Evolution of physical oceanography*. Cambridge, MA: Scientific Surveys in Honor of Henry Stommel, MIT Press. 623pp.

Webster, W. J., Wilheit, T. T., Ross, D. B., & Gloersen, P. (1976). Spectral characteristics of the microwave emission from a wind-driven foam-covered sea. *Journal of Geophysical Research, 81*, 3095–3099. https://doi.org/10.1029/JC081i018p03095.

Whitelock, C. H., Bartlett, D. S., & Gurganus, E. A. (1982). Sea foam reflectance and influence on optimum wave-length for remote sensing of ocean aerosols. *Geophysical Research Letters, 9*, 719–722. https://doi.org/10.1029/GL009i006p00719.

Williams, G. F., Jr. (1970). Comments on "fresh water whitecaps". *Journal of the Atmospheric Sciences, 27*, 1220. https://doi.org/10.1175/1520-0469(1970)027<1220:COWW>2.0.CO;2.

Woodcock, A. H. (1940). Convection and soaring over the open sea. *Journal of Marine Research, 3*, 248–253.

Woodcock, A. H. (1944). A theory of surface water motion deduced from the wind-induced motion of the *Physalia*. *Journal of Marine Research, 5*, 196–205.

Woodcock, A. H. (1953). Salt nuclei in marine air as a function of altitude and wind force. *Journal of Meteorology, 10*, 362–371. https://doi.org/10.1175/1520-0469(1953)010<0366:SNIMAA>2.0.CO;2.

Wu, J. (1969). Wind stress and surface roughness at air-sea interface. *Journal of Geophysical Research, 74*, 444–455. https://doi.org/10.1029/JB074i002p00444.

Wu, J. (1975). Wind-induced drift currents. *Journal of Fluid Mechanics, 68*, 49–70. https://doi.org/10.1017/S0022112075000687.

Wu, J. (1979). Oceanic whitecaps and sea state. *Journal of Physical Oceanography, 9*, 1064–1068. https://doi.org/10.1175/1520-0485(1979)009<1064:OWASS>2.0.CO;2.

Wu, J. (1982). Comments on "Optimal power-law description of oceanic whitecap dependence on wind speed". *Journal of Physical Oceanography, 12*, 750–751. https://doi.org/10.1175/1520-0485(1982)012<0750:COPLDO>2.0.CO;2.

Wu, J. (1988). Variations of whitecap coverage with wind stress and water temperature. *Journal of Physical Oceanography, 18*, 1448–1453. https://doi.org/10.1175/1520-0485(1988)018<1448:VOWCWW>2.0.CO;2.

Wu, J. (1989). Reply. *Journal of Physical Oceanography, 19*, 710–711.

Wu, J. (1992). Individual characteristics of whitecaps and volumetric description of bubbles. *IEEE Journal of Oceanic Engineering, 17*, 150–158. https://doi.org/10.1109/48.126963.

Wu, J. (2000). Bubbles produced by breaking waves in fresh and salt waters. *Journal of Physical Oceanography, 30*, 1809–1813. https://doi.org/10.1175/1520-0485(2000)030<1809:BPBBWI>2.0.CO;2.

Yuan, Y., Han, L., Hua, F., Zhang, S., Qiao, F., Yang, Y., & Xia, C. (2009). The statistical theory of breaking entrainment depth and surface whitecap coverage of real sea waves. *Journal of Physical Oceanography, 39*, 143–161. https://doi.org/10.1175/2008JPO3944.1.

Zheng, Q. A., Klemas, V., Hayne, G. S., & Huang, N. E. (1983). The effect of oceanic whitecaps and foams on pulse-limited radar altimeters. *Journal of Geophysical Research, 88*, 2571–2578. https://doi.org/10.1029/JC088iC04p02571.